Study of Performance of Geosynthetic-Reinforced Pavements by Full-Scale Field Study, Laboratory Testing, and Numerical Modelling

by

Danrong Wang

A thesis

presented to the University of Waterloo

in fulfillment of the

thesis requirement for the degree of

Doctor of Philosophy

in

Civil Engineering

Waterloo, Ontario, Canada, 2024

Examining Committee Membership

The following served on the Examining Committee for this thesis. The decision of the Examining Committee is by majority vote.

External Examiner	**Dr. Hosin (David) Lee** Civil and Environmental Engineering, University of Iowa
Supervisor	**Dr. Susan Tighe** Civil and Environmental Engineering, University of Waterloo
Supervisor	**Dr. Shunde Yin** Civil and Environmental Engineering, University of Waterloo
Internal Member	**Dr. Hassan Baaj** Civil and Environmental Engineering, University of Waterloo
Internal Member	**Dr. Giovanni Cascante** Civil and Environmental Engineering, University of Waterloo
Internal-External Member	**Dr. Kaan Inal** Mechanical and Mechatronics Engineering, University of Waterloo

Author’s Declaration

This thesis consists of material all of which I authored or co-authored: see Statement of Contributions included in the thesis. This is a true copy of the thesis, including any required final revisions, as accepted by my examiners. I understand that my thesis may be made electronically available to the public.

Statement of Contribution

Chapter 4 of the thesis is based on a journal paper published on Applied Sciences. The detailed citation can be found at: Wang, D., Wang, S.-L., Tighe, S., Bhat, S., & Yin, S. (2023). Construction of Geosynthetic–Reinforced Pavements and Evaluation of Their Impacts. Applied Sciences, 13(18), 10327.

Chapter 5 of the thesis is extended based on a conference paper accepted for publication and presentation at the 14th International Society for Asphalt Pavements (ISAP) Conference that will be hosted in Montreal, Canada in June 2024. The paper is entitled “Evaluation of Rutting and Moisture-Susceptibility of Geogrid-Embedded Asphalt by Hamburg Wheel-Track Testing”.

The methodology of Chapter 6 of the thesis is developed based on a journal paper co-authored by Dr. Wang, myself, Dr. Tighe, Mr. Bhat, and Dr. Yin. Dr. Wang and I developed the methodology and research design of the paper. The detailed citation can be found at: Wang, S.-L., Wang, D, Tighe, S., Bhat, S., & Yin, S. (2023). Investigation of Rutting Performance in Geogrid-Reinforced Asphalt by Penetration Test. Materials, 16(22), 7221. The content presented in this thesis is based on the experiments solely performed by myself with the methodology extended from the paper.

Part of Chapter 7 of the thesis is incorporated into a conference paper submitted for publication and presentation at the 5th Pan-American Conference on Geosynthetics of GeoAmericas 2024 which will be hosted in Toronto, Canada in April 2024. The paper is entitled "Monitoring the Performances of a Geosynthetic-Reinforced Pavement During Construction”.

Part of Chapter 7 with the information supplemented by Section 4.3 of the thesis is incorporated into a conference paper submitted for publication and presentation at the 10th International Conference on Maintenance and Rehabilitation of Pavements (MAIREPAV10) that will be hosted in Portugal in July 2024. The paper is entitled "Investigating the Performances of Geosynthetic-Reinforced Pavement During Construction by Field Testing and Laboratory Testing”.

Chapter 9 of the thesis is extended based on a conference paper published and presented at the Canadian Society of Civil Engineering (CSCE) Annual Conference 2021 that was hosted in June 2024. The detailed citation can be found at: Wang, D., Tighe, S. L., & Yin, S. (2023). Preliminary Analysis of Permafrost Degradation in Ingraham Trail, Northwest Territories. Proceedings of the Canadian Society of Civil Engineering Annual Conference 2021, 109–121.

Abstract

This study provides a comprehensive understanding of geosynthetic-reinforced pavements from different perspectives including small-scale laboratory testing, a full-scale field study, and numerical simulation. This study on geosynthetic-reinforced pavements evaluated two geosynthetic materials: fibreglass geogrid in the asphalt layer; and geogrid composite at the interface of base and subgrade.

Fibreglass geogrid-embedded asphalt samples were made with three types of fibreglass geogrids – Geogrid 11, Geogrid 11 EPM (Engineered Polymeric Membrane) and Geogrid 10. The samples were tested with a conventional Hamburg Wheel-Tracking Test (HWTT) in a small-scale laboratory facility to evaluate the rutting and moisture susceptibility. The test outcomes indicate that Geogrid 11, characterized by larger openings, exhibits superior resistance to rutting. Conversely, Geogrid 10, with smaller openings, demonstrates lower susceptibility to moisture. Geogrid 11 EPM, featuring an additional adhesive membrane, exhibits the poorest performance in terms of both rutting resistance and moisture susceptibility. This suboptimal performance is attributed to the insufficient compaction effort, which further initiated another test proposed to evaluate the rutting resistance, namely the dynamic creep test. The proposed test was built upon the existing flow number test, with the stressed importance of extended testing protocols. The test results were analyzed with three major indicators, flow number, mean creep rate, and ultimate creep modulus, which highlight that fibreglass geogrid reinforcement plays a crucial role in enhancing resistance to permanent deformation, thereby increasing the asphalt's resistance to rutting. Results demonstrate a contrary conclusion with the HWTT, that Geogrid 11 EPM with larger openings but extra bonding provides the best rutting resistance. A less aggressive freeze-thaw (F-T) conditioning procedure was introduced to integrate with the dynamic creep test for geogrid-embedded asphalt samples to assess the impact of moisture damage on permanent deformation. The findings reveal that unreinforced samples consistently exhibit the poorest performance. In contrast, geogrids with larger openings and additional bonding demonstrate a capacity to mitigate the detrimental effects of moisture-induced damage.

The feasibility, constructability, and impacts of construction activities on pavements reinforced by these two types of materials were assessed during the construction of the field trial sections, and evaluated against an unreinforced control section. Post-construction field performance was monitored by field testing and instrumentation. Pavement stiffness tested by the Light Weight Deflectometer in the control section was notably influenced by ambient and pavement temperatures, indicating the effect

of geosynthetic materials in preventing pavement stiffness from varying from temperature changes. Roughness measurements underline the need for an overlay of the surface course with geogrid reinforcement in the asphalt concrete layer. Truck testing further demonstrates the load-distribution capabilities facilitated by the fibreglass geogrid embedded in the asphalt layer. Field instrumentation was monitored for a year after construction completion, which demonstrates negative temperature differentials in the geogrid composite section during winter, indicating the effectiveness of the geogrid composite in regulating subgrade temperature and mitigating frost-related risks. Moisture data further illustrates relatively drier conditions in the geogrid composite section, underscoring its draining behaviour, particularly pronounced during thawing seasons. In the fibreglass geogrid section, a lower level of strain variation and pressure experienced at the bottom of the asphalt highlights the reinforcement capabilities and strain-absorption properties facilitated by the fibreglass geogrid. Additionally, the geogrid composite section exhibits lower strain and pressure on the subgrade compared to the control section, highlighting the reinforcing impact of the geogrid composite on the subgrade.

Lastly, pavement layer temperature predictive models with the input of ambient temperature were developed. A numerical model coupled with thermal-hydro-mechanical processes was created to simulate the pavement performance under freeze-thaw actions and examine the use of geogrid composite on the subgrade. The simulation from 2022 to 2023 using the developed model, with the input of pavement layer temperature predictive models and characterized field material properties, demonstrates less temperature variation in the subgrade, lower saturation levels, and reduced displacement after the thawing period in the geogrid composite section compared to the control section. This highlights the crucial role of the geogrid composite in drainage, subgrade temperature stabilization, and mitigating freeze-thaw disturbances in the pavement.

Acknowledgements

I would like to express my deepest gratitude to my supervisor, Dr. Susan Tighe, whose impactful lecture during my second year of undergraduate studies sparked my keen interest in transportation engineering. Throughout my Ph.D., Dr. Tighe provided invaluable support and guidance, serving not only as a supervisor in academia but also as a life mentor. Her encouraging words and motivational spirit have been influential in shaping my academic journey. As a female professional in the field of engineering, she has been setting a remarkable example. I am truly grateful for the invaluable mentorship and inspiration she has provided. I extend my sincere appreciation to my supervisor, Dr. Shunde Yin, whose abundant knowledge has been influential in shaping my research journey. Dr. Yin's support and guidance, coupled with his remarkable patience and understanding, have created an enriching academic setting for me. His dedication to fostering learning and research has been a source of inspiration throughout my Ph.D. I am truly grateful for the privilege of working under his mentorship.

I would like to acknowledge my Ph.D. committee members Dr. Hassan Baaj, Dr. Giovanni Cascante, and Dr. Kaan Inal from the University of Waterloo, and my external examiner Dr. Hosin (David) Lee from the University of Iowa for being willing to participate in my Ph.D. defence and their input to improve this work.

Thanks to the Natural Sciences and Engineering Research Council of Canada (NSERC) Collaborative Research and Development Program and TITAN Environmental Ltd. for funding this project. I would like to thank Sam Bhat from TITAN Environmental Ltd. for his valuable technical guidance and support on this research.

I would like to express my gratitude to the dedicated members of the Civil and Environmental Engineering (CEE) Department staff: Peter Volcic, Robert Kaptein, Isabelle Graansma, and Richard Morrison. Their invaluable technical support and advice in both laboratory and field settings have significantly enhanced the quality and depth of my research.

My sincere appreciation goes to Ken Brisbois from the Region of Waterloo and Josh Eldridge and Jeremy Bieniarz from WalterFedy. Their steadfast support, before, during, and after the construction of the field sections, has been contributory in facilitating the success of this project. Their collaborative efforts have significantly contributed to the seamless execution of the construction phase.

My genuine gratitude extends to my dearest friends and colleagues in the Centre for Pavement and Transportation Technology (CPATT) and the Civil and Environmental Engineering (CEE) Department at the University of Waterloo. Special thanks to Dr. Shenglin Wang, Dr. Roberto Aurilio, and Jonathan Zingaro for their help and support throughout this project. I am also grateful to Dr. Pejoohan Tavassoti, Dr. Abimbola Grace Oyeyi, Dr. Vimy Henderson, Crystal Xinyue Ni, Dr. Hui Liao, Dr. Dandi Zhao, Tianshu Zhang, Dr. Ali Qabur, Dr. Saeid Salehiashani, Aditi Sharma, Leila Miri, Dr. Nadine Ibrahim, Yifei Yang, Matea Ceric, Dr. Frank Yang Liu, Dr. Jessica Achebe, and many others who offered their assistance without hesitation. The collaborative efforts of these individuals have significantly enriched the depth and scope of my research, and I am truly thankful for their contributions.

I extend heartfelt appreciation to my dearest friends and family who have been pillars of support throughout my academic journey. Thanks to my grandparents, for their love and encouragement that have been constant in my life. A special acknowledgment to my grandfather, my guiding light in the field of engineering. Grandaunt, your food filled with love has been a source of strength, and I am truly grateful. A sincere thank you to Jerry Daixuan Li, whose love and companionship during my Ph.D. journey have been invaluable. Your patience and support have made a significant impact. To my friends scattered around the globe, your positive energy and encouragement have been a constant source of inspiration. A warm thanks to Xueer Zhang, Niklas Tianhao Wu, Rex Chijung Lee, Tess Alexander, Siyu Chen, Jinyi Jinny Lee, Jiaqi Qiu, Jeff Jieyu Wu, Qingsheng Xu, Katherine Shuqing Liu, Jiali Luo, Coco Jiahui Hu, Bolin Chen, Rahanuma Wafa, and Morgan Yi Xuan. Your friendship has made this academic journey richer, and I am grateful for each of you.

I express my deepest gratitude to my parents, Xiaoli Huang, and Jun Wang, for their unconditional love and support throughout my life. Thank you for the sacrifices you made to make everything possible and help me to pursue my education, leading me to where I am today. Your continuous support has been my foundation, which gives me the courage to face and embrace a larger world. Thank you for always being my backbone and inspiring me to reach greater heights.

Lastly, thanks to God, whose unstoppable love has guided me through all the obstacles. In moments of uncertainty and challenges, His steadfast presence has provided me with comfort, strength, and resilience.

Dedication

This thesis is dedicated to my Mom and Dad.

Your love and sacrifices mean everything to me.

Table of Contents

List of Figures

List of Tables

Chapter 1
Introduction

1.1 Background

Canada maintains, manages and operates more than 765,000 km of roads, and road assets account for around 50% of the total replacement value for infrastructure in poor condition that needs rehabilitation or replacement in the country (Government of Canada, 2018). As global warming intensifies, climate change increasingly brings adverse effects on infrastructure. Three major climate change impacts on pavements have been identified by the Government of Canada: rutting with increased temperature; pavement deformation due to freeze-thaw cycles; and ground settlements due to excessive precipitation (Maadani, Shafiee, & Egorov, 2021). In light of the impacts of climate change on pavements, it is necessary to study these challenges on pavements to formulate effective mitigation strategies.

Flexible pavement is one of the most common pavement types worldwide, which takes up to 95% of the roads globally (Yue Huang, Bird, & Heidrich, 2007). In Canada, flexible pavements make up approximately 64% of federal and provincial road networks and a significant 76% of municipal roads (Tighe, 2013). However, flexible pavement faces a critical challenge in terms of premature failure, primarily attributed to rutting and fatigue cracking. Specifically, rutting as the accumulation of permanent deformation describes the depression along wheel paths in flexible pavements. Due to the impermeability of asphalt concrete, the water could be trapped and can subsequently cause vehicle hydroplaning (Farashah, Salehiashani, Varamini, & Tighe, 2021). Additionally, such distresses could accelerate moisture damage on asphalt materials (Kim, Zhang, & Ban, 2012). A recent study suggests that asphalt materials can be more prone to permanent deformation with an increase in temperature and the occurrence of extreme weather events (Maadani et al., 2021).

The impacts and potential risks arising from freeze-thaw cycles extend across various domains, affecting vegetation, biochemical processes, hydrological systems, and engineering infrastructures (Frederick E. Nelson, Anisimov, & Shiklomanov, 2001). Freeze-thaw is also one of the reasons leading to pavement deterioration in the Northern Hemisphere in high-latitude and colder regions (T. Zhang, Barry, Knowles, Heginbottom, & Brown, 1999). These regions have been significantly impacted due to their sensitivity to changes in ground and ambient temperatures (Anisimov et al., 2001; Guo & Wang, 2013). In addition, the decreasing number of frozen days caused by global warming also results in the occurrence of freeze-thaw actions more frequently, where the pavement temperature oscillates above

and below the freezing point more regularly. This increased frequency of temperature fluctuations further highlights the challenges posed by freeze-thaw cycles on pavement structures. In these areas, significant changes in the lengths of freeze and thaw cycles have also been observed (X. Li, Jin, Pan, Zhang, & Guo, 2012). These are considered to be even more sensitive to temperature change as the ground has higher temperatures and the soil contains more ice content (Cheng & Wu, 2007). Consequently, significant pavement damage in cold areas can be caused by frost heaves and thaw settlements, namely differential settlements.

Various maintenance and reinforcement measures have been developed to extend pavement service life. Some rehabilitation strategies such as asphalt overlays may allow the existing cracks and discontinuities to easily propagate, which are called reflective cracks. Some techniques have been introduced and developed to mitigate these problems, namely one in the form of interlayers. Interlayers serve as a preventive measure against reflective cracks and employ a range of materials. The commonly used interlayer materials include woven and non-woven geotextiles, fibreglass geogrids, and stress-absorbing membrane interlayers (SAMI) (Sudarsanan, Mohapatra, Karpurapu, & Amirthalingam, 2018). Geosynthetic materials describe polymeric synthetic materials used for civil and geotechnical applications including fibreglass geogrid, geotextile, geogrid composite, geocell, etc. (Titan Environmental Containment, 2021a).

As one of the commonly used interlayer solutions, it is necessary to examine the inclusion and performance of geosynthetics in flexible pavement structures. Geosynthetic-reinforced pavements incorporate geosynthetic materials, such as geotextiles or fibreglass geogrids, within the unbound granular base or subbase layer of pavement structures to enhance stiffness and stability. Geotextiles function as a membrane between the granular course and subgrade soils. Woven geotextiles primarily serve for separation and erosion control, while non-woven geotextiles are selected for filtration and drainage purposes. In the unbound granular layer, fibreglass geogrids play a crucial role in providing lateral confinement under traffic loading. Stretched geosynthetics effectively restrain the lateral movement of unbound materials, generating lateral confinement forces that can be represented by a triangularly distributed confining stress distribution (Gu et al., 2016). Additionally, fibreglass geogrids contribute to enhancing the base material modulus through confinement, increasing bearing capacity, reducing vertical stress, improving vertical stress distribution on the base and subgrade, and mitigating shearing at the top of the subgrade (Perkins, Christopher, Lacina, & Klompmaker, 2012). Targeting an emerging trend of application of geosynthetics in pavements, it is important to optimize the geosynthetic materials in design and application to effectively mitigate the climate impacts. Therefore,

it emphasizes the necessity to study and characterize the construction and performances of geosynthetic-reinforced pavements from a sophisticated and comprehensive perspective.

The overall performance of geosynthetic-reinforced pavement is subjected to various factors, such as geosynthetic properties such as its aperture size, stiffness, as well as the location of geosynthetics within the pavement structure (Abu-Farsakh & Chen, 2011). Other influencing factors include the pavement structure itself, subgrade conditions, traffic loading, construction quality, climate conditions, etc. However, few studies have comprehensively addressed all these variables, quantified their interactions, and investigated the thermal, hydraulic, and mechanical behaviour of geosynthetic reinforced-pavement structures. This lack of comprehensive understanding highlights the need for research on this topic. Therefore, this thesis studies two geosynthetic products, geogrid composite for unbound layers and fibreglass geogrid for asphalt course, which is suited for applications in Canada.

1.2 Terminology

In this thesis, the geogrid composite indicates the material installed at the interface of the base/subbase and subgrade. Geogrid indicates the fibreglass geogrid installed within the asphalt. Geosynthetics or geosynthetic materials are general terms indicating both geogrid composite and fibreglass geogrid. When referring to the field trial sections, the unreinforced control section with conventional flexible pavement structure is represented by Section 1, the CT section. The section with fibreglass geogrid installed in the middle of the asphalt binder course is indicated by Section 2, the GG section. The section with geogrid composite installed at the interface of base and subgrade is indicated by Section 3, the GC section.

1.3 Research Hypotheses

The primary hypotheses for this research are the followings:

- Geosynthetic materials as an interlayer system can not only prevent reflective cracking, but also provide reinforcement, separation, and filtration to the pavement. Due to its adaptability to different climates, ease of installation, and cost-efficiency, it can be used as an efficient tool to prevent adverse impacts of freeze-thaw cycles on pavements.
- Placing fibreglass geogrid within the asphalt course can provide reinforcement to the asphalt layer by offering lateral restraints and load distribution.
- The inclusion of fibreglass geogrid in the asphalt layer could be easily planned, installed, and constructed without sacrificing the structural integrity of pavements.

- Geogrid composite can offer drainage, filtration, and reinforcement to unbound materials and subsequently prevent moisture damage on weak soils. Structural integrity could also be provided by facilitating draining water when the pavement is thawing.

1.4 Research Scope and Objectives

The primary focus of this study is on flexible pavement structures that undergo the challenges posed by climate change. The central objective is to optimize the utilization of geosynthetic materials, considering various factors such as aperture sizes, material properties, traffic loading, construction, and diverse climate conditions. Laboratory testing was performed to investigate the mechanism of geogrids within the asphalt layer including rutting and moisture susceptibility. A Thermo-Hydro-Mechanical (THM) finite element model was developed to simulate the pavement structures under freeze-thaw cycles with and without interlayer systems. A full-scale study was conducted with field instrumentation and field testing to monitor the performance of pavements under construction as well as the performance of in-service pavements. Three sections were studied including a reinforced section with geogrid installed in the asphalt layer; a reinforced section with geogrid composites installed on the subgrade; and an unreinforced section.

The main objectives of this research include:

- Characterize the properties of pavement materials sampled from the field including subgrade soils, base aggregates, and asphalt mixtures to evaluate their interactions with geosynthetics.
- Evaluate the constructability and impacts of construction activities on geosynthetic-reinforced pavements during the construction of the field trial sections.
- Perform small-scale laboratory performance testing on asphalt materials embedded with geogrids to investigate their resistance to rutting and moisture damage.
- Monitor the field performances by instrumentation and conducting field testing on the trial sections to examine the pavement structures reinforced with geosynthetics against the unreinforced conventional flexible pavements with the interaction with environmental factors.
- Develop a thermal-hydraulic-mechanical numerical model to predict the effectiveness of geogrid composite as an interlayer system in the pavement to mitigate the adverse effects of freeze-thaw cycles.

1.5 Thesis Organization

This thesis is composed of the following ten chapters, which can be broken down into the following:

- Chapter 1 Introduction - presents the background information and the research scope and objectives to summarize the structure of the thesis.
- Chapter 2 Literature Review - details the literature review conducted that initiated this study and identified the research gap.
- Chapter 3 Methodology and Data Sources - presents the methodology used in this study to achieve the objectives. The overall structure of the approaches as well as the methods used in the tasks were explained.
- Chapter 4 Construction of Geosynthetic-Reinforced Pavements and Evaluation of their Impacts by a Large-Scale Field Study - presents the details of the field construction and instrumentation plan for the trial sections. The material characterization sampled from the field was presented. The constructability and impacts of construction activities on geosynthetic-reinforced pavements during the construction were also evaluated.
- Chapter 5 Evaluation of Permanent Deformation and Moisture Damage on Geogrid-Reinforced Asphalt by Hamburg Wheel-Track Testing - evaluates the rutting and moisture susceptibility of geogrid-embedded asphalt samples by the conventional Hamburg Wheel-Tracking test.
- Chapter 6 Evaluation of Permanent Deformation and Moisture Damage on Geogrid-Reinforced Asphalt by Dynamic Creep Testing - evaluates the rutting resistance of geogrid-embedded asphalt samples by a modified dynamic creep test. Subsequently, the resistance to moisture damage was also evaluated by freeze-thaw conditioning.
- Chapter 7 In-Service Pavement Performance Monitoring by Field Testing - investigates the in-service geosynthetics-reinforced pavement performances by field testing to examine the roughness, stiffness, and critical mechanical response from heavy traffic loading with instrumentation.
- Chapter 8 In-Service Pavement Performance Monitoring by Instrumentation - investigates the use of geosynthetics in in-service pavement performances with data obtained from instrumented sensors including temperature, moisture, pressure, and strain.
- Chapter 9 Model Development for Pavement Reinforced by Geogrid Composite with the Impact of Freeze-Thaw Cycles - presents the numerical model developed to simulate the

pavement performance under freeze-thaw actions and examine the use of geogrid composite on the subgrade.

- Chapter 10 Conclusion - summarizes the main findings and provides recommendations for future studies.

Chapter 2
Literature Review

2.1 Introduction

This chapter details the literature review conducted that initiated this study. The background information including the impact of freeze-thaw actions on pavements and flexible pavement distresses related to climate change such as rutting, and moisture damage was presented. Then, a thorough literature review was conducted on the numerical modelling of Freeze-Thaw (F-T) actions. Geosynthetic materials were introduced with their applications and current studies including laboratory testing, field testing, and numerical modelling. The chapter concludes by identifying research gaps to help conceptualize the framework of this study.

2.2 Impact of Freeze-Thaw Cycles on Pavements

Human infrastructures are mostly designed based on current climate and soil conditions. Attention has to be paid to F-T actions and their adverse effect on infrastructure. In Northern climates, F-T actions associated with frost heave and thaw settlement can significantly damage infrastructure built in cold areas affecting its structural resilience. To demonstrate this point, in Norilsk, Russia, 20 people lost their lives when a building collapsed due to a melting foundation and more than 300 buildings experienced similar structural deterioration. Similarly, an investigation in 1990 revealed that about 83.5% of the damage to the Qinghai-Tibet Highway was caused by thaw settlement, while 16.5% of the damage was caused by frost heave (Tong & Wu, 1996). These examples demonstrate that differential thawing settlement in the cold areas (Guo & Sun, 2015; F. E. Nelson, Anisimov, & Shiklomanov, 2002) and the resultant thaw settlement and frost heave can cause major damage to the infrastructure located in these regions.

2.2.1 Frost Heave and Thaw Settlement

For a pavement structure, frost heave happens in the foundation, where water is trapped in the soil, leading to crystallization and an ice layer when frozen. When a frost susceptible soil freezes, the water within the soil experiences a phase change and consolidates (Sheng, Axelsson, & Knutsson, 1995a). The remaining water migrates from the unfrozen zone of the soil to the frozen zone through the capillary rise, which results in the segregated ice which may form “ice lenses”. The ice segregation along with the accumulated water at the freezing front increases the volume of the soil (Hansson, Šimůnek,

Mizoguchi, Lundin, & Genuchten, 2004). As the ice lens expands, the resulting increasing in volume can lead to an upward movement of the subgrade, causing cracks in the upper layers of the pavement.

On the other hand, as the weather becomes warmer, the ice within the pavement melts and softens the subgrade. The melting occurs from top to bottom, and the drainage of melted water is a critical issue as the ice below is still frozen. Due to the thaw, ice lenses melt and the water escapes resulting in the softening of the soil due to a higher void ratio. This leads to the loss of bearing capacity and decreases the stability of the pavement; thaw settlement is then likely to occur due to the downward movement of the soil with additional pore pressure induced by heavy traffic loading.

2.2.2 Freeze-Thaw Protections

One cost-effective technology to mitigate the adverse impact of F-T cycles is to use insulation materials to lower the speed of heat transfer and delay the thawing process of the underlying soil by increasing the thermal resistance of the pavement (Cheng, Zhang, Sheng, & Chen, 2004). Typical insulation materials include turf, moss, expanded polystyrene (EPS), extruded polystyrene (XPS), and polyurethane (PU). The main characteristic of these materials is their low thermal conductivity, which provides high heat resistance preventing heat from transferring to the soil (Doré & Zubeck, 2009). Modern insulation materials like EPS and XPS provide extremely low thermal conductivity that is much lower than the ground thermal conductivity. This creates great differences between the temperature above and below the insulation layer, and the penetration of heat from the surface can be impeded into the ground (Zhi, Yu, Wei, Jilin, & Wu, 2005). However, the insulation method has some limitations. For example, the long-term has challenges as the insulation boards may degrade (Regehr, Milligan, Montufar, & Alfaro, 2013). It is calculated that the stability of the embankment can only be ensured with the insulation materials when the mean annual temperature is lower than -3.84 ºC (X. Q. Chen, Li, Wang, & Zhang, 2012). Therefore, this method is only effective in regions with low ground temperature and may not be suitable in warmer regions with more active F-T actions. To mitigate F-T impacts, some innovative methods have been developed to actively cool embankments using heat pipes. The embedded heat pipes control heat convection with the condensing and vaporizing cycle of anhydrous ammonia in a pipe (Yaling, Gongqi, Baoan, & Yu, 2014). Sloped crushed rock revetments or raising the height of the embankment can also be implemented to increase thermal resistance with the conductivity of the gravel layer (Cheng, Wu, & Ma, 2009; M. Zhang, Lai, Li, & Zhang, 2006). Ventilation pipes have also been used to control heat radiation by extracting the heat from the pipe using cold air and wind (B.-X. Sun et al., 2012; B. Sun et al., 2011). However, these techniques have

some downsides such as high installation and maintenance costs, large construction footprint, and requirement of large quantities of materials.

2.3 Flexible Pavement Distresses

With the escalation of global warming, climate change is exerting growing adverse effects on infrastructure. As mentioned, the Government of Canada has identified three significant climate change impacts on pavements: increased temperature leading to rutting of the asphalt mixtures, pavement deformation resulting from freeze-thaw cycles, and ground settlements due to excessive precipitation. (Maadani et al., 2021). Given the adverse impacts of climate change on pavements, this section discusses these distresses on flexible pavements and corresponding common testing practices.

2.3.1 Permanent Deformation

In asphalt pavements, rutting is one of the major distresses with increased traffic and axial loading. Rutting typically appears as longitudinal depression along the wheel paths (Simpson, 1999). As defined, rutting represents the accumulation of permanent deformation which develops with increased applied loading as well as high temperature (Albayati, 2023). Permanent deformation in the asphalt layer is a combination of two types of deformation: densification which is the consolidation of pavement occurring in the wheel paths; and shear deformation which is developed with asphalt shear flow (Xu & Huang, 2012).

Several laboratory tests have been developed to investigate the resistance potential of permanent deformation of asphalt (Golalipour, 2020), which evolves from empirical testing (e.g., Hubbard-Field, Marshall, and Hveem tests) to characterize the asphalt stability, through simulation testing (e.g., wheel tracking test), to fundamental test (e.g., static and dynamic creep tests) (Witczak, Kaloush, Pellinen, El-Basyouny, & Quintus, 2002; F. Zhou, Fernando, Scullion, & Institute, 2008). In North America, the Hamburg Wheel Tracking Test (HWTT) is one of the most common tests to evaluate the rutting resistance adopted by various Department of Transportation (DOT) agencies and agencies (AASHTO, 2019a).

To achieve the closest in situ pavement conditions in real life, the dynamic creep test was also believed to be a good tool to evaluate the permanent deformation potential of asphalt mixtures with repeated loading to reproduce the main causes of rutting (Khodaii & Mehrara, 2009). The implementation of the repeated creep test is suggested as a technique for isolating the dissipated energy and approximating the resistance to the buildup of permanent strain for asphalt binders (Golalipour,

2020). Creep behaviour can symbolize the viscoelastic response exhibited by asphalt materials. A previous study indicates that the slope of the secondary stage which signifies the steady creep rate in the creep curve, can capture the material's creep characteristics, which reflects the material's deformation properties (J.-Shan. Zhang, 2010). Both static creep test with flow time and dynamic creep test with flow number as indicators have been reported to show good correlation with field measurements (Kaloush et al., 2002). In this study, it is important to assess the permanent deformation potential of geogrid-embedded asphalt specimens.

2.3.2 Freeze-Thaw Impacts and Moisture Damages

Moisture-induced damage can decrease the adhesion between binder and aggregate and subsequently result in stripping. Different laboratory testing was developed to investigate the asphalt mixture's moisture susceptibility, including immersing asphalt materials in water for a specific length of time, or assigning rolling bottle or F-T cycles on asphalt samples (Omar, Yusoff, Mubaraki, & Ceylan, 2020; Soenen, Vansteenkiste, & Kara De Maeijer, 2020). Water saturation and freeze-thaw cycles were observed to have no significant impact on the fatigue performance of asphalt materials. Asphalt was saturated in water to different levels and assessed with tensile strength (Behiry, 2013). As mentioned, F-T cycles in cold regions could contribute to result in moisture damage to asphalt concrete (Kavussi & Hashemian, 2012). With the lack of a standardized F-T conditioning procedure, various approaches were used to better replicate the local climate. In one study, the asphalt samples were frozen at −5 °C for 16 hr and +30 °C for 8 hr and subjected to different numbers of F-T cycles (R. Tarefder, Faisal, & Barlas, 2018). Another study used -18 °C as freezing for 24 hr and 25 °C as thawing temperature at 24 hr (Lachance-Tremblay, Perraton, Vaillancourt, & Di Benedetto, 2017). AASHTO T283 specified a preconditioning procedure to assess the moisture susceptibility by freezing the samples at -18 °C for 16 hr while thawing at 25 °C for 24 hr (AASHTO, 2014). Some studies follow a similar conditioning process (Duojie et al., 2021; Kringos, Azari, & Scarpas, 2009; Y. Liu, Ni, Pickel, Tighe, & Kou, 2022; Yu, Jing, & Liu, 2022). Some other studies referred to the standard developed for F-T conditioning on concrete, as per ASTM C666 (ASTM, 2016), by storing samples in a temperature chamber with different freezing and thawing temperatures specified (Attia, Asce, Abdelrahman, & Asce, 2010; Badeli, Carter, & Doré, 2018). Tran et al. (2022) conditioned the asphalt samples by saturating first, followed by F-T cycles in a thermal chamber from -15 °C to 10 °C with the samples sealed in plastic bags (Tran, Sauzéat, Di Benedetto, & Pouteau, 2022).

As the rutting is shown as bowl-like distress along the wheel path with upheavals to the sides, water can be easily trapped by ruts, which could cause hydroplaning (Fontes, Trichês, Pais, & Pereira, 2010). Also, it has been stated that asphalt materials are more prone to moisture damage with the occurrence of permanent deformation (Maadani et al., 2021). With the two major mechanisms contributing to rutting: densification, and shear plastic deformation (Collop, Cebon, & Hardy, 1995), F-T cycles could rearrange the structure within asphalt mixture (Ud Din, Mir, & Farooq, 2020a). The asphalt samples subjected to F-T cycles in Wong et al's study were found to be more rutted compared to unconditioned ones (Wong et al., 2004). Liao et al (2023) utilized the Stripping Inflection Point (SIP) as well as three proposed parameters including stripping number, moisture ratio, and stripping life obtained from HWTT results to evaluate the asphalt mixtures' moisture susceptibility (Liao, Tavassoti, Sharma, & Baaj, 2023). Overall, in this study, it is important to investigate how geosynthetic materials could help mitigate moisture damage.

2.4 Numerical Modelling

2.4.1 Early Frost Action Modelling

Only in the last century, engineers have noticed the problems caused by the freeze-thaw cycles of the soil to the infrastructures in the cold regions (Ferrians, Kachadoorian, & Greene, 1969). The major causes of the frost heave within the soil were demonstrated to be not only the freezing of the in-situ pore water but also the water migration (Taber, 1930). The capillary theory was raised to illustrate the thermodynamics of the soil and the formation of the ice lenses (Everett, 1961).

A secondary heaving theory was suggested to address the underestimation of the heaving of the soils with the sole consideration of capillary theory (R. D. Miller, 1972). The secondary heaving theory generally proposed an idea of frozen fringe, referred to as the zone without frost heaves, located between the freezing area and the base of warm ice lenses. The frozen fringe is greatly determined by the soil parameters and the overburden effect.

Numerous numerical models have been developed to quantify the frost penetration and heave of soils. One early model was developed using the soil properties with various surface temperatures and overburden pressure to model the heaving rate (Gilpin, 1980). The rigid ice model was then developed based on the secondary frost heave theory to illustrate the formation, distribution, and development of ice lenses (O'Neill & Miller, 1985), based on which the more generalized and simplified rigid ice model

was developed (Fowler & Krantz, 1994). The rigid ice model however ignores the heat transfer due to heat convection.

2.4.2 Models with Coupled Physical Processes

With the temperature and mass transfer as well as water migration, models were developed that coupled together multiple processes. The temperature-hydraulic coupling theory was first proposed with a nonlinear relationship between temperature gradients and fluid flow in porous media (Philip & De Vries, 1957). Then, the first thermo-hydro (TH) coupling model was developed to simulate the heat and moisture transport in freezing porous media (Harlan, 1973), followed by a modified model utilizing an implicit finite-difference scheme to integrate the fluid and heat equations (Taylor & Luthin, 1978b). Meanwhile, the Richards equation was introduced into the heat transfer process and the equilibrium equation was solved with regard to pore water pressure and temperature (Gary L. Guymon & Luthin, 1974). Clapeyron equation was introduced to solve the ice pressure in the frozen fringe to simulate the formation of the ice lenses and the frost heave (Sheng, Axelsson, & Knutsson, 1995b). In general, the TH models work by leveraging the law of mass and energy conservation.

A thermo-mechanical (TM) model was developed based on linear momentum equations, in which a porosity rate function, rather than fluid mass, was proposed to simulate mechanical features in the freezing soil (Michalowski & Zhu, 2006).

Finally, thermo-hydro-mechanical (THM) models were developed integrating the dynamic interactions of the thermal, hydraulic, and mechanical processes. For example, the THM mechanism during the freeze-thaw processes of rock was investigated by a non-linear constitutive model (Neaupane & Yamabe, 2001). THM processes of frost behaviour in unsaturated porous media were simulated (Z. Liu & Yu, 2011a). THM models were also developed in saturated porous media using the void ratio separation concept (J. Zhou & Li, 2012a) and the phase-field method (Sweidan, Heider, & Markert, 2020). In addition, another recent THM model was developed to simulate artificial ground freezing (Tounsi, Rouabhi, & Jahangir, 2020).

2.4.3 Multilayer Models Simulating Freeze-Thaw

While extensive study has been done to model the heave in the freezing soil and rock, the investigation of the freezing and thawing processes in pavement systems has rarely been addressed. Among the few models, a multi-physical model was developed for heave prediction in an instrumented pavement section (Z. Liu & Yu, 2011b). The FROST model was developed to predict the frost heave and thaw

settlement in the pavements (G L Guymon, Berg, & Hromadka, 1993) and has been validated with large-scale experiments with acceptable frost penetration and heave (Shoop & Bigl, 1997).

The finite element method is the most common method to numerically simulate the thaw settlement. In pavement engineering particularly, Hildebrand (1985) uses the finite element method to discretize the pavement into one-dimension elements with vertical nodes, where the ground is treated as a continuous medium and is evaluated linearly throughout the space domain. A finite element model predicting thaw settlement with the incorporation of surface roughness was also developed (Hildebrand, 1985). A second-order time integration scheme was employed by Hildebrand's model with the application of Galerkin's method of weighted residuals, while the basic function was replaced by quadratic functions. Another model, called SHAW, utilizes the finite difference method to solve the flux equations for each time step with Newton-Raphson iterations (Flerchinger, 2000).

2.5 Geosynthetic Materials

Flexible pavement is one of the most common pavement types worldwide. However, premature failure caused by rutting and fatigue cracking is a critical issue of this pavement type. The most common rehabilitation method is milling and constructing an asphalt overlay over the milled surface. However, as surveyed in the United States, the average service life of an asphalt overlay in thickness of 40-50 mm was 1-6 years in most states, as depicted in Figure 2-1 (Kwon, Kim, & Tutumluer, 2005). Such short service life on a rehabilitated infrastructure generates environmental, financial, and social concerns. Therefore, different techniques have been proposed to extend pavement's service life.

Figure 2-1 Average Service Life of A 40–50 mm Asphalt Overlay in the United States (Kwon et al., 2005)

A greater thickness of overlay could mitigate the reflective cracking propagated from the lower cracked pavement (Sherman, 1982). Another method utilizing open-graded asphalt was observed to effectively control reflective cracking on asphalt overlays on Portland cement and asphalt concrete (Hensley, 1980). Interlayer systems have been widely applied to enhance pavement integrity. The commonly used interlayer materials include woven and non-woven geotextiles, geogrids, and stress-absorbing membrane interlayers (SAMI) (Sudarsanan et al., 2018).

2.5.1 Development and Current Use of Geosynthetics

Early in 1982, geogrids were installed at Canvey Island, England, with the initial purpose of controlling reflective cracking on concrete pavements (Austin & Gilchrist, 1996). Then, geosynthetics including geotextiles and geogrids, become popular as an interlayer system to provide structural reinforcement, filtration, and separation by strengthening and controlling reflective cracking, and by providing a moisture barrier between asphalt pavement layers. The stiffness and stability of the pavements can be enhanced with geosynthetics by increasing the tensile strength when the bonding is effective. To control the cracks, geosynthetics can re-direct the movement of the cracks from vertical to horizontal along the interface. A stress-relieving interlayer can also be provided by geosynthetics by absorbing stresses at the crack tip with lower elastic stiffness (Lytton, 1989a). As moisture barriers, geosynthetics can limit the fluid filtration into the lower level of pavement to ensure the stability of the underlying soil. In addition, geosynthetics can effectively reduce pavement thickness, do not corrode, and are easy to

install in different climatic conditions (Saghebfar, Hossain, & Lacina, 2016). Recently, there has been a development of geogrid composites tailored for pavement applications, combining the advantageous features of both fibreglass geogrids and geotextiles (Bhat & Thomas, 2015b).

Therefore, geosynthetics offer several major functions to pavements for reinforcement, filtration and drainage, and separation. Geosynthetics are used to stabilize and reinforce the subgrade by increasing the bearing capacity of weak soils, as well as providing restraints to minimize the accumulation of permanent deformation in the subgrade (M. Shabbir Hossain, Hoppe, & Weaver, 2019). Geotextile was applied in Virginia between the subgrade and base course and successfully reduced about 20% surface permanent deformation on a weak subgrade (M. Shabbir, Hossain, Schmidt, Council, & Transportation, 2009). Also, geosynthetics can stiffen the unbound base/subbase materials by minimizing lateral movement with their interlocking and restraint effects. A variety of geosynthetic materials were constructed as subgrade stabilization and base/subbase reinforcement, which shows their successful applications by reducing the base/subbase thicknesses (Cuelho & Perkins, 2017). Despite the various studies and conclusions regarding the optimum location of geosynthetics, most studies found that the best location of geosynthetics to serve as stabilization and reinforcement of unbound course is the interface of subgrade and base/subbase course (Zheng et al., 2021). In general, typical applications of geosynthetics for reinforcement and stabilization involve improving, construction efficiency on the weak subgrade, saving base/subbase aggregate materials, and providing an alternative solution to replace thick granular backfill (Qamhia & Tutumluer, 2021). Geosynthetic materials such as geotextiles or paving fabrics can also assist in draining the control moisture in pavements by facilitating lateral drainage to enable in-plane flow (Zornberg, Azevedo, Sikkema, & Odgers, 2017). This contributes to enhanced pavement performance by minimizing pore water pressure resulting from traffic loading. Consequently, it aids in moisture content control and ensures the structural capacity of the pavement (Qamhia & Tutumluer, 2021). Also, the use of geosynthetics, particularly geotextiles, contributes significantly to the maintenance of pavement performance through their separation function. This function helps prevent the intermixing of pavement layers, effectively avoiding contamination of the unbound base/subbase layer by fine soils. This separation function plays a critical role in maintaining the structural integrity of unbound materials within the pavement system. (Giroud, Han, Tutumluer, & Dobie, 2022).

With the wide applications of geosynthetics in pavements, as discussed, the absence of a well-defined design method that can capture the mechanical behaviour of geosynthetics was noted (Solatiyan, Bueche, & Carter, 2020). Addressing this challenge involves developing a method that can reflect the

mechanical behaviour of geosynthetic-reinforced pavements subjected to both traffic loadings and environmental factors (Gupta & Mishra, 2016). A comprehensive understanding of how geosynthetics performs within the pavement structure, considering both the dynamic stresses from traffic and the varying environmental conditions can ensure a robust and effective application of geosynthetics.

2.5.2 Geogrid

Geogrids are typically made by extruding Polyethylene (PE) or Polypropylene (PP) or weaving Polyester (PET) ribs with open grids (Nader Ghafoori & Sharbaf, 2016a). Geogrid is defined as "a geosynthetic material consisting of connected parallel sets of tensile ribs with apertures of sufficient size to allow for strike-through of the surrounding soil, stone, or other geotechnical material" (Koerner, 1998). Geogrids have been widely used in civil engineering applications, such as in brick structures to mitigate the impact of seismic activity (Behera & Nanda, 2022), in pile-supported deep foundation structures to enhance their resilience (Han & Akins, 2002), to reinforce and stabilize soils on slopes for building construction (Jain, Nusari, Shrestha, & Mandal, 2023), and to reinforce weak subgrade materials in railway construction (B. M. Das, 2016). Geogrids can greatly strengthen an asphalt layer and mitigate reflective cracking when placed between layers; the geogrid will function as a tensile element redirecting a crack horizontally along the interlayer (Caltabiano & Brunton, 1991). The open apertures can also provide interlock and effective bonding with the asphalt particles.

The manufacturing direction can be used to define the ribs of geogrid. The longitudinal ribs are parallel to the machine direction, while the ribs that are perpendicular to the machine direction are transverse. The intersections of the ribs in two directions are junctions, and the openings are named apertures. The plain view with the terms is illustrated and labelled in Figure 2-2.

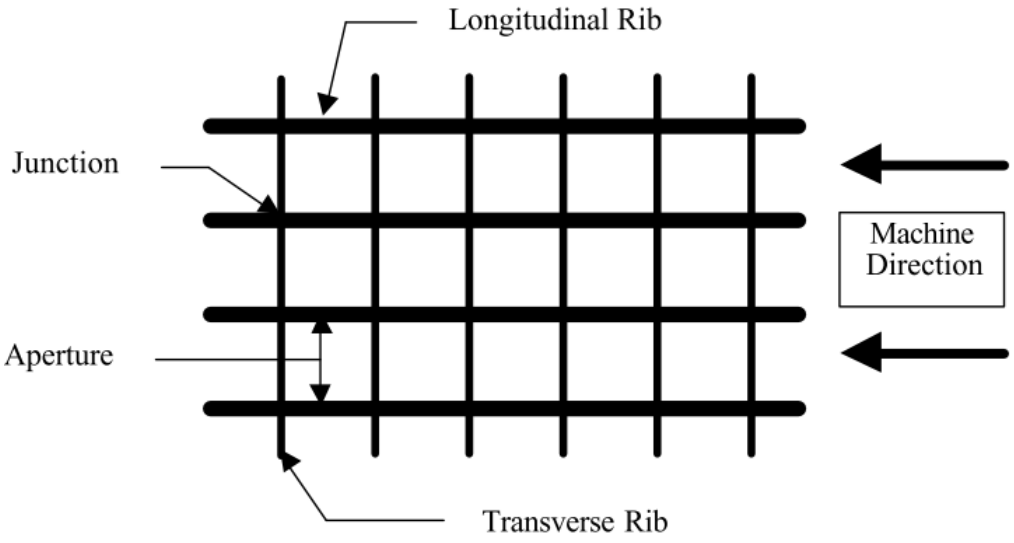

Figure 2-2 Geogrid Plain View (Stadler & Carolina, 2001)

Geogrids can be then categorized by the shape of apertures, including uniaxial, biaxial, and triaxial geogrids, as shown in Figure 2-3. In this case, tensile strength is provided in one, two, or three directions, respectively. Thus, uniaxial geogrids are used to reinforce retaining walls and slopes, whereas biaxial and triaxial geogrids are more commonly applied in pavement structures (Abd El-rahman Fares, Hassan, & Arab, 2020).

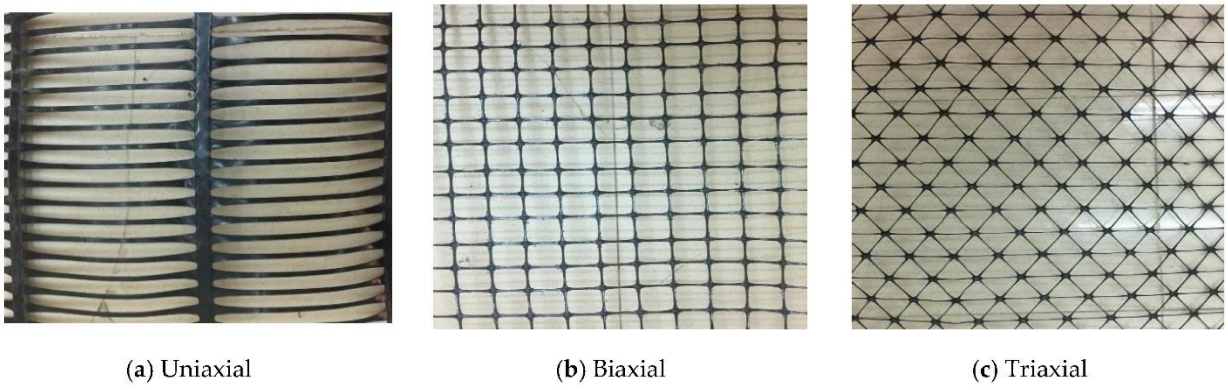

Figure 2-3: Different Types of Geogrids (Abd E Fares, Hassan, & Arab, 2020)

Geogrid mainly serves as reinforcement and separation by increasing bearing capacity and providing interlocking in the unbound granular base (Hass, Walls, & Carroll, 1988a). Lateral confinement is provided by the friction and interlocking between the course materials and geogrid. The interlocking effect increases the tensile strength under traffic loading, and the shear stress is reduced by the lateral

restraint (Gu et al., 2016). In terms of asphalt reinforcement, geogrids can greatly strengthen the asphalt and mitigate reflective cracking by serving as a tensile element. The geogrid redirects the cracks to the horizontal direction dissipating the stress on the asphalt layer (Aran, 2006). The open apertures can also provide interlock and effective bonding with the asphalt particle that penetrates through the grids. The load distribution and lateral movement restraint provided by geogrid in the pavement structure are shown in Figure 2-4.

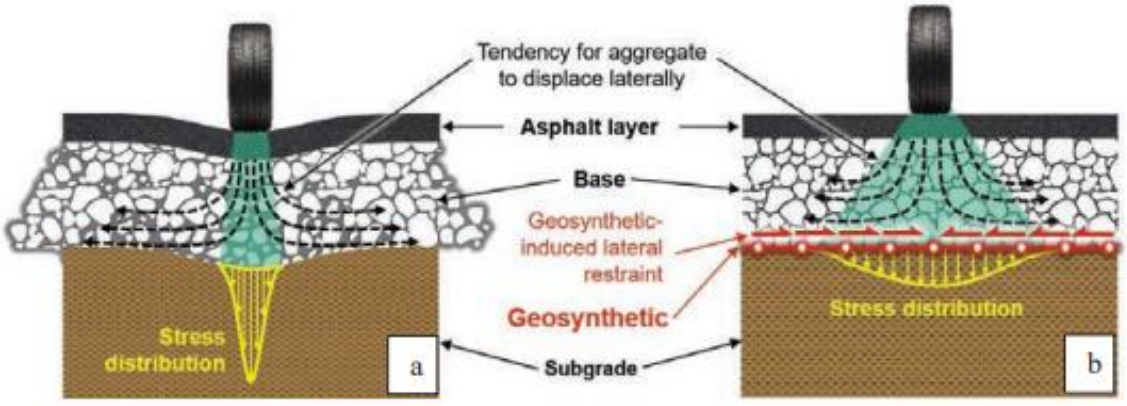

Figure 2-4: Use of Geogrid as Reinforcement by Load Distribution and Lateral Restraint: a) without geogrid; b) with geogrid (Zornberg, 2017)

Several studies have been conducted to assess the performance of geogrids by means of modelling and testing. A numerical model, originally created by Gu et al. (2016), simulated geogrid-reinforced flexible pavements and demonstrated that geogrid can effectively minimize rutting damages but does not mitigate the fatigue damage (Gu et al., 2016), which was then reconfirmed with the incorporation into Pavement Mechanistic-Empirical (ME) Design (Gu, Luo, Luo, Hajj, & Lytton, 2017). Similar studies using finite element modelling show that geogrids can reduce vertical strain and deformation as well as improve the loading distribution (Abu-Farsakh, Gu, Voyiadjis, & Chen, 2014; Ahirwar & Mandal, 2017). Another model also showed that the overall bearing capacity can be effectively improved when geogrids are placed within the asphalt layers (Correia, Esquivel, & Zornberg, 2018). A study using finite element modelling found that the Von Mises stresses in the geosynthetics-reinforced asphalt concrete layer can be reduced and can subsequently mitigate reflective cracking (Sobhan & Tandon, 2008). A 3D finite element analysis performed by Saad et al. (2006) concluded that the fatigue strain is reduced the most when geogrid is placed at the bottom of the asphalt concrete layer (Saad,

Mitri, & Poorooshasb, 2006). When used in pavement rehabilitation, geogrids placed underneath asphalt overlays were shown to reduce rutting in the surface course (Correia & Zornberg, 2016).

Some small-scale laboratory studies have been performed to investigate the optimum position of geogrid within the granular base/subbase. It has been found that geogrid is optimal to be placed at the interface of subbase and subgrade for a thin aggregate layer while it is better to be placed at the mid-point (Hass, Walls, & Carroll, 1988b) or the upper one-third (Abu-Farsakh & Chen, 2011) of a thicker base layer. Laboratory testing by Brown et al. (2001) was used to create a theoretical model to study the mitigation of reflective cracking of geogrid in an asphalt layer (Brown, Thom, & Sanders, 2001). Lee (2008) reported that the rate of upward crack propagation was decreased by the geogrid (Lee, 2008). The fibreglass geogrid reinforcement in asphalt mixtures was studied to effectively inhibit crack propagation through 3D Digital Image Correlation analysis on various configurations of pre-notched beams, especially under high-strain conditions (R. A. Freire, Di Benedetto, Sauzéat, Pouget, & Lesueur, 2021). Solatiyan et al. (2023) used a crack-widening device to quantify the crack resistance of geosynthetic interlayers, showing that reinforcement geogrids could enhance initial stiffness, particularly in coarse hot mixtures (Solatiyan, Ho, Bueche, Vaillancourt, & Carter, 2023).

The fatigue resistance of prismatic asphalt beams with and without geogrid reinforcement was also investigated by Lee (2008), where it was demonstrated that geogrid-reinforced specimens exhibited significantly greater fatigue resistance compared to unreinforced control specimens (Lee, 2008). Similar performance improvements were also observed in the study by Arsenie et al. (2016) which used finite element modelling to demonstrate that the fatigue life of asphalt concrete could be increased with geogrid reinforcement (Arsenie, Chazallon, Duchez, & Mouhoubi, 2016). Laboratory testing was also performed to verify the capability of geogrid to enhance the fatigue resistance of asphalt concrete by bending tests (Darzins, Qiu, & Xue, 2021) as well as flexural testing combined with digital image correlation techniques (Kumar, Saride, & Zornberg, 2021). Li et al. (2022) also found that the cracking resistance of asphalt specimens was enhanced by the installation of a geogrid interlayer when undergoing fatigue testing at lower temperatures (Q. Li, He, Yang, Su, & Li, 2022). By employing a three-point bending test to assess J-integral and crack resistance against bottom-up crack propagation, geogrid reinforcement was shown to improve the fracture toughness and resist the bottom-up crack propagation, which subsequently improved the fatigue cracking resistance (Solatiyan, Bueche, & Carter, 2021). The improvement of fatigue resistance was observed at high strain levels in geogrid-reinforced asphalt samples with cyclic tension and compression tests (R. Freire, Di Benedetto, Sauzéat, Pouget, & Lesueur, 2022a).

Bonding between geogrid and asphalt is also a concern. Solatiyan et al. (2021) introduced an indicator called the Coefficient of Interface Bonding measured with a modified slant shear device to represent the bonding quality, which reveals that the enhanced fraction toughness is attributed to the bonding quality at the interface (Solatiyan et al., 2021). A shear-torque fatigue test was used to evaluate the interfacial behaviour, which found that the fibreglass geogrid exhibited lower shear fatigue performance at 20 °C compared to other interfaces yet displayed significant improvement at 10 °C (Ragni, Canestrari, Allou, Petit, & Millien, 2020). Shear tests and pull-off tests conducted in another study demonstrated that the interlayer shear strength was decreased for geogrid-reinforced samples, while such reduction is less dominant at higher temperatures and with geogrids in less thickness (Canestrari et al., 2018). The 2 Springs, 2 Parabolic Elements and 1 Dashpot (2S2P1D) model can be used to model the interfacial behaviour with geogrids, while the usage of tack coat was shown to improve the interface stiffness by separating the complex modulus of interface and asphalt materials (R. A. Freire, Di Benedetto, Sauzéat, Pouget, & Lesueur, 2022). Another novel methodology was proposed to evaluate the interfacial behaviour of geogrid-reinforced asphalt with an axial tension test, which demonstrated that the geogrid thickness had influences on the results while the tension resistance was increased with geogrid reinforcement at 40 °C (R. Freire, Di Benedetto, Sauzéat, Pouget, & Lesueur, 2022b). In general, various types of tests were developed to evaluate the interfacial behaviour of multilayered asphalt specimens such as direct shear and torque tests, while it was demonstrated that specimen clamping, interlayer gap, testing mode and applied loading amplitude should be consistent (Canestrari et al., 2022). The sustained loading tests on three types of geogrids revealed that creep is not a degrading phenomenon with the consistency between the tensile rupture strength measured during subsequent monotonic loading and continuous monotonic loading, showing the strength of geogrid can be sustained (Kongkitkul, Hirakawa, & Tatsuoka, 2007).

Large-scale field tests have also been done to assess the more realistic performance of geogrid. It has been observed that rutting depths are significantly reduced with the reinforcement at the base and subgrade interface (Perkins, 2002). A long-term monitoring test was conducted from 1991 to 2005, with two flexible pavements reinforced with geogrids at the midpoint or bottom of the base layer. It was found that geogrid can effectively replace some thickness of pavement materials as the reinforced pavements showed similar performance to the control sections with either a 50 mm thicker hot mix asphalt layer or with 100 mm thicker base aggregate materials (Aran, 2006). Geogrids have also been tested in the base layer and base subgrade interfaces, demonstrating a notable reduction in rutting depth and permanent deformation (Al-Qadi, Dessouky, Kwon, & Tutumluer, 2008). In a subsequent study on

the same trial section, it was demonstrated that at least a 20% reduction in rutting depth could be provided by installing geogrid at the interface of the base and subgrade (Al-Qadi, Dessouky, Kwon, & Tutumluer, 2012). A further review of full-scale studies using geosynthetic-reinforced flexible pavements found that they could reduce vertical deformation and delay rutting (Alimohammadi, Schaefer, Zheng, & Li, 2021). In terms of the applications of geogrids in cold regions. Geogrids can significantly reduce the deformation of the embankment under freeze-thaw cycles in the Qinghai-Tibet railway compared to the sections without geogrid installation (Ge et al., 2008).

Generally, there are a limited number of studies examining the performances of pavement reinforced with geogrids within the asphalt layer through laboratory testing and field monitoring. The main challenge of these studies is determining the effect of different properties of geogrids such as aperture size, stiffness, modulus, and installation positions using lab specimens. However, due to the adaptability of geogrid in different climates, it exhibits great potential in pavements suffering from freeze-thaw cycles although few studies have been done to specifically investigate its effect on mitigating differential settlements caused by F-T actions.

2.5.3 Geotextile

Geotextiles are a widely used geosynthetic material that is made of non-woven, woven, or knitted textiles and is typically porous. The difference between woven and non-woven geotextiles is the manufacturing methods. A woven geotextile is produced by interlacing two sets of parallel yarns with warp yarns in the machine direction and weft yarns in the cross-machine direction, while a non-woven geotextile can be produced by needle-punching or bonding the filaments or fibres (Giroud, 1984; Nader Ghafoori & Sharbaf, 2016b). Figure 2-5 shows both woven and non-woven products.

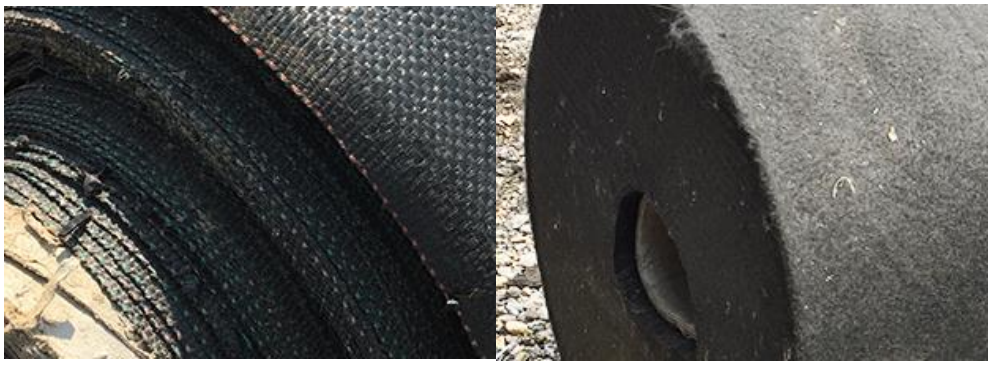

Figure 2-5: Geotextile Products: a) Woven; b) Non-Woven (Titan Environmental Containment, n.d.)

Geotextiles can function as filtration, separation, and reinforcement. As a separator, the geotextile inhibits the upward migration of fine particles into the voids of the coarse materials. As such, they are usually placed over finer materials and are commonly placed in the pavement structure between the subgrade and coarser subbase material. The migration of the soil into the base aggregate may cause the loss of the full function of the base structural layer, so a separator may be deemed necessary in some situations. Figure 2-6 illustrates the geotextiles as a separator between the base layer and subgrade, illustrating geotextiles as a barrier to prevent the mixing of different soil layers. They separate the subgrade from the aggregate base, keeping the materials distinct and maintaining the integrity of the pavement structure.

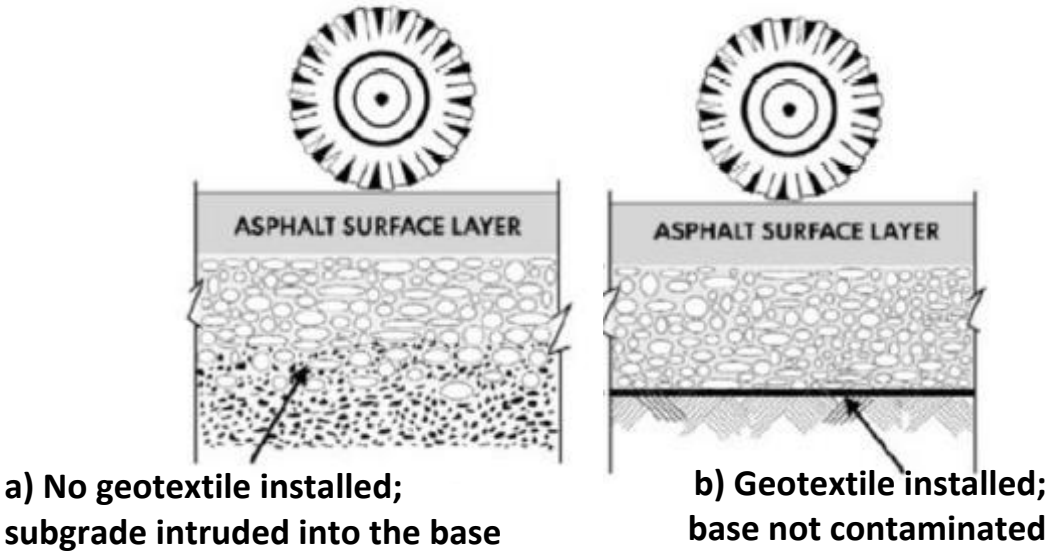

Figure 2-6: Geotextile Working as A Separator Between Base Aggregate and Subgrade: a) without geotextile; b) with geotextile (S. C. Das, Paul, Fahad, & Islam, 2017)

Typically, if melted water in warmer periods cannot drain downwards into the still-frozen soil, a high pore pressure will be induced under traffic loading. The placement of a geotextile can help dissipate and drain the water by acting as a filter while limiting the movement of soil particles (Raymond, 1999). Geotextiles allow water to pass through while retaining soil particles. Figure 2-7 illustrates geotextile serving as filters, to prevent the migration of fine particles from the subgrade into the base layers but allowing water to pass through so that the soil stability is maintained.

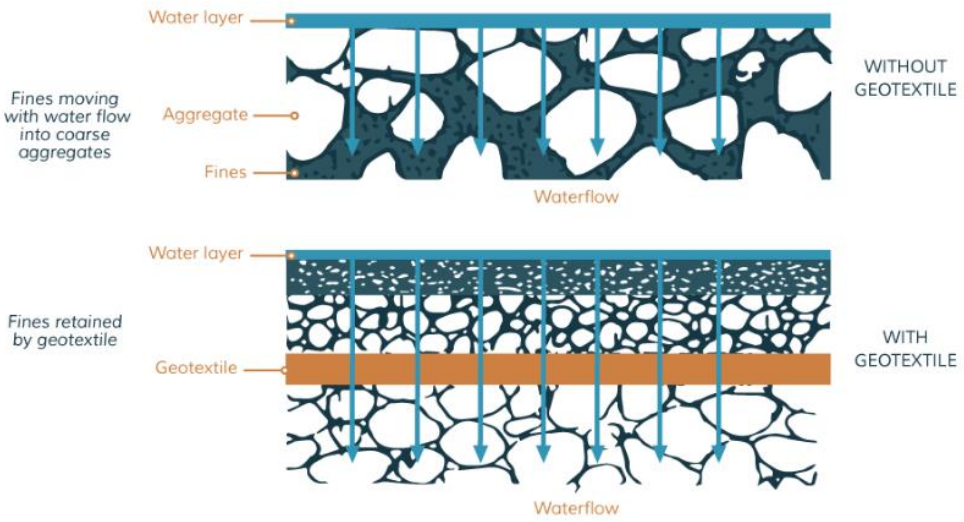

Figure 2-7 Geotextile Working as A Filter (Randall MFG, 2023)

Geotextiles have a drainage function, allowing the flow of water while preventing soil intrusion. They promote subsurface drainage, reducing water accumulation and potential damage to the pavement structure (Ghazavi & Roustaei, 2013). Subsurface drainage is critical in resisting the flow of water to prevent the rise of pore pressure. Typically, the drainage system is put in the form of trenches on the sides. Geotextile can be placed in line with the trenches. Such configuration can yield a drainage system with a specific zone which holds smaller particles while serving as a conduit to transfer the pores in the geotextile, as shown in Figure 2-9 (Randall MFG, 2023).

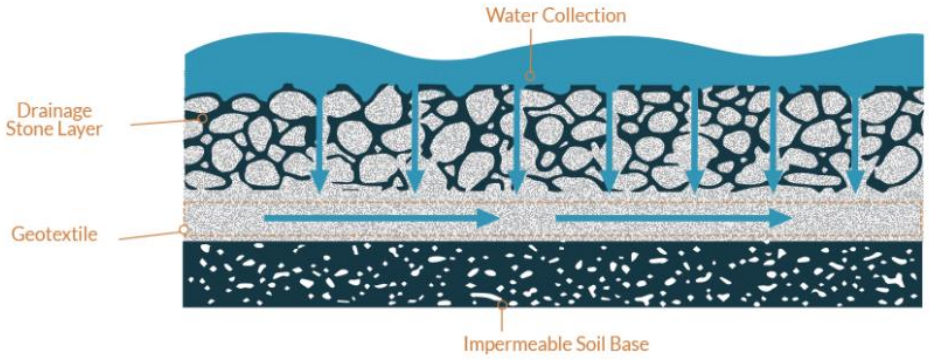

Figure 2-8 Geotextile Working as A Drainer (Randall MFG, 2023)

As reinforcement, geotextiles provide high tensile strength as well as high contact shear strength with the soil. Solatiyan et al. (2023) used a crack widening device to quantify the crack resistance of

geosynthetic interlayers, revealing that paving fabric outperforms in energy dissipation and stiffness modulus retention during crack propagation (Solatiyan et al., 2023). To control the reflective cracking, the geotextile can act as a stress-relieving interlayer by absorbing stresses at the crack tip with lower elastic stiffness (Lytton, 1989b). The reinforcement application of geotextiles is illustrated in Figure 2-9.

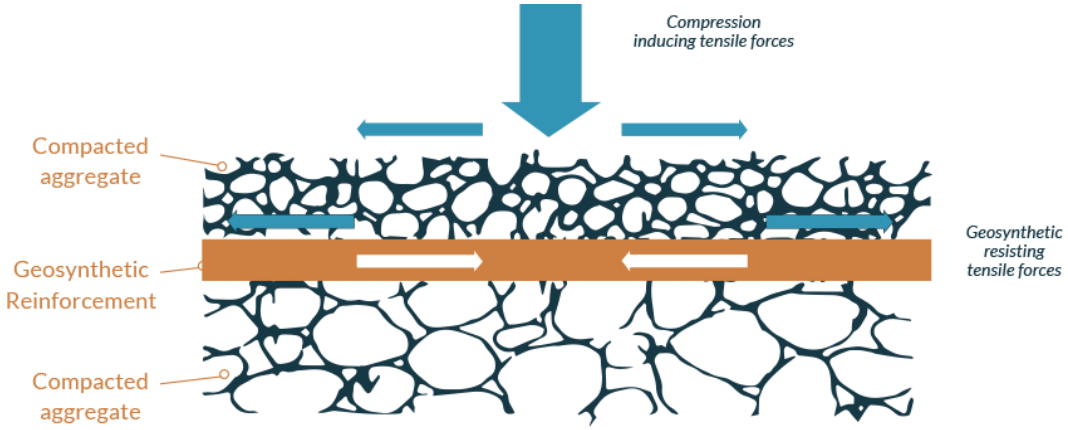

Figure 2-9: Geotextile Working as Reinforcement (Randall MFG, 2023)

A capillary barrier is defined as a barrier in the ground to prevent or intercept the movement of fluid or fine particles, based on the concept of capillary action. When water flows in the ground, there is a force named capillary force that induces water to rise and reach the pore walls, subsequently forming water columns, known as capillaries. Such capillaries retain water and stop the movement of water and fine particles, generating capillary barriers (Richards, 1931). Capillary barriers can be created artificially to change the pore structure in the ground. Some common applications include the filling of granular materials. Geotextile can also be used as a capillary barrier with its small pore sizes in the fabric to trap water and restrain movement (Henry & Holtz, 2001). Figure 2-10 illustrates how geotextile can effectively inhibit the saturated capillary rise.

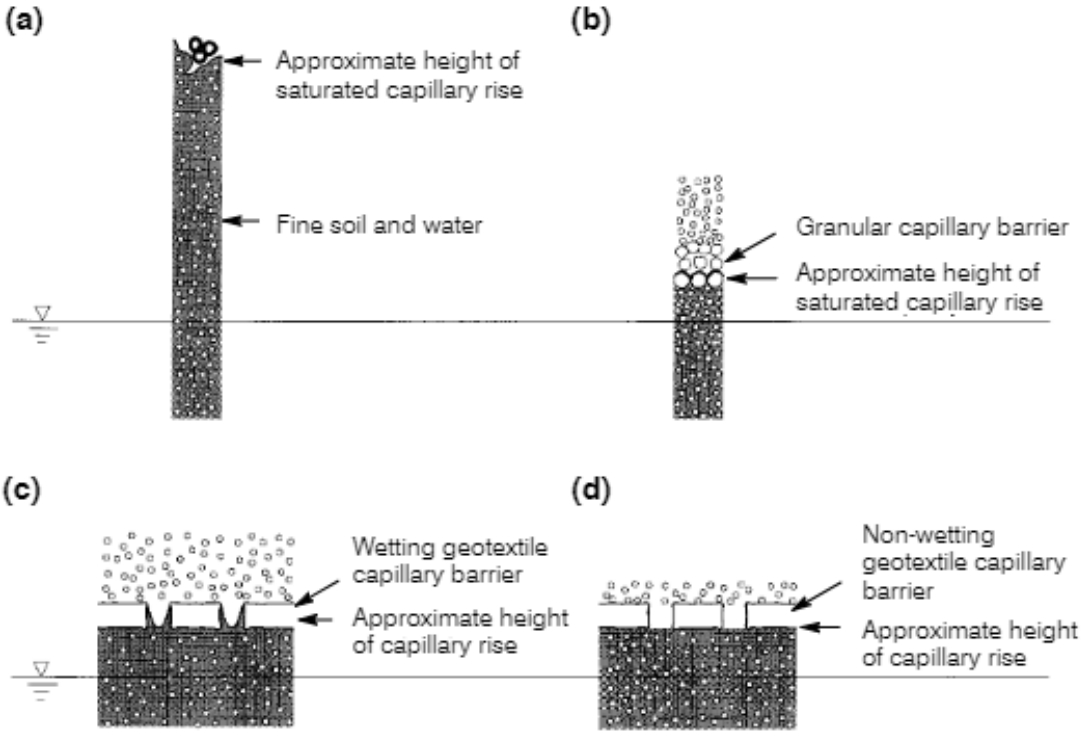

Figure 2-10 Geotextile Working as A Capillary Barrier (Henry, 1995)

While geotextile can resist the migration of fine particles but allow the water to pass through, it can also function as a capillary barrier to reduce frost heave by preventing upward water migration (Jie & Yan, 2013). It has also been tested on the Qinghai-Tibet highway that a structure with crushed rock and geotextile can reduce the frost penetration and thaw depth thus maintaining the underlying soil, which demonstrated that the drainage effect of geotextiles also reduced the frost penetration and thaw depth, thus preserving the underlying soil and minimizing further thaw (Lai, Zhang, & Yu, 2012).

2.5.4 Geogrid Composite

Geogrid composites are the combination of geogrids bonded with geotextiles. As such, the reinforcement of geogrids can work along with the separation and filtration of geotextiles.

A geogrid composite (i.e., a geogrid bonded to a geotextile) has the combined functions of separation, filtration, and drainage provided by the geotextile and reinforcement provided by the geogrid. These composites are more commonly used for weak subgrade and frost-susceptible soils. The usage of

geogrid composites has been demonstrated to reduce stresses within the subgrade (C. Jayalath, Gallage, Wimalasena, Lee, & Ramanujam, 2021) as well as save construction costs through the reduction of the granular base thickness (C. P. G. Jayalath, Gallage, & Wimalasena, 2022). A full-scale test has been done on an unpaved road with geogrids laid over non-woven geotextiles embedded at the interface of base and subgrade layers. This study demonstrated that the geogrid composite can reduce 50% of the base aggregate materials while achieving a similar rutting depth and subgrade bearing capacity compared with the unreinforced section (Tingle & Webster, 2003). A field trial with geogrid composite serving as an interlayer treatment was evaluated by testing cored samples in the laboratory using an interlayer shear test (Pasquini, Pasetto, & Canestrari, 2015). Another full-scale test has been performed by Helstrom et al. (2007) with the inclusion of geogrid and geogrid composites in flexible pavements in cold regions. It has been found that the base course structural coefficients can be increased by 5% with geogrid and 17% with geogrid composite. Also, the forces per unit width in the geogrids composite appear to decrease during summer and increase during winter. With the exclusion of the thermal expansion and contraction of composite by strain measurement, the seasonal fluctuations of the forces were concluded to be attributed to the soil conditions (Helstrom, Humphrey, & Hayden, 2007).

2.6 Research Gaps

In summary, although innovative materials of geogrids and geogrid composites are being developed and designed with their outstanding adaptability in different climatic conditions, several research gaps still exist, as listed in the following:

- Many studies investigated the interfacial behaviour of multilayered geogrid-reinforced asphalt samples. Performance testing conducted also revealed the effectiveness of geogrid in inhibiting crack propagation and extending the fatigue life of asphalt materials. The investigation of the rutting resistance of asphalt mixtures provided by geogrid to asphalt was lacking. Also, studies investigating the behaviour of moisture damage in geogrid-reinforced pavements are needed
- There are limited studies examining the performance of geosynthetic-reinforced pavements in the real world and with a fully instrumented large-scale study. Asphalt layers with geogrid reinforcement are rarely discussed in the context of full-scale field studies, and even less commonly studied with sophisticated instrumentation and sensors to monitor the actual pavement response during geogrid installation. Limited research has been conducted on geogrid composites during installation thus the impacts of these interlayer systems under construction are still unexplored.

- Large-scale on-site monitoring and instrumentation studies are also needed to assess the performance of geogrids and geogrid composites under different environmental impacts. Few studies on their ability to mitigate the negative impact of F-T actions on pavements in cold regions have been done.
- Furthermore, it is necessary to examine the heaves and settlements caused by pavement freeze-thaw cycles in cold regions by having a practical and robust model to predict geosynthetic-reinforced pavement performances.

Chapter 3
Methodology and Data Sources

3.1 Overview

This chapter presents the research methodology to address the research gaps and achieve the objectives. The overview of the methodology structure is illustrated in Figure 3-1. The study starts with the initial phase by identifying the problem and conducting a literature review to identify the current research gaps. Subsequently, a full-scale study was initiated with the design and construction of three trial sections: the CT section with conventional flexible pavement design, the GG section with fibreglass geogrid in the asphalt layer, GC section with geogrid composite on the subgrade. Instrumentation was used in this field study to monitor the pavement performances. Meanwhile, the on-site monitoring was conducted to evaluate the constructability and construction impact on the trial sections. Then, materials sampled from the field were characterized in the laboratory by analyzing particle distribution, Atterberg limits, optimum water content, and California Bearing Ratio (CBR) of unbound materials, as well as theoretical maximum density and dynamic complex modulus of asphalt mixtures. The results would be used for further analysis of the field trial performances and serve as the inputs of the developed model.

The fibreglass geogrid embedded in the asphalt layer was investigated by laboratory testing, particularly in the aspect of resisting permanent deformation and moisture susceptibility. The Hamburg Wheel-Tracking Test was conducted, while a modified dynamic creep test with F-T conditioning on the samples was proposed.

Regarding the effect of geogrid composite, a sophisticated numerical model was developed by coupling thermal-hydro-mechanical (THM) processes to simulate the pavement structure under F-T cycles. Aside from the materials properties obtained from laboratory testing as mentioned, the temperature data measured by the instrumentation in the field trial sections were analyzed and subsequently used to produce layer temperature models to be assigned to the numerical models representing the CT and GC sections. The in-service pavement performances of the trial sections were also evaluated with instrumentation including temperature, moisture, strain, pressure, and frost conditions in three sections. Additionally, field testing was conducted seasonally to evaluate pavement stiffness and roughness with the impact of seasonal changes to see the differences between different sections.

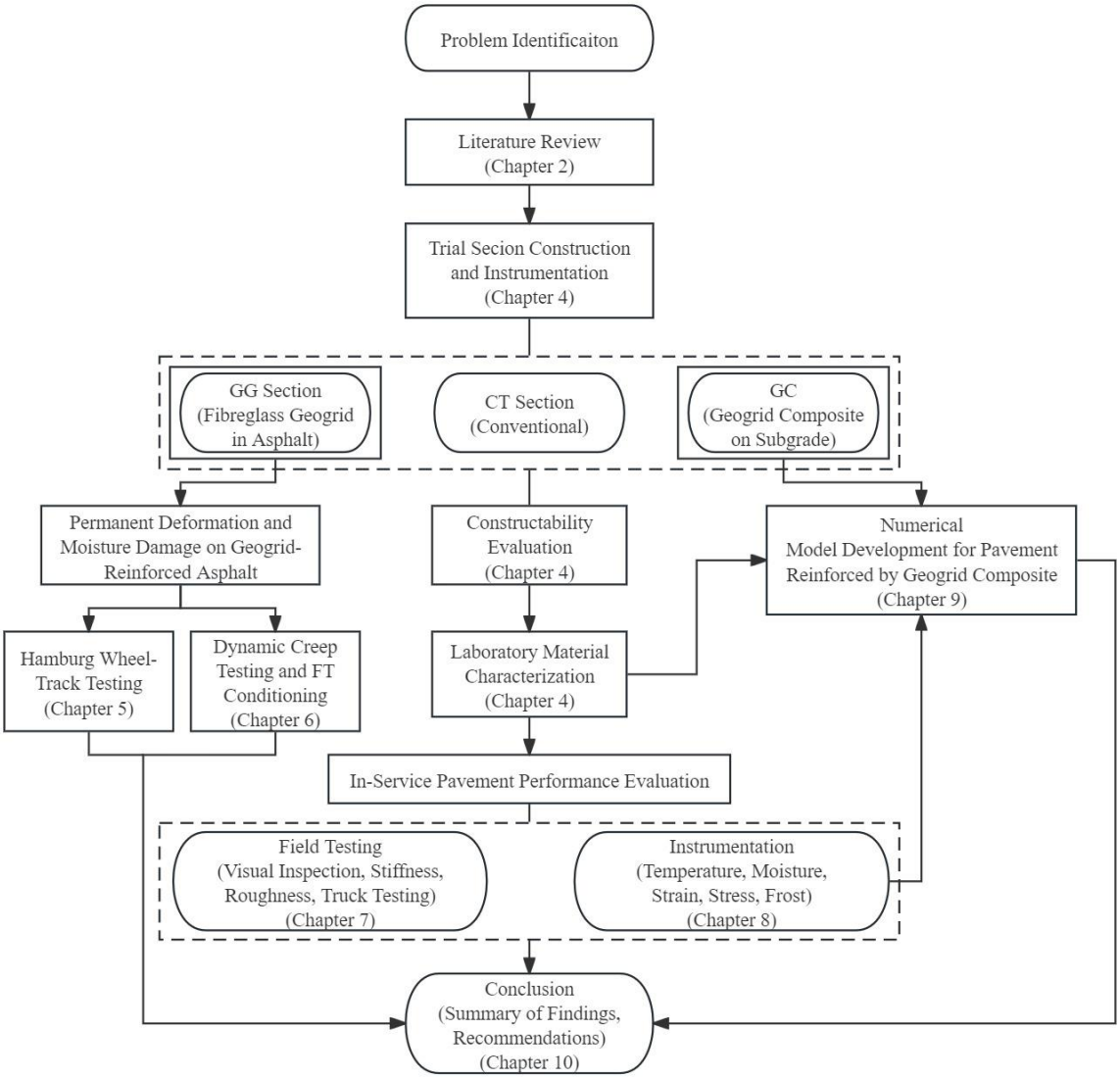

Figure 3-1 Research Methodology Structure

3.2 Large – Scale Field Study

Three sections were constructed, as listed below:

- One unreinforced section with conventional flexible pavement structure (CT).
- One section reinforced by fibreglass geogrid in the asphalt layer (GG).
- One section reinforced by geogrid composite on the subgrade (GC).

An instrumentation plan was developed to track the field performances including temperature, moisture, strain, stress, and frost conditions. Field testing was conducted routinely to monitor the stiffness, roughness, and critical mechanical responses. On-site monitoring was conducted during construction with the aid of pictures, videos, and notes, to understand the constructability of geosynthetics. Instrumentation measurements were recorded at a higher frequency to capture the impact of construction activities. In-service pavement performances were monitored with the instrumentation records taken every five minutes as well as with field testing performed seasonally.

3.2.1 Instrumentation

The instrumentation type, location, and quantity are summarized in Table 3-1.

Table 3-1 Instrumentation Plan

Sensor	Model	Measurement	Depth (mm)	Quantity
Temperature sensor	IRROMETER Model 200TS	Temperature (°C)	200	1
			425	1
			750	2
Moisture probe	IRROMETER Model 200SS	Water potential (kPa)	200	2
			425	2
			750	2
Dynamic strain gauge	Geocomp Model ASG/VASG	Longitudinal strain (με)	200	1
			650[1]	1
		Transverse strain (με)	200	1
Total Earth Pressure Cell	RST Instrument LPTPC-S	Stress (MPa)	650	1
Frost Probe	ROCTEST FR-1149050100	Frost condition with colour variation	200 - 3000	1

Note: [1]Only in the CT and GC sections

The readings were sent from the sensors and stored in Campbell dataloggers. The records were subsequently transmitted to a multiplexer and the data was collected by connecting the multiplexer to a computer every month. The dataloggers and multiplexer were connected to a battery. These tools are shown in Figure 3-2.

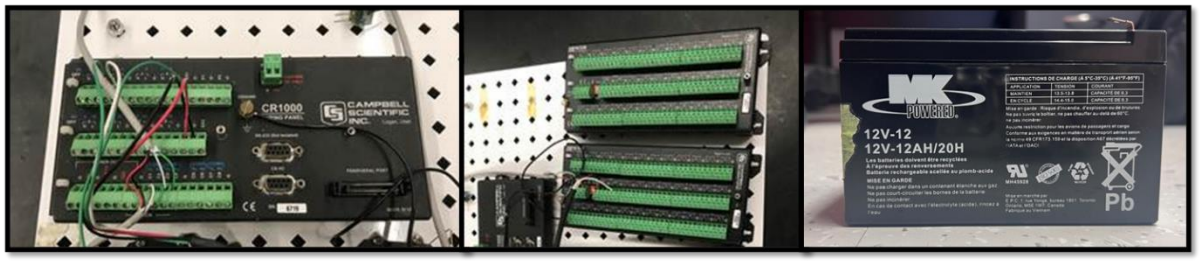

Figure 3-2 Multiplexer, Datalogger, Battery

In addition to the instrumentation deployed in the trial section, data from a nearby weather station were also collected for a comprehensive understanding of external environmental factors. The weather station included a rain gauge and a temperature sensor, both shielded by a solar radiation cover, as illustrated in Figure 3-3. This weather station facilitated the measurement of ambient temperature and precipitation, providing valuable supplementary information to contextualize and analyze the performance of the trial section under varying weather conditions.

Figure 3-3 Weather Station (Oyeyi, 2022)

3.2.2 Field Testing

3.2.2.1 Visual Condition Inspection

Visual condition inspection was conducted monthly from August 2022 to December 2023 during the data collection to identify any distresses.

3.2.2.2 Light Weight Deflectometer

Light Weight Deflectometer (LWD) can be used to measure the deflection and stiffness of the subgrade, base, and pavement by releasing and applying loads on the layer. A 15 kg weight is dropped from a height of 100 cm. The sudden drop of the weight can transmit the load to the ground, and the deflection can be used to calculate the stiffness. At least three consistent outcomes were ensured at one spot before moving to the next to obtain reliable measurements. A 300 mm-diameter plate was used when performing the testing on the unbounded materials during construction. A 200 mm-diameter plate was used for the testing on the binder course and surface course as well as on the in-service pavement. Figure 3-4 shows the LWD equipment.

Figure 3-4 Light Weight Deflectometer Equipment

3.2.2.3 Roughness

The SurPro walking profiler was used to measure the roughness of the pavements, including the paved binder course and surface course during construction and after construction, as shown in Figure 3-5. The road was profiled by walking this equipment along both LWP and RWP on both lanes. The walking speed cannot exceed 2.5 m/s. The equipment was calibrated first before the testing by walking 50 m

forward and 50 m reverse. The International Roughness Index (IRI) was generated, which is a commonly used standard indicator representing the roughness of a pavement.

Figure 3-5 SurPro Equipment

3.2.2.4 Truck Driving Test

To capture the mechanical responses of identical traffic loading on the three trial sections by mechanical instrumentation, a driving test was performed on the sections. A heavy construction dump truck was slowly moving on the sections. As per the categorization of vehicles, the truck used was tandem axle, while the middle wheels were lifted as unused, as shown in Figure 3-6 (FHWA, 2014). The truck driving test was performed twice, with one unloaded and the other loaded, to evaluate the impact of change of loading on the pavement.

Figure 3-6 Truck Used for Driving Test

3.3 Material Properties

Field-sampled materials were tested in the laboratory, which can serve for further analysis and as input for the developed model. Particle distribution, Atterberg limits, optimum water content, and California Bearing Ratio (CBR) were tested for unbound materials. Theoretical maximum density and dynamic complex modulus were tested for asphalt mixes. The properties were compared and verified with the information provided by the contractors.

3.3.1 Field Sampled Subgrade Soil Properties

The subgrade soil was sampled in each section of the field when preparing the surface before construction. Laboratory testing and field testing were performed on the sampled soil and in-situ to characterize the properties for performance evaluation and input of modelling.

3.3.1.1 Particle Size Distribution

The sampled soil from each section was air-dried and pulverized by a hammer. Then, after being oven-dried, the soil was sieved using the sieves shown in Figure 3-7 following ASTM D6913 (ASTM, 2017). The soil was washed on the No. 200 sieve (75 μm) since many small particles were found to be hard to pulverize.

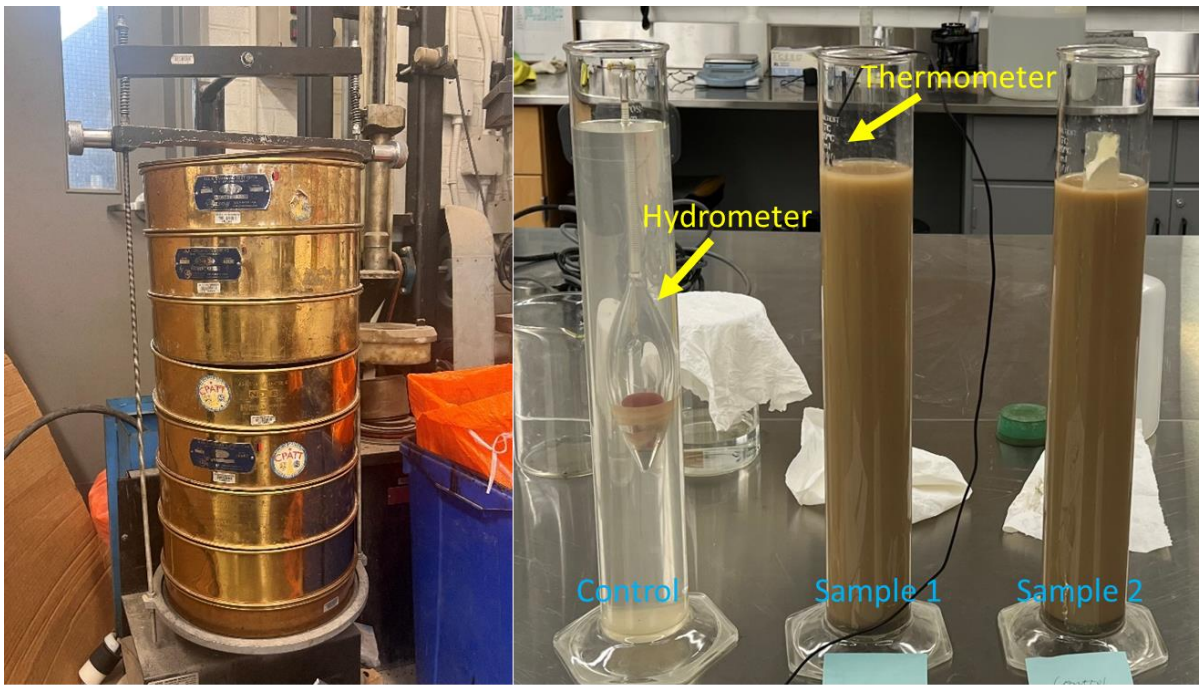

Figure 3-7 Particle Size Distribution Test Set-up Using: (a) Sieves and (b) Hydrometer

Due to this reason, hydrometer analysis was also performed to determine particle size distribution according to ASTM D422-63 (ASTM, 2007). 40 g of sodium hexametaphosphate was used as the dispersing agent to separate the particles. 50 g of oven-dried soil mixed with 125 ml of dispersing agent were conditioned and stood for 16 hours. A control cylinder with distilled water was prepared to rinse and calibrate the hydrometer as the composite correction. Figure 3-7 shows the test set-up with the hydrometer in the control cylinder.

3.3.1.2 Optimum Water Content and Density

The optimum water content and the maximum dry density were determined with a standard proctor compaction test as per ASTM D698-12 (ASTM, 2021a). Soils were mixed with increasing water

content. The mixed soil was compacted in three layers in a 4-in mould using a rammer with 25 blows per layer.

3.3.1.3 Atterberg Limits

Atterberg Limits were determined for sampled soil from three test sections following ASTM D4318 (ASTM, 2018). The plastic limit test set-up is shown in Figure 3-8.

Figure 3-8 Particle Size Distribution Test Set-up

3.3.1.4 California Bearing Ratio and Resilient Modulus

California Bearing Ratio (CBR) was performed in the laboratory following (ASTM, 2021b). The sampled soil from each section was fully mixed with their corresponding optimum water content determined previously using the mixer shown in Figure 3-9 (a).

Then, the mixed soils were compacted in a 6-in diameter mould with 56 blows in each layer following ASTM D698 (ASTM, 2021a). With 4.54 kg of surcharge weights applied to the compacted samples, the samples were soaked in water for 96 hours. A tripod dial gauge was placed on the sample shown in Figure 3-9 (b) to take the reading before and after the soaking period to measure the percentage of swell.

During the penetrating test, the piston was loaded to the sample at a rate of 1.27 mm/min with the surcharge weights placed on the sample. The penetration can be measured by a Linear Variable Differential Transformer (LVDT) attached to the piston, as shown in Figure 3-9 (c).

Figure 3-9 CBR Test Equipment including (a) Mixer, (b) Soaking and (c) Penetration Test

Resilient modulus was calculated from CBR results by empirical models used in the AASHTO 93 guide (AASHTO, 1993b) and the AASHTOWare Pavement ME method (MEPDG) (Powell, POTTER, Mayhew, & NUNN, 1984). Light Weight Deflectometer (LWD) was performed on compacted subgrade surface in the field during construction to correlate with resilient modulus of in-situ soil as well. The methodology of the LWD test was introduced in Section 3.2.2.2.

3.3.1.5 Soil Classification

The sampled soil from three sections was classified based on particle size distribution and Atterberg limits using the Unified Soil Classification System (USCS) in ASTM D2487 (ASTM, 2020) and AASHTO Soil Classification in AASHTO M145 (AASHTO, 2021).

3.3.2 Granular Base Material Properties

The aggregates used in the base layer are Granular A specified in the Ontario Provincial Standard Specification (OPSS) as per OPSS 1010 (OPSS, 2013). These aggregates were sampled from three sections during base layer construction. Particle size distribution, optimum water content, and CBR were determined for sampled Granular A. The methodology is similar to that described in Section 3.3.1.

3.3.3 Asphalt Concrete Mix Properties

Asphalt mixes were sampled on the days of construction from the field, including SP (Superpave) 19 used for the binder course and SP (Superpave) 12.5 used for the surface course.

3.3.3.1 Theoretical Maximum Specific Gravity

The theoretical Maximum Specific Gravity (G_{mm}) of loose asphalt mixes was determined following AASHTO T209. The vacuum equipment used in the test is shown in Figure 3-10 (AASHTO, 2016a).

Figure 3-10 Maximum Relative Density Test

3.3.3.2 Bulk Specific Gravity and Air Void Content

Bulk Specific Gravity (G_{mb}) and air void content of compacted specimens in SP 19 were determined as per AASHTO T 166 (AASHTO, 2016b). An adjustment factor was determined to correct the increased air void contents caused by the embedded geogrid.

3.3.3.3 Dynamic (Complex) Modulus Test

Dynamic (complex) modulus test was performed on both mixes following AASHTO T 342 (AASHTO, 2019b). A sinusoidal cyclic loading was applied on cored asphalt specimens with a height of 150 mm and in diameter of 100 mm. Three extensometers were attached to the studs glued around the specimens at three locations 120° apart, as shown in Figure 3-11. The loading was applied at five temperatures (-10°C, 4°C, 21°C, 37°C, 54°C) in an environmental chamber and at six frequencies (25 Hz, 10 Hz, 5 Hz, 1 Hz, 0.5 Hz, 0.1 Hz). The test was running from 25 Hz to 0.1 Hz and from low temperature to high temperature. A thermocouple was installed within a dummy sample of the same size as the specimens to represent the specimen's temperature. The stress level was adjusted before the test to

achieve an axial strain level within the range (i.e., 50 to 150 microstrain) as per the standard (AASHTO, 2019b).

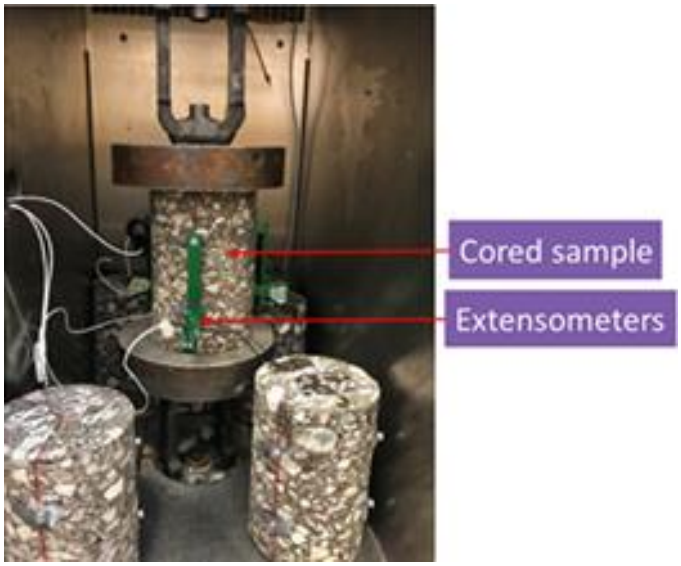

Figure 3-11 Dynamix Modulus Test Setup

3.3.4 Geosynthetic Materials Property

The properties of geosynthetic materials were provided by the manufacturer, Titan Environmental Ltd.

3.4 Laboratory Performance Testing of Geogrid-Embedded Asphalt

The rutting and moisture susceptibility of geogrid-embedded asphalt were investigated in the laboratory by Hamburg Wheel-Track Testing (HWTT) and a newly proposed dynamic creep test. Three different types of geogrids were tested to compare geogrids with/without membrane, and geogrids with different aperture sizes. They are Geogrid 10, Geogrid 11, and Geogrid 11 EPM.

3.4.1 Hamburg Wheel-Track Testing

Hamburg Wheel-Track Testing was conducted on geogrid-embedded asphalt following AASHTO T324 (AASHTO, 2019a). Four cylindrical samples in height of 63 mm and in diameter of 150 mm were grouped in pairs and mounted in the mounting tray. They were submerged in water in a chamber at the required temperature (i.e., 50°C) for 45 min as a preconditioning process. Loads of 705 ± 4.5 N were applied on both sides of the wheels. Linear Variable Displacement Transducer (LVDT) was installed on both sides to measure the deformation along each wheel-track, which is considered to be rut depth. The test equipment is shown in Figure 3-12.

Figure 3-12 HWTT Equipment

Conventional analysis was conducted to evaluate the rutting resistance of geogrid-embedded asphalt. In addition, sixth-degree polynomial analysis developed by the Iowa Department of Transportation (DOT) was adopted to analyze the HWTT results from three stages. The moisture susceptibility was also evaluated by combining both approaches.

3.4.2 Dynamic Creep Testing and Freeze-Thaw Conditioning

The specimens were subjected to testing within a controlled temperature chamber. A top plate with a diameter of 100 mm was employed for loading purposes attached to the actuator. Linear Variable Differential Transformers (LVDTs) were positioned on both sides of the frame to quantify vertical displacements, with the average being computed during axial strain calculations. Figure 3-13 illustrates the test set-up in the chamber.

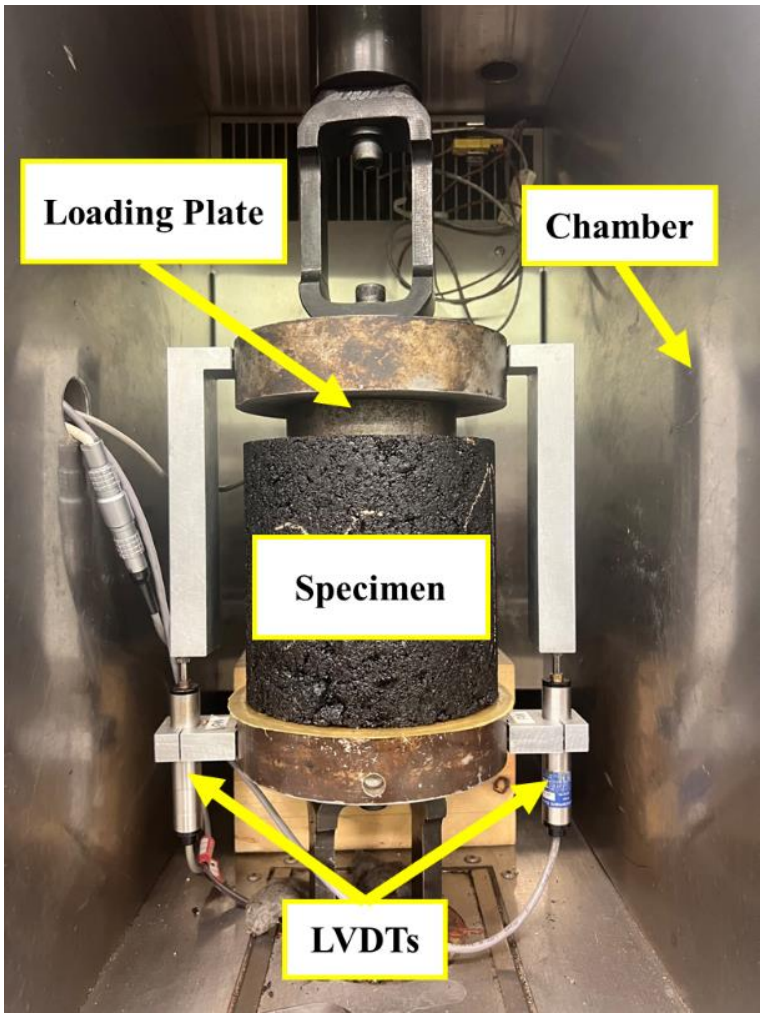

Figure 3-13 Dynamic Creep Test Set-Up

The loading cycle consisted of three stages: a loading stage (0.05 s), an unloading stage (0.05 s), and a resting stage (0.9 s), in accordance with AASHTO T378-17 (AASHTO, 2017). Each complete loading cycle spanned 1 second. Following the specifications outlined in the standard, the contact stress was determined to be 30 kPa and the repeated axial stress as 600 kPa, leading to calculated contact force and axial haversine loading force values of 235 N and 4700 N, respectively.

To examine the creep behaviour of geogrid-reinforced specimens at various temperatures, the tests were conducted at -10 °C, 25 °C, and 50 °C. At -10 °C and 25 °C, the application of loading comprised 150 cycles. Within this, the initial 100 cycles were designated for preloading, followed by the application of the actual periodic loading pulse for 50 cycles. Measurements were initiated and recorded immediately following the preloading phase. Similarly, at 50 °C, following the 100-cycle preloading

phase, the first 50 cycles were dedicated to creep analysis, mirroring the procedure followed for the initial two temperature conditions. Subsequently, the specimens were loaded until failure to explore permanent deformation. Additionally, a dummy sample identical in size and asphalt mixture type to the testing samples was utilized to monitor the temperature. A thermistor was buried at the center of the dummy sample and secured with an aluminum sticker to facilitate the monitoring of temperature fluctuations.

In order to replicate field conditions more accurately, in addition to the standardized 100 mm diameter samples, samples with larger diameters (150 mm) were also prepared and subjected to testing. Despite this variation, the loading plate maintained a diameter of 100 mm, allowing the applied load to penetrate the sample along with the surrounding asphalt serving as confinement.

Furthermore, a separate set of 150-diameter samples underwent preconditioning through a freeze-thaw (F-T) process. Considering the unique nature of the geogrid-embedded asphalt samples, a less aggressive approach was adopted. Initially, each sample was submerged in a water-filled container and subjected to a vacuum of 13 kPa absolute pressure. Following several trial-and-error tests, two cycles of vacuum treatment were determined to be conducted on each sample. Each cycle involved a continuous 7-minute vacuum treatment and a subsequent 5-minute resting period, facilitating a saturation level of 55%-60%. The samples were then carefully wrapped with plastic to prevent water loss and promptly placed in a freezer set at -18 °C. After 16 hours, the samples were removed from the freezer and allowed to thaw at room temperature, while still wrapped. After 24 hours, the wrapping was removed, enabling the samples to air-dry for two days before undergoing the actual dynamic creep test. Despite the conservative nature of this preconditioning F-T process, the results of the dynamic creep tests still displayed notable differences between samples that underwent the F-T process and those that did not.

3.5 Numerical Modelling

The efficacy of geogrid composite in mitigating freeze-thaw disturbances was emphasized, particularly regarding its drainage and filtration capabilities. The study employed a one-dimensional THM coupled model established and solved using COMSOL Multiphysics. Material properties were input based on laboratory and field testing, along with relevant literature. A predictive model for layer temperature was developed for both conventional pavement structures and geogrid composite-reinforced pavements. This model aimed to establish correlations between ambient temperature and pavement

temperature, utilizing data collected from field instrumentation during the first year after construction completion (August 2022 to August 2023).

The model was initially calibrated with the developed layer temperature predictive model and subsequently compared with data collected in the subsequent three months (August 2023 to October 2023). Following the calibration, it was applied to simulate the performance of the pavement structure, specifically evaluating the impact of geogrid composite in terms of minimizing the differential settlement of the pavement structure. This simulation allowed for a comprehensive assessment of the geogrid composite's effectiveness in addressing differential settlement issues associated with freeze-thaw cycles.

Chapter 4
Construction of Geosynthetic–Reinforced Pavements and Evaluation of their Impacts by a Large-Scale Field Study

4.1 Introduction

In this chapter, a practical field study regarding the construction and instrumentation of geosynthetic-reinforced pavements was presented; the characterization of the materials sampled from the field was presented; the installation of both geosynthetics and sensors was introduced, and the effect of these interlayer systems was investigated during construction. In this large-scale study, geogrid reinforced asphalt and geogrid composite on the subgrade were investigated during construction in real-time using pressure, strain temperature, and moisture instrumentation, and post-construction deflectometer measurements were conducted to verify instrument readings and demonstrate the resultant benefits of these interlayer systems.

4.2 Field Construction

4.2.1 Overview

The project site is located on Snyder Road East, Baden, Ontario. The test section is 45 meters in length in total, composed of three trial sections that are each 15 meters long. As shown in Figure 1, the pavement structure was composed of a 200 mm thick asphalt concrete layer and a 450 mm thick granular base layer, underlain by the subgrade. The asphalt layer is composed of one lift of 50 mm surface course using a Superpave (SP) 12.5 asphalt mix compacted over two 75 mm binder course lifts using an SP 19 asphalt mix. The "12.5" and “19” in the designations refer to the maximum aggregate size (MAS), which is 12.5 mm and 19 mm, respectively. These mixes are commonly used in pavement design standards in Southern Ontario (OPSS, 2006). The base for all three sections is composed of an unbounded granular layer using Granular A materials (OPSS, 2013). The pavement structural design is based on an Average Annual Daily Traffic (AADT) of 9,573 and cumulative Equivalent Single Axle Loading (ESAL) of 3,608,000 ESALs with 5% trucks, 2% growth rate, and 20 MPa estimated resilient modulus (Pinchin Ltd., 2020). The use of fibreglass geogrid located at either the center of asphalt or geogrid composite laid on the subgrade can be an optimum solution to reconstruct a poor-condition pavement (Bhat & Thomas, 2015a). To better study this effect, three pavement structures were designed for the trial sections in this project. These sections are listed below:

- Control section without reinforcement (referred to as Section #1, or the Control Section)
- A section with fibreglass geogrid installed within the two binder course lifts (referred to as Section #2, or the Fibreglass Geogrid Section).
- A section with geogrid composite laid at the interface of base and subgrade (referred to as Section #3, or the Geogrid Composite Section).

The fibreglass geogrid was installed in the asphalt layer to study its capability to reinforce asphalt concrete, while the geogrid composite bonded to geotextile has draining and filtering functions, which is more crucial in the subgrade where water and fine particles can have big impacts on the soil especially at lower temperatures.

Instrumentation was prepared to monitor the temperature, moisture, and mechanical behaviour of the pavement. The section side view presents the detailed instrumentation layout and pavement structures in Figure 4-1. All the sensors testing mechanical behaviour were installed along the right wheel path of the westbound lane. The data from the sensors were logged using a data logger installed in a cabinet on the sideway.

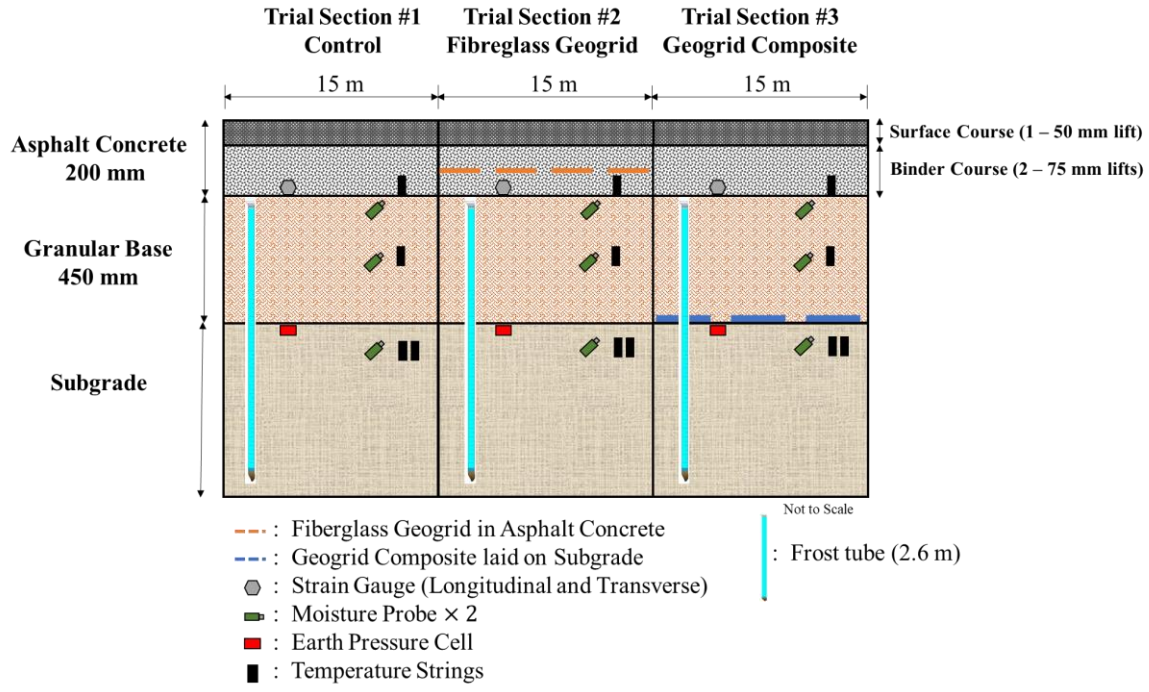

Figure 4-1 Section Side View of Field Instrumentation and Construction

Figure 4-2 presents the plan incorporated with the typical cross-section design provided by the Region of Waterloo and the general contractor through the test area (Region of Waterloo, 2021).

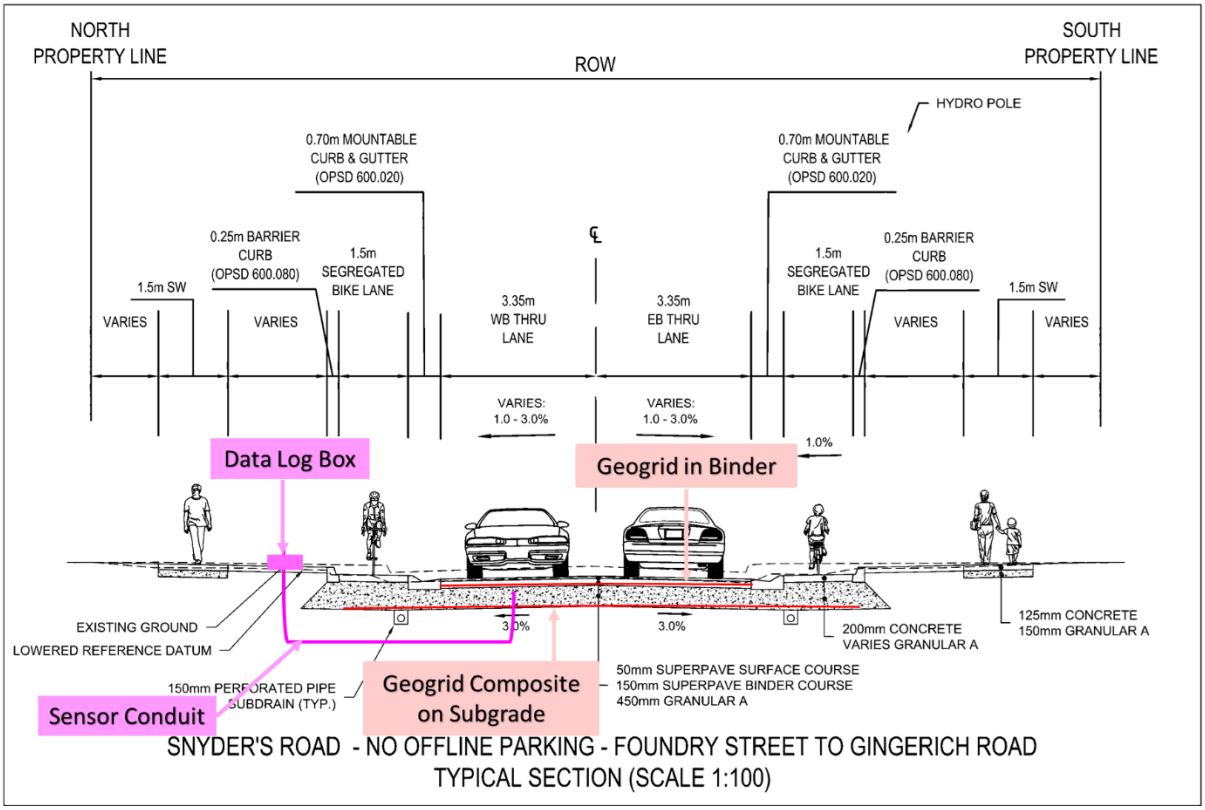

Figure 4-2 Cross-Section Design through Test Area (Modified from source: Region of Waterloo (2021))

4.2.2 Geosynthetics Installation

Two types of geosynthetic materials were used in two test sections: a geogrid composite and a fibreglass geogrid. Section #3 was constructed first, and the geogrid composite was installed directly on the subgrade. The fibreglass geogrid was installed on Section #2 after paving the first binder course lift; it is located between the two lifts of SP 19 asphalt concrete.

4.2.2.1 Geogrid Composite on Subgrade

The geogrid composite was placed at the interface between the base and subgrade (Figure 4-3); from laboratory testing, the subgrade had a California Bearing Ratio (CBR) of 2%. The geogrid composite is made of biaxial polypropylene geogrid manufactured using a punching and drawing process, heat

bonded to a continuous filament non-woven polyester geotextile. The reinforcement is offered by the geogrid element while the mechanically and chemically stable geotextile acts as a filter/separator preventing the movement of fine soils in saturated soil (Titan Environmental Containment, 2021b).

Figure 4-3 Installation of Geogrid Composite on the Subgrade

As per the installation guide (Titan Environmental Containment, 2022), the subgrade was prepared by removing debris, remnants, or any plants before installation. The surface was graded, and the geogrid composite was unrolled over the surface as shown in Figure 4-3. As each section is only 15 meters, special attention should be paid during the manual installation of the geogrid composite material. As it is usually stored in rolls, the geogrid composite may not be completely flat when placed in the field and at least four workers were needed to hold each corner of the sheet during placement to reduce wrinkles. After rolling out the product, several shovels of fill were placed on the edges and corners to hold down the geogrid composite, as depicted in Figure 4-3. When necessary, adjacent geogrid composite rolls were overlapped by at least 500 mm (Titan Environmental Containment, 2022).

Heavy equipment is not recommended to directly drive on top of geogrid composite, especially when the subgrade is relatively soft. In this case, the granular base material was first dumped and gradually pushed over the geogrid composite, with the dozer blade raising slowly to spread the fill material. After levelling the granular materials, more loads were dumped over the ground until it reached the design thickness as demonstrated in Figure 4-3. Finally, the base layer was compacted and graded to be ready for the asphalt placement. Using this construction procedure, it is recommended to sample granular materials after levelling the base surface and verify that no aggregate segregation occurs with gradation analysis. In addition, the lightweight deflectometer (LWD) testing was conducted; LWD results showed that the modulus for the base on top of the geogrid composite was consistent after installation.

4.2.2.2 Fibreglass Geogrid in Asphalt Binder Course (SP 19)

In this study, a biaxial fibreglass geogrid was used. This product is made of high-modulus glass filaments with a polymeric coating; the coated filaments are then bonded to an engineered polymeric membrane (EPM). The fibreglass geogrid has an opening of 25.4 mm × 25.4 mm, while the elastic modulus is 73,000 MPa and the ultimate tensile strength is 100 kN/m in both directions. During placement, the polymer-coated grids are placed directly on the asphalt surface after a tack coat is applied. As the EPM is designed to melt at elevated temperatures (around 80°C), it provides more adhesion between the grids and asphalt overlays (Titan Environmental Containment, 2017). The product is stable mechanically, chemically, and biologically. As this product is particularly engineered for asphalt reinforcement, this type of fibreglass geogrids can resist high temperatures with the polymer coating melting at temperatures >400°C and the glass melting at 820°C (Titan Environmental Containment, 2017)

As shown in Figure 4-4, the first 75 mm lift of SP 19 was placed on the base layer. A tack coat was placed on the first lift after one hour when the first lift had hardened and cooled down sufficiently. Due to the short length of this trial section, the tack coat was placed using hand rollers as shown in Figure 4-4 (left). The tack coat used in this study is Clean Bond Coat (CBC), which is a slow-setting asphalt emulsion and cures fast. It was diluted in a ratio of 50/50 with water. With the calculated one-lane pavement area of 50 m^2, approximately 50 L of diluted tack coat was applied on one lane using hand rollers to ensure even application. This process was repeated twice until the lane was fully coated. After the tack coat was applied, it was allowed time to cure as indicated by a colour change from brown to black as depicted in Figure 4-4 (middle). For the proper installation of the fibreglass geogrid, it is important not to disturb the surface while it cures; workers stepping and vehicles driving on tack-coated surfaces should be avoided. As such, the fibreglass geogrid was rolled out on the sidewalk first to minimize the potential loss of the tack coat during curing.

After the tack coat was cured, the fibreglass geogrid was placed; several people held the edges of the geogrid to reduce wrinkles during placement as shown in Figure 4-4. Wrinkle removal is also critical to ensure the bonding between the geogrid and the underlying asphalt. Several measures were taken including a drum roller running on the entire length (Figure 4-5), a small hand roller rolling on the wrinkle (Figure 4-5), as well as cutting from the middle of the wrinkle. After the placement, the second binder course lift was paved. The paver and other heavy equipment must be driven to the starting point of the paving direction before the tack coat application to prevent loss of the tack coat by the tires.

Figure 4-4 Installation of Fibreglass Geogrid in the Asphalt

Figure 4-5 Special Measures Taken during Fibreglass Geogrid Installation

Another challenge that occurred during the paving of the second lift overlying the geogrid. Due to insufficient adhesion, the geogrid was lifted and picked up by the paver which may be attributed to the tack coat not being fully cured before paving. Placing some loose asphalt mix in advance on the longitudinal and transverse edges of the geogrid, as shown in Figure 4-5, was found to improve the paving process. Using the same asphalt cement, as was used in the asphalt mixes, as a tack coat could perform better than emulsions and provide better adhesion (Titan Environmental Containment, 2017). In the future, this method could be compared to the usage of emulsion tack coats as was conducted in this study.

As per the manufacturer's recommendation, adjacent geogrids had at least 25 mm overlap. In this study, due to the width of the geogrid (i.e., 1.5 m), three sheets of the geogrid were needed on one lane, with two sheets at full width and one sheet of 0.9 m width. When placing the geogrid on the first lane, the geogrids were placed one after another, with the narrower one placed last, closest to the centerline. Due to the overlap of adjacent geogrids, some portions of the geogrid could not directly adhere to the tack-coated surface. As such, some parts of the narrower geogrid were picked up and lifted by the paver

during the paving process for the first lane. During the installation of the geogrid in the second lane, the narrower geogrid was placed first in the middle of the lane with the other two sheets at full width placed on top, thus, the lifting issue was minimized. In this case, the narrower geogrid fully adhered to the tack coat. Future on-site non-destructive testing and visual inspection can be performed to compare the long-term performance of the two lanes.

4.2.3 Field Instrumentation

As shown previously in Figure 1, each section was instrumented to monitor the temperature, moisture, and mechanical behaviour during construction as well as the future life of the pavement. The following subsection details the installation of temperature strings, moisture probes, pressure cells and strain gauges in the trial sections.

4.2.3.1 Temperature Sensor

One temperature string was instrumented in the base lift of the binder course and the middle of the base layer. Two temperature strings were installed at 10 cm below the surface of the subgrade. In this case, 4 strings were installed in each section with a total of 12 strings installed in the three sections. The resistor of the calibrated temperature sensor was measured and converted to temperature based on the following equation.

Equation 4-1

$$T = \frac{1}{1.127355 \times 10^{-3} + 2.343978 \times 10^{-4} \ln R} + 8.674848 \times 10^{-8} \times (\ln R)^3 - 273.15$$

where:

T = temperature (°C)

R = measured electrical resistance (Ω)

For the temperature sensors installed in the asphalt layer, heat shrink wrap was put around the wire of the sensors as protection from the high paving temperatures. Before the pavement of the first lift, the sensor was buried in the top of the base layer with only a small portion exposed to protect it from heavy equipment when paving. The temperature sensors were dug out after the first lift was paved. Figure 4-6 illustrates one temperature sensor that was dug out. The sensors have an operating range from -55°C to +150°C.

Figure 4-6 Temperature Sensor in the First Lift of the Binder Course

4.2.3.2 Moisture Probe

Two moisture probes were instrumented at three depths within the pavement structure: 10 cm below the surface of the subgrade, the middle of the base layer, and the top of the base layer. Therefore, 6 moisture probes were installed in each section and 18 moisture probes in total were instrumented in three sections. The probes used in this project are stable at temperatures below freezing. The moisture probes were programmed and calibrated in advance. The electrical resistance was measured and then the electrical resistance was calibrated to water potential as per Equation 4-2 (Irrometer, 2022).

Equation 4-2

$$\begin{cases} \Psi = 0, \quad if\ R < 0.55\ k\Omega \\ \Psi = (R \times 23.156 - 12.736) \times [-1 - 0.018(T - 24)], \quad if\ 0.55\ k\Omega < R < 1\ k\Omega \\ \Psi = \dfrac{-3.213 \times R - 4.093}{1 - 0.009733 \times R - 0.01205 \times T} \quad if\ 1\ k\Omega < R < 8\ k\Omega \\ \Psi = -2.246 - 5.239 \times R \times (1 + 0.018 \times (T - 24) - \\ \quad 0.06756 \times R^2 \times [1 + 0.018 \times (T - 24)]^2, \quad if\ R > 8\ k\Omega \end{cases}$$

where:

Ψ = water potential for the soil water tension in the pavement (kPa)

R = measured electrical resistance (kΩ)

T = obtained from the measured temperature in the corresponding location by the temperature strings (°C)

The calibrated moisture probes read water potential from 0 to 200 kPa, which represents the potential of how fluid flows, with a reading of 0 meaning the soil is saturated and 200 kPa indicating dry conditions.

Before installation, the probes were saturated in water for one hour and submerged in dry sand overnight, then they were saturated in the water again to activate the probes. Such a process was repeated several times until activation was successful. Finally, the moisture probes were conditioned by soaking in the water for at least 24 hours before they were installed. To ensure saturation before the installation, the probes were soaked in plastic bags filled with water and fastened with zip ties allowing for transport to the site.

4.2.3.3 Total Earth Pressure Cell on Subgrade

One earth pressure cell was installed on the subgrade in each section, with three in total. The pressure cell can measure the stress on a plane surface; the installed pressure cells have an operating temperature range from -29°C to +65°C. The current can be measured and converted to pressure by using the calibration equation provided by the manufacturer shown in Equation 4-3.

Equation 4-3

$$\sigma = mX + b$$

where:

σ = the measured stress (MPa)

X = the measured current (mA)

m = scale factor (MPa/mA)

b = offset (MPa)

The calibrated readings show negative values when representing compressive stress. The pressure cells were placed along the right wheel path (RWP). Fine sand was placed beneath the pressure cell to act as a flat base as well on the sensor to provide a stable environment for reading. Metal U-shaped pegs were used to hold the pressure cells in position, as shown in Figure 4-7. In Section #3 (control section), the geosynthetics were placed above the pressure cell to measure the benefit provided by the geogrid composite.

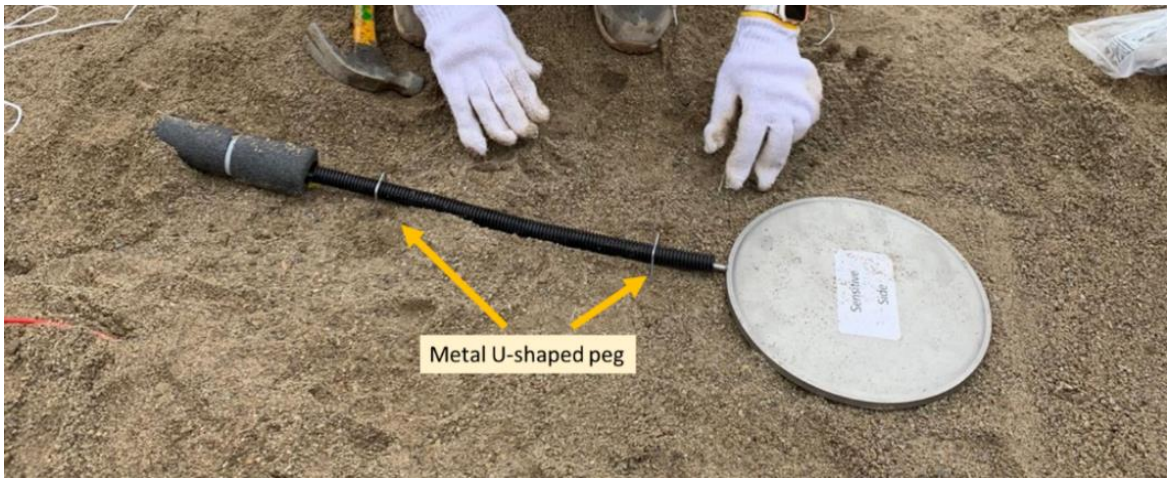

Figure 4-7 Installation of Pressure Cell

4.2.3.4 Dynamic Strain Gauges in Asphalt

Two strain gauges were installed in the base lift of the asphalt binder course, with one in the longitudinal and the other in the transverse direction. These strain gauges were designed to measure the horizontal axial strain under high-frequency loads and can work at temperatures ranging from -34°C to +200°C. High-temperature wires are used to ensure that the cabling will be undamaged from the high-temperature paving process. The strain gauges are all placed along the RWP.

These strain gauges were calibrated by zeroing the voltages first. The resultant voltage measured from the sensor was multiplied by the calibration factor (units: με/mV/V) provided by the manufacturer. A positive reading represents tensile strain and a negative reading represents compressive strain. Like the installation of the temperature sensors in the asphalt, the strain gauges were dug out right after paving the first lift and before the asphalt cooled. Metal U-shaped pegs were used to hold the gauges in longitudinal and transverse directions. Care was taken to avoid vibration of the roller compactor directly on the sensors. The installation of the strain gauge is shown in Figure 4-8.

Figure 4-8 Installation of Starin Gauge

4.2.3.5 Installation of Sensor Tree and Protection

To ensure that all the sensors measure the corresponding properties at the designed depth, a sensor "tree" was built for each section. The trees were made with PVC pipes with a diameter of 0.75 inches (19 mm). Branches were connected at specific heights of the tree with the sensors attached and all the wires can be accessed from the middle of the tree which is located at the top of the subgrade as illustrated in Figure 4-9. As seen in Figure 7, one temperature sensor and two strain gauges are located at the top of the tree that was buried in the asphalt. Two moisture probes are located at the branch at the top of the base layer. Two moisture probes and one temperature sensor are located at the branch in the middle of the base layer, which is approximately 22.5 cm from the top of the base layer. Then, one pressure cell is located at the top of the subgrade. Lastly, two moisture probes and two temperature sensors are located at the branch that is 10 cm below the surface of the subgrade.

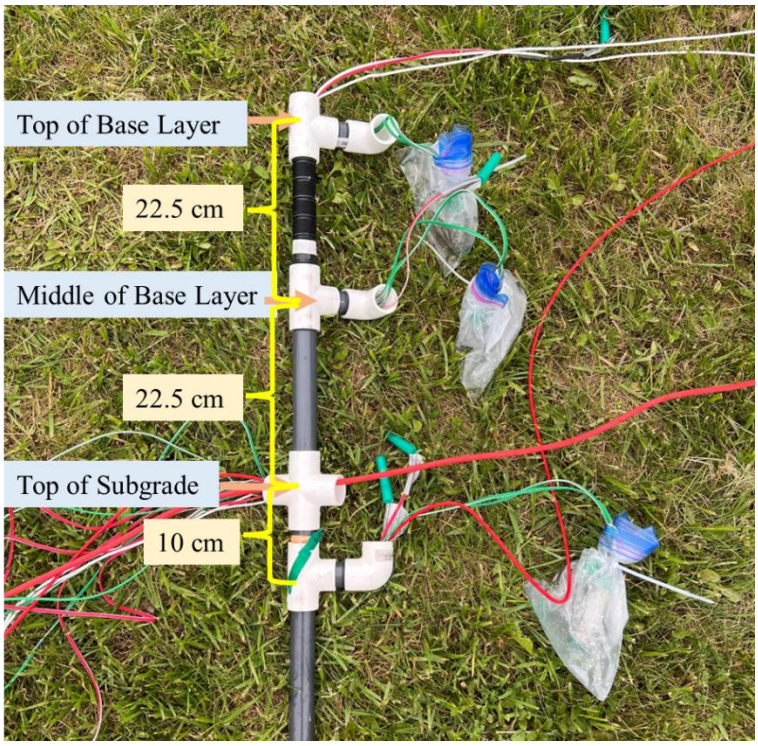

Figure 4-9 Sensor Tree

To install the sensor tree, a hole was dug from the subgrade and placed in the soil. The location of the tree was carefully examined to ensure the lowest branch of the tree was 10 cm below the surface of the subgrade. Then, the surrounding area of the tree was backfilled with excavated subgrade soil, as shown in Figure 4-10. The backfilled soil was manually compacted with a hand compactor. Wood boxes were used to cover the sensor trees temporarily to protect them from heavy equipment during construction. A similar procedure also was used to backfill and compact the granular base, as shown in Figure 4-11.

Figure 4-10 Installation of Sensor Tree in the Subgrade

Figure 4-11 Backfilling and Hand Compaction of Granular Base around Sensor Tree

4.2.3.6 Connection to Data Logging Box

After the installation of the sensor tree in the subgrade, the wires of all the sensors running out from the tree were fished through the white PVC conduits laid out on the subgrade. As shown in Figure 4-10, a connector was used to connect the tree with the conduit. The conduits then connect the three sensor

trees and meet at the location of the data box, in the middle of the second section, which is shown in Figure 4-12.

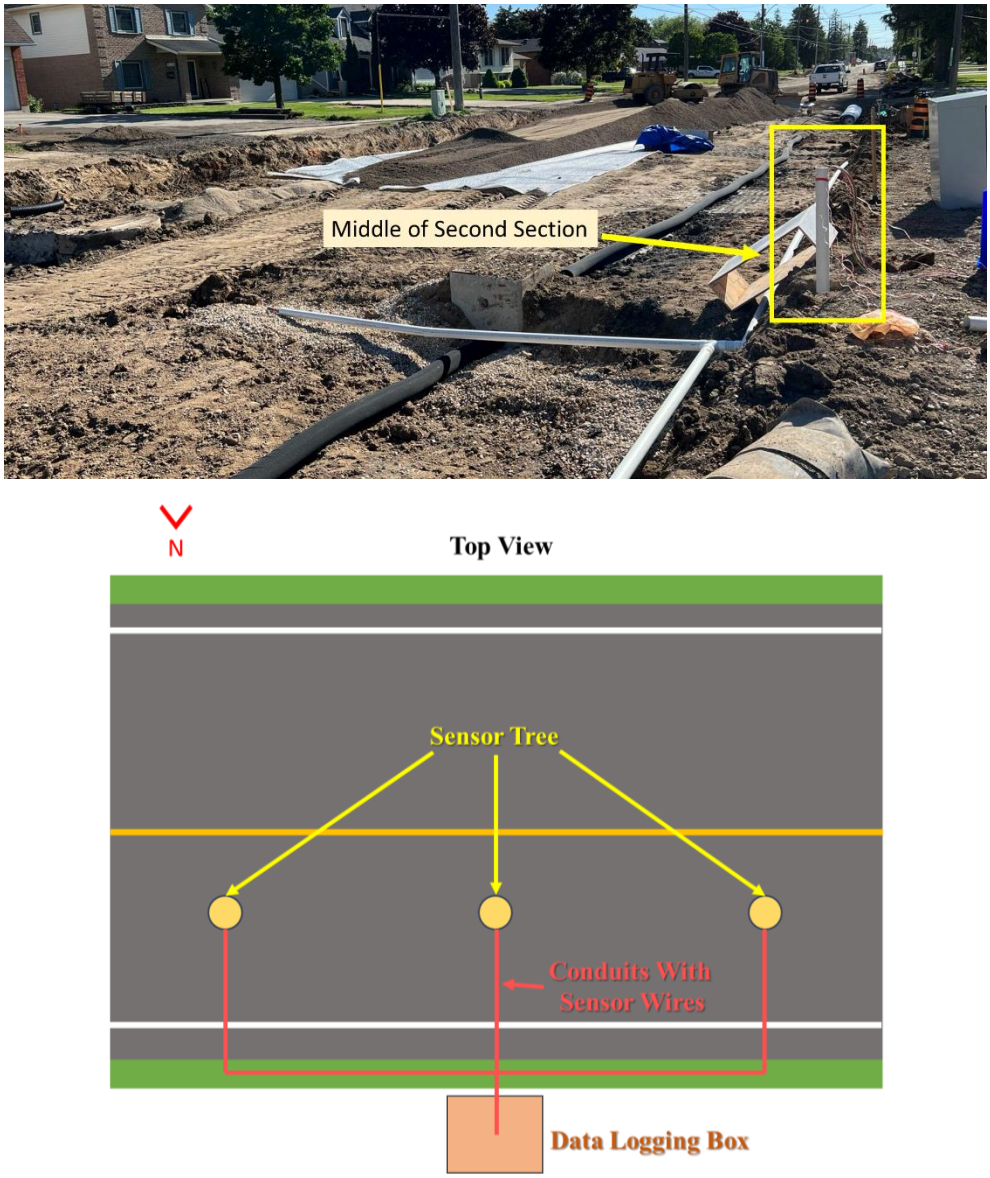

Figure 4-12 Layout of the Conduits

The construction process involved the casting of a concrete base around the conduit, facilitating the installation and secure housing of various wires, as shown in Figure 4-13. A concrete base provides a stable foundation and reliable support for the subsequent installation of the data box. Additionally, the construction of a steel box, housing the data logger and battery, further enhances the protective enclosure for these essential components.

The steel box, once carefully positioned, was securely fastened and affixed to the concrete base, ensuring a stable and durable mounting for the data logger and battery. This meticulous installation process guarantees the safety and security of the electronic equipment, protecting it from potential environmental hazards and ensuring its functionality and longevity over an extended operational period.

Figure 4-13 Data Logging Unit

4.2.3.7 Frost Tube

Other than sensors connected to the data logger, a frost tube was installed in each section to measure frost depth in the soil. The frost tube is composed of an exterior PVC pipe serving as a protection envelope, and an interior clear pipe to be filled with diluted methylene solution. The inner tube is attached to a removal cap at the top of the pipe envelope, which enables it to be pulled out of the inner tube and monitor the frost penetration. The composition of the frost tube is illustrated in Figure 4-14. A methylene solution should be injected into the inner tubing, which is a blue chemical solution with low density at room temperature. Therefore, when the soil freezes, it will remain in the unfrozen zone and the rest will become colourless. In other words, the solution in the inner tubing is blue when the soil is unfrozen and becomes white when the soil is frozen.

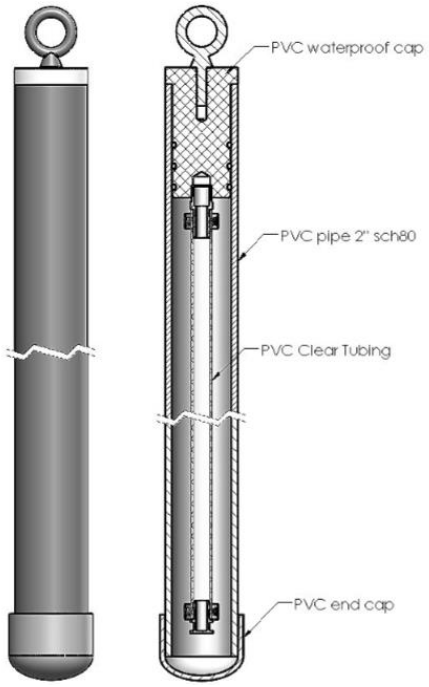

Figure 4-14 Frost Tube Configuration (Roctest, 2018)

The methylene power was diluted with distilled water and filled in the inner tube as shown in Figure 4-15. After the construction of the granular base, a hole was drilled in each section for about 3 m vertically downwards. The soil and stone particles were vacuumed out so that the pipe envelope could be inserted into the ground. Then, extra fill and granular were backfilled around the pipe. After the construction of the asphalt binder course and surface course, the pipe was brought upwards with a metal cap sealed at the top so that the riding quality would not be affected. The inner tube was inserted into the pipe envelope with a removable cap attached. The installation process is illustrated in Figure 4-16. The frost tube was supposed to measure the frost penetration from the top of the base layer to 3 m below.

Figure 4-15 Methylene Solution Filled in Frost Tube

Figure 4-16 Frost Tube Installation Process

4.3 Material Characterization

In this section, the laboratory testing performed on the materials sampled from the construction of the field trial sections was discussed to characterize the material and for further evaluation of field performances. Particle distribution analysis, optimum water content, Atterberg limits, and California Bearing Ratio (CBR) tests were performed to classify the soils. Particle distribution analysis, optimum water content, and California Bearing Ratio (CBR) tests were performed on sampled granular base materials to compare with the information provided by the consultant to verify. Lastly, the complex dynamic modulus was tested on asphalt mixes sampled from the field.

4.3.1 Field Sampled Subgrade Soil

With the limited number of boreholes performed by geotechnical investigation, the subgrade soil was sampled in each section of the field. During construction, the subgrade was excavated around 800 mm below the final grade. At this time, subgrade soil was sampled from the control, geogrid, and geogrid composite sections, as shown in Figure 4-17.

Figure 4-17: Subgrade Sampling from the Field

Laboratory testing was performed on the sampled soil to characterize the properties, including the sieve analysis, hydrometer analysis, Plastic Index and Liquid Limit, optimum water content, and California Bearing Ratio (CBR). The soil classification was determined with these laboratory results, which can be further referenced for performance evaluation and modelling.

.

4.3.1.1 Sieve Analysis

The soils were dry sieved as per ASTM D6913 (ASTM, 2017) with two trials first, and the gradation results are shown in Figure 4-18.

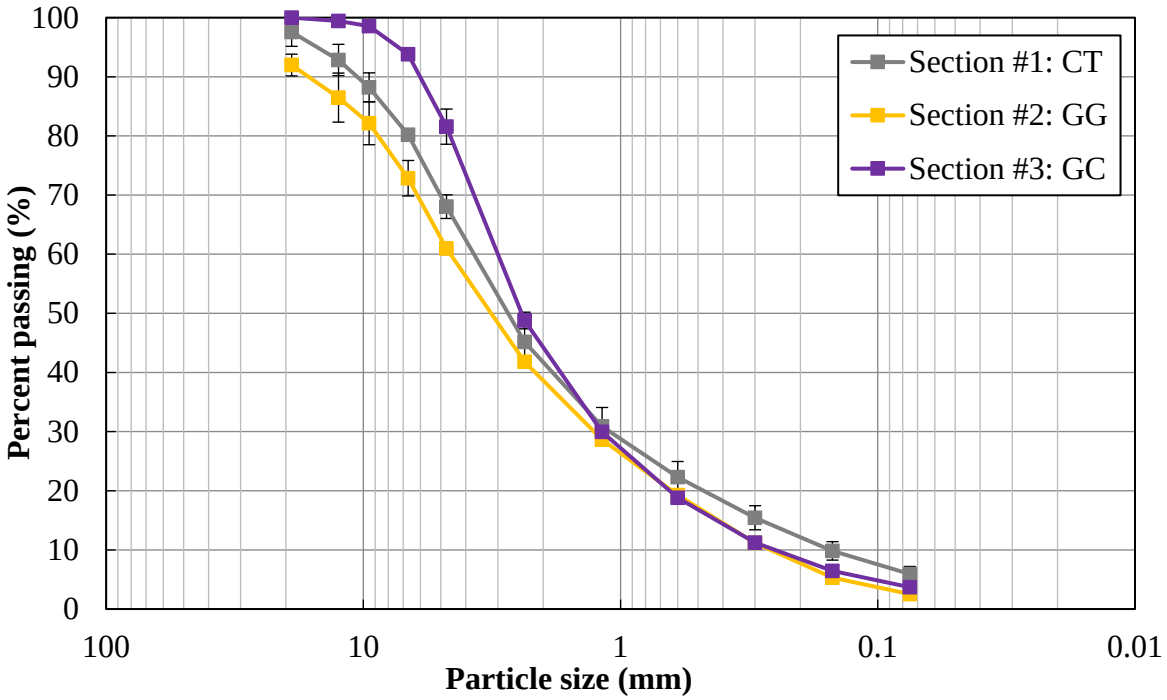

Figure 4-18 Particle Size Distribution of Sampled Soil with Dry Sieve Analysis

During the sieving, it was found that a considerable number of fine particles were attached to the coarser ones. The conventional sieve analysis cannot represent the gradation of the soils as the manual pulverization cannot completely separate the fine particles into their actual sizes. Therefore, another set of soil samples with 3000 g of soil samples from each section was washed on the No. 200 sieve (75 μm). The weight of soils before and after washing is listed in Table 4-1.

Table 4-1 Weight of Soils Before and After Wash

Section	Mass (g)		Particles smaller than 75 μm	
	Before Wash	After Wash	Mass (g)	Ratio by Mass (%)
Section #1: CT	3000.0	1656.8	1343.2	44.77%
Section #2: GG	3000.0	1783.6	1216.4	40.55%
Section #3: GC	3000.0	1256.3	1743.7	58.12%

It was concluded from the percentages of the fine particles smaller than 75 μm that a hydrometer analysis is needed to classify the fines. The washed soils retained on the No. 200 sieve were oven-dried and sieved to determine the gradation of gravels (i.e., soils larger than 4.75 mm) and sands (i.e., soils smaller than 4.75 mm but larger than 75 μm). The gradation of these materials is plotted in Figure 4-19.

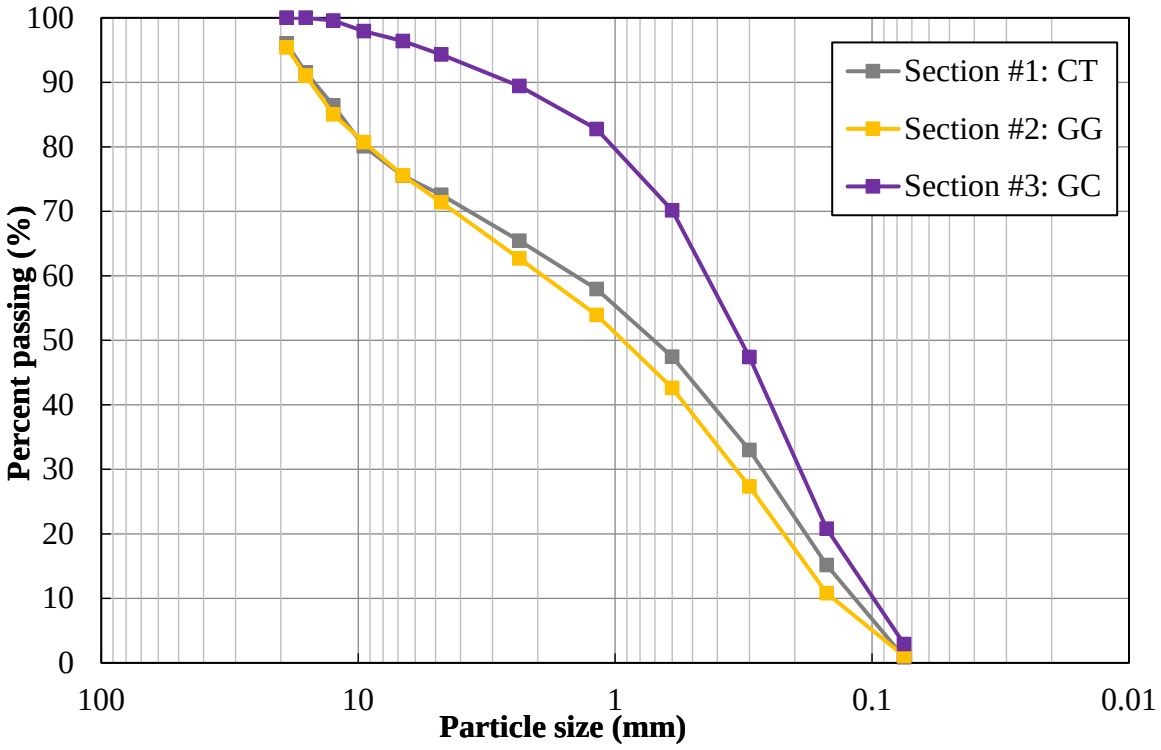

Figure 4-19 Particle Size Distribution of Sampled Soil with Sieve Analysis After Wash

4.3.1.2 Hydrometer Analysis

Given the considerable amount of fines in the sampled soil, hydrometer analysis was performed according to ASTM D422-63 (ASTM, 2007). The mass of the actual soil sample was corrected by

considering the humidity in the air absorbed by the soil by calculating hygroscopic moisture content, as shown in Equation 4-4 and Equation 4-5. The percentage of soils passing 2.00 mm sieve was obtained by interpolating from Figure 4-19 and taking the percentage of particles smaller than 75 μm in Table 4-1 into account.

Equation 4-4

$$\boldsymbol{H_{cf} = \frac{M_{od}}{M_{ad}}}$$

Equation 4-5

$$M_{hydro} = \frac{hs \times H_{cf}}{\%\ passing\ 2.00\ mm\ sieve}$$

where:

H_{cf} = hygroscopic correction factor

M_{od} = mass of oven-dried soil (g)

M_{ad} = mass of air-dried soil (g)

M_{hydro} = hygroscopic corrected soil sample (g)

hs = mass of tested sample (g)

The difference of specific gravity between the dispersing agent and distilled water (a), meniscus correction, and temperature correction factor (C_T) was considered when doing the calculations as per Equation 4-6 to Equation 4-8 based on the standard (ASTM, 2007).

Equation 4-6

$$R_{actual} = hydrometer\ reading + meniscus\ correction$$

Equation 4-7

$$R_c = R_{actual} - composite\ reading + C_T$$

Equation 4-8

$$P = \frac{R_c a}{M_{hydro}} \times 100$$

where:

R_{actual} = hydrometer reading corrected by the meniscus correction

R_c = Corrected hydrometer reading

C_T = temperature correction factor

The corresponding diameter of particle size was determined by Equation 4-9 based on Stokes' Law.

Equation 4-9

$$D = K\sqrt{\frac{L}{t}}$$

where:

D = particle diameter (mm)

K = constant based on water temperature and specific gravity of soil

L = effective depth based on hydrometer (cm)

t = elapsed time from the beginning of the test (min)

After 1440 min as the final reading, the sample was washed on the No. 200 sieve (75 μm), dried, and sieved to determine the distribution of those bigger than 75 μm.

4.3.1.3 Particle Size Distribution

Sieve analysis was performed to determine the distribution of particles larger than 75 μm and hydrometer analysis was done to analyze the gradation of soils passing the 75-μm sieve. The percentage of particles smaller than 75 μm specified in Table 4-1 was incorporated with the results in Figure 4-19 to produce the sieve analyses and amalgamated with the hydrometer analyses. The gradation and percentages of subgrade soil are listed in Table 4-2. The final particle size distribution of the sampled soil from three sections is provided in Figure 4-20. It can be seen that the subgrade soil from CT and GG has similar particle size distribution, while the soil from GC has a higher percentage of clay accounting for 50.02% by weight. This can be due to the elevation of GC being lower compared to the other two sections, so water and fines tend to flow to this section. This can be verified with the SurPro® profiling results in a subsequent section. For CT and GC, more than half of the material is larger than 0.075 mm, and more than 12% of the material is fine material.

Table 4-2 Gradation of Sampled Soil with Sieve and Hydrometer Analysis

	Section #1: CT	Section #2: GG	Section #3: GC
% Gravel (> 4.75 mm)	15.15	17.02	2.38
% Sand (4.75 mm - 0.075 mm)	39.63	41.76	19.84
% Silt (0.075 mm - 0.002 mm)	27.00	23.43	27.65
% Clay (< 0.002 mm)	18.22	17.79	50.12

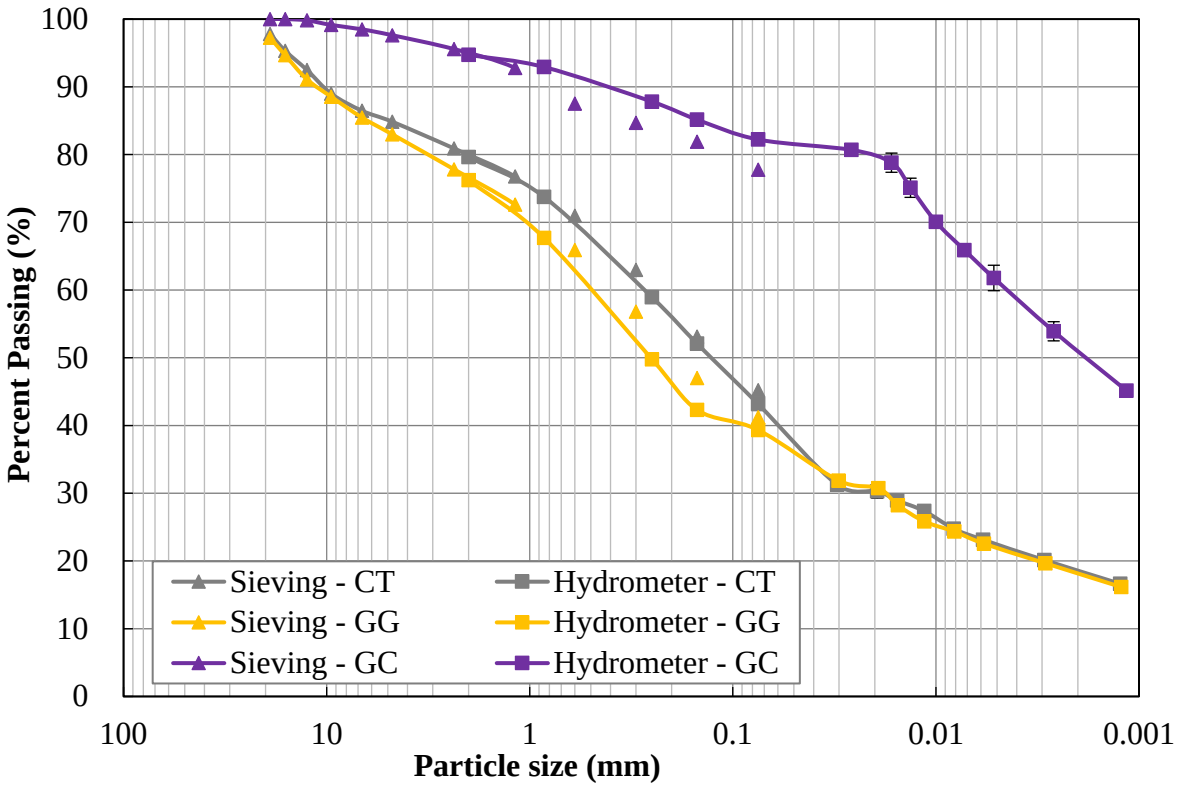

Figure 4-20 Particle Size Distribution of Sampled Soil with Sieve and Hydrometer Analysis

4.3.1.4 Optimum Water Content and Density

The optimum water content and the corresponding density were determined as per ASTM D698-12 (ASTM, 2021a). After recording the mass of the compacted specimen and a representative portion, the procedure was repeated several times with more moisture added until the wet weight reached the maximum to produce a dry density compaction curve. The dry density and saturation point can be calculated using Equation 4-10 to Equation 4-11, and (ASTM, 2021a).

Equation 4-10

$$\rho_{wet} = \frac{M_{total} - M_{mold}}{V}$$

Equation 4-11

$$\rho_{dry} = \frac{\rho_{wet}}{1 + \frac{w}{100}}$$

Equation 4-12

$$w_{sat} = \frac{\gamma_w G_S - \gamma_{dry}}{\gamma_{dry} G_S} \times 100$$

where:

ρ_{wet} = wet density of compacted specimen (g/cm^3)

M_{total} = mass of compacted specimen and mould (g)

M_{mold} = mass of mould (g)

V = volume of mold (cm^3)

ρ_{dry} = dry density at compaction point (g/cm^3)

w = water content at compaction point (%)

w_{sat} = saturated water content (%)

γ_{wet} = unit wight of water (= 9.789 kN/m^3)

γ_{dry} = dry unit weight of soil (= 9.81×ρ_{dry})

G_S = specific gravity of soil

The dry density curve was plotted in Figure 4-21 along with a 100% saturation curve. The optimum water content with the maximum dry density and their saturated water content are listed in Table 4-3. Results show that the subgrade soil sampled from CT and GG have similar optimum water content, while soil from GC has a higher optimum water content, with a higher fraction of clay analyzed from particle size distribution.

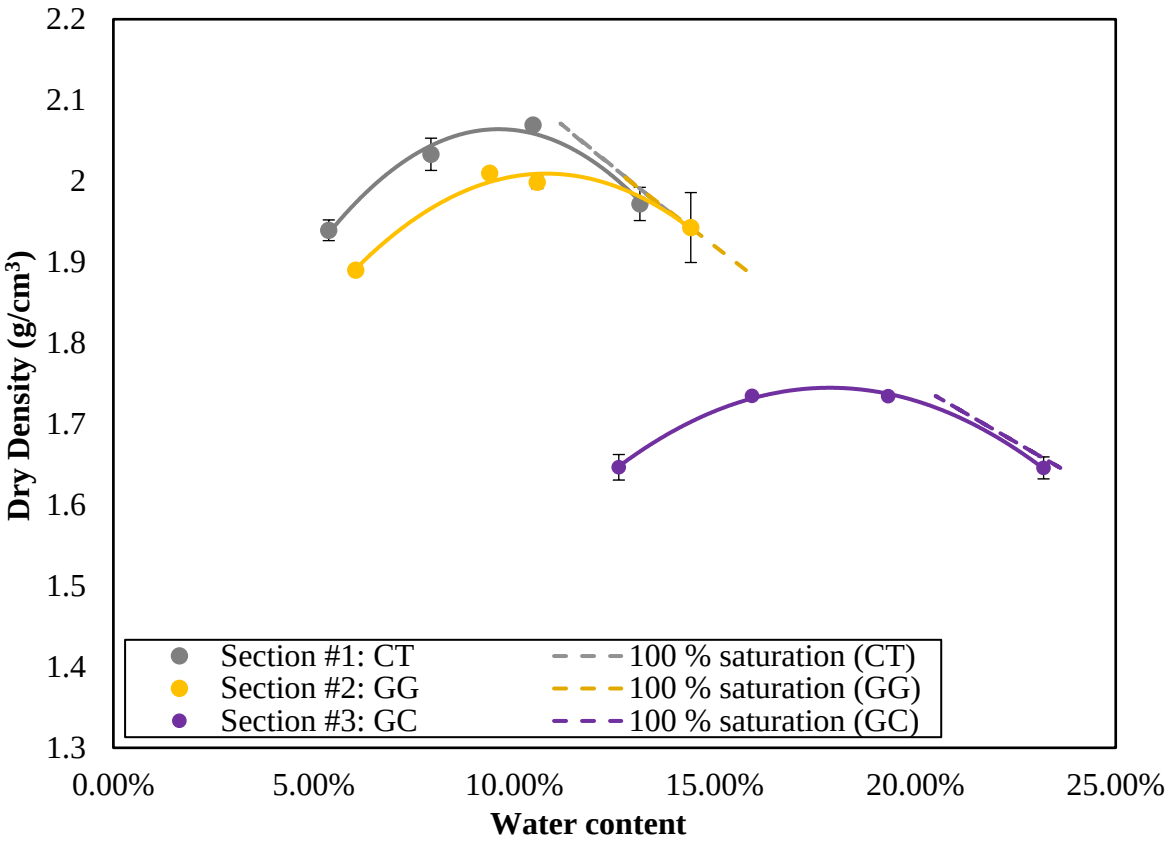

Figure 4-21 Moisture - Density Relationship of Sampled Soil

Table 4-3 Optimum and Saturated Water Content and Density of Sampled Soil

Section	Maximum Dry Density (g/cm^3)	Optimum Water Content (%)	Saturated Water Content (%)
Section #1: CT	2.06	9.61%	11.31%
Section #2: GG	2.01	10.79%	12.63%
Section #3: GC	1.75	17.87%	20.15%

4.3.1.5 Atterberg Limits

Atterberg limit tests were determined for sampled soil from three test sections following ASTM D4318 (ASTM, 2018). Plasticity indexes were calculated by subtracting the plastic limit from the liquid limit. The results are presented in Figure 4-22. Soils from all three sections have a liquid limit of less than 50% and plasticity indexes greater than 7, with the soil from GG exhibiting the lowest value.

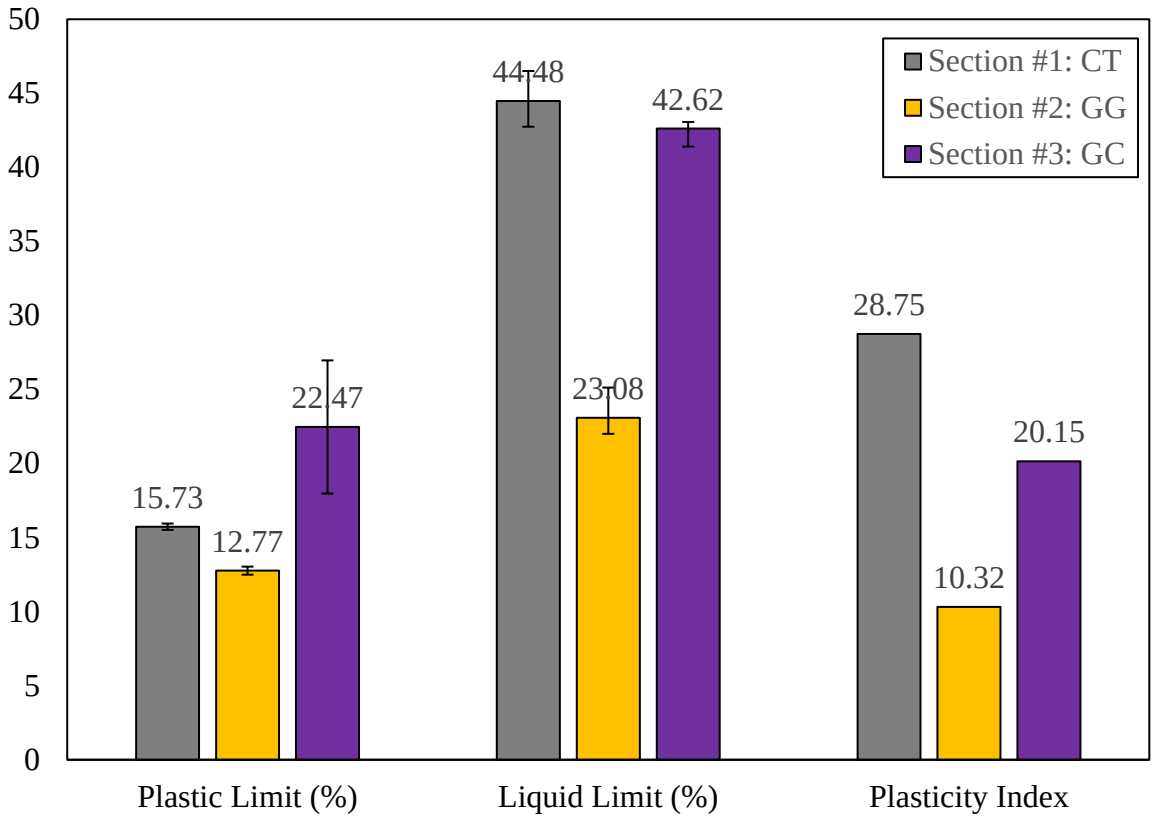

Figure 4-22 Atterberg Limits of Sampled Soils

4.3.1.6 California Bearing Ratio and Resilient Modulus

California Bearing Ratio (CBR) is an indicator of the bearing capacity of compacted soils. The test is performed by penetrating a piston into the soil as per ASTM D1883 (ASTM, 2021b). The percentage of swell before and after the soaking period was measured and calculated using Equation 4-13.

Equation 4-13

$$Swell = \frac{D_f - D_i}{h} \times 100$$

where:

$Swell$ = swell during the 96-hour soaking (%)

D_f = dial reading after 96-hour soaking (mm)

D_i = dial reading before 96-hour soaking (mm)

h = height of specimen before soaking (mm)

Moisture content before soaking and after testing were determined on representative soil samples following ASTM D2216 (ASTM, 2019). Results of these moisture contents and swell during soaking are shown in Table 4-4.

Table 4-4 Moisture Contents and Swell of Sampled Soils During Soaking

Section	Moisture Content		Swell
	Before Soaking	After Testing	
Section #1: CT	10.41%	10.05%	2.78%
Section #2: GG	9.31%	9.80%	0.00%
Section #3: GC	18.55%	24.79%	7.96%

By recording the load readings at multiple penetration points, a load-penetration curve can be plotted and CBR can be calculated using Equation 4-14.

Equation 4-14

$$CBR_{XX} = \frac{SOP}{Standard\ Stress} \times 100$$

where:

XX = penetration (= 2.5 mm or 5.1 mm)

SOP = stress on piston (MPa)

$Standard\ Stress$ = 6.9 MPa for XX = 2.5 mm

= 10.3 MPa for XX = 5.1 mm

The load-penetration curve of sample soil from each section was plotted in Figure 4-23 and their CBR at 5.1 mm penetration is shown in Figure 4-24. In the figure, CBR at 2.5 mm penetration was represented by the error bars. As per the standard, $CBR_{5.1}$ is taken as the bearing ratio when the two values are similar (ASTM, 2021b).

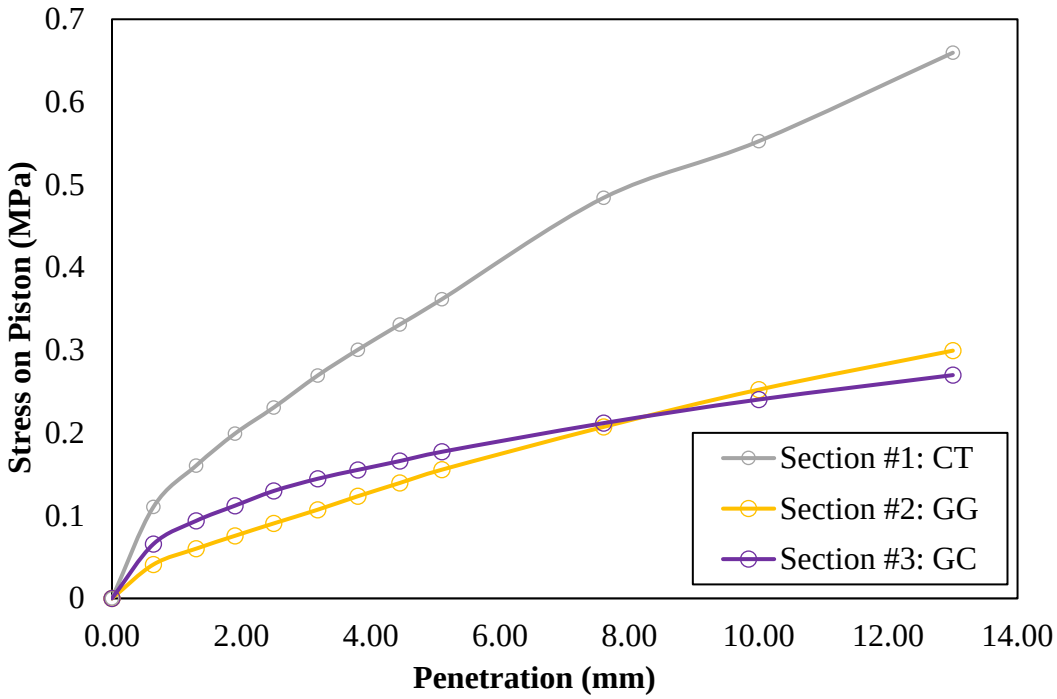

Figure 4-23 Load-Penetration Curves of Sampled Soil

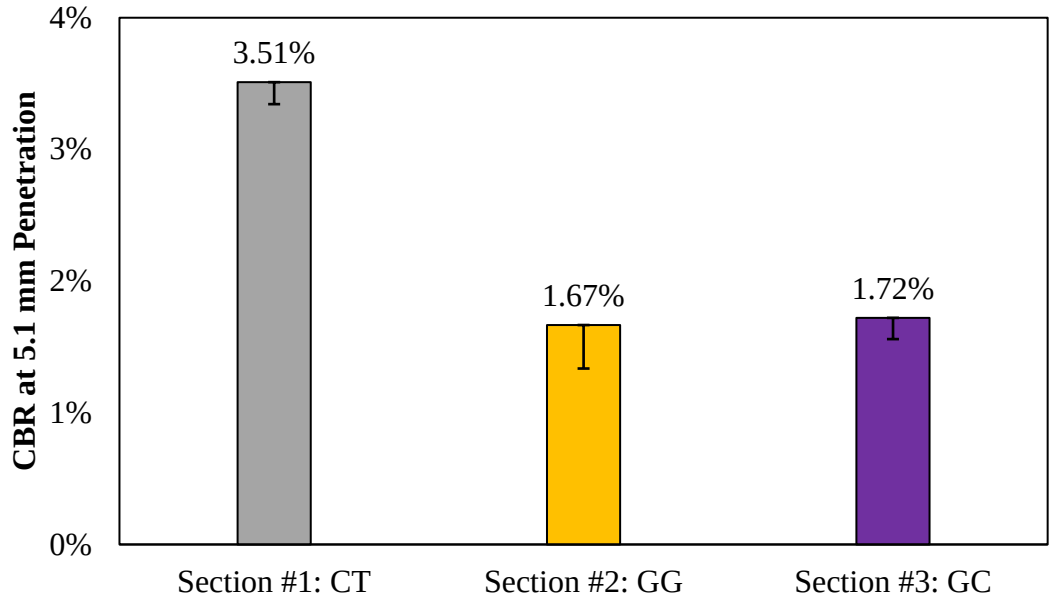

Figure 4-24 CBR values of Sampled Soil

In North America, resilient modulus is a common property for unbound materials. Many correlations were developed between resilient modulus and CBR. Empirical models used in AASHTO 93 guide

(AASHTO, 1993b) in Equation 4-15 and AASHTOWare Pavement ME method (MEPDG) (Powell et al., 1984) in Equation 4-16 were used in this study to calculate the resilient modulus, shown in respectively. The correlated results are listed in Table 4-5. CBR correlated M_R by the two models are similar to each other. CT has the highest resilient modulus, while GG and GC show similar values.

Equation 4-15

$$M_R = 10.3 \times CBR \qquad (CBR < 10)$$

Equation 4-16

$$M_R = 17.6 \times CBR^{0.64}$$

where:

M_R = correlated resilient modulus (MPa)

Table 4-5 Correlated Resilient Modulus of Sample Soil from CBR (MPa)

	$CBR_{5.1}$	**Correlated from CBR (AASHTO 93)**	**Correlated from CBR (MEPDG)**
Section #1: CT	3.51%	39.32	36.30
Section #2: GG	1.67%	24.40	17.23
Section #3: GC	1.72%	24.91	17.79

4.3.1.7 Soil Classifications

From the previous results, the sampled soil from three sections was classified using the Unified Soil Classification System (USCS) (ASTM, 2020) and AASHTO Soil Classification (AASHTO, 2021). The classification is listed in Table 4-6.

USCS classifies soils from CT and GG as clayey sand / sand-clay mixtures (SC), and those from GC as inorganic clays with low to medium plasticity (CL). CT and GG are classified as coarse-grained soils, while GC is fine-grained soil. As per the MEPDG-Ontario pavement design model, the susceptibility to frost action in GC is slight to severe, while that in CT and GG is negligible to slight. The drainage characteristics can be practically impervious in all three sections (MTO, 2019). Based on correlated M_R from CBR in Table 4-5, the subgrade condition in CT is good-fair; the subgrade condition in GG is poor; and the subgrade condition in GC is fair-poor. The correlated M_R results from CBR show good subgrade conditions in all three sections.

Table 4-6 Soil Classification by USCS

Section	USCS	AASHTO
Section #1: CT	SC	A-7-5
Section #2: GG	SC	A-6
Section #3: GC	CL	A-7-5

AASHTO Soil Classification System classifies soils from all three sections as silt-clay materials with more than 35% of materials passing 75μm-sieve. Soils sampled from CT and GC are classified in the A-7-5 group as clayey soils with moderate plasticity. GG is classified in the A-6 group as plastic clay soil. The general rating of soils in these groups as subgrade is fair to poor.

From the geotechnical report conducted before the construction provided to the Region of Waterloo (Pinchin Ltd., 2020), only one borehole was investigated on the trial sections (BH21 as shown in Figure 4-25). According to the borehole log provided in Figure 4-26, below the old pavement structure, there was some sandy silt fill and clayey silt with traced sand and gravel. This matches the soil characterization conducted in the laboratory, with clayey sand / sand-clay mixtures.

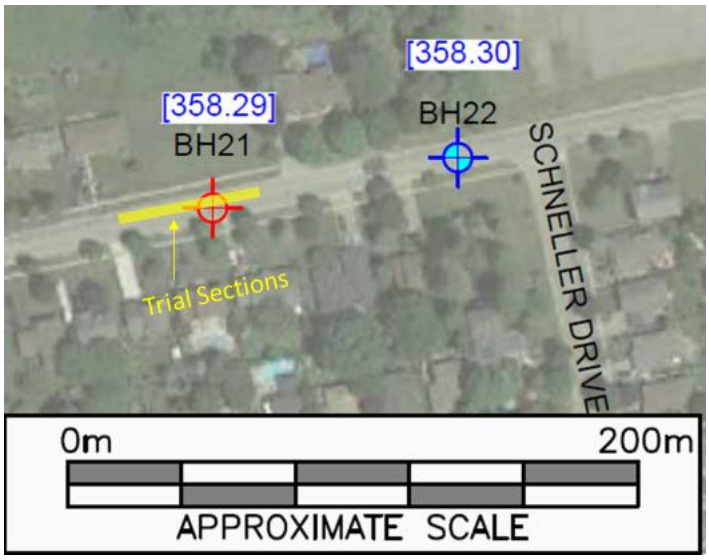

Figure 4-25 Borehole Locations (Base: Pinchin Ltd., (2020))

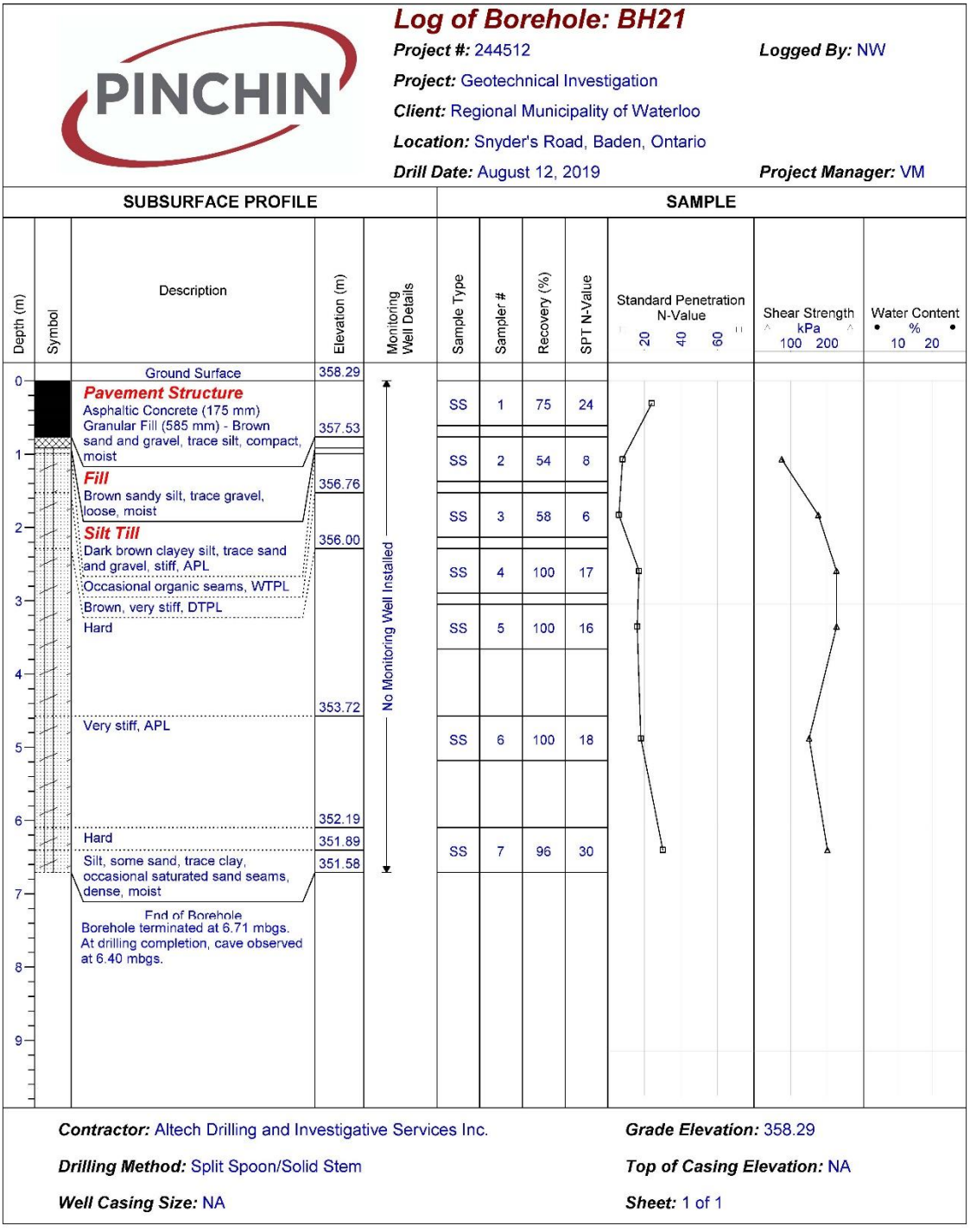

Figure 4-26 Borehole Log (Pinchin Ltd., 2020)

4.3.2 Granular Material Used for Base Layer

The aggregates used in the base layer are Granular A materials as per Ontario Provincial Standard Specifications (OPSS), which is a type of dense graded aggregate completely passing a 26.5 mm sieve. A minimum of 50% crushed particles is required (MTO, 2013). Granular A materials sampled from three sections during base layer construction were tested in the laboratory.

4.3.2.1 Particle Size Distribution

Sieve analysis was performed following ASTM D6913 (ASTM, 2017). The results were compared with the results provided by the consultant (Englobe, 2022) and checked against the Specification Gradation Requirements in OPSS 1010 (OPSS, 2013). The results and comparison are plotted in Figure 4-27.

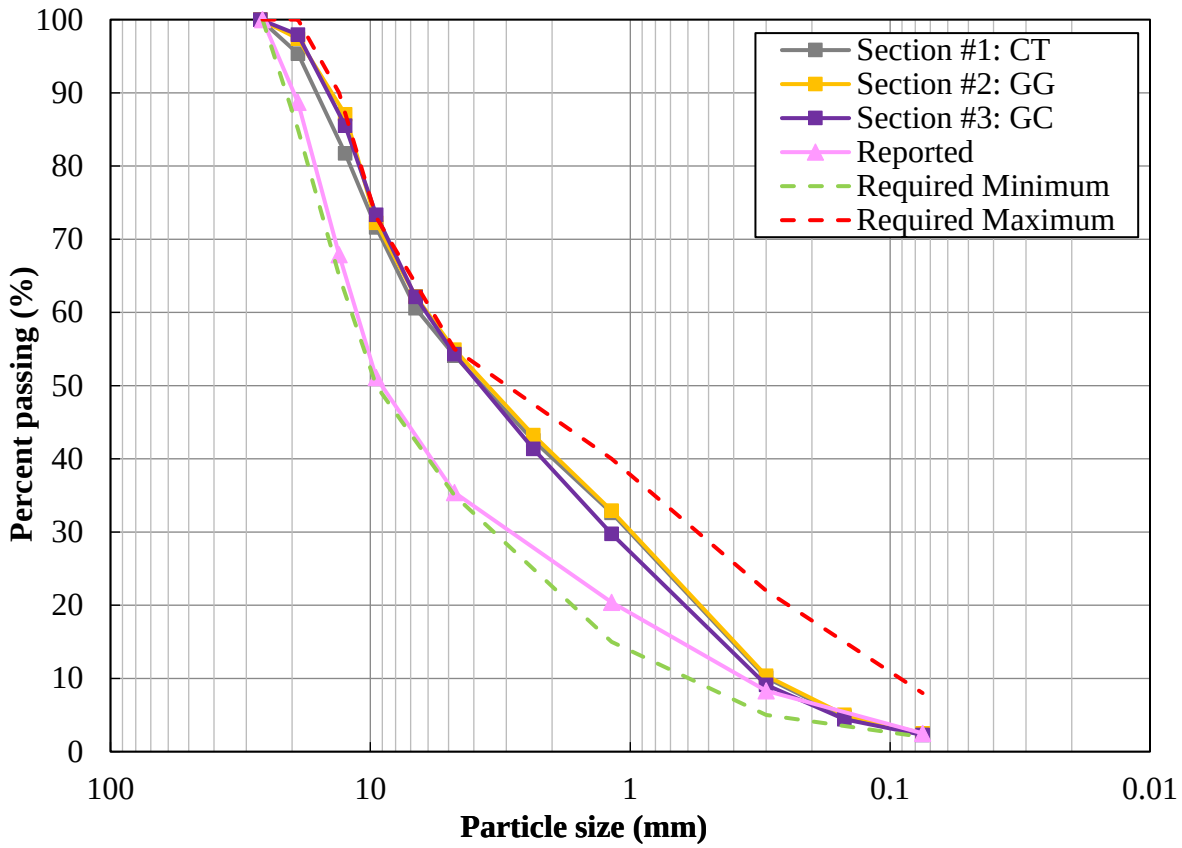

Figure 4-27 Particle Size Distribution of Sampled Granular Base Material

Sampled granular base materials have slightly different particle size distributions from results reported by the consultant, while all three sections have similar particle size distributions. They all meet the gradation requirement specified in OPSS 1010 (OPSS, 2013).

4.3.2.2 Optimum Water Content and Density

Proctor testing was conducted, and optimum water content was obtained for granular aggregates sampled from three sections, following a similar procedure for subgrade soils. Table 4-7 lists the results, which are consistent for three sections.

Table 4-7 Optimum and Saturated Water Content and Density of Sampled Base Aggregates

Section	Maximum Dry Density (g/cm^3)	Optimum Water Content (%)	Saturated Water Content (%)
Section #1: CT	2.05	10.20%	11.53%
Section #2: GG	2.02	10.20%	12.34%
Section #3: GC	2.05	10.72%	11.59%

4.3.2.3 California Bearing Ratio and Resilient Modulus

CBR testing was also conducted on compacted specimens using sampled base aggregates in the laboratory. Results of the moisture contents and swell during soaking are shown in Table 4-4. No swelling occurred during soaking.

Table 4-8 Moisture Contents and Swell of Sampled Base Aggregates During Soaking

Section	Moisture Content		Swell
	Before Soaking	After Testing	
Section #1: CT	12.23%	8.71%	0.00%
Section #2: GG	11.22%	8.66%	0.00%
Section #3: GC	11.61%	8.61%	0.00%

Load-penetration curve of sampled aggregates from three sections was plotted in Figure 4-28, with the CBR results shown in Figure 4-29. CBR at 2.5 mm penetration was represented by the error bars. $CBR_{5.1}$ is taken as the bearing ratio as they are closer to the typical values of Granular A (AASHTO, 1993a).

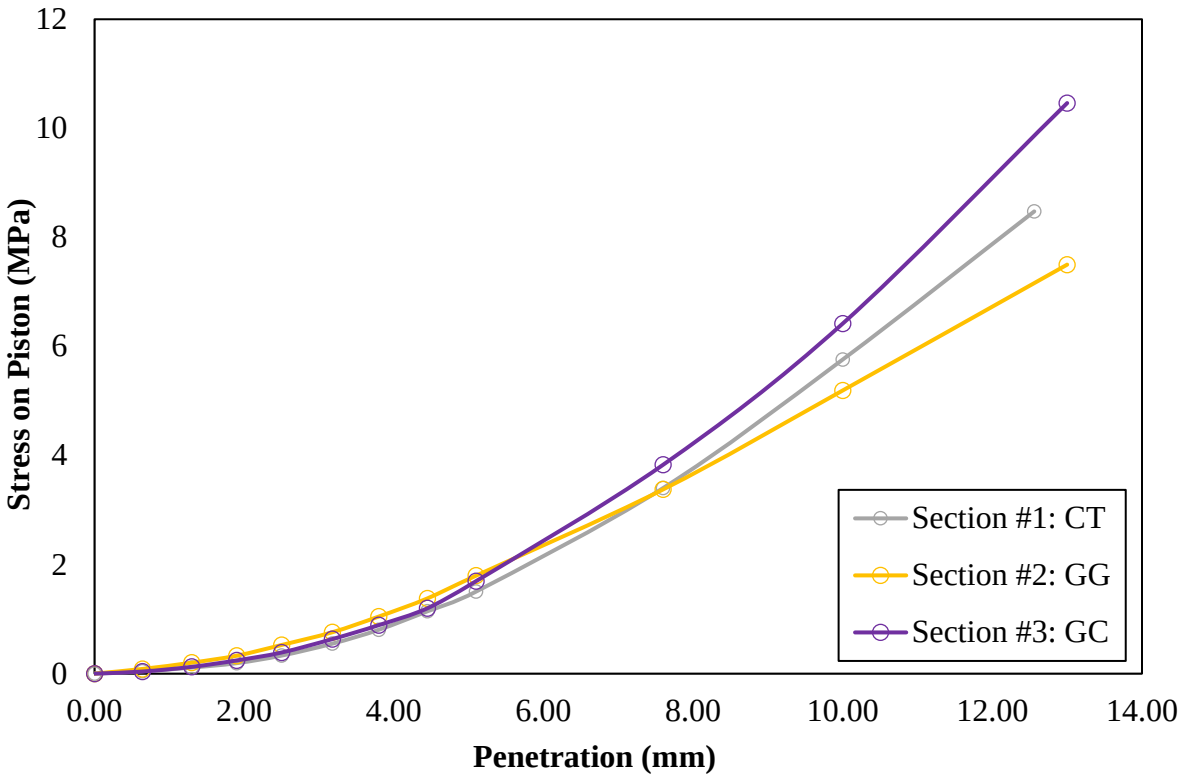

Figure 4-28 Load-Penetration Curves of Sampled Base Aggregates

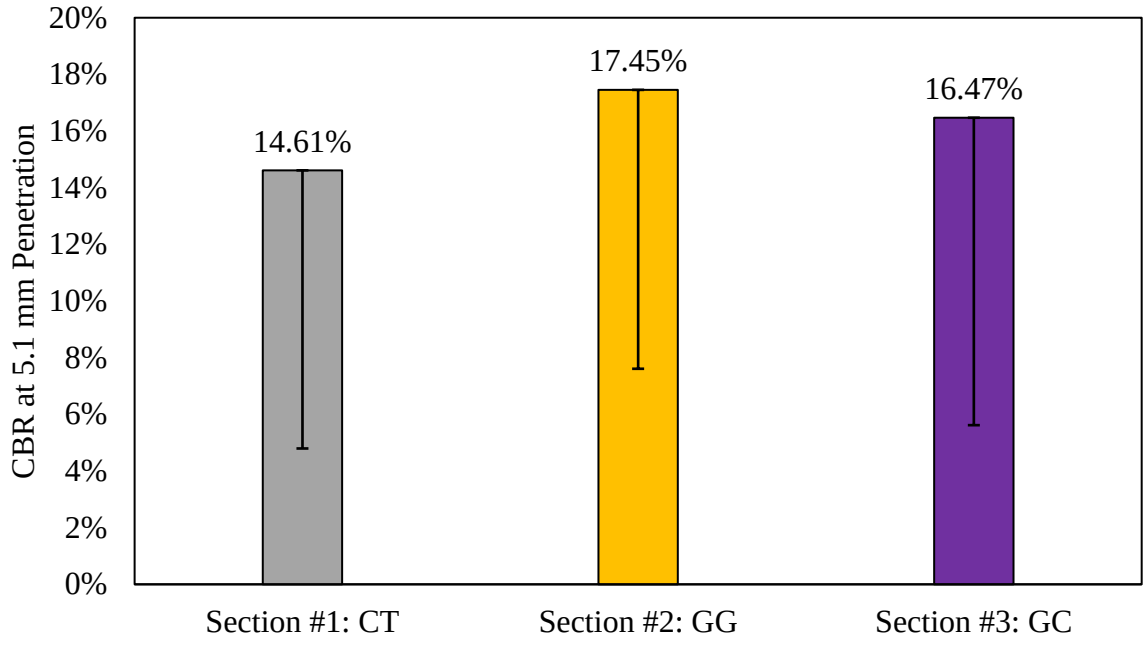

Figure 4-29 CBR values of Sampled Granular Base Materials

Resilient modulus was also computed using Equation 4-16 as listed in Table 4-9. It can be seen that the granular base materials show similar M_R for all three sections, which are around 100 MPa. However, the typical value of Granular A provided by the Ontario Ministry of Transportation (MTO) is 250 MPa (Ministry of Transportation, 2013). With the underestimation of laboratory testing that may be caused by the disturbance during material sampling, in-situ testing is recommended to verify the results.

Table 4-9 Correlated Resilient Modulus of Sample Base Aggregates from CBR

	$CBR_{5.1}$	**Correlated from CBR (AASHTO 93)**
Section #1: CT	14.61%	97.93
Section #2: GG	17.45%	109.73
Section #3: GC	16.47%	105.72

4.3.3 Asphalt Concrete

In order to understand materials used in the field and investigate the asphalt mixes performance in the laboratory, asphalt mixes were sampled on the days of construction from the field. The SP 19 mix and SP 12.5 mix with PG 64-28 were used for the binder course and surface course, respectively.

The theoretical Maximum Specific Gravity (G_{mm}) of loose asphalt mixes was tested to verify the information provided by the consultant. The Bulk Specific Gravity (G_{mb}) of the compacted specimen was tested to determine the optimal way to produce geogrid-embedded specimens to reach the required air void content for laboratory testing. Dynamic (complex) modulus testing was performed to comprehend the mechanical properties of the mixes. Samples were compacted at 150° C for SP 19 mixes and 155° C for SP 12.5 mixes.

4.3.3.1 Verification of Theoretical Maximum Specific Gravity

The theoretical Maximum Specific Gravity (G_{mm}) of loose asphalt mixes was determined following AASHTO T209. The results of both SP 19 and SP 12.5 are listed in Table 4-10, along with the G_{mm} values provided by the consultant (PNJ Engineering Inc., 2022). The differences between the average of the two test trials and the reported values are 0.002 and 0.000 for SP 19 and SP 12.5, respectively. They are both within the acceptable range of difference (i.e., 0.014) as per AASHTO T209 (AASHTO, 2016a). The average of two test trials was taken for the determination of G_{mb}.

Table 4-10 G_{mm} Testing Results and Reported Values

	SP 19			SP 12.5		
	Trial 1	**Trial 2**	**Reported[1]**	**Trial 1**	**Trial 2**	**Reported[1]**
G_{mm}	2.574	2.569	2.566	2.627	2.630	2.618
Average	2.570			2.629		
Difference			0.002			0.011

[1] Provided by the consultant (PNJ Engineering Inc., 2022)

4.3.3.2 Bulk Specific Gravity and Air Void Content

Bulk Specific Gravity (G_{mb}) and air void content of compacted specimens in SP 19 to be tested with asphalt mix performance testing in subsequent chapters were determined as per AASHTO T 166 (AASHTO, 2016b). Due to the nature of compacting geogrid-embedded asphalt specimens in the laboratory, two layers of material must be compacted. Trials and errors were done with different amounts of materials for compaction to reach the required air void content and height by corresponding laboratory testing. During the trial-and-error process, the specimens were tested with their air void contents as a whole specimen first, and then they were cut into three pieces in equivalent height as shown in Figure 4-30. The air voids were tested on the cut pieces to ensure the air void contents were consistent for the bottom and top layers. The results are illustrated in Figure 4-31 (a) for the specimen in height of 63 mm and Figure 4-31 (b) for the specimen in height of 150 mm. The results will be discussed in the later corresponding chapter.

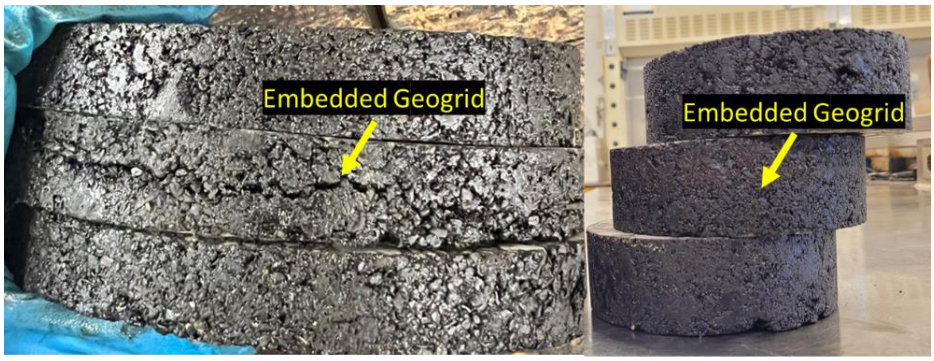

(a) **(b)**

Figure 4-30 Compacted Specimen Cut into Three Pieces for Air Void Contents of (a) 63 mm and (b) 150 mm

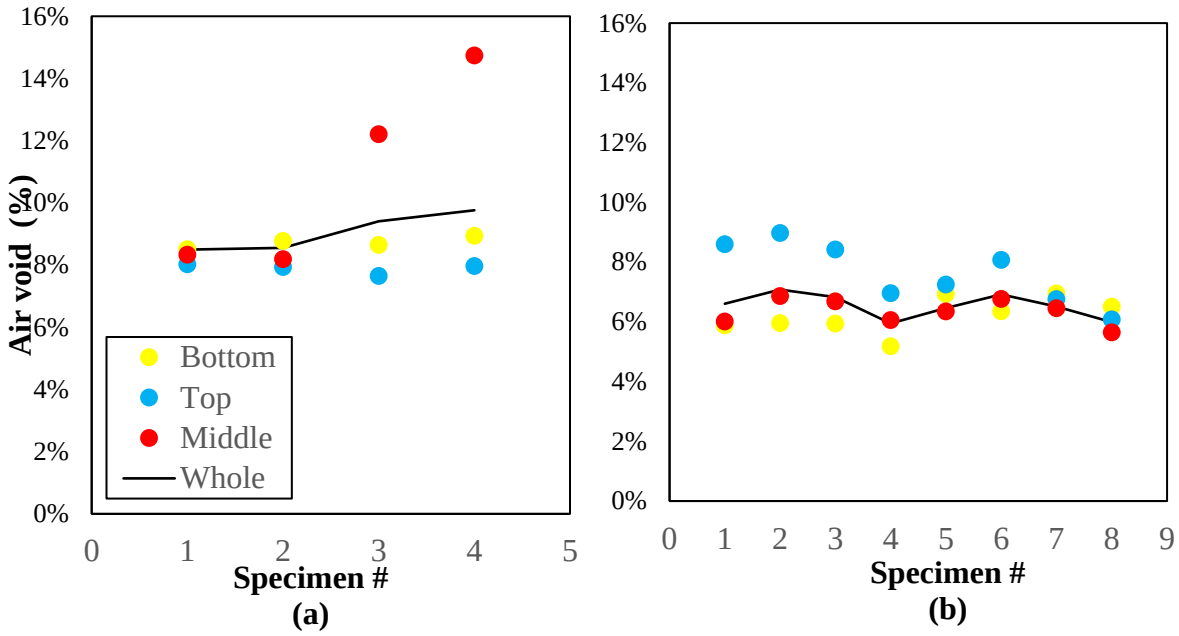

Figure 4-31 Air Void Contents of Bottom, Middle, and Top Layer for Specimen in Height of (a) 63 mm and (b) 150 mm

4.3.3.3 Complex Dynamic Modulus

A Complex Dynamic Modulus test was performed on both plant-produced mixes (SP 19 and SP 12.5) to comprehend the properties of the asphalt mixes. As mentioned, the binder used for both mixes is PG 64-28. The modulus obtained from the applied stress and measured strain were averaged by two replicates. The modulus under different temperatures and loading frequencies are illustrated in Figure 4-32 for SP 12.5 mixes and Figure 4-33 for SP 19 mixes.

As the laboratory testing is limited, the shifting method was used based superposition principle to move to other frequencies and loading times. A reference temperature was chosen, and the corresponding frequencies used at the reference temperature with the same response were determined.

There are three common time-temperature superposition shifting techniques to model the relationship for viscoelastic materials, log-linear, Arrhenius equations, and Williams-Landel-Ferry (WLF) equation (Pellinen, Witczak, & Bonaquist, 2003). As shown in Equation 4-17, the WLF equation is an empirical equation that was stated to fit for asphalt binders from -20°C (i.e., glass transition point of asphalt binder) to 60°C (D. Anderson, Christensen, & Bahia, 1991; Painter & Coleman, 1997). In this study,

the reference temperature was chosen to be 21°C and the master curves were shifted using the WLF equation.

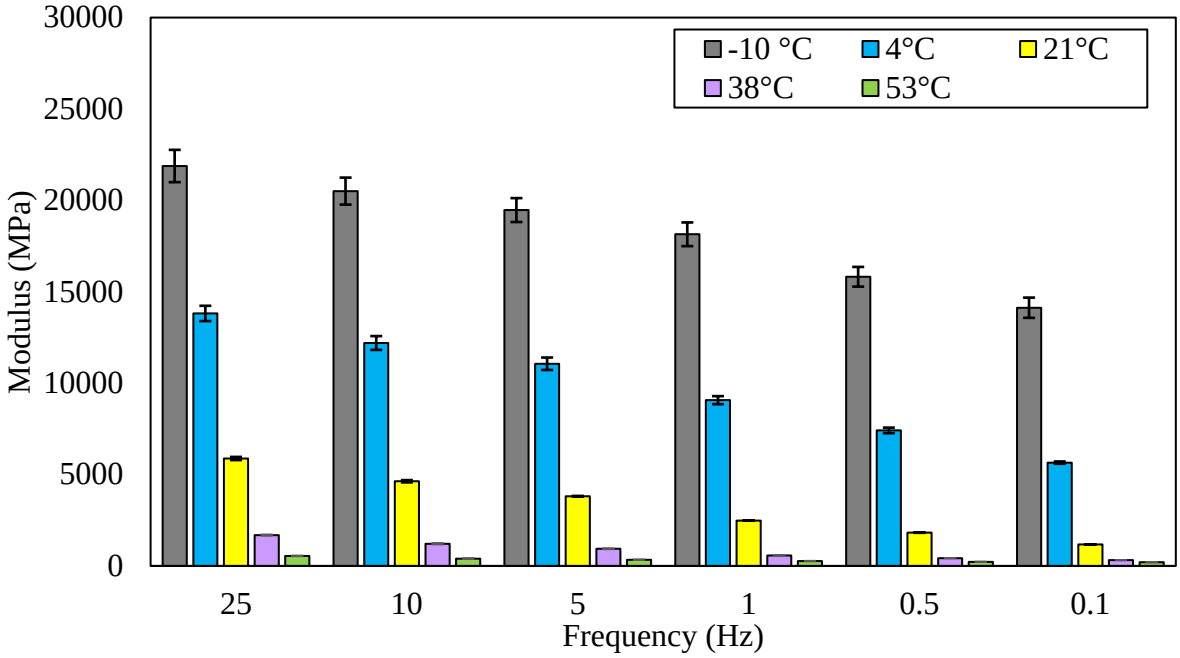

Figure 4-32 Surface Course Asphalt Mixes Modulus

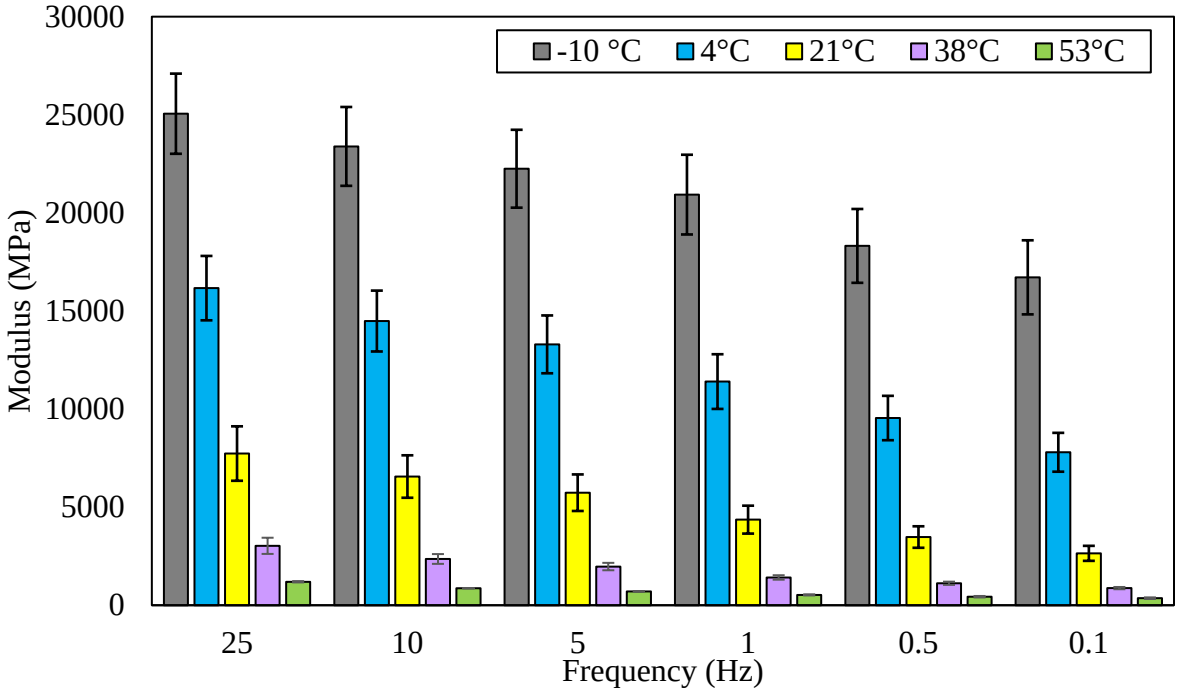

Figure 4-33 Binder Course Asphalt Mixes Modulus

Equation 4-17

$$\log a(T) = \frac{-C_1(T-T_0)}{C_2+T-T_0}$$

where:

$a(T)$ = shift factor

T = temperature (°C)

T_0 = reference temperature (°C)

C_1, C_2 = empirical constants

To extrapolate the produce the master curve, the generalized sigmoid model was used as shown in Equation 4-18 (G. Rowe, G. Baumgardner, & M. Sharrock, 2009). The master curves of the dynamic modulus of both mixes are shown in Figure 4-34. Meanwhile, the master curves of the phase angle can be constructed as per Equation 4-19 based on the generalized sigmoidal model and the Kramers-Kronig (K–K) relationship. The master curves of the phase angle of both mixes are shown in Figure 4-35. The plots of fitted modulus against phase angle are shown in Figure 4-36. The fitting parameters are listed in Table 4-11. It can be seen SP 19 mixes have slightly higher complex dynamic modulus than SP 12.5, while they show similar dynamic responses as the binder for both mixes is at the same performance grade.

Equation 4-18

$$\log E^* = \delta + \frac{\alpha}{\left[1+\lambda e^{(\beta+\gamma(\log\omega))}\right]^{\frac{1}{\lambda}}}$$

Equation 4-19

$$\phi = -\frac{\pi}{2}\alpha\gamma\frac{e^{(\beta+\gamma(\log\omega))}}{\left[1+\lambda e^{(\beta+\gamma(\log\omega))}\right]^{\frac{1}{\lambda}+1}}$$

where:

E^* = complex dynamic modulus (MPa)

ω = reduced frequency (Hz)

δ = lower asymptote

α = difference between upper and lower asymptote

ϕ = phase angle (°)

λ, β, γ = defines the shape between asymptotes and the location of the inflection point

Table 4-11 Fitting Parameters for Generalized Sigmoidal Model for Master Curves

Mix	C_1	C_2	α	β	δ	γ	λ	T_0 (°C)
SP 12.5	32.29	256.74	2.33	-0.32	2.15	-0.42	0.30	21
SP 19	31.53	253.29	2.51	-0.59	2.09	-0.32	0.33	21

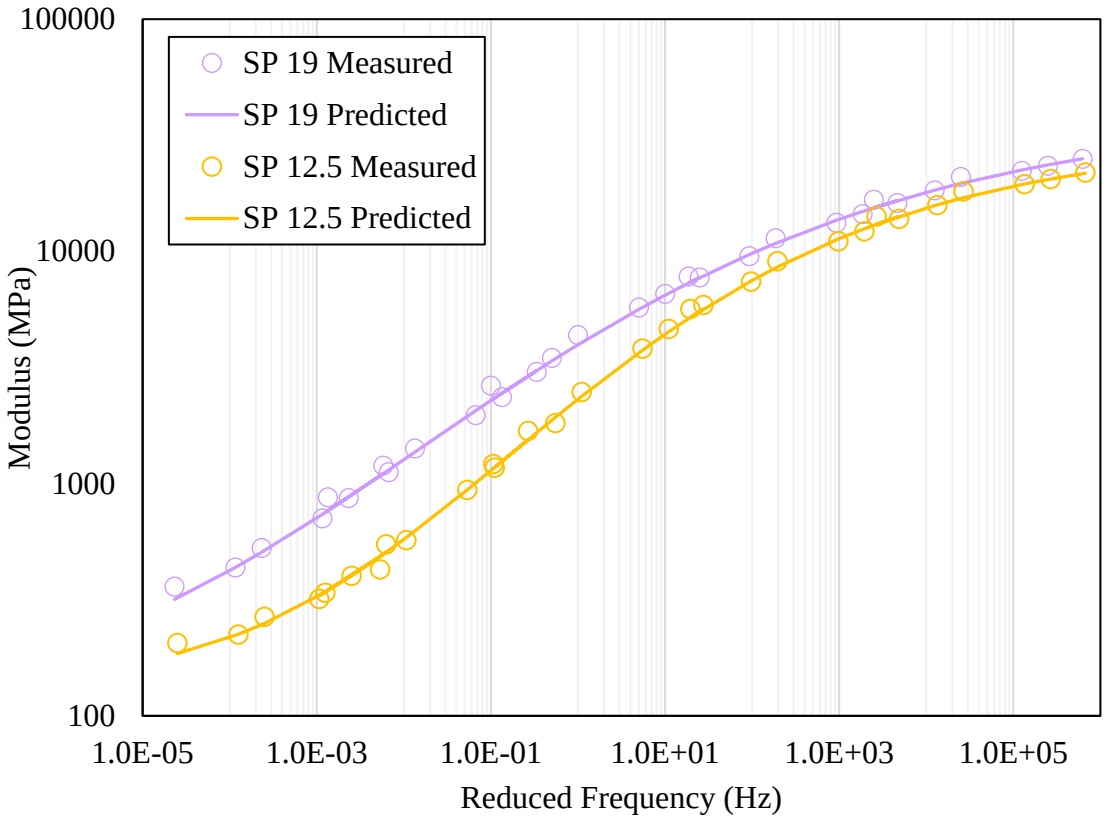

Figure 4-34 Asphalt Mixes Master Curves of Dynamic Modulus

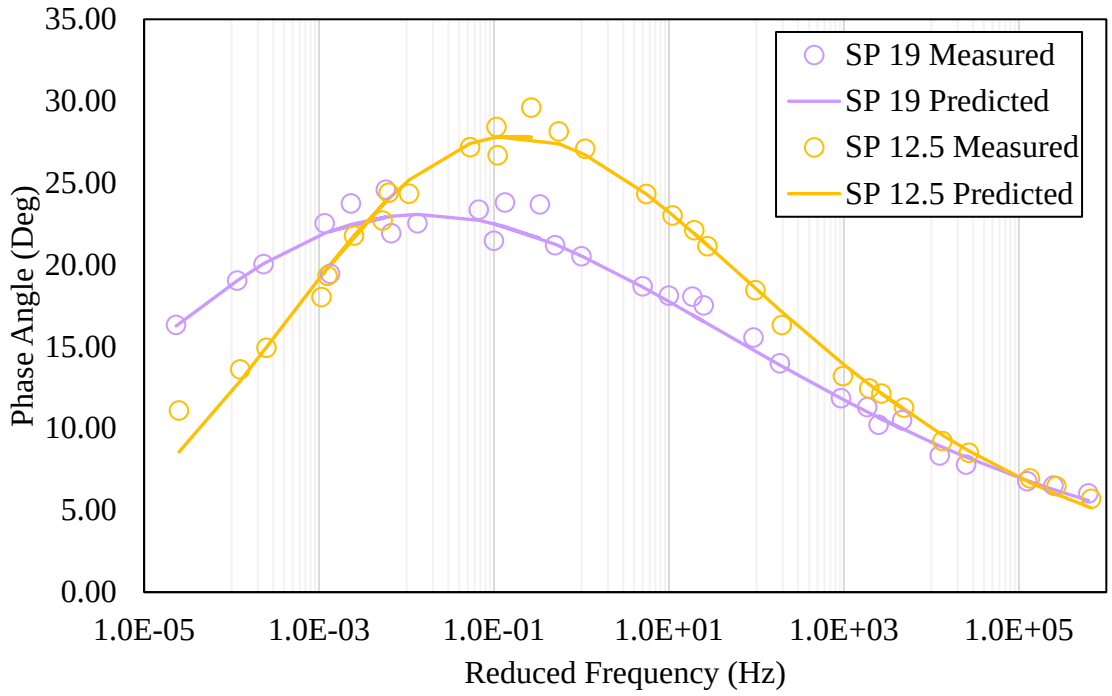

Figure 4-35 Asphalt Mixes Master Curves of Phase Angle

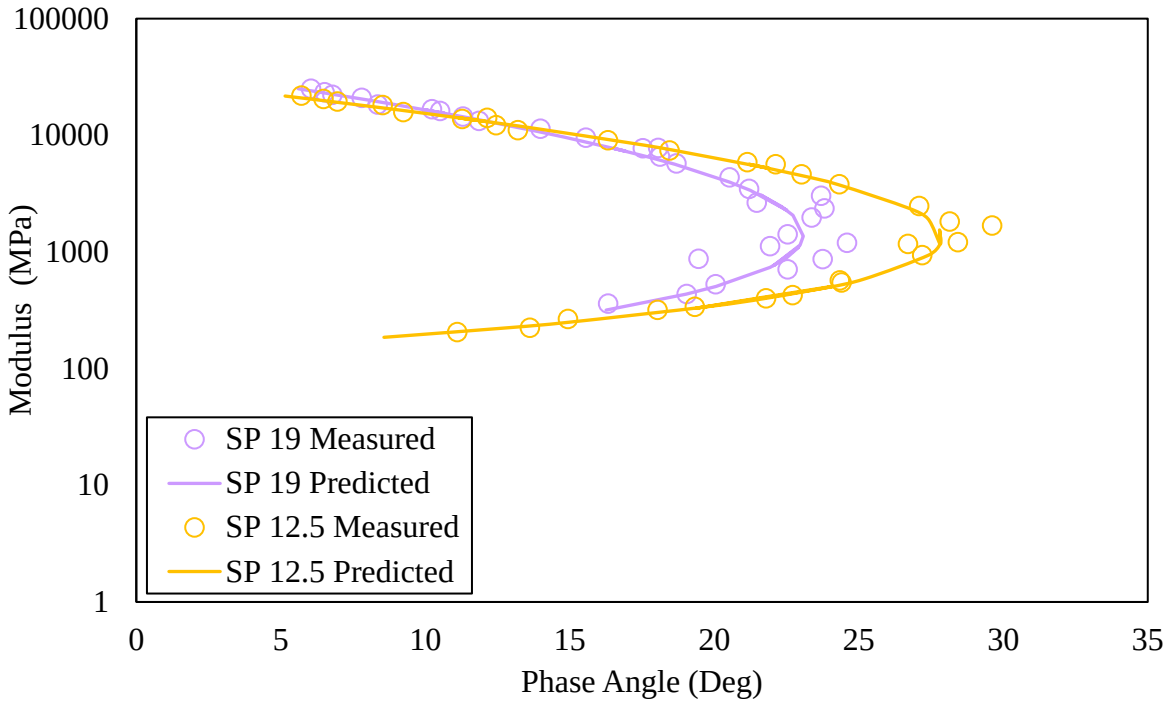

Figure 4-36 Fitted Modulus Against Phase Angle of Asphalt Mixes

4.3.4 Summary

This section details the material characterization of the materials sampled from the construction of the field trial sections. A weaker subgrade was noted in the GC section with more clayey materials. The laboratory testing results performed on the granular base materials ensured the consistency of the base layer throughout all three sections, with satisfactory alignment with the information provided by the consultant. The development of a novel method to investigate the air void contents of geogrid-embedded asphalt samples prepared in the laboratory was proposed. Additionally, the testing of complex dynamic modulus on asphalt mixes sampled directly from the field serves as a crucial step toward comprehensively assessing the performance and structural characteristics of the asphalt materials. These results collectively contribute to a deeper understanding of the properties and behaviour of the pavement materials in the field trial, thereby facilitating more informed analysis in this study.

4.4 Construction Impacts on the Geosynthetic–Reinforced Pavements

4.4.1 Pressure at the Interface of Subgrade and Base

The readings of the pressure cells at the interface of the subgrade and base layer were taken during the construction of the asphalt binder course (SP 19), and asphalt surface layer (SP 12.5). The data was collected every 10 seconds during binder course construction while it was collected every minute during construction of the surface layer. Although the traffic volume and construction truck specifications were not available, the construction equipment was consistent for all sections during each stage of construction by designating equipment to a specific lane in the test sections. All other construction traffic was kept on the lane that was not instrumented during the data collection period.

The differences in the pressure cell readings were taken between an individual real-time sensor reading at the time, t, and the first reading before construction (representing the zero condition). The granular base overlying the geogrid composite was constructed on June 3, 2022, and the base layer in the geogrid and control sections was constructed together on June 6, 2022, thus the results were plotted on two graphs in Figure 4-37. This figure can suggest some impacts of the geogrid composites on the subgrade when pressure was exerted on them since the geogrid has not been in the asphalt. It can be seen that the geogrid composite section shows more noise, compared with the other two sections. This can be due to the heavy trucks being driven on the geogrid composite section more frequently in 15 m, while the trucks were driven on two sections on the other day since the construction of the granular A

was constructed together in 30 m. Another factor contributing to these results can be the geogrid composite material. Despite the higher noises of the data in the geogrid composite, the peak values are not obvious (around -0.02 MPa) and are less than the peak pressure experienced in the other two sections (around -0.025 MPa).

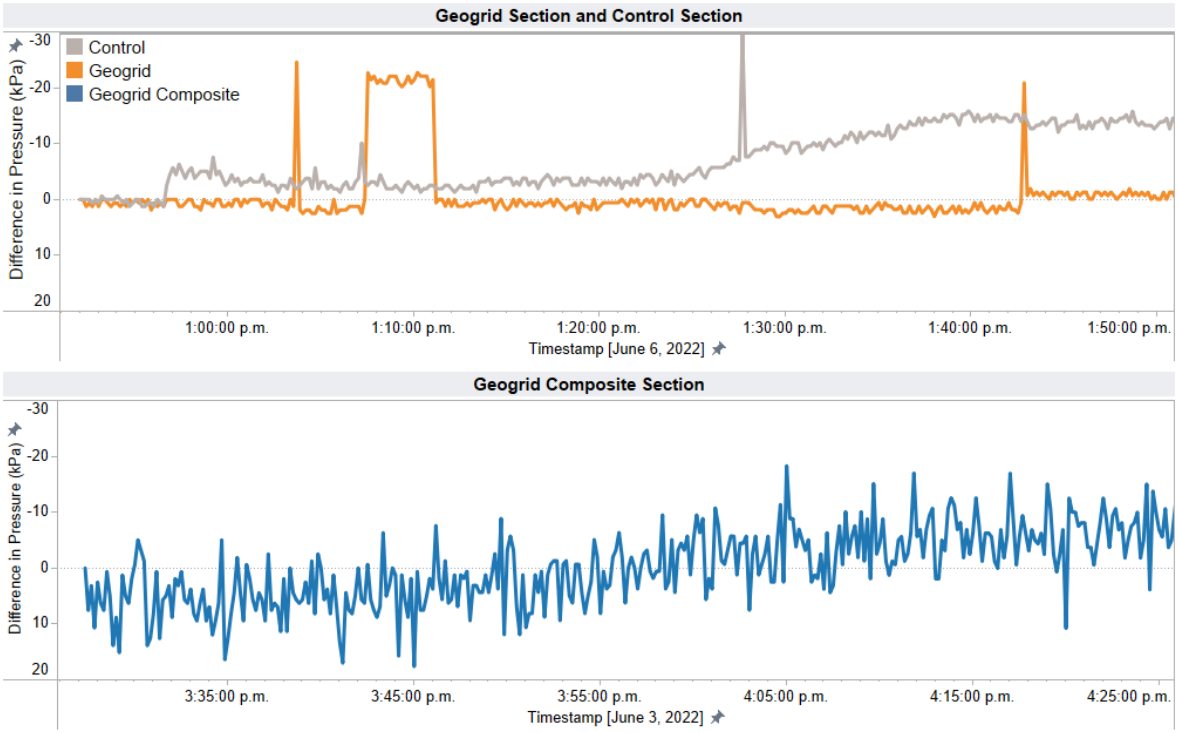

Figure 4-37 Pressure at the Interface of Subgrade and Base during Base Construction

From the readings taken during the construction of base compaction, it can be found that less and lower peak pressure was experienced at the interface of the subgrade and base layer in the geogrid composite section. This implies that the geogrid composite installed on the subgrade can distribute the load and pressure exerted by the heavy trucks for construction, thus leading to less disturbance to the subgrade.

The readings of the pressure cells during the construction of the asphalt binder course were plotted in Figure 4-38. Figure 9 details the readings from approximately 8:30 a.m. until 3:30 p.m. corresponding to the start and finish of construction, respectively. The construction timeline can be observed more clearly from the pressure readings of control and geogrid composite sections. The pressure increase ending at approximately 1 p.m. corresponds to the paving and compaction of asphalt concrete. During this time, the contribution of the geogrid composites on the subgrade as well as the

fibreglass geogrid in the binder course can be inferred. It can be observed that the geogrid composite section (Section #3) shows more noise, but with a similar trend to the control section, and experiences a maximum pressure of approximately 0.10 MPa. However, the pressure cell on the subgrade in the fibreglass geogrid section (Section #2) experienced a much lower pressure (0.03 MPa). Due to the absence of the paver and compaction equipment, the pressure levelled out as shown in control and geogrid composite sections. During the paving of the binder course, the Geogrid Section experienced approximately 70% lower pressure on the subgrade compared with the other two sections, which may be attributed to the fibreglass geogrid reducing the impact of heavy construction trucks on the base and subgrade. It is believed that these measurements demonstrate the ability of the fibreglass geogrid to distribute the load and provide reinforcement during construction.

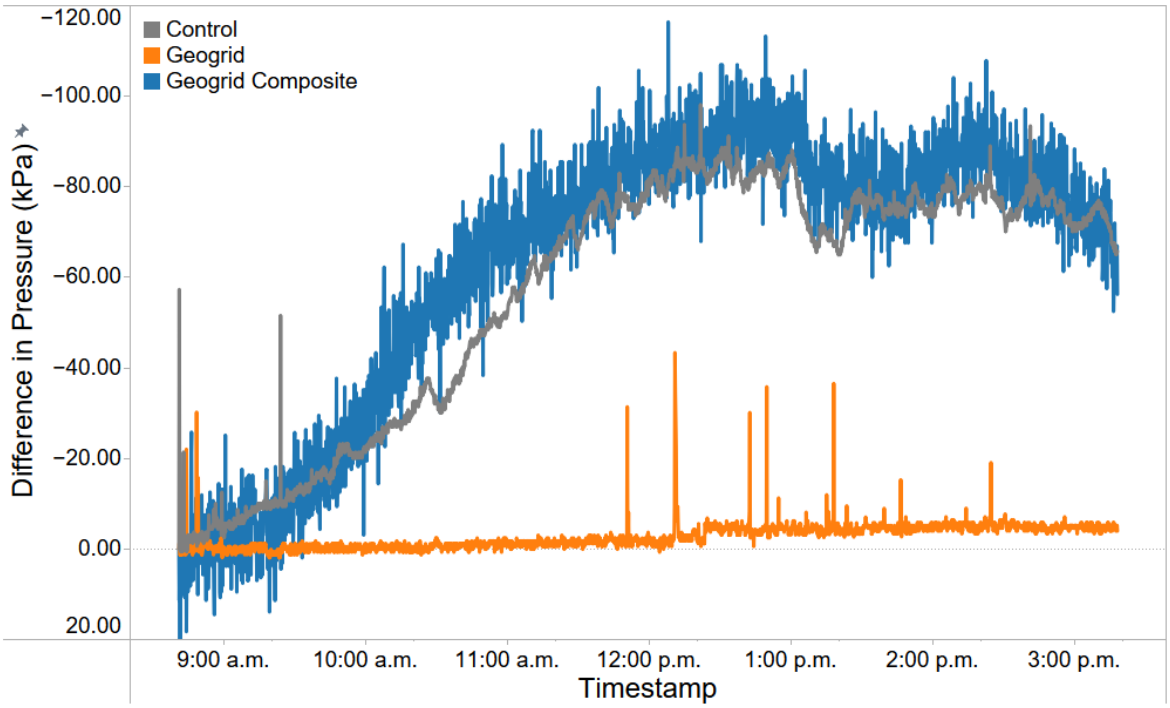

Figure 4-38 Pressure at the Interface of Subgrade and Base during Binder Course Construction

Figure 4-39 shows the readings of the pressure cells collected during the construction of the asphalt surface course. From these results, a similar level of noise was demonstrated in all three sections. This may be attributed to the different data collection frequency (i.e., one measurement per minute) from the previous two construction activities. As shown in Figure 4-39, the trends of all three pressure cells

are similar, however, larger peak pressure values were observed in the control section and geogrid composite sections.

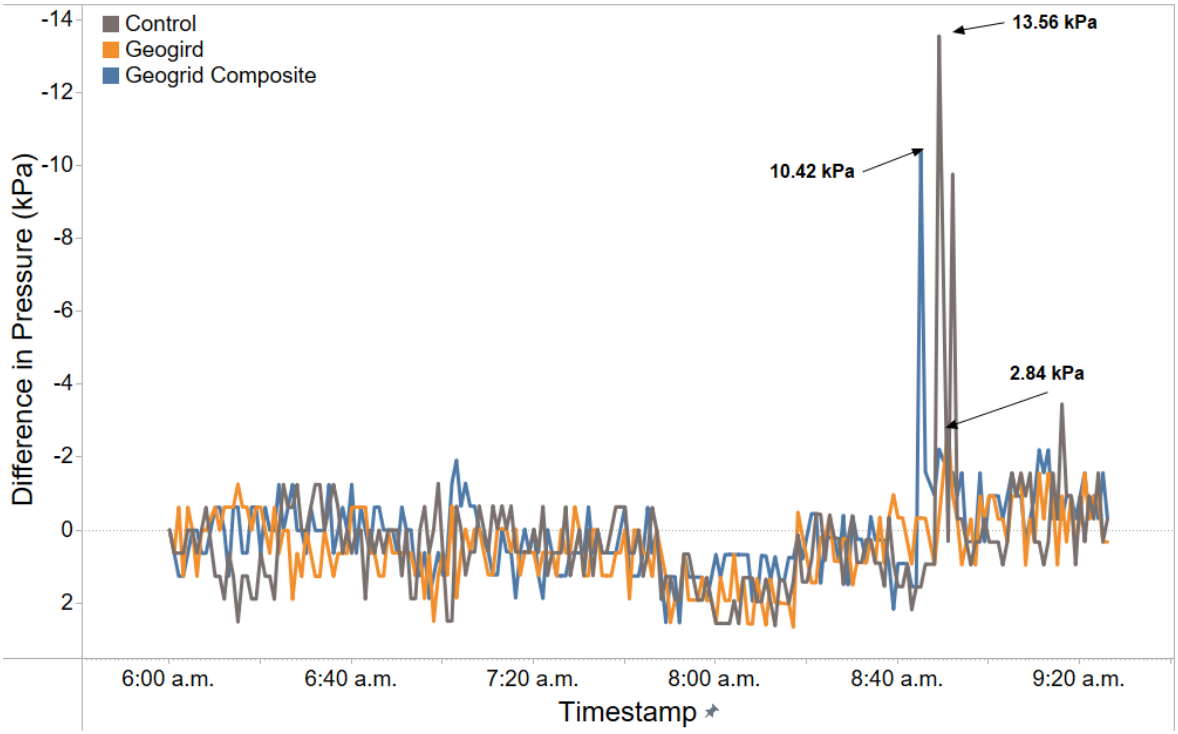

Figure 4-39 Pressure at the Interface of Subgrade and Base during Surface Course Construction

4.4.2 Strain within the Asphalt Binder Course

The readings of the strain gauges (longitudinal and transverse) installed in the binder course were taken during the construction of the asphalt binder course (SP 19), and asphalt surface layer (SP 12.5). The data was collected every 10 seconds during the construction of the binder course, and it was collected every minute during the construction of the surface layer. Similar to the process of data of pressure cells, the measurements were offset to the zero point by taking the difference with the first reading. A positive result indicates the tensile strain, while a negative value indicates the compressive strain. The readings of the asphalt strain gauges during the construction of the binder course are plotted in Figure 4-40. These results reflect the impacts of the fibreglass geogrid in the binder course when stress was exerted on them. The readings taken from both longitudinal and transverse gauges illustrate similar

trends in the three sections. The gauges were experiencing compressive strains from 9 a.m. to around 12:30 p.m., which matches the construction timeframe discussed previously in regard to Figure 4-38.

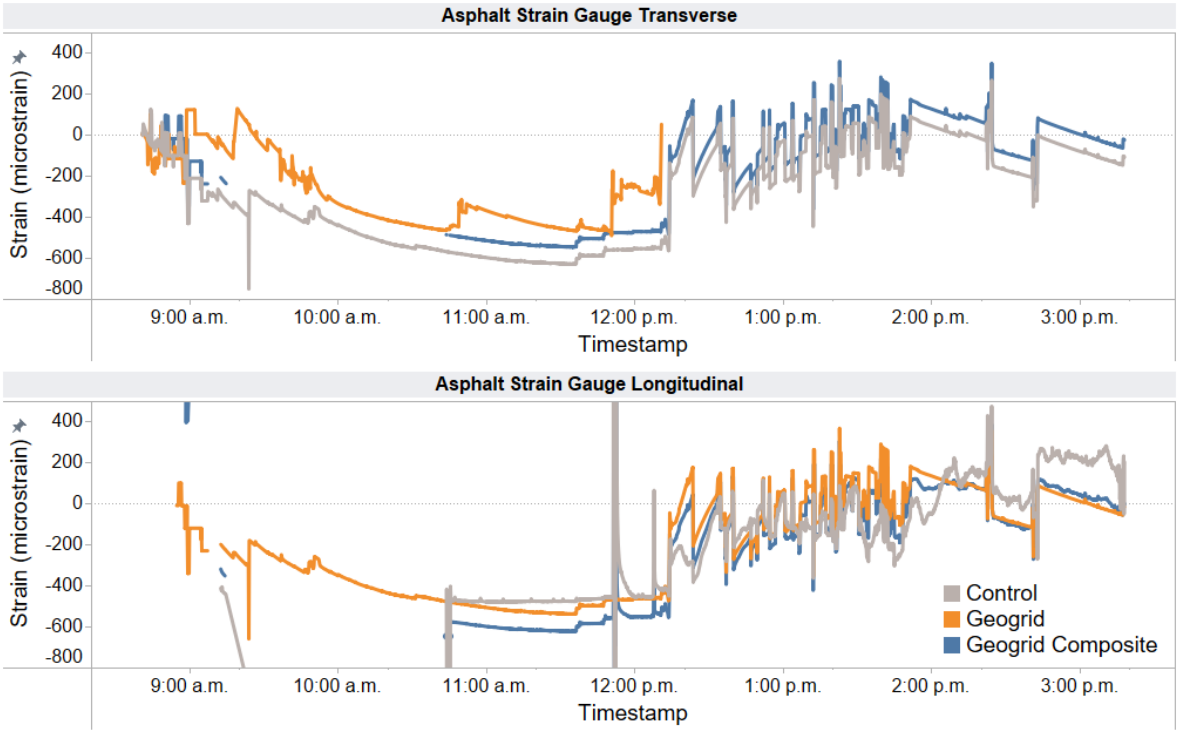

Figure 4-40 Asphalt Strain Gauge Reading during Binder Course Construction

Due to the completion of construction activities as well as the viscoelastic nature of asphalt materials, the strains experienced at the bottom of the asphalt layer increase after 1 p.m. In the transverse direction, the fibreglass geogrid section (Section #2) experienced lower strains during the construction. It is also notable that some exceptionally high values were exhibited in the control section in the longitudinal direction. This observation aligns with previous studies that demonstrated that the longitudinal strain is typically higher than the transverse values (Grellet, Doré, & Bilodeau, 2012; Talebsafa, Romanoschi, Papagiannakis, & Popescu, 2019).

Figure 4-41 shows the readings of the asphalt strain gauges collected during the construction of the surface course. Similar to the reading of pressure cells, lower noise was observed due to a lower frequency of data collection, although this could also be attributed to the additional thickness of surface course material being paved. In the transverse direction, the control and geogrid composite sections both capture high strain values around 7:10 a.m. Other than these peak values, the tensile strain experienced at the bottom of the binder course reached the highest level during the paving after 8:00

a.m., with the fibreglass geogrid section showing a lower level of strain. A similar trend is also exhibited in the longitudinal direction.

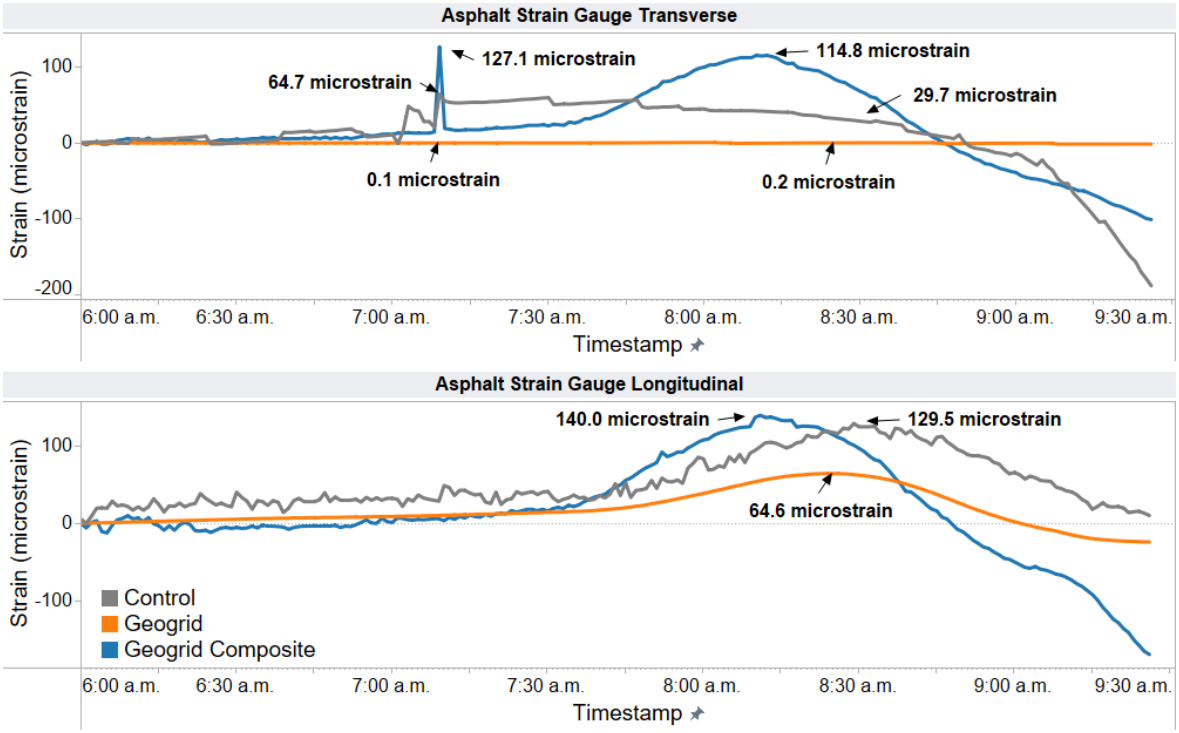

Figure 4-41 Asphalt Strain Gauge Reading during Surface Course Construction

As shown in Figure 4-41 (top), the transverse strain in the binder course caused by the construction of the surface course is reduced in the fibreglass geogrid section by more than 99% compared with the other two sections. As the fibreglass geogrid-reinforced asphalt course can better distribute stress under loading, this leads to less disturbance to the binder course, granular base, and subgrade. In the longitudinal direction, the fibreglass geogrid can reduce about 54% and 50% strain compared with control and geogrid composite sections.

Although higher strains in longitudinal directions are typically observed, higher longitudinal strains may also be attributed to the aperture size spacing of the longitudinal filaments of the geogrids; larger apertures may reduce the interaction between grid filaments improving the pull-out resistance in the longitudinal direction. However, the spacing between transverse members has little impact on the pull-out resistance (Bhowmik, Shahu, & Datta, 2023; Pant, Datta, Ramana, & Bansal, 2019). With regards to the lower strain level experienced in both longitudinal and transverse directions, the results align

with the lower pressure cell measurements observed in Figure 4-39, which signifies the impacts of load distribution provided by the fibreglass geogrid on the RWP.

4.4.3 Moisture

The readings of the moisture probes installed at the top of the granular base layer, middle of the granular base layer, and 10 cm below the subgrade were taken during the construction of the asphalt surface layer (SP 12.5). Data was collected every minute during construction. The lower the reported moisture value is, the more saturated the probe is, which can provide information about the drainage capability of both fibreglass geogrid and geogrid composites.

The water potential profile in the pavement structure based on each section is plotted in Figure 4-42 while Figure 4-43 displays the water potential of each layer. The measured water potential in the subgrade in all three sections is close to 0 (i.e., almost fully saturated) while draining behaviour can be observed in the geogrid composite section (Section #3). It can also be observed that the water potential in the subgrade in the geogrid composite is slightly higher, indicating a drier condition. At the middle of the base layer, the geogrid composite section generally shows a drier condition, with the control section showing a saturated condition. Lastly, at the top of the base layer, the geogrid composite is very much drier. The water potential readings in the fibreglass geogrid and control sections are close, with a slightly higher water potential in the fibreglass geogrid section. As the geogrid composite material serves as both a filter and separator, the water drains downwards more quickly, but it also prevents the upward migration of moisture and fine soils. As the same granular and asphalt material was used in all sections, the improved draining behaviour can be attributed to the geogrid composite material installed in Section #3, thus, demonstrating the potential of the geogrid composite to mitigate the consequences of freeze-thaw cycles in the future. This observation can be confirmed when monitoring the water potential of the geogrid composite section during the colder winter months after construction.

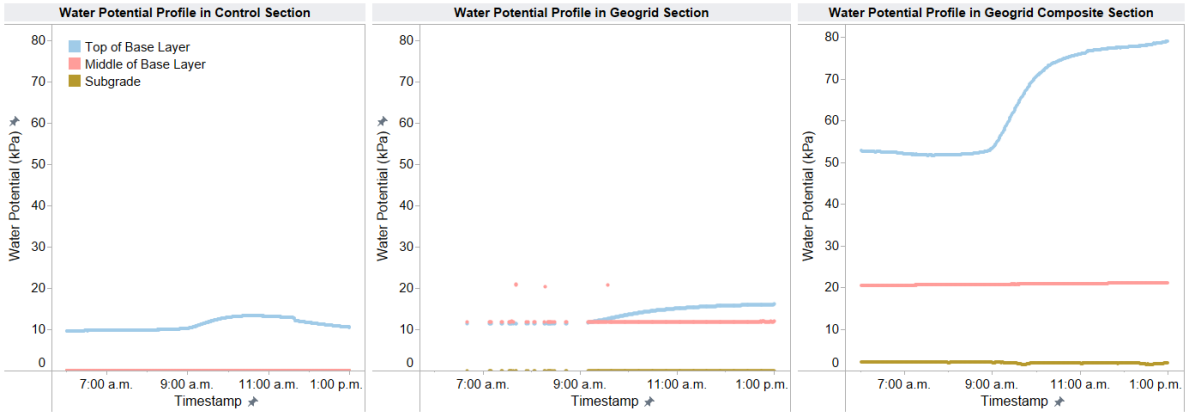

Figure 4-42 Water Potential Profile for Each Section during Surface Course Construction

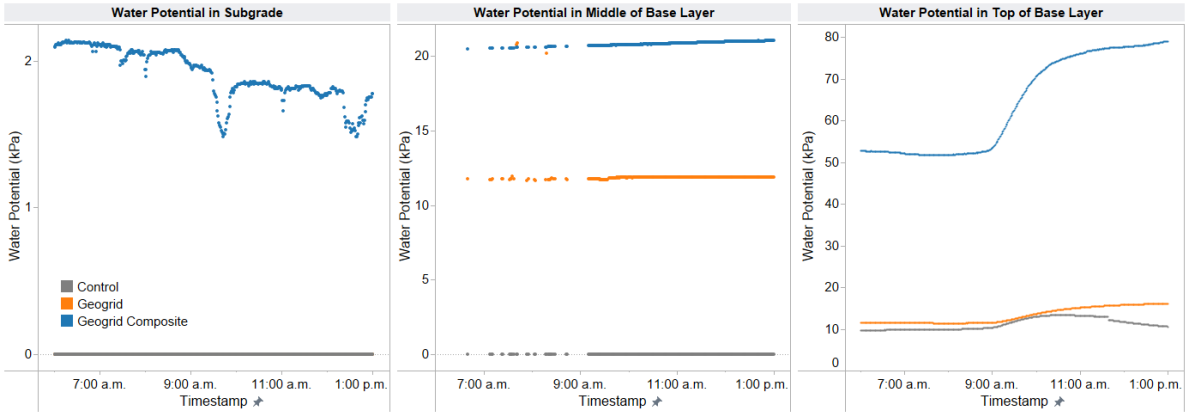

Figure 4-43 Water Potential in Each Layer during Surface Course Construction

4.4.4 Temperature

The readings of the temperature sensors installed in the base lift of the binder course, the middle of the granular base layer, and 10 cm below the subgrade were taken every minute during the construction of the asphalt surface layer (SP 12.5).

The temperature in different sections was plotted based on each layer in Figure 4-44. It can be observed that the temperature in the subgrade in the geogrid composite is the lowest. These results may indicate the indirect insulation potential of these materials provided by the draining effect. As discussed previously, the moisture conditions in these sections shown in Figure 4-42 also contribute to the temperature change in the three sections. From the results, the geogrid composite exhibits a lower temperature in the subgrade and middle of the base layer which may be attributed to the filtering, draining, and inhibiting upward migration of moisture and fine particles. This is especially beneficial

to the climate conditions in Canada with an increased frequency of freeze and thaw cycles that have adverse impacts on the pavement performance during the winter and spring seasons. However, as the data were collected during construction, which was a relativity short period, long—term monitoring is necessary to evaluate the freeze-thaw impacts on geosynthetic-reinforced pavements and to verify this observation.

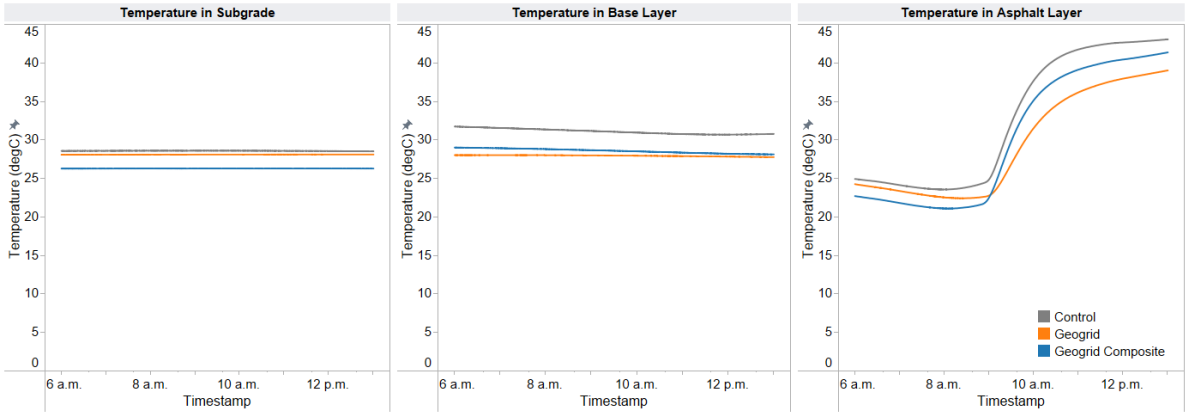

Figure 4-44 Temperature in Each Layer during Surface Course Construction

4.5 Post-Construction Impact Assessment

Light Weight Deflectometer (LWD) can be used to measure the stiffness of the subgrade, base, and pavement by releasing and applying loads on the pavement surface. Deflections are measured when a 15 kg weight is dropped from a height of 100 cm. The sudden drop of the weight transmits a stress pulse to the ground, and the deflection can be used to calculate the modulus at the surface. A 300 mm diameter plate was used when performing the testing on the subgrade and granular base. A 200 mm diameter plate was used for the testing on the binder course and surface course. The tests were performed on both the left wheel path (LWP) and the right wheel path (RWP) on the westbound lane. Fewer points were tested on subgrade and base due to the consistent outcomes, while the LWD was performed every 5 m along the lane on both wheel paths on the binder course and surface course. At least three measurements were taken from one location before moving to a new location. The before-installation stiffness values were calculated as shown in Figure 4-45; the geogrid composite section showed the weakest subgrade. The weaker subgrade in the geogrid composite section (Section #3) is consistent with the higher level of pressure experienced on the subgrade (Figure 4-38) and higher horizontal tensile strain experienced at the bottom of the binder course (Figure 4-41).

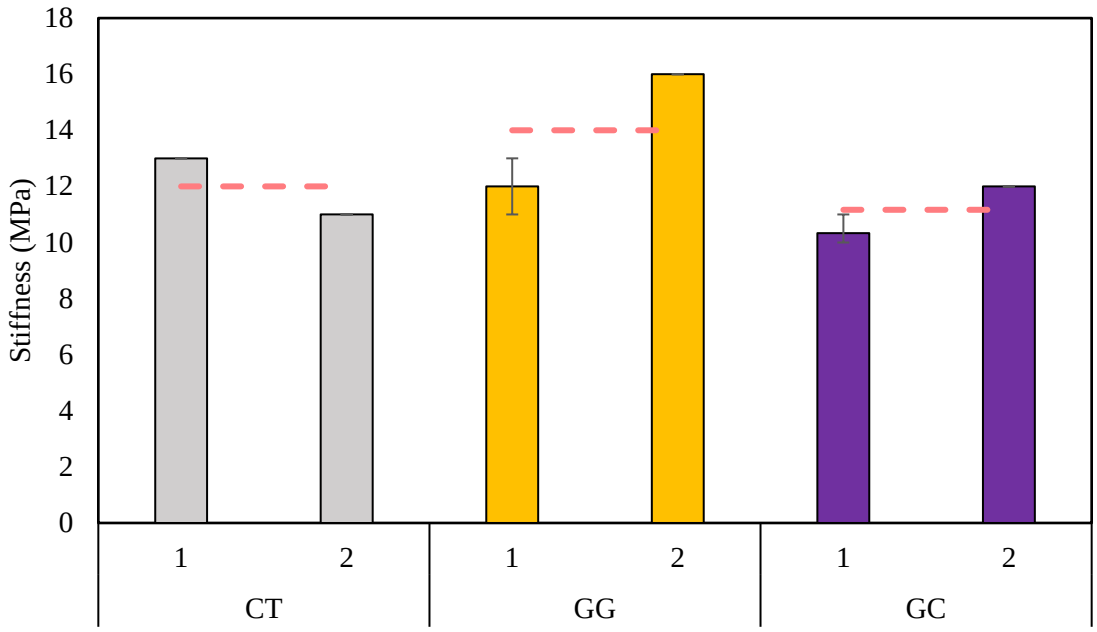

Figure 4-45 LWD Results Tested on Compacted Subgrade

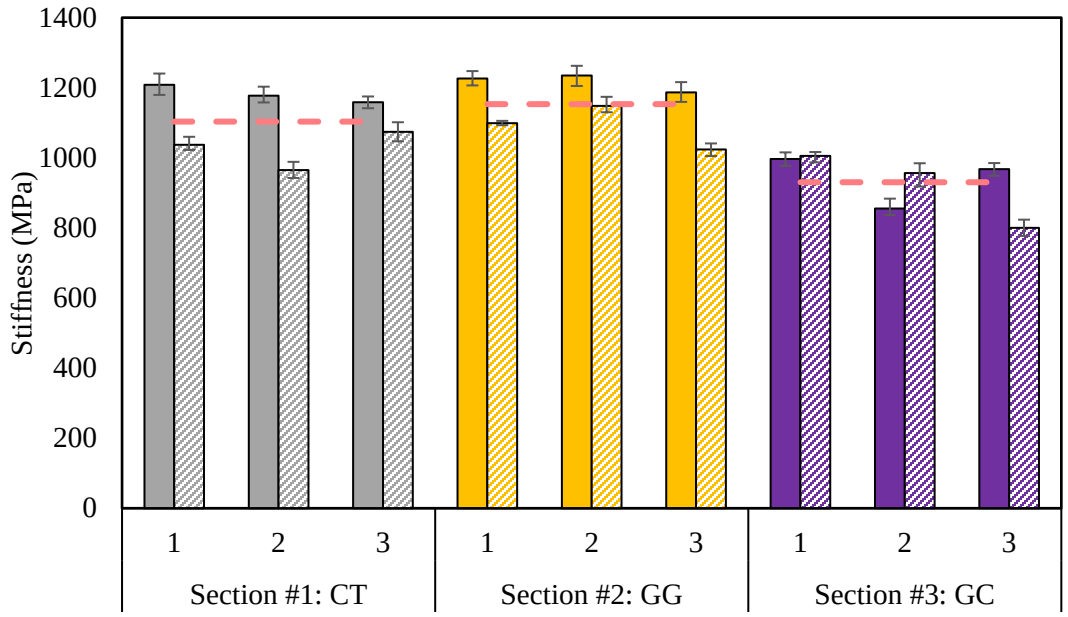

Figure 4-46 LWD Results Tested after Surface Course Construction

The deduced surface moduli after the placement of the asphalt surface course are plotted in Figure 4-46. From these measurements, the geogrid composite section shows the lowest stiffness measurements which is consistent with weak subgrade measurements as indicated in Figure 4-45. It

can be observed that the fibreglass geogrid section (Section #2) exhibits the highest measurements in surface moduli further indicating the benefit of the fibreglass geogrid within the asphalt layer and its ability to mitigate of the impact construction activities.

4.6 Chapter Summary

In general, this chapter develops the procedures and techniques of a full-scale field study regarding the geosynthetics-reinforced pavement in Southern Ontario, Canada. This study includes two types of geosynthetic interlayer systems: the geogrid composite installed on the subgrade, and a fibreglass geogrid installed in the asphalt binder course. This paper describes the installation practices of these geosynthetics. During geogrid composite installation, required overlaps of adjacent geosynthetic sheets based on the subgrade strength, removal of wrinkles, and the flat tiling of the materials were noted to require careful attention. More measures and caution should be taken during the installation of geogrid within the asphalt to ensure adequate bonding between the geogrid and the asphalt pavement. Special measures should also be taken on the application of tack coat, the wrinkle removal, the order of installing the geogrid materials in different widths, and the paving of the second lift overlying the geogrids.

This full-scale study also introduces instrumentation for long-term monitoring in Canada. The calibration and installation of the sensors were presented, including temperature strings, moisture probes, pressure cells, and asphalt strain gauges.

The results collected during construction were analyzed and some field tests were performed to show the impacts of geosynthetics, as listed below:

- The readings taken from pressure cells on the subgrade show that the geogrid in the binder course can diminish the mechanical disturbances vertically from the construction of the binder course and surface course by distributing the load. The geogrid composite can offer little reinforcement of the entire structure during the construction with a similar pressure reading to the control section.
- The horizontal strain in the first lift of the binder course caused by construction activities of asphalt placement can be significantly reduced by the geogrid installed between the two lifts of the binder course in the transverse direction, with some reduction in the longitudinal direction. The geogrid composite section shows similar horizontal strain values in the binder course during construction with the control section.

- Geogrid composite on the subgrade shows an improved drainage capability and produces a distinct water potential profile within the pavement structure. The draining, filtering, and inhibition of upward migration of moisture and fine particles were observed in the geogrid composite section with a drier condition in different depths of the pavements. This finding indicates an improved performance of the pavements undergoing freeze-thaw cycles and can be verified with future field work at the site.
- From the temperature monitoring, the geogrid composite shows indirect insulation capability due to the drainage effect provided by the geotextile, which may decrease the potential for severe freeze-thaw damage.
- The results of LWD testing indicate the reinforcement of the geogrid with the highest stiffness measurements after the asphalt placement. Future field work can be used to determine the long-term benefits of the geosynthetic installation and also the validity of these initial measurements.

Chapter 5
Evaluation of Rutting and Moisture-Susceptibility of Geogrid-Embedded Asphalt by Hamburg Wheel-Track Testing

5.1 Introduction

Geogrid mainly serves as reinforcement and separation by increasing bearing capacity and providing interlocking in the unbound granular base (Hass et al., 1988a). The interlocking effect increases the tensile strength under traffic loading, and the shear stress is reduced by the lateral restraint (Gu et al., 2016). The fatigue resistance of fibreglass geogrid-embedded-asphalt was investigated by laboratory testing in previous studies, the results indicate extended fatigue life provided by the geogrid (Arsenie et al., 2016; Darzins et al., 2021; Kumar et al., 2021; Lee, 2008).

Many types of failure can occur on asphalt pavement, among which three main types of distress have been studied extensively, including fatigue, low-temperature cracking, and rutting. Rutting, also known as a type of accumulation of permanent deformation of pavement, can happen in the subgrade soil or asphalt layer. The former type can be attributed to weak subgrade, heavy traffic, etc., while rutting can be severe in the asphalt layer due to low shear strength and lateral movement caused by heavy wheel loading (Faruk, Lee, Zhang, Naik, & Walubita, 2015; Zakaria & Lees, 1996). In this case, the restraint provided by the interlocking capability of geogrid within the asphalt can reduce the lateral movement. With the resistance of fatigue damage in asphalt provided by geogrid researched and verified with extensive studies, the resistance of rutting of geogrid-reinforced-asphalt can be also investigated.

In this chapter, the rutting resistance provided by geogrid to asphalt specimens was investigated by conducting Hamburg Wheel-Track Testing (HWTT). The practice of making cylindrical geogrid-embedded asphalt specimens was developed to be compatible with the test. Different analysis approaches were adopted to evaluate the rutting resistance and moisture susceptibility of the samples.

5.2 Materials

The materials used in the study were introduced, including three types of geogrids, asphalt mixes, and asphalt emulsion.

5.2.1 Geogrid

Three types of fibreglass geogrids were tested in this study, Geogrid 11 EPM, Geogrid 11, and Geogrid 10, as shown in Figure 4-17. The properties of these three geogrids are listed in Table 5-1. The characteristics of the geogrids are listed as follows:

- Geogrid 10: smaller aperture size (12.7 mm × 12.7 mm).
- Geogrid 11: larger aperture size (25.4 mm × 25.4 mm).
- Geogrid 11 EPM: larger aperture size (25.4 mm × 25.4 mm); bonded to an engineered polymeric membrane (EPM).

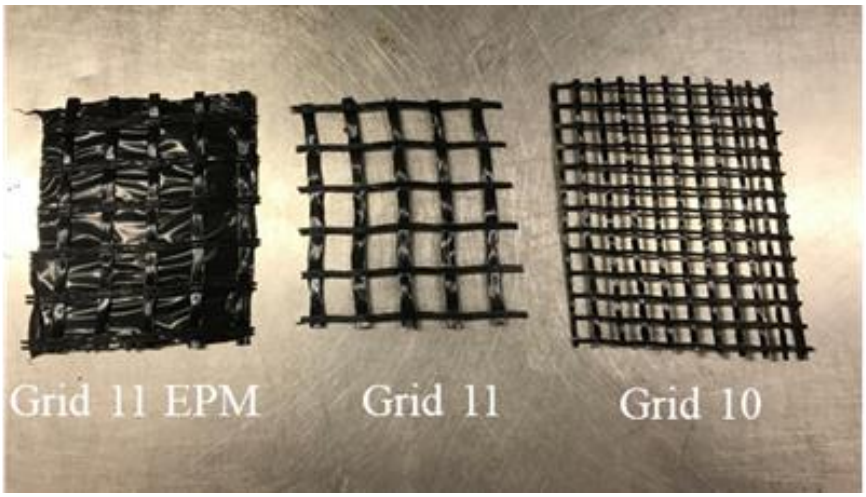

Figure 5-1 Geogrid Materials

Table 5-1 Geogrid Properties (Titan Environmental Containment, 2021a)**.**

Type of Geogrid	Ultimate Tensile Strength (kN/m)	Tensile Strength at 2% Strain (kN/m)	Optimum Elasticity Modulus (MPa)	Aperture Size (mm)
Geogrid 11 EPM	100	75	75	25.4
Geogrid 11	100	80	80	25.4
Geogrid 10	100	80	80	12.7

5.2.2 Asphalt Mixes

The asphalt mixes tested in this study are Superpave (SP) 19 mixes, with a PG 64-28 binder, sampled from the field construction, discussed in Section 4.3.

5.2.3 Tack Coat

The same asphalt emulsion used in the field construction was used when preparing the sample in the laboratory to provide adhesion to the geogrid placed on the asphalt surface. Clean Bond Coat (CBC) was used, which is an anionic, slow-setting asphalt emulsion. This type of tack coat allows for a faster curing time. It was diluted 50/50 by volume with water and applied at a rate of 0.5 L/m^2. Therefore, about 9 g of diluted tack coat were used on a 150 mm-diameter-surface.

5.3 Sample Preparation

The practice of compacting geogrid-embedded-asphalt in the laboratory is challenging due to two layers of asphalt that may cause inconsistent air void contents and application of geogrid. This section explains how to ensure the consistency of air void contents throughout the specimen and the steps to prepare a sample.

5.3.1 Air Void Adjustment

One of the challenges to test the geogrid is the lack of a standardized procedure to prepare the geogrid-embedded samples. The specimens were compacted using the Superpave Gyratory Compactor, as shown in Figure 5-2.

Figure 5-2 Superpave Gyratory Compactor

The geogrids were placed in the middle of the depth of the specimen, which was standardized as 63 mm as per the specification of HWTT (AASHTO, 2019a). The compaction was performed at the required temperature (150°C). Due to the special compaction practice in this study, the air void for the top and bottom layers needs to be consistent. To determine the required amount of materials for the top and bottom layers to ensure consistent air void, the specimens were tested with their air void contents as a whole specimen first, and then they were cut into three pieces in equivalent height as shown in Figure 4-30. The air voids were tested on the cut pieces to ensure the air void contents were consistent for the bottom and top layers.

It can be seen that from Figure 5-3, the air voids are consistent for the entire specimen, top, middle and bottom pieces for the control specimen with a height of 63 mm. The air voids tested as a whole specimen of the control specimens were approximately the average of air voids of top and bottom pieces. However, the middle portion of the specimens where geogrid is located has significantly higher air voids compared to the top and bottom parts, which brings the air voids of the specimen as a whole higher.

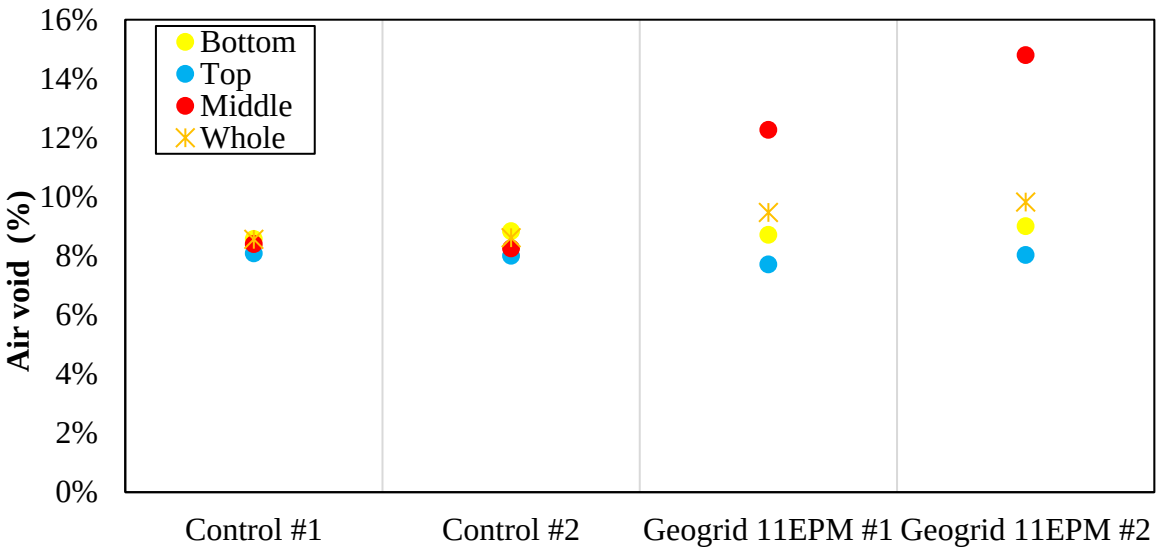

Figure 5-3 Air Void Contents of Bottom, Middle, and Top Layer of Asphalt Specimens

Therefore, some adjustments are needed when finalizing the air voids of asphalt concrete to eliminate the effect caused by embedded geogrid. To eliminate the effect of the increase of air void results caused by embedded geogrid, the adjustment factor of air void contents was determined based on Equation 5-1. The adjustment factors for the two trial samples were calculated to be 0.8662 and 0.8661. Then,

the final adjustment factor was determined by averaging these two values (i.e., 0.8662) and it was multiplied by the air void results of the samples to be tested by HWTT. The air voids of the sample that were tested by HWTT are listed in Table 2, which are within the range of 7% ± 1%, as per the standard (AASHTO, 2019a).

Equation 5-1

$$Adjustment\ factor = \frac{AV_{bottom}+AV_{top}}{2} \times \frac{1}{AV_{whole}}$$

where:

AV_{bottom} = air voids of the lower layer

AV_{top} = air voids of the upper layer

AV_{whole} = air voids of the specimen tested as a whole

Table 5-2 Air Void Results of Sample to be Tested

Specimen		% Air Void Before Adjustment	% Air Void After Adjustment
Control	1	7.54%	7.54%
	2	7.18%	7.18%
	3	7.11%	7.11%
	4	7.40%	7.40%
Geogrid 11 EPM	1	8.98%	7.97%
	2	8.04%	7.14%
	3	8.37%	7.43%
	4	8.38%	7.44%
Geogrid 11	1	8.20%	7.28%
	2	8.01%	7.12%
	3	7.85%	6.97%
	4	8.08%	7.17%
Geogrid 10	1	8.25%	7.33%
	2	7.85%	6.97%
	3	7.42%	6.59%
	4	8.45%	7.51%

5.3.2 Sample Compaction

Figure 5-4 illustrates the process of the sample compaction. The tack coat was applied on geogrid-embedded samples.

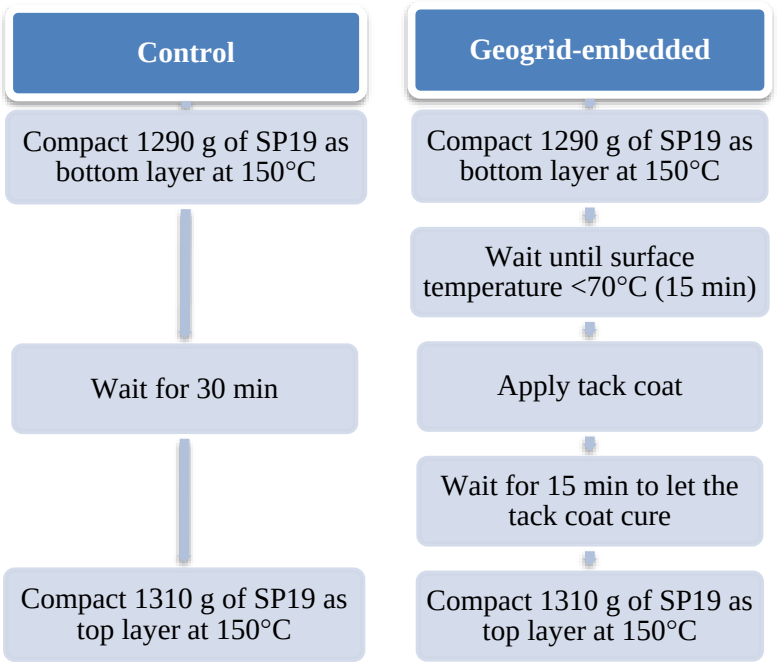

Figure 5-4 Process of Specimen Preparation

5.4 Hamburg Wheel-Track Testing Protocol

Hamburg Wheel-Track Testing is one of the common testing methods to evaluate the rutting and moisture-susceptibility of asphalt specimens. The test follows the standard by AASHTO (AASHTO, 2019a). Four cylindrical specimens in diameter of 150 mm and height of 63 mm were grouped in the mounting tray. The Departments of Transportation (DOT) throughout North America have varying requirements for testing temperatures. Generally, as a function of the high-temperature PG of the binder, the binder of PG 64-XX is required to be tested at 50°C required by most DOTs (Liao et al., 2023; West, Rodezno, Leiva, & Yin, 2018). Therefore, the testing temperature was set to be 50°C. The samples were submerged in the water at 50°C and conditioned for 45 min. 705 ± 4.5 N were applied on both wheels. The finish point of the testing is either the completion of 20,000 wheel passes or the point when one side of the rut depth reaches 20 mm.

As shown in Figure 5-5 as an example of control samples, one side of the sample was much more rutted compared to the other for all trials. Therefore, the average was not taken as per the standard. Instead, the failure side was analyzed and compared.

Figure 5-5 Samples After Testing

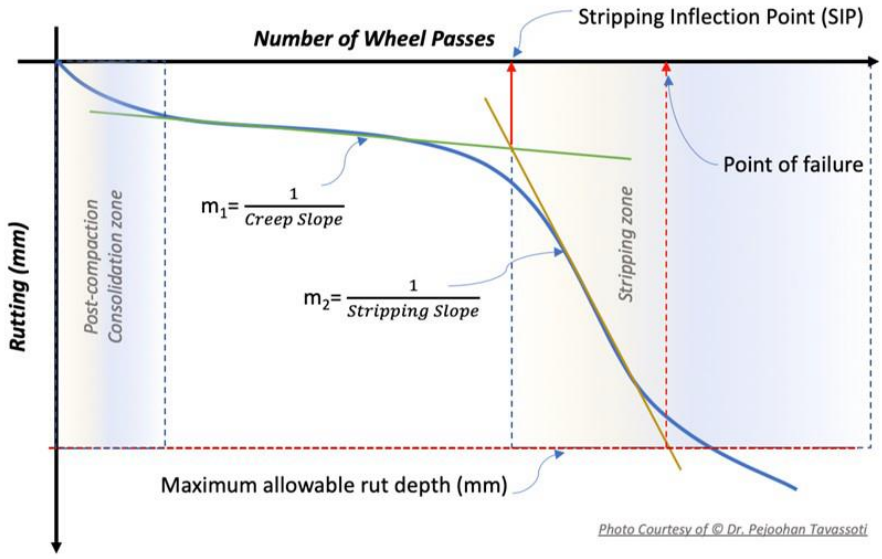

Figure 5-6 Typical Plot of HWTT Results (Liao et al., 2023)

A typical plot of HWTT results is shown in Figure 5-6, in which three stages are exhibited. The first stage is the post-compaction stage which shows the process of densification. This stage is typically the first 1,000 passes (Lv, Huang, Sadek, Xiao, & Yan, 2019). The secondary stage represents the creeping

stage with a smaller slope experiencing shear stress on the material. The beginning of the tertiary stage is also denoted by Stripping Inflection Point (SIP), which is determined by the intersection of the fitted slope of the secondary stage and tertiary stage. The tertiary stage is dominated by moisture damage in the stripping process (Liao et al., 2023).

5.5 Results and Analysis

The results of HWTT are presented and discussed in this section. Conventional analysis to evaluate rutting resistance from HWTT data was performed, while a new approach to analyze the results to eliminate human bias and evaluate the three stages separately was adopted. The moisture susceptibility of geogrid-reinforced-asphalt was also evaluated by combining both the conventional and the new approaches.

5.5.1 Rutting Resistance by Conventional Analysis Approach

The results of the rut depth against the number of passes from HWTT are plotted in Figure 5-7.

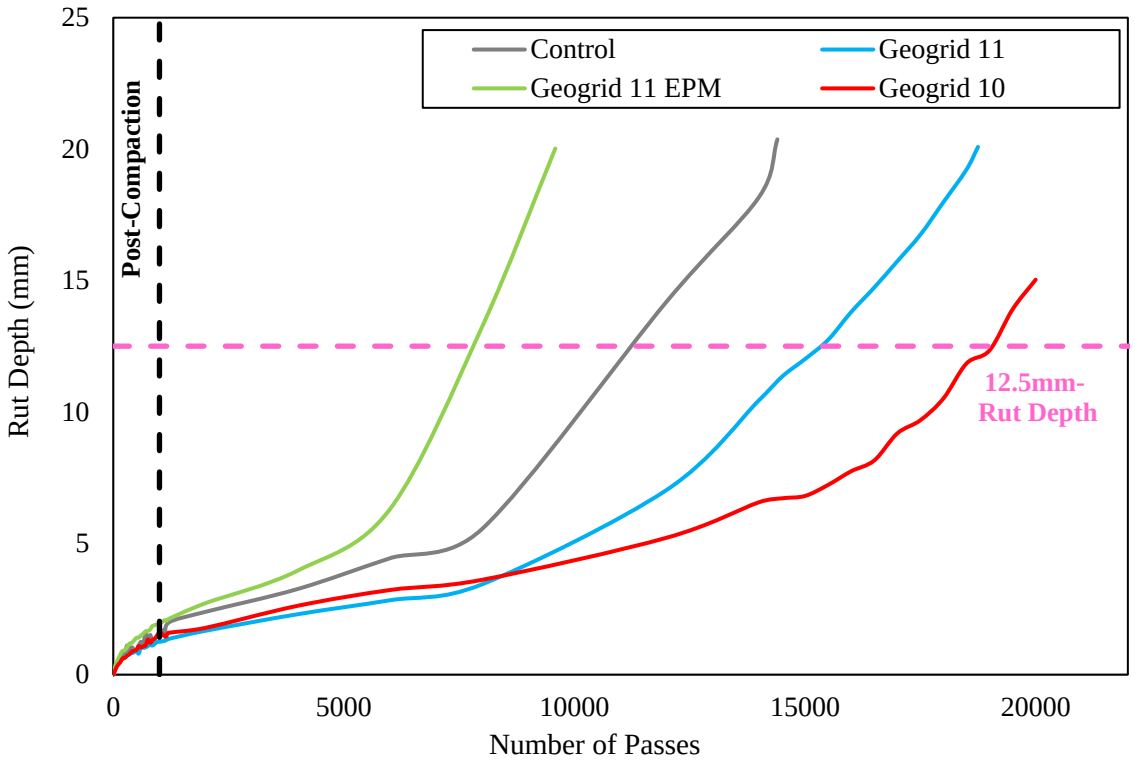

Figure 5-7 HWTT Results

From the figure, the post-compaction stage outlines the stage before the 1000 wheel passes to be the post-compaction stage, with rut depths at the end of the first stage in Figure 5-8. The sample with Geogrid 11 EPM has the highest rut depth at the 1000th wheel pass, which can be attributed to the extra EPM sheet bonded to the geogrid causing insufficient compaction, which can be also visualized in Figure 4-31 (a). Geogrid 10 has the lowest rut depth, which indicates the densification potential that may be caused by traffic is the lowest.

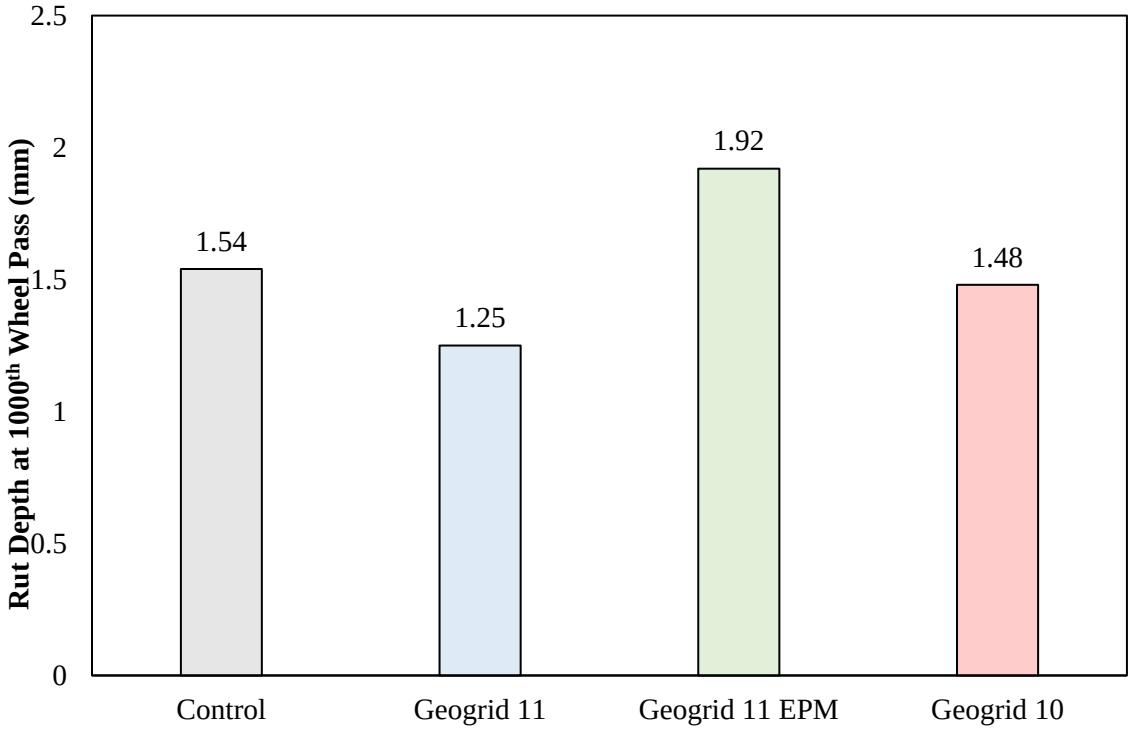

Figure 5-8 Rut Depth at the End of Post-Compaction Stage

Furthermore, as all trials failed before the completion of 20,000 wheel passes except Geogrid 10, the rutting resistance of each type of specimen was analyzed with conventional rutting resistance parameters: maximum number of wheel passes and number of passes when reaching 12.5 mm. The results are shown in Figure 5-9. Geogrid 10 has the best performance. Even when Geogrid 11 and Control have similar rut depth at the end of the first stage, Geogrid 10 has a better performance analyzed by the conventional analysis approach.

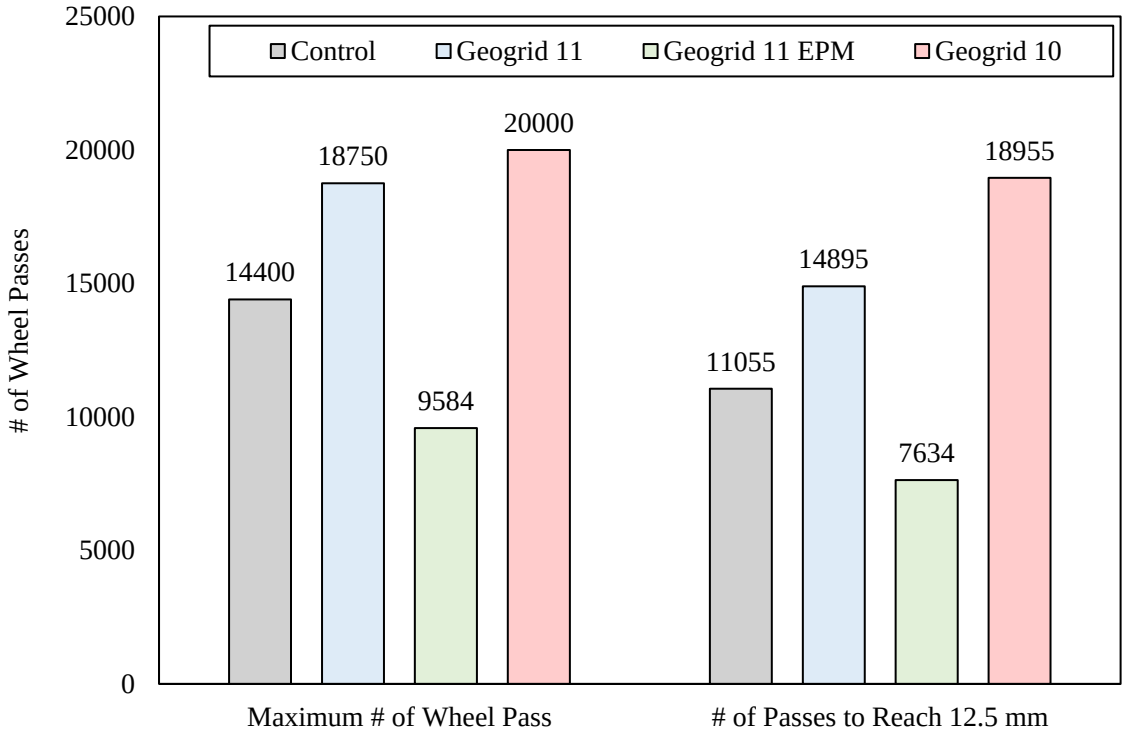

Figure 5-9 Conventional Rutting Resistance Parameters

All types of specimens failed when one side of the rut depth reached 20 mm, except the Geogrid 10 specimens failed at the completion of 20,000 wheel passes. Due to the different failing conditions of these four trials, another indicator was analyzed (rutting resistance index) to evaluate both rut depth and the number of wheel passes (Equation 5-2) (Wen et al., 2016). The results are shown in Figure 5-10. The results still show that Geogrid 10 has the best performance, with Geogrid 11 EPM performing the worst.

Equation 5-2

$$RRI = N_{max} \times \left(1 - \frac{RD_{max}}{25.4}\right) \times 25.4$$

where:

RRI = rutting resistance index (mm)

N_{max} = maximum number of wheel passes

RD_{max} = rut depth at completion (mm)

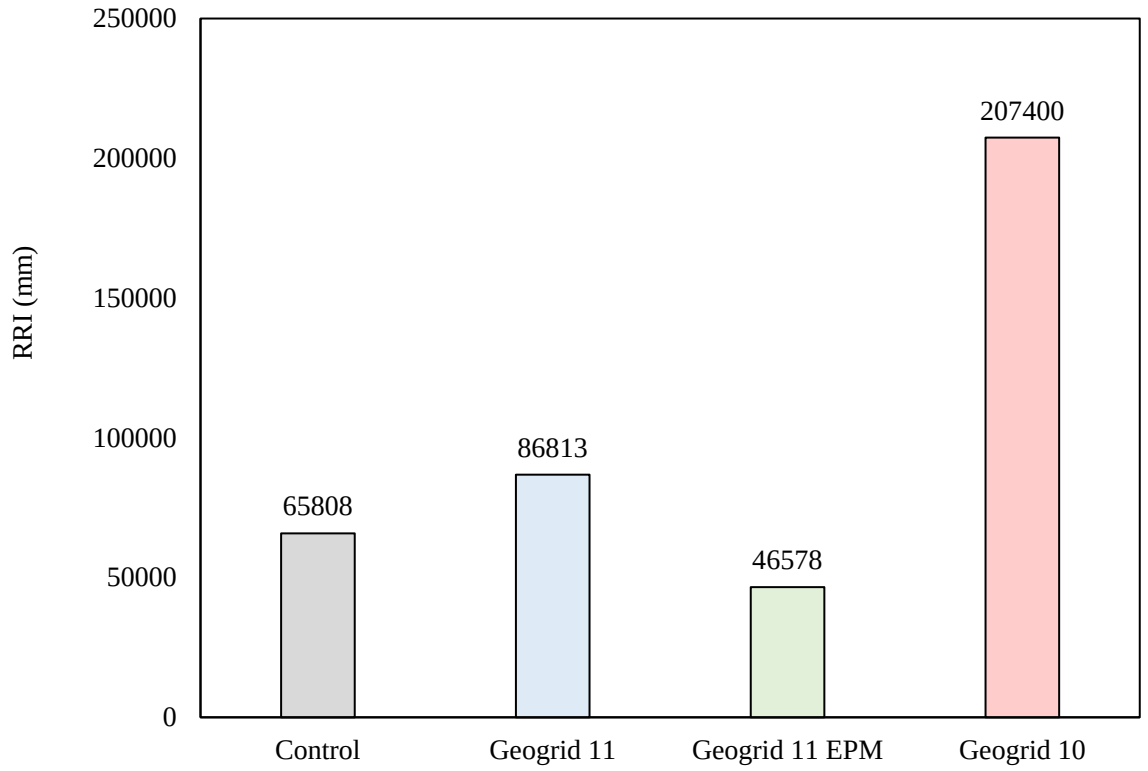

Figure 5-10 Rutting Resistance Index Results

5.5.2 Rutting Resistance by Iowa DOT's Analysis Approach

The conventional analysis is performed by manually fitting the curve, so errors may be introduced with biases. Also, since the test was performed in a submerged condition, moisture can have some impact on the results (Domingos & Faxina, 2015; Xu & Huang, 2012). Therefore, to solely analyze and characterize the results from different stages, Iowa DOT has developed an analysis approach to distinguish and quantify the creep and stripping stages from the HWTT results. A sample analysis of Geogrid 10 samples is shown in Figure 5-11 and Figure 5-12, with the sixth-degree polynomial fitted from the measured data. The least square regression method was used to fit the curve using Excel Solver. First, the stripping pass was determined when the first derivative of the fitted curve was maximum closing to the end of the test. This represents the passes at the maximum slope of the fitted curve closing to the end of the test. Then, before the stripping pass, the creep pass can be determined at the smallest slope (i.e., the first derivative is the smallest). Both creep and stripping slope can then be calculated.

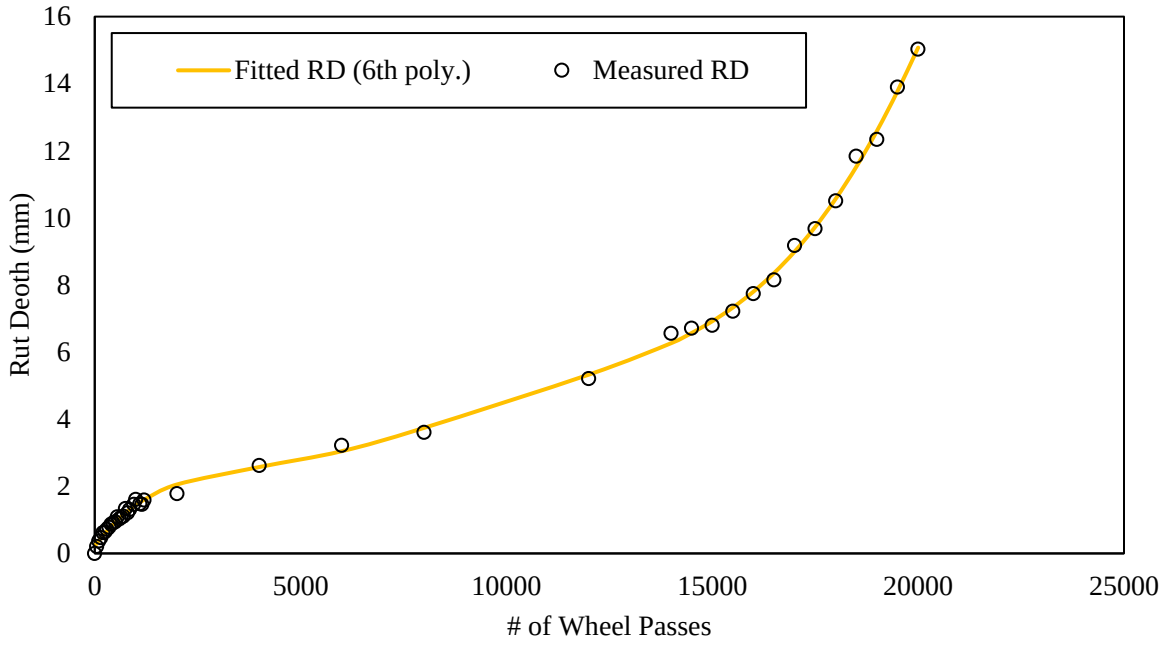

Figure 5-11 Geogrid 10 HWTT Data Fitted by Iowa Analysis for HWTT (Iowa DOT, 2013)

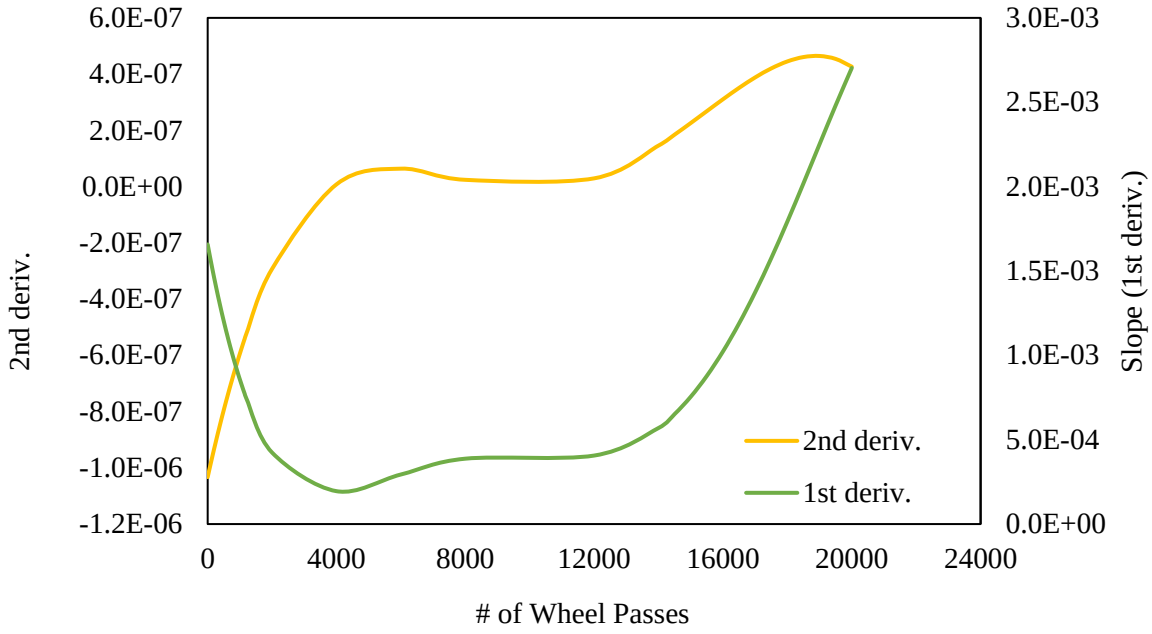

Figure 5-12 Geogrid 10 HWTT Data Processed by Iowa Analysis for HWTT (Iowa DOT, 2013)

The creep slope and stripping slope for each type of specimen are shown in Figure 5-13. Similar to conventional rutting parameters, Geogrid 11 EPM has the lowest resistance to rutting with the highest

creep slope. However, Geogrid 10 and Control specimens have similar creep slopes, while Geogrid 11 has the lowest. With Geogrid 10 showing the best performance illustrated in the previous section, this can be attributed to the lowest stripping slope. As mentioned, moisture damage is the dominant mechanism in the stripping stage (Liao et al., 2023). Thus, moisture susceptibility should be analyzed.

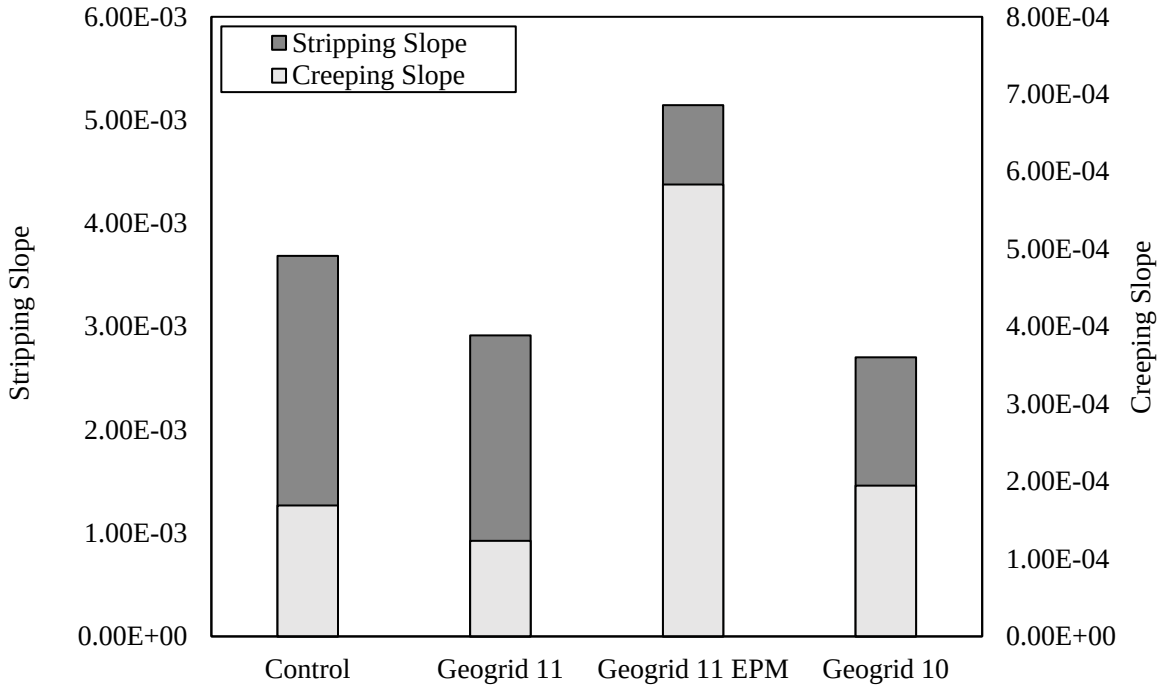

Figure 5-13 Creep and Stripping Slope Results

5.5.3 Moisture Susceptibility

Stripping Inflection Point (SIP) is the number of wheel passes at the onset of the tertiary stage, which can be found by the intersection of the fitted tangent lines of creep and stripping stages, calculated by Equation 5-3. A high SIP typically indicates higher resistance to moisture damage (Yin, Chen, West, Martin, & Arambula-Mercado, 2020).

Equation 5-3

$$SIP = \frac{intercept\ (stripping\ stage) - intercept\ (creep\ stage)}{slope\ (creep\ stage) - slope(stripping\ stage)}$$

SIP results determined by Iowa sixth-degree polynomial methods are shown in Figure 5-14. It can be seen that Geogrid 10 has the highest SIP, which is considered to be the least moisture-susceptible specimen. This also corresponds to the best performance in the previous section. Geogrid 11 EPM still

performs the poorest, which can be attributed to the possibility of the membrane not melting fully as Geogrid 11 has the second-best performance. The insufficient compaction can be also visualized in Figure 4-31 (a).

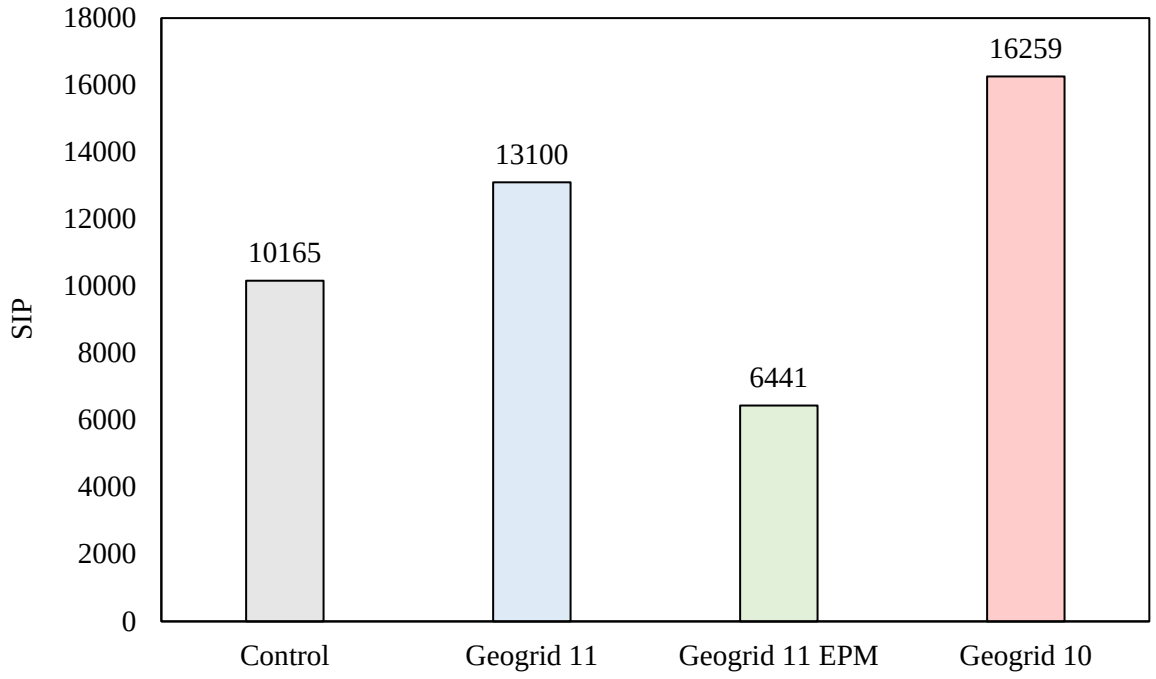

Figure 5-14 SIP Results

5.6 Chapter Summary

In summary, due to the special practice of making geogrid-embedded asphalt samples, the air void is found to be significantly high in the middle part where the geogrid is located. Some adjustments were made to the air void results to eliminate the high air void introduced by the geogrid.

HWTT was conducted on Geogrid 11, Geogrid 11 EPM, Geogrid 10, and Control Specimens. Different parameters were analyzed, which concludes the following remarks:

- By conventional analysis of rutting resistance, fibreglass geogrid can provide rutting resistance with better rutting resistance parameters. It can also provide resistance to moisture damage with higher SIP than control specimens. Geogrid with smaller aperture sizes demonstrated better rutting performances.
- With manual curve-fitting, errors may be introduced with biases. Also, since the test was performed in a submerged condition, moisture can have some impact on the results.

Therefore, to solely analyze and characterize the results from different stages, the HWTT data were analyzed by Iowa six-degree polynomial analysis. Geogrid 11 with larger openings has a lower creep slope, which indicates a better rutting resistance.

- Geogrid 10 with smaller openings has a lower stripping slope, representing less moisture susceptibility. Also, SIP was analyzed with the creep and stripping slopes obtained by Iowa's approach and combined with conventional calculations. Geogrid 10 has the highest SIP, which verifies its best resistance to moisture damage.
- Geogrid 11 EPM has the worst performance including rutting resistance and moisture susceptibility, which can be attributed to the extra membrane. The membrane likely did not fully melt during the compaction. This can be due to the small amount of material to compact the specimens, which brings little heat to melt the membrane.

Based on the conclusions, the following recommendations have been made:

- With the variability of the high air void introduced by the geogrid, the compaction practice can be optimized by compacting samples of greater height, using more materials, and applying more compaction effort. In this case, the first stage of densification can be consistent to better compare the second and third stages.
- Other tests can be conducted to investigate the rutting resistance and moisture susceptibility separately, as the overall HWTT data are still a combination of both post-compaction, creep, and moisture damage.

Chapter 6
Evaluation of Permanent Deformation and Moisture Damage on Geogrid-Reinforced Asphalt by Dynamic Creep Testing

6.1 Introduction

Rutting in asphalt pavements is a critical issue that can compromise road safety and durability. It is typically characterized by two significant stages: the initial stage involving the consolidation of asphalt mixtures and the second stage, which primarily deals with the development of shear flow. The primary goal of this chapter is to assess the effectiveness of incorporating geogrid reinforcement in enhancing the asphalt's resistance to rutting, with a specific focus on investigating the secondary stage of rutting.

To ensure the validity of the findings, it is necessary that the conditions in the primary stage remain consistent across all experiments. This means that the compaction effort used to prepare the asphalt samples must be uniform, ensuring that the initial density and structure of the specimens are identical. Thus, maintaining a consistent level of air voids within the samples is crucial to isolate the influence of the geogrid in the secondary stage of rutting. This approach will allow to isolate the effects of geogrid reinforcement on rutting behavior accurately. As recommended in the last chapter, specimens of a greater height could be compacted to waive the air void adjustment factor and maintain consistent air void in the top and bottom layers. Also, the HWTT requires samples to be submerged in water, while the results are isolated into three stages and the third stage (i.e., stripping zone) represents the moisture damage. However, an alternative testing approach has been proposed in this chapter. This approach aims to evaluate the permanent deformation potential and moisture susceptibility of asphalt mixtures separately. This test allows the samples to be tested in a dry condition first. Then, freeze-thaw conditioning can be conducted, and the conditioned samples can be tested again.

In this chapter, to replicate real-world traffic conditions that contribute significantly to permanent deformation in asphalt pavements, a fundamental test called the dynamic creep test was performed. It involves subjecting the samples to repeated axial loading, utilizing haversine loading profiles interspersed with rest periods, to mimic the traffic that is the main cause of the accumulation of permanent deformation. Such a test is called the dynamic creep test. The concept of flow number corresponding to dynamic creep test was raised which can be derived from the testing results. Other outcomes of dynamic creep tests can also be considered to be indicators of rutting resistance, including ultimate strain and mean strain rate (Airey, 2004; Zhao et al., 2020). To ensure the accuracy of the

dynamic creep test, specimens are prepared with standardized sizes, matching the diameter of the loading plate, as per AASHTO T378 (AASHTO, 2017). However, an advanced approach was also explored, where larger specimens were used, and the loading plate was designed to penetrate into the samples. This design closely replicates real field conditions, where the surrounding asphalt acts as confinement, and provides a more realistic assessment of rutting resistance.

Furthermore, the moisture susceptibility was assessed. Freeze-thaw conditioning was applied to the samples to induce moisture damage, then the conditioned samples were tested by dynamic creep testing. Their performance is subsequently compared with that of non-conditioned samples. This comparative analysis helps in understanding how moisture susceptibility impacts the asphalt's resistance to permanent deformation, providing insights into the function of the geogrid within the asphalt samples when they are subjected to moisture damage.

In order to comprehensively understand the behaviour of the geogrid-embedded asphalt samples in response to varying temperature conditions, the dynamic creep tests were conducted at three distinct temperature settings: -10°C, 25°C, and 50°C. This temperature range was selected to simulate a wide spectrum of environmental conditions that asphalt pavements might encounter in the real world.

6.2 Methodology and Materials

In this section, the material used in this chapter was introduced and the test set-up was discussed including the equipment and protocol. To investigate the moisture susceptibility of geogrid-reinforced asphalt samples, pre-test conditioning was performed by freezing and thawing the sample.

6.2.1 Materials

The asphalt mixes used in this study were the same as those used in the Hamburg Wheel Tracking Test in Chapter 5, which were SP 19 mixes sampled from the field trial. Three types of geogrids including Geogrid 11, Geogrid 11 EPM, and Geogrid 10, as shown in Figure 5-1, were tested in this study as well. The same tack coat (i.e., CBC) was applied during sample preparation.

6.2.2 Test Equipment

The specimens were tested in a chamber to control the temperature. A 100 mm-diameter top plate was used as the loading plate. A Linear Variable Differential Transformer (LVDT) was installed on each side of the frame to measure the vertical displacements. The average was taken when calculating the axial strain. Figure 6-1 illustrates a 150-mm diameter specimen loaded in the frame. Silicone sheets

were placed at the top and bottom of the specimen to prevent slipping. As shown in the figure, the specimens are larger than the loading plate in diameter, which was modified from AASHTO T378 (AASHTO, 2017). In this case, the surrounding asphalt can act as confinement,

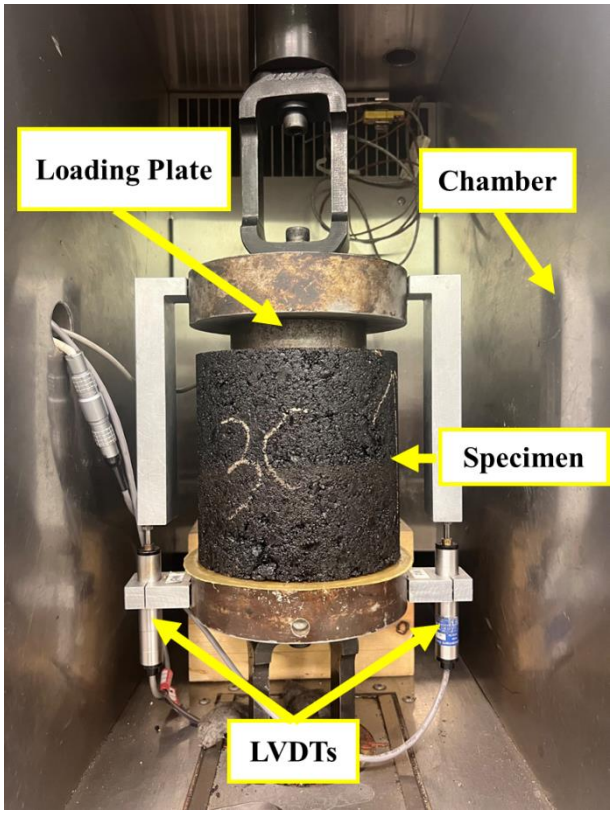

Figure 6-1 Test Set-up of Dynamic Creep Test

6.2.3 Testing Temperature Calibration

The specimens were also preconditioned for them to reach certain temperatures. For 100 mm-diameter specimens, they were conditioned for 2 hr, 2 hr, and 1.5 hr under -10 °C, 25 °C, and 50 °C, respectively. For 150-diameter specimens, they were conditioned for 4 hr, 4 hr, and 4 hr under -10 °C, 25 °C, and 50 °C, respectively. The condition time was determined using a dummy sample of the same size as the testing samples. A thermistor was installed in the middle of the dummy sample and was sealed with an aluminum sticker to monitor its temperature changes, as shown in Figure 6-2.

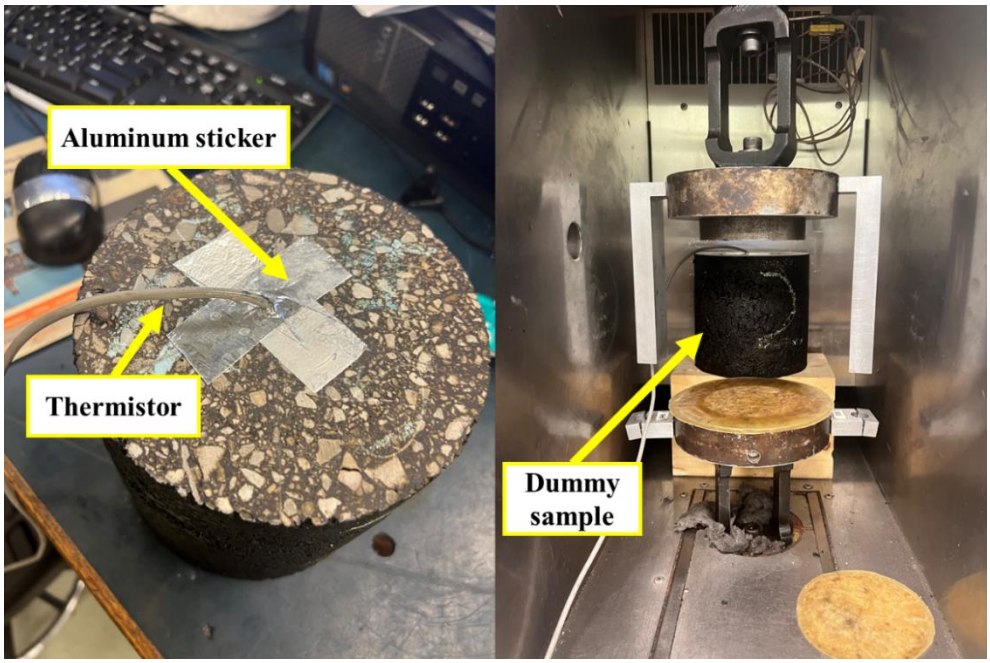

Figure 6-2 Dummy Sample in the Chamber Monitoring Temperature

The dummy sample was first conditioned for 6 hours at each temperature condition and the length of actual conditioning time was determined based on the actual change of the dummy temperature. Figure 6-3 plots the calibration of preconditioning time under different temperatures for 150-diameter specimens. It can be seen that the dummy specimens took around 3-4 hours to reach and stabilize at certain temperatures.

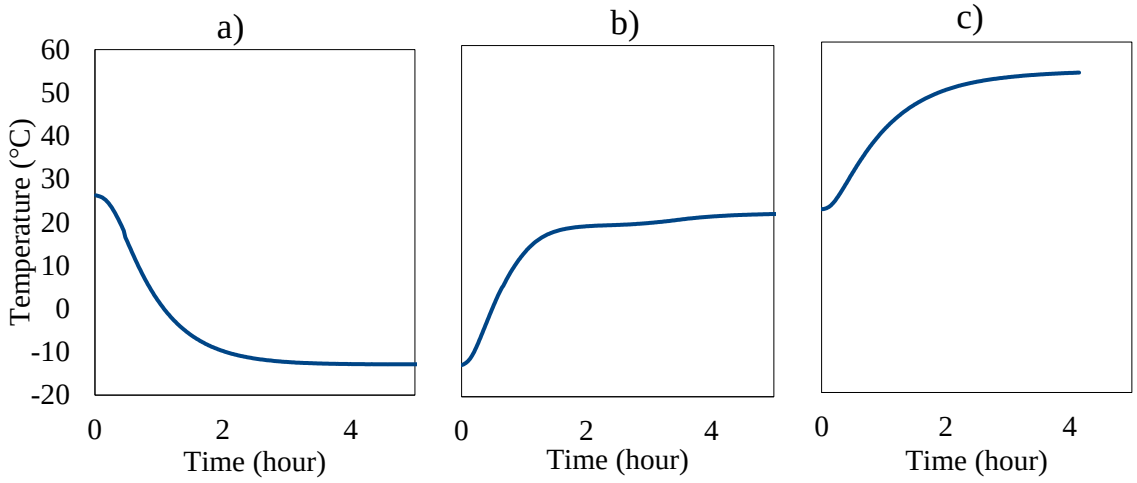

Figure 6-3 Pre-conditioning Time Calibration for 150 mm-Diameter Specimens at a) -10 °C; b) 25 °C; c) 50 °C

6.2.4 Test Protocol

The loading cycle consists of 3 stages: the loading stage (0.05 s), the unloading stage (0.05 s), and the resting stage (0.9 s), as per AASHTO T378-17 (AASHTO, 2017). One loading cycle takes 1 s. As specified by the standard that contact stress is 30 kPa and repeated axial stress is 600 kPa, the contact force and axial haversine loading force were determined to be 235 N and 4700 N, respectively, based on the contact area between the 100-diameter loading plate and the specimen. Figure 6-4 and Figure 6-5 illustrate the loading curve and displacement accumulation.

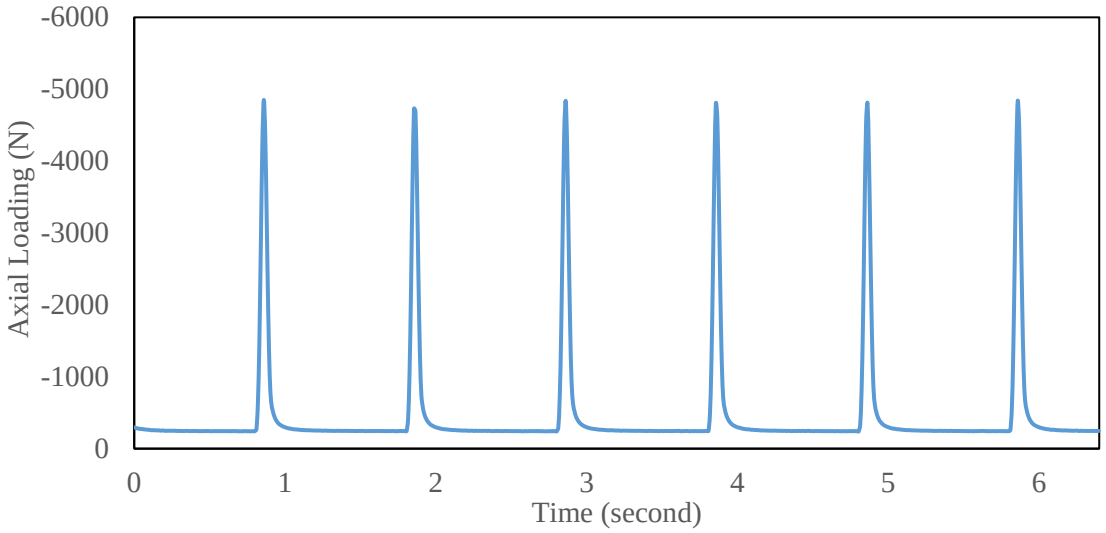

Figure 6-4 Loading Pattern of Dynamic Creep Test

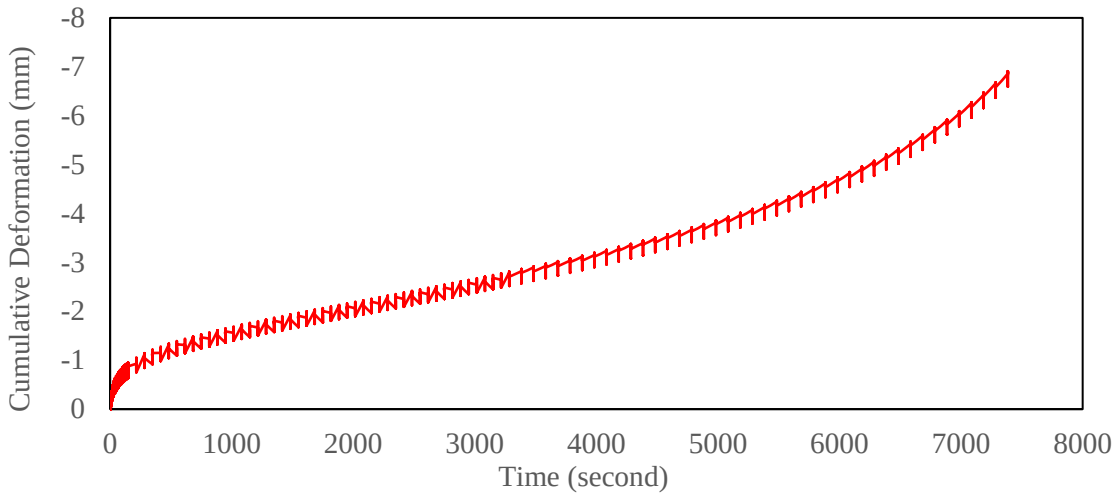

Figure 6-5 Cumulative Deformation of Dynamic Creep Test

To investigate the creeping of geogrid-reinforced specimens under different temperatures, the test was run at -10 °C, 25 °C, and 50 °C. Under -10 °C and 25 °C, only 150 cycles of loading were applied. The first 100 cycles were preloading time, while immediately after the preloading, the actual periodic loading pulse was applied with 50 cycles, where the measurements were started to be recorded. Under 50 °C, after the 100-cycle preloading, the first 50 cycles were taken for creeping analysis, same with the first two temperature scenarios. Afterwards, the samples were loaded until failure to investigate the permanent deformation. The failure criterion was determined to be the moment when the absolute displacement of either LVDT has reached 8 mm. To ensure the complete failure of the specimen before the test was terminated, the initial readings of both LVDTs were set to be below 0.5 mm when loading the sample. 50 °C was chosen to evaluate the rutting resistance as per the asphalt binder grade (i.e., PG 64-28) (Liao et al., 2023; West et al., 2018). Meanwhile, other studies assessing rutting performances also apply the same temperature conditions (Fang et al., 2017; Jiupeng Zhang, Fan, Fang, Pei, & Xu, 2016; Jun Zhang, Alvarez, Lee, Torres, & Walubita, 2013).

To better reproduce the actual field conditions, apart from the standardized 100 mm diameter samples, samples in a larger diameter were also prepared and tested. The loading plate is still 100 mm in diameter; thus, the applied load would penetrate into the sample with the surrounding asphalt as confinement.

6.2.5 Freeze-Thaw Conditioning

Another set of 150-diameter samples was preconditioned by freezing and thawing (F-T). At first, the freeze-thaw process follows AASHTO T283 and ASTM D4867 (AASHTO, 2014; ASTM, 2022). The sample was first saturated by water and frozen at -18 °C for 16 hours. Then, the sample was thawed in water at 60 °C for 24 hours. However, it turned out that such a freeze-thaw process was too aggressive for such geogrid-embedded asphalt samples compacted in the laboratory. Figure 6-6 shows how the sample was separated after such freeze-thaw conditioning.

In such cases, a less aggressive process was adopted. In one study, the asphalt samples were frozen at -5 °C for 16 hr and +30 °C for 8 hr (R. Tarefder et al., 2018). Another study used -18 °C as freezing for 24 hr and 25 °C as thawing temperature at 24 hr (Lachance-Tremblay et al., 2017). In this study, the samples were frozen at -18 °C for 16 hr as per AASHTO T283, while 25 °C (i.e., room temperature) was determined for thawing for 24 hr.

Figure 6-6 Sample Separated After Standardized Freeze-Thaw Conditioning

Figure 6-7 illustrates the entire F-T process. First, the sample was placed in a container filled with water and vacuumed at 13 kPa absolute pressure. After several trial-and-error tests, two cycles of vacuum were performed on each sample. Each cycle consisted of a 7-minute continuous vacuum and a 5-minute resting period afterwards. It was found that the maximum saturation degree the samples could reach was around 60%, while AASHTO T283 specifies that the saturation degree is 70%-80% (AASHTO, 2014). However, ASTM D4867 specifies that 55% - 80% saturation is acceptable (ASTM, 2022). The saturation degree can be calculated by Equation 6-1 to Equation 6-3. The degree of saturation of each specimen is listed in Table 6-1. After the samples were at 55% saturation, they were wrapped with plastic wraps to prevent water loss. The samples were immediately transported to the freezer at -18 °C. After 16 hr, they were taken out from the freezer and thawed at room temperature with the wrap on. After 24 hr, the wrap was removed to let the sample dry for 2 days before the actual dynamic creep test. Such preconditioning F-T process was more conservative, while the results of dynamic creep testing still show significant differences between samples with/without F-T.

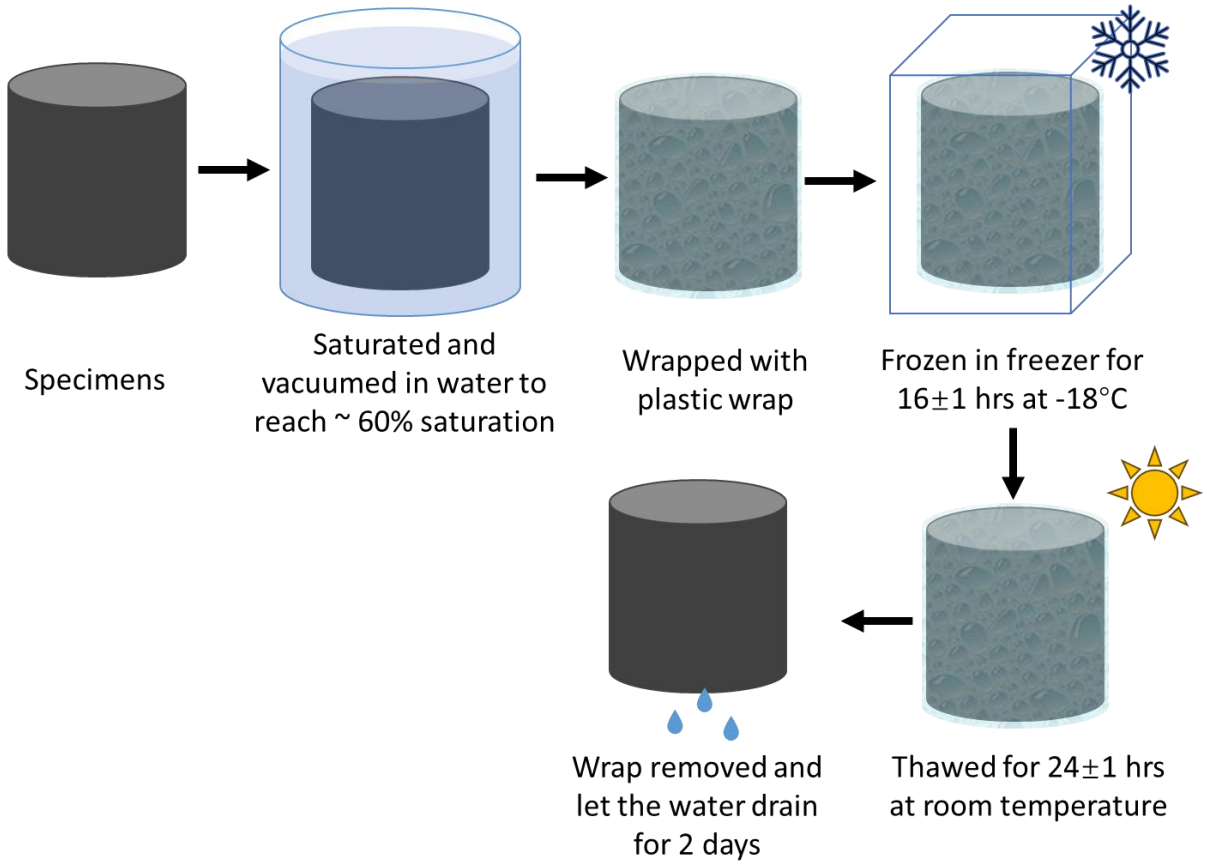

Figure 6-7 Freeze-Thaw Conditioning Process

Equation 6-1

$$V_a = \frac{P_a E}{100}$$

Equation 6-2

$$J' = B' - S$$

Equation 6-3

$$S' = \frac{100 j\prime}{V_a}$$

where:

V_a = volume of air voids (cm^3)

P_a = air voids (%)

E = specimen volume (cm^3)

J' = volume of absorbed water (cm^3)

B' = mass of saturated and surface-dry specimen after vacuum (g)

A = mass of dry specimen in air before vacuum (g)

S' = degree of saturation (%)

Table 6-1 Degree of Saturation

Specimen		S'
CT	1	56.6%
	2	57.5%
	3	58.9%
Geogrid 11	1	59.4%
	2	55.3%
	3	72.8%
Geogrid 11 EPM	1	57.7%
	2	56.8%
	3	58.3%
Geogrid 10	1	56.9%
	2	56.7%
	3	57.5%

6.2.6 Analysis Method

The testing results were analyzed utilizing the method specified in European standard EN 12697 – 26 (BSI, 2018) to evaluate the creep rate and modulus at different temperatures, and the method in AASHTO T378 (AASHTO, 2017) to evaluate the cumulative permanent deformation. Visual inspection was also conducted to observe the effect of inhibiting crack propagation provided by geogrid.

6.2.6.1 Creep Rate and Creep Modulus

Creep behaviour is a manifestation of how viscoelastic materials behave. In order to calculate the rate the specimen creeps, the cumulative strain is required, which can be calculated by Equation 6-4 with the cumulative deformation measured by the LVDTs.

Equation 6-4

$$\varepsilon_n = 100 \times \frac{u_n}{t_i}$$

where:

ε_n = cumulative axial strain after n loading cycle (%)

u_n = cumulative deformation after n loading cycle (mm)

t_i = initial thickness of the specimen (mm)

After the preloading period (i.e., the first 100 cycles) after the conditioning at each temperature, the next 50 cycles were used to calculate the creep rate and creep modulus using Equation 6-5 and Equation 6-6, respectively.

Equation 6-5

$$f = \frac{\varepsilon_{n1} - \varepsilon_{n2}}{n_1 - n_2} \times 10000$$

Equation 6-6

$$E_n = \frac{\sigma}{10\varepsilon_n}$$

where:

f_c = creep rate (μm/m/cycle)

n_1, n_2 = number of cycles

E_n = creep modulus after n loading cycle (MPa)

σ = applied stress (kPa)

6.2.6.2 Permanent Deformation

It can be identified from Figure 6-5 that the testing results can be classified into three stages, where the specimen is damaged at a high rate in the primary zone and deformed at a slow and stable rate in the secondary zone, followed by a fast creep in the tertiary stage. The flow number can be identified by the number of cycles where the secondary stage finishes, and where the tertiary stage starts, as denoted in Figure 6-8.

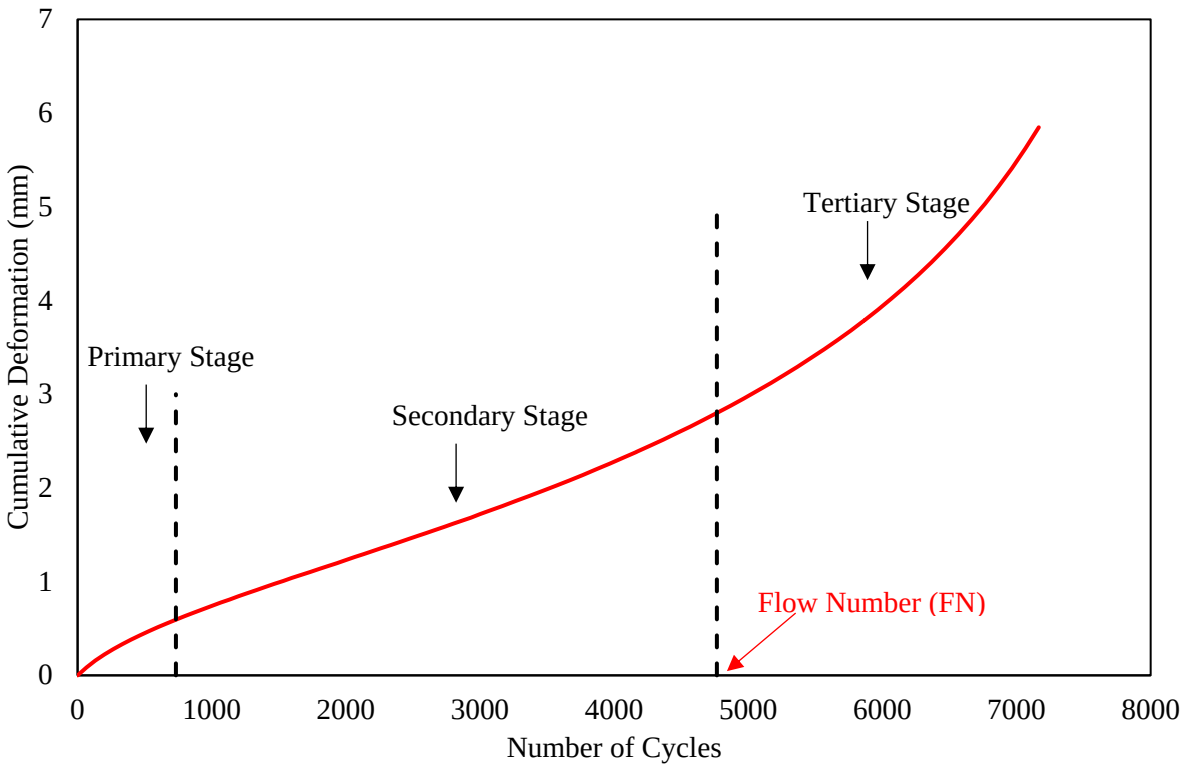

Figure 6-8 Cumulated Deformation Results under Repeated Load with Three Stages

It can be calculated by interpolating this flow number point using smoothed raw data and moving averages to compute the permanent axial strain rate using Equation 6-5. The flow number can be obtained by the number of cycles where the strain rate reaches the minimum (Witczak et al., 2002). However, such an analysis method with a smoothed central difference is highly dependent on the sampling interval and is sensitive to the electrical noise from the transducers. Arizona State University (ASU) has proposed another algorithm to compute the flow number named the Francken model, which considers all three stages of permanent deformation as a comprehensive model (Biligiri, Kaloush, Mamlouk, & Witczak, 2007). The axial strain calculated from the raw deformation data can be first fitted to the Francken model, which is a combination of a power and exponential equation, listed in Equation 6-7

Equation 6-7

$$\varepsilon_n = An^B + C(e^{Dn} - 1)$$

where:

A, B, C, D = regression constants

The axial strain data can be fitted to Equation 6-7 by achieving the minimum mean-square error with the aid of Excel Solver. Then, the first and second derivatives of the fitted results can be computed using Equation 6-8 and Equation 6-9. The first derivative represents the permanent axial strain rate. As mentioned, the flow number can be denoted as the cycle number where the strain rate is the minimum. Therefore, as the second derivative computed by Equation 6-9 changes from negative value to positive, in other words, when the strain rate begins to increase, the FN can be obtained.

Equation 6-8

$$\frac{d\varepsilon_n}{dn} = ABn^{B-1} + CDe^{Dn}$$

Equation 6-9

$$\frac{d^2\varepsilon_n}{dn^2} = AB(B-1)n^{B-2} + CD^2e^{Dn}$$

A sample fitting result from the ASU model and the computed derivatives are plotted in Figure 6-9 and Figure 6-10. It can be seen that the experimental data fits both models well.

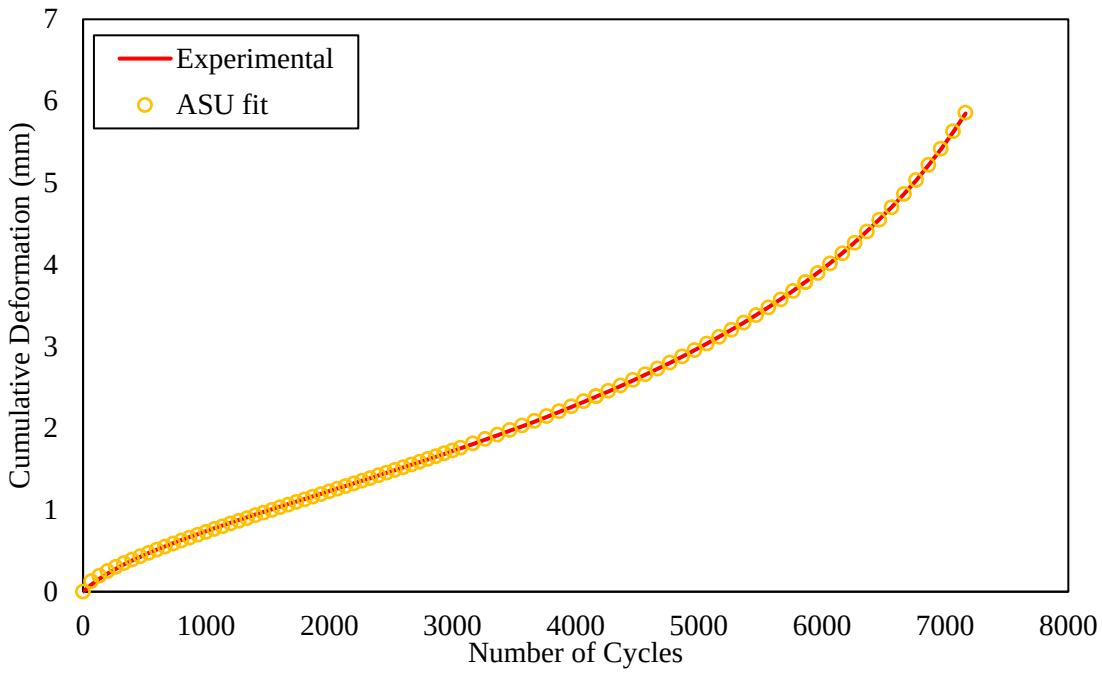

Figure 6-9 Sample Fitting of Permanent Deformation Results

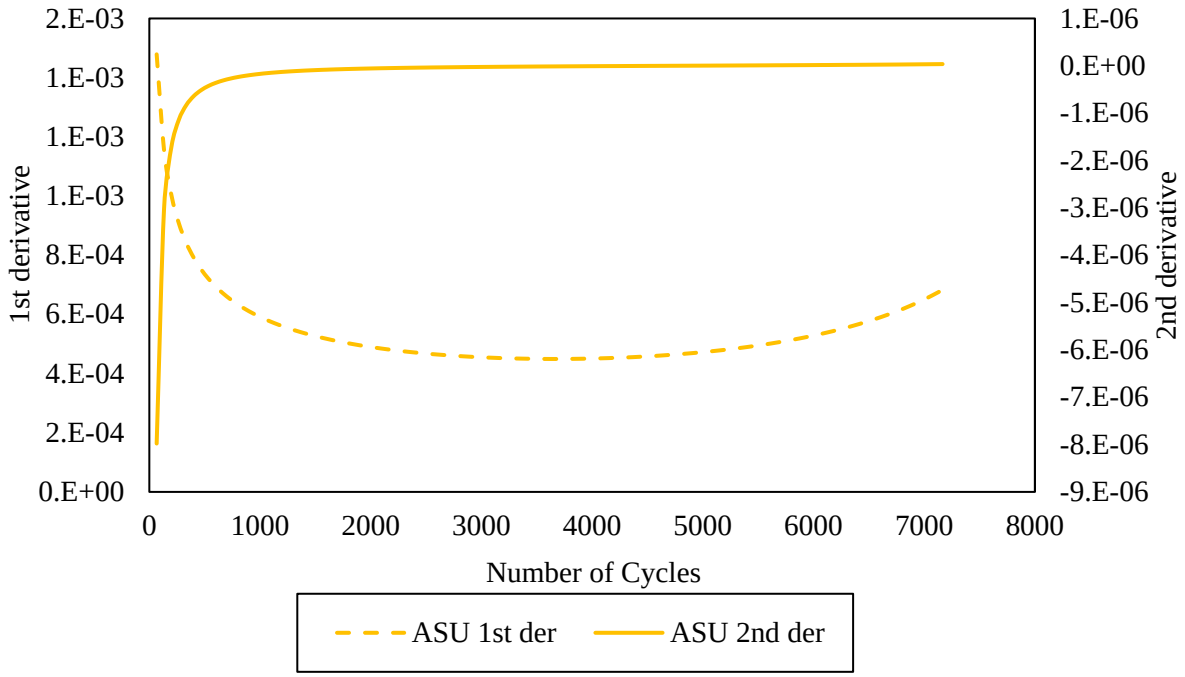

Figure 6-10 Sample Analysis of Permanent Deformation Results

6.3 Sample Preparation

As mentioned, the process of compacting geogrid-embedded asphalt samples in the laboratory poses challenges due to the presence of two layers of asphalt, which can lead to inconsistent air void contents. While an adjustment factor of air void content was applied on specimens with a height of 63 mm, the sample height for the testing in this chapter is 150 mm. This section provides an explanation of how to maintain uniform air void contents throughout the specimen and outlines the steps involved in preparing a sample.

6.3.1 Air Void Adjustment

The specimens were compacted using the Superpave Gyratory Compactor, as shown in Figure 5-2. The geogrids were placed in the middle of the depth of the specimen, which was standardized as 150 mm as per AASHTO T378-17 (AASHTO, 2017). The compaction was performed at the required temperature for the asphalt mixes (150°C). Some samples were tested with their air void contents as a whole specimen first. Subsequently, they were cut into three sections of equal height, as depicted in Figure 4-30. The air voids in these segmented pieces were then assessed to obtain the appropriate

amount of material for both layers to ensure uniformity in air void contents for both the bottom and top layers.

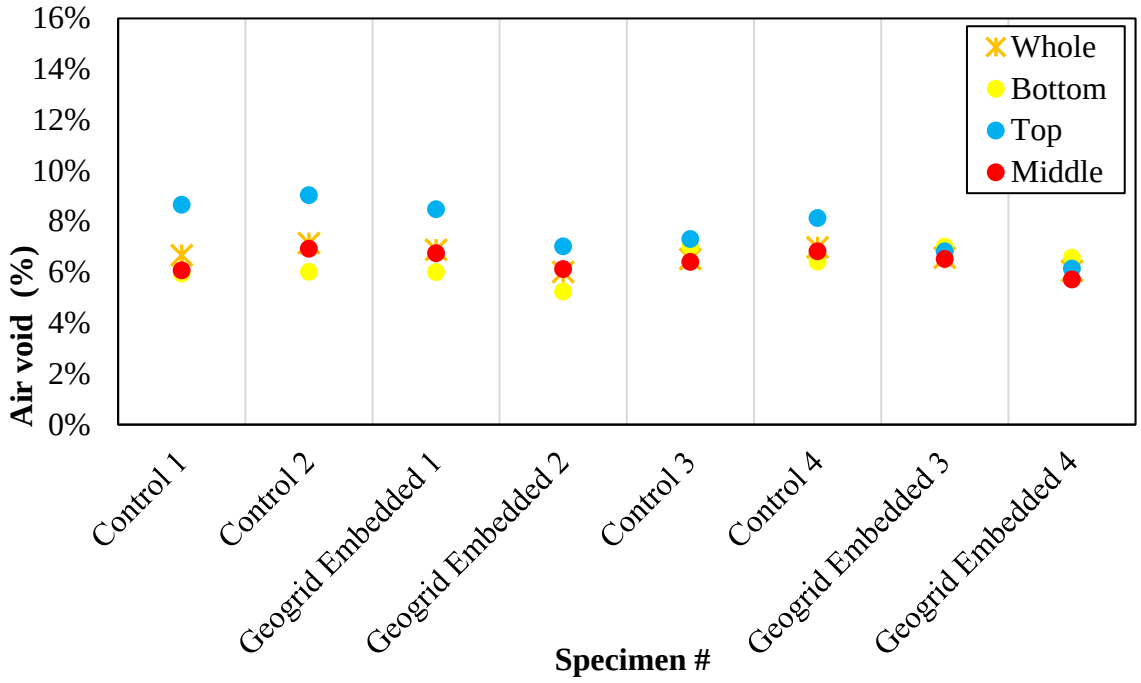

Figure 6-11 Air Void Contents of Bottom, Middle, and Top Layer of Asphalt Specimens

From Figure 6-11, it can be seen that after the first few trials, the middle piece of all specimens has similar air voids to the air voids as a whole, and they were also approximately the average of air voids of top and bottom pieces. In this case, no adjustment was made to the air voids of the specimens in 150 mm height.

The air voids of the sample tested in this chapter are listed in Table 2, which are all within the range of 7% ± 0.5%.

Table 6-2 Air Void Results of Sample to be Tested

Specimen		150 mm - diameter	150 mm – diameter F - T	100 mm - diameter
Control	1	6.88%	6.94%	6.54%
	2	6.77%	6.79%	6.32%
	3	6.58%	6.70%	6.53%
Geogrid 11 EPM	1	6.95%	7.24%	7.15%
	2	7.03%	6.76%	6.93%
	3	6.85%	6.83%	7.20%
Geogrid 11	1	6.64%	7.31%	7.04%
	2	6.51%	7.11%	7.14%
	3	7.13%	7.17%	7.44%
Geogrid 10	1	6.93%	6.84%	6.63%
	2	7.42%	7.14%	7.02%
	3	6.92%	7.28%	7.01%

6.3.2 Sample Compaction

The process of the sample compaction follows the same procedure as shown in Figure 5-4, while the material used for the bottom layer was 3030 g and that for the top layer was 3220 g instead. The specimens with a diameter of 100 mm were compacted following a similar process and were cored from the 150 mm-diameter samples.

6.4 Evaluation of Creeping under Different Temperatures

In line with the methodology described earlier, the dynamic creep tests were conducted on two different sample sizes: one with a diameter of 150 mm and the other with a diameter of 100 mm. Notably, the samples with a 150 mm diameter were subjected to loading using a 100 mm-diameter loading plate that penetrated into the specimen, while the 100 mm-diameter samples were loaded uniformly across their entire cross-section using the same loading plate.

Following an initial pre-loading phase of 100 cycles, the subsequent 50 cycles were meticulously analyzed to calculate two essential parameters: the ultimate creep modulus and the mean strain rate. This analysis was performed to understand how the reinforced asphalt samples creep under the specified

temperature conditions of -10 °C, 25 °C, and 50 °C, taking into account the variations in sample size and loading practice. To ensure the reliability of the results, three replicated specimens with a 100 mm diameter and four replicated specimens with a 150 mm diameter were subjected to the dynamic creep tests. Figure 6-12 and Figure 6-13 plot the results of the ultimate creep modulus and mean strain rate, respectively.

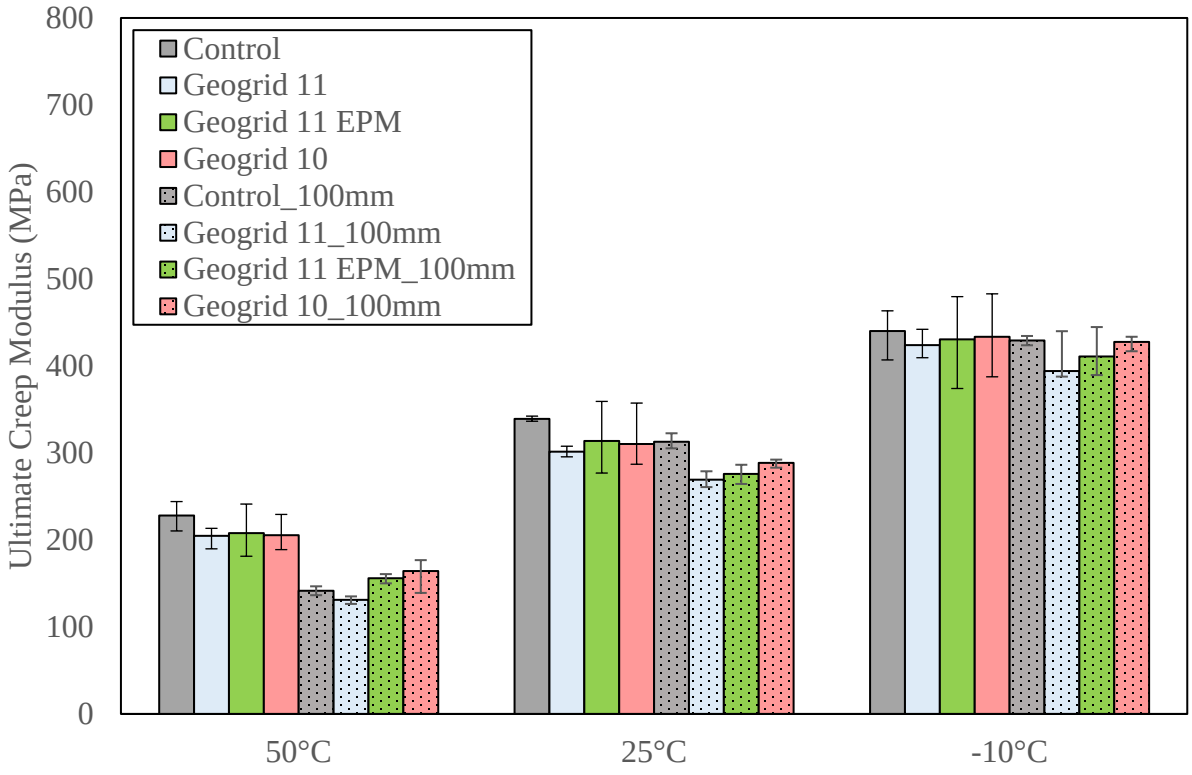

Figure 6-12 Ultimate Creep Modulus Results for Specimens in Two Sizes

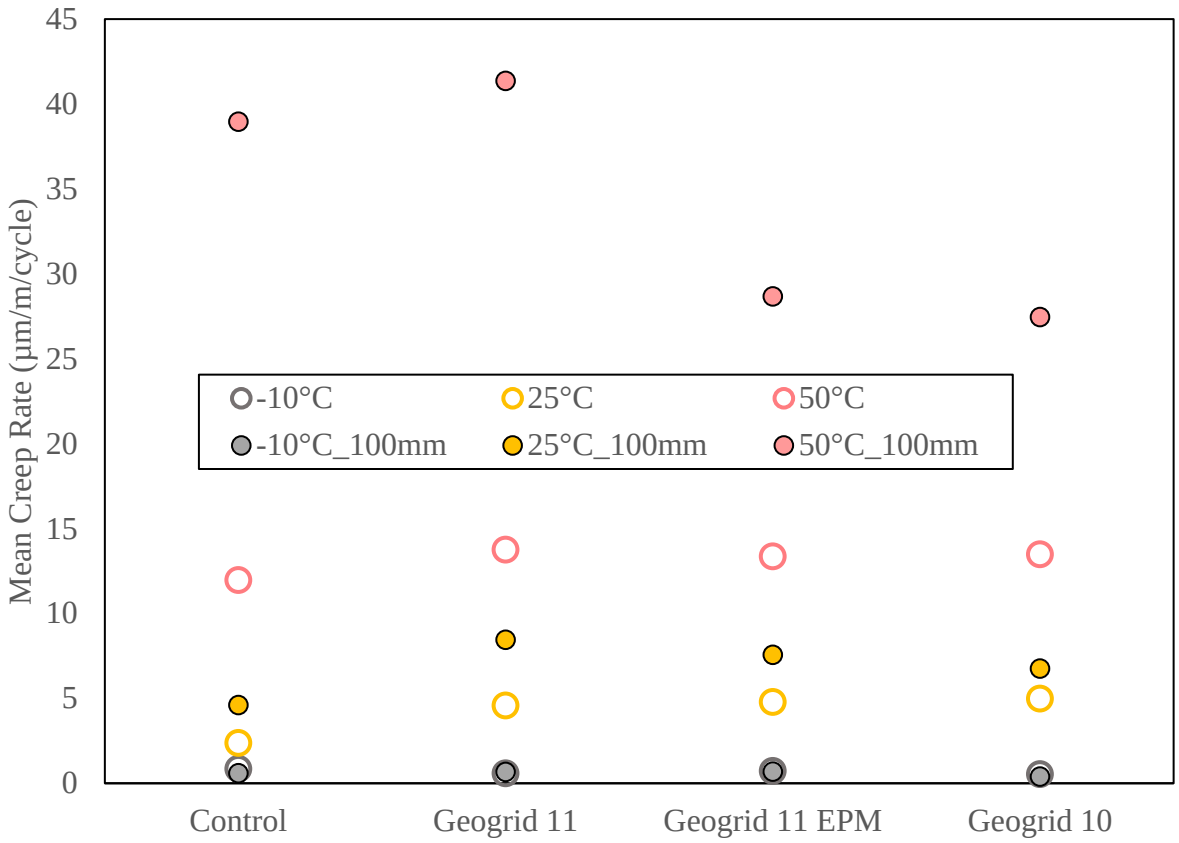

Figure 6-13 Mean Creep Rate Results for Specimens in Two Sizes

It can be seen from Figure 6-12 that the ultimate creep moduli for 100 mm samples consistently appear to be comparatively lower than those observed for the 150 mm samples, particularly noticeable under the 50°C temperature condition. Similarly, the findings in Figure 6-13 also demonstrate that the 100 mm samples exhibit a relatively faster rate of creep when compared to the 150 mm samples. These trends collectively suggest a potential discrepancy in the current understanding of the asphalt samples' creep behaviour, as stipulated by the standards outlined in AASHTO T378. A significant contributing factor to this observed variation in behaviour can be attributed to the absence of confinement surrounding the loaded area when the sample size is identical to the size of the loading plate. This lack of confinement fails to fully replicate the real-life field conditions that asphalt pavements are subjected to, thereby potentially leading to an overestimation of the samples' actual creep behaviour. Consequently, the current testing protocols, as per AASHTO T378, might not fully capture the comprehensive performance of the asphalt material under realistic traffic loading scenarios.

Meanwhile, a significant trend appears among samples in both sizes that the ultimate creep modulus decreases as the temperature increases. Subsequently, the asphalt samples creep faster as the temperature increases. This happens because asphalt is viscous-elastic material, which is sensitive to temperature. The decrease in the ultimate creep modulus with an increase in temperature can be attributed to the transition of asphalt's behaviour from a more elastic state to a closer approximation of a viscous material. At lower temperatures, asphalt tends to exhibit a more rigid behaviour, characterized by its higher capacity to resist deformation. On the contrary, as temperatures rise, the asphalt gradually shifts towards a more viscous phase, rendering it more susceptible to deformation under applied loads (P. Li, Jiang, Guo, Xue, & Dong, 2018). The testing results show that the temperature has a significant impact on the creep behaviour. In Figure 6-14 and Figure 6-15, the effect of temperature on mean creep rate and ultimate creep modulus were correlated and plotted, respectively.

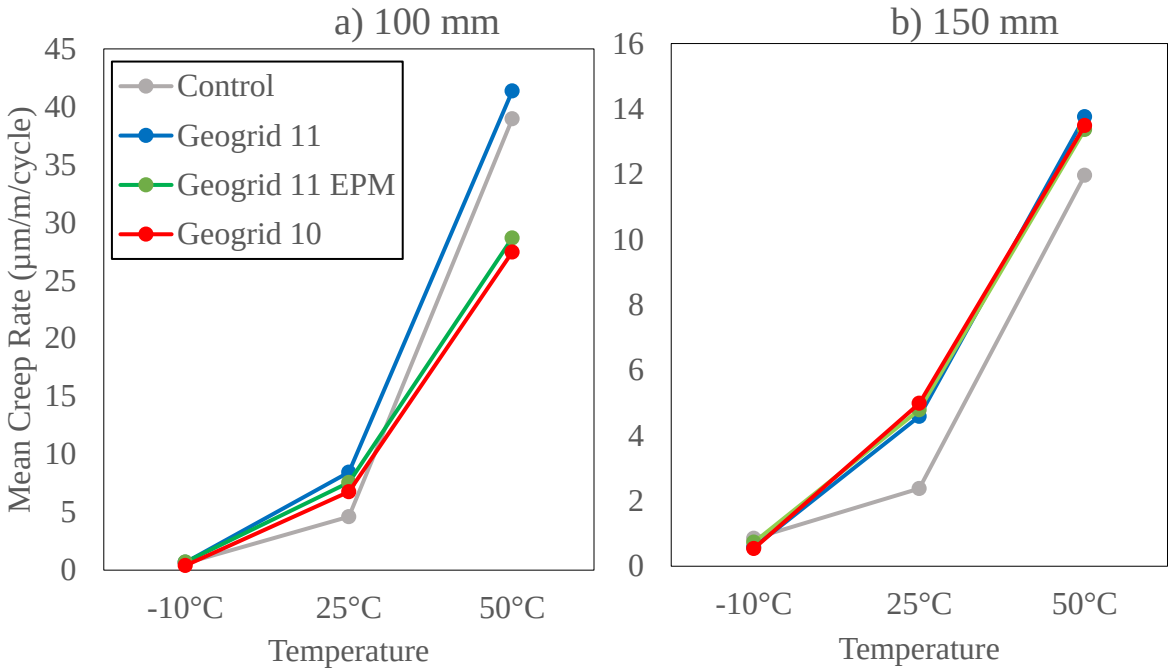

Figure 6-14 Effect of Temperature on Mean Creep Rate for Samples in Different Sizes

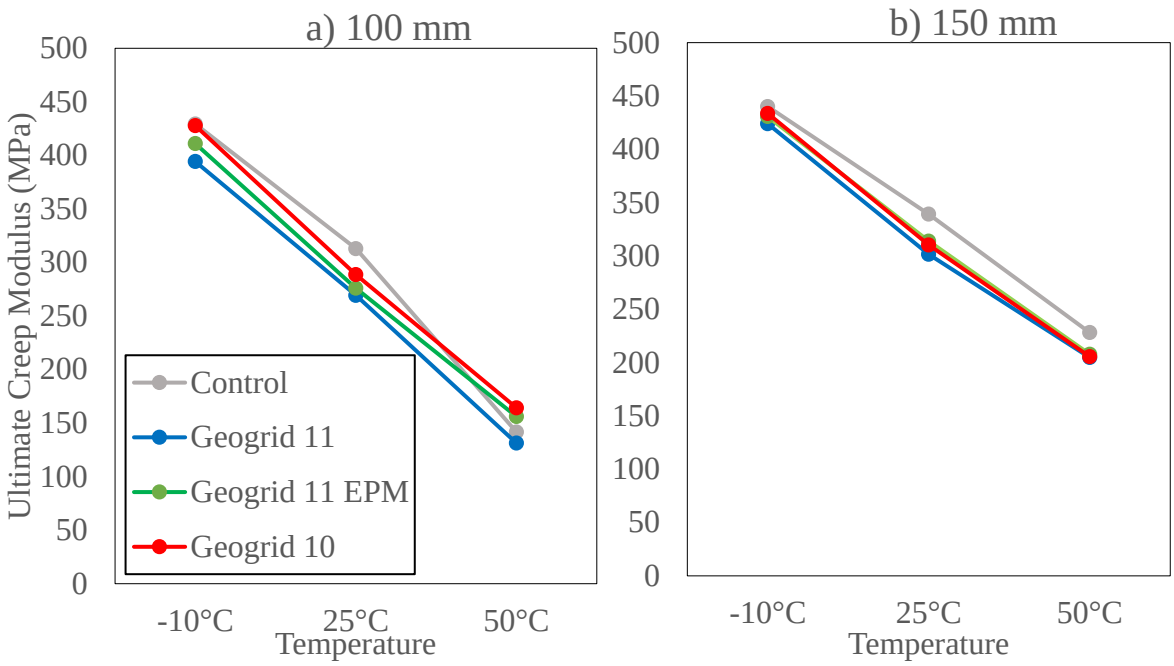

Figure 6-15 Effect of Temperature on Ultimate Creep Modulus for Samples in Different Sizes

In Figure 6-14, the following observations were made:

- The reinforced samples in both sizes crept faster than unreinforced samples (control) from -10 °C to 25 °C, which can be the reason that the reinforced samples have lower ultimate creep moduli than control samples in Figure 6-12.
- From 25 °C to 50 °C, the 100 mm samples reinforced by Geogrid 11 EPM and Geogrid 10 crept slower with a smaller slope than samples reinforced by Geogrid 11 and unreinforced samples. As the creeping of asphalt mixtures is more substantial under higher temperatures (D. A. Anderson, Petersen, & Christensen, 1986), it can be concluded that Geogrid 11 EPM and Geogrid 10 reinforcement can help to slow down asphalt mixtures creep. Geogrid 11 EPM is the same material as Geogrid 11 with an additional membrane bonding. The difference signifies the function of the extra bonding between asphalt and geogrid.
- For samples in 150 mm diameter, at 50 °C, the reinforced samples have a similar creep rate to unreinforced samples, which can be explained by the same slope from 25 °C to 50 °C in Figure 6-14 b). It can be concluded that embedded geogrid may cause asphalt samples to creep faster under lower temperatures, while it does not bring a negative effect under high temperatures.

Moreover, the results were analyzed by computing the standard deviation and coefficient of variances (CV). The CVs can represent the variation among samples of the sample type. Also, a one-way analysis of variance (ANOVA) was performed to evaluate the variances among results of different types. The analysis was based on a null hypothesis at a 95% significance level. The analysis results of the ultimate creep modulus for samples in 100 mm and 150 mm are listed in Table 6-3 and Table 6-4, respectively. The observations of the CVs of the ultimate creep modulus across all samples of the same type, consistently below 15%, provide strong evidence of the reliability and consistency of the obtained results, thereby validating the reliability of the experimental data and the accuracy of the conclusions drawn from the study. Despite the control samples exhibiting the highest creep modulus across most temperature conditions, except for the 100 mm diameter samples at 50 °C, the analysis based on the ANOVA reveals that the differences between the various types of asphalt specimens are not statistically significant, as indicated by the p-values exceeding 0.05. This suggests that the variations observed in the ultimate creep modulus values between the different sample types are likely within the expected range of experimental error and not significant enough to draw definitive conclusions that the asphalt mixtures reinforced by geogrids have significantly lower creep modulus.

The analysis results of the mean creep rate for samples in 100 mm and 150 mm are listed in Table 6-5 and Table 6-6, respectively. The CVs of the mean creep rate are higher than those of creep modulus, which signifies a more pronounced variation in the rate of creep across the samples. This emphasizes the significance of the variations in the creep rate among different experimental conditions, which could potentially influence the overall performance assessment of the asphalt samples. The ANOVA results reveal that the 100 mm-diameter samples do not show significant differences in creep rate between different types at -10 °C and 50 °C. In contrast, the 150 mm-diameter samples show significant differences in creep rate at 25 °C and 50 °C with p-values less than 0.05.

Table 6-3 Statistical Analysis of Ultimate Creep Modulus for Samples in 100 mm Diameter

	Mean (MPa)	Rank	CV (%)	Among Types	Different
-10°C					
Control	429.28	1	1%	0.366	N
Geogrid 11	394.17	4	7%		
Geogrid 11 EPM	410.91	3	7%		
Geogrid 10	427.69	2	2%		
25°C					
Control	312.85	1	3%	0.006	Y
Geogrid 11	269.21	4	3%		
Geogrid 11 EPM	275.83	3	4%		
Geogrid 10	288.60	2	2%		
50°C					
Control	141.58	3	25%	0.256	N
Geogrid 11	131.20	4	3%		
Geogrid 11 EPM	156.02	2	3%		
Geogrid 10	164.17	1	13%		

Table 6-4 Statistical Analysis of Ultimate Creep Modulus for Samples in 150 mm Diameter

	Mean (MPa)	Rank	CV (%)	Among Types	Different
-10°C					
Control	440.05	1	7%	0.686	N
Geogrid 11	423.88	4	4%		
Geogrid 11 EPM	430.63	3	12%		
Geogrid 10	433.55	2	10%		
25°C					
Control	339.09	1	1%	0.165	N
Geogrid 11	301.46	4	2%		
Geogrid 11 EPM	313.83	2	12%		
Geogrid 10	310.21	3	10%		
50°C					
Control	228.09	1	7%	0.109	N
Geogrid 11	204.70	4	6%		
Geogrid 11 EPM	207.79	2	12%		
Geogrid 10	205.49	3	8%		

Table 6-5 Statistical Analysis of Mean Creep Rate for Samples in 100 mm Diameter

	Mean (μm/m/cycle)	Rank	CV (%)	Among Types	Different
-10°C					
Control	0.59	2	38%	0.332	N
Geogrid 11	0.67	3	31%		
Geogrid 11 EPM	0.69	4	29%		
Geogrid 10	0.40	1	40%		
25°C					
Control	4.61	1	31%	0.020	Y
Geogrid 11	8.45	4	6%		
Geogrid 11 EPM	7.57	3	10%		
Geogrid 10	6.76	2	15%		
50°C					
Control	38.96	3	32%	0.148	N
Geogrid 11	41.36	4	7%		
Geogrid 11 EPM	28.67	2	5%		
Geogrid 10	27.46	1	31%		

Table 6-6 Statistical Analysis of Mean Creep Rate for Samples in 150 mm Diameter

	Mean (μm/m/cycle)	Rank	CV (%)	Among Types	Different
-10°C					
Control	0.85	4	19%	0.176	N
Geogrid 11	0.58	2	29%		
Geogrid 11 EPM	0.73	3	16%		
Geogrid 10	0.54	1	25%		
25°C					
Control	2.38	1	41%	0.016	Y
Geogrid 11	4.59	2	19%		
Geogrid 11 EPM	4.79	3	34%		
Geogrid 10	4.98	4	25%		
50°C					
Control	11.96	1	27%	0.750	Y
Geogrid 11	13.76	4	22%		
Geogrid 11 EPM	13.37	2	25%		
Geogrid 10	13.49	3	19%		

Despite the lack of significance of the ultimate creep modulus results, the findings suggest that the mean creep rate can serve as a valuable parameter for evaluating the effectiveness of geogrid-reinforced asphalt. It has also been supported that the mean creep rate is a more reliable indicator compared to the ultimate strain, considering the ultimate creep modulus was derived from the ultimate strain, as the ultimate strain depends on the initial strain (Airey, 2004). From the results, the unreinforced samples have the slowest creep rate, which can primarily be attributed to their slower deformation under low-temperature conditions, as discussed earlier.

6.5 Evaluation of Permanent Deformation

At 50 °C, after the first 150 loading cycles, the samples were continuously loaded until failure. Data collection at regular intervals, with deformation measurements taken every 66 cycles for the first 3000 cycles and subsequently every 1000 cycles, allowed for the compilation of average deformation data points. These data points were then averaged and plotted against the corresponding cycle numbers, as depicted in Figure 6-16 and Figure 6-17 for the 100 mm and 150 mm sample sizes.

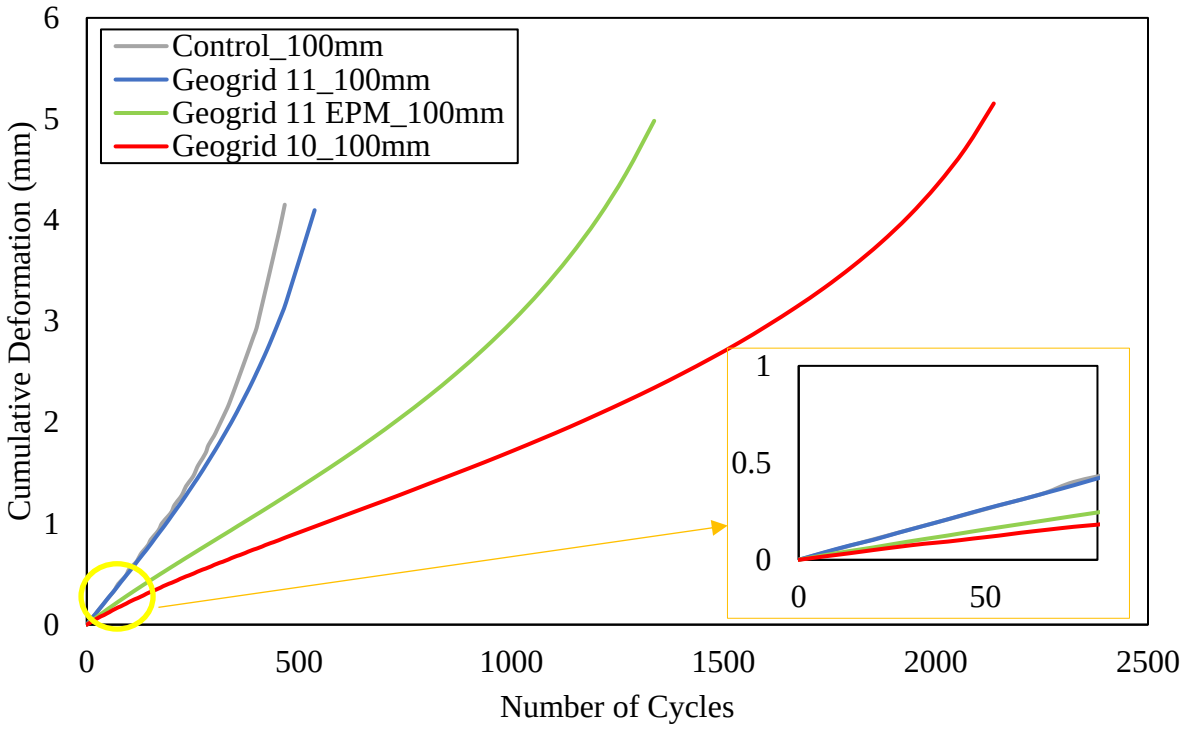

Figure 6-16 Permanent Deformation Curve for Samples in 100 mm Diameter

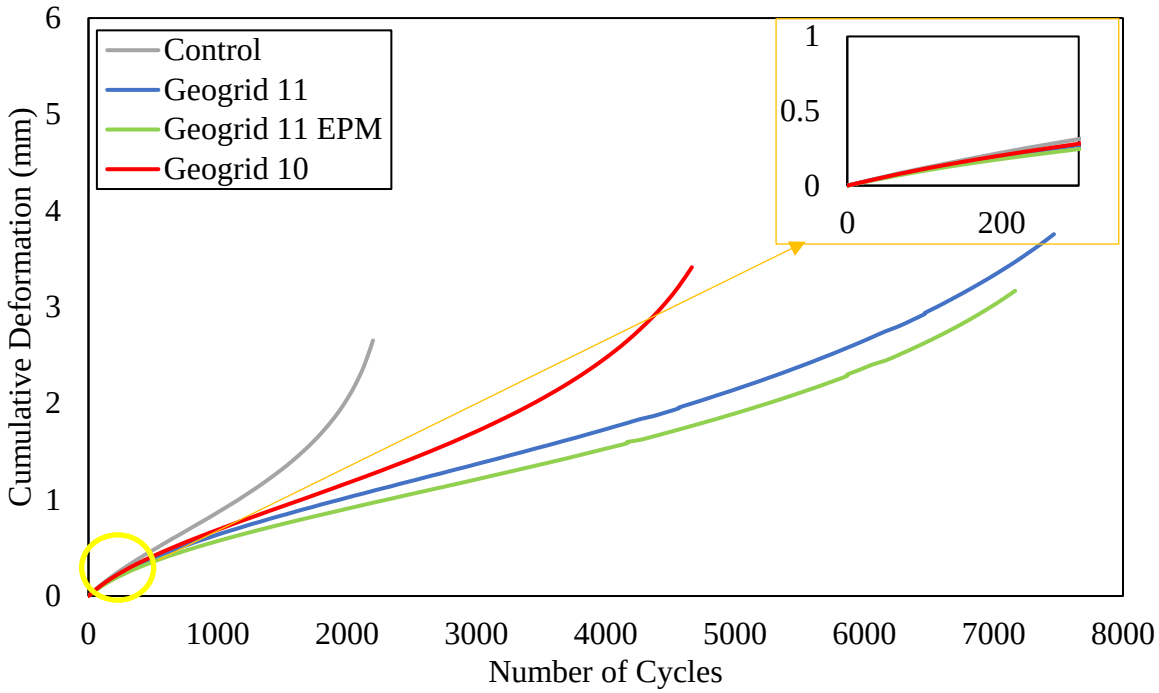

Figure 6-17 Permanent Deformation Curve for Samples in 150 mm Diameter

The analysis of Figure 6-17 reveals a noteworthy observation concerning the prolonged resistance to permanent deformation exhibited by the 150 mm-diameter samples. This observation serves to reinforce the notion that the current testing standards may tend to underestimate the permanent deformation resistance of asphalt mixtures, thereby emphasizing the importance of incorporating more comprehensive testing methodologies that accurately capture the full spectrum of material behaviour under extreme temperature conditions.

Moreover, the contrasting results observed in the failure times of the control samples, which exhibited the fastest failure, compared to the previous findings related to the mean creep rate, underline the complex nature of asphalt material behaviour and the critical influence of testing duration on the evaluation of creeping behaviour. This discrepancy indicates that the 50 cycles used in the mean creep rate analysis might not be sufficient to capture the complete picture of the asphalt mixtures' creeping behaviour accurately.

As mentioned, the slope in the secondary stage of the curve can be a good representative of the resistance to permanent deformation. From the results of samples in 100 mm diameter, the initial stage was short for all types of samples with the secondary stage immediately following to show. A more detailed examination of the zoomed-in figure allowed for a comprehensive evaluation of the first stage,

providing critical insights into the initial phase of the testing process. Notably, the analysis of 100 mm-diameter samples revealed that the control samples and Geogrid 10 samples exhibited a similar duration in reaching the secondary stage, indicating comparable initial responses under the testing conditions. On the other hand, the samples featuring Geogrid 11 EPM and Geogrid 10 demonstrated a slightly longer period to transition to the secondary stage. From the results of 150 mm-diameter samples, all samples have similar slopes in the primary stage, which also signifies the proposed protocol can ensure consistency in evaluating the secondary stage.

From the pictures taken on failed samples as shown in Figure 6-18, the resistance of crack propagation provided by the geogrid in the middle can be clearly identified.

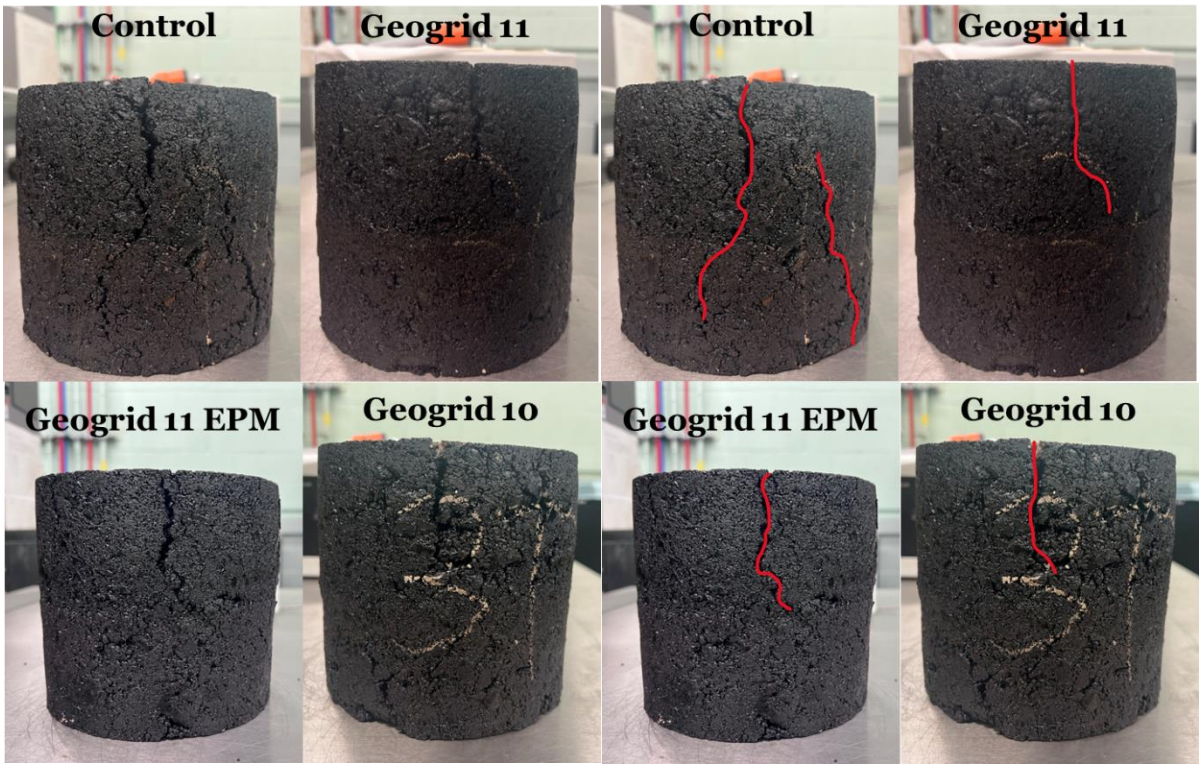

Figure 6-18 Samples in 150 mm Diameter After Failure

The results from samples of both sizes also reveal that the fibreglass geogrid, serving as reinforcement, can help improve resistance to permanent deformation, thereby extending the asphalt's rutting life. Further examination of the cumulative deformation data highlighted substantial differences, primarily occurring during the secondary stage. This is evidenced by the varying slopes associated with the different sample types. These differing slopes signify distinct rates of deformation and emphasize

the functional impact of geogrids on the overall deformation behaviour during the secondary stage. The variations observed in the secondary stage indicate the significant impact of the geogrid type on the deformation characteristics of the asphalt mixtures, further underscoring the importance of selecting appropriate geogrid materials that effectively contribute to the enhanced mechanical properties and long-term performance of asphalt pavements.

For samples with a 100 mm diameter, those embedded with Geogrid 11 exhibited slightly better performance than control samples, while samples with Geogrid 11 EPM demonstrated better resistance to permanent deformation, as evidenced by the smaller slope in the secondary stage compared to Geogrid 11. With the fibreglass geogrid configuration used in both materials, the additional polymeric membrane offering extra bonding can be the reason for extending the rutting life.

On the other hand, the examination of the 100 mm diameter samples featuring Geogrid 10, has revealed their superior potential in resisting permanent deformation. This finding suggests that geogrids with smaller apertures possess the capacity to provide more effective reinforcement by facilitating a strong interlocking mechanism within the asphalt mixtures. The smaller aperture size likely enables a more secure bonding between the geogrid and the surrounding asphalt mixes, thereby enhancing the material's resistance to permanent deformation under applied loads.

Conversely, the assessment of the 150 mm diameter samples highlights a relatively lower potential for resisting permanent deformation when using Geogrid 10. This comparison implies that geogrids with larger apertures might exhibit superior performance characteristics when the loading area is adequately confined. The presence of such confinement surrounding the loading area could optimize the distribution of stresses and strains, allowing geogrids with larger apertures to effectively reinforce the asphalt mixtures and improve their resistance to permanent deformation.

Additionally, the flow number was also computed using the ASU fitting model. The results are shown in Figure 6-19, which once again corroborate the prevalent underestimation of the flow number using the current testing protocol. Notably, 150 mm samples with Geogrid 11 EPM display considerable variability, primarily attributed to a single replication that did not undergo essential failure. This discrepancy highlights the necessity for quality control measures of geogrid-embedded asphalt samples to ensure the reliability and consistency of experimental data. Geogrid 10 and Geogrid 11 samples (150 mm) have similar flow numbers, while the resultant curve in Figure 6-17 suggests that Geogrid 11 samples have a larger slope in the secondary stage. Overall, the control samples consistently

demonstrate the poorest performance with a significantly smaller flow number, which highlights the critical role of geogrid reinforcement in effectively extending the rutting life of asphalt pavements.

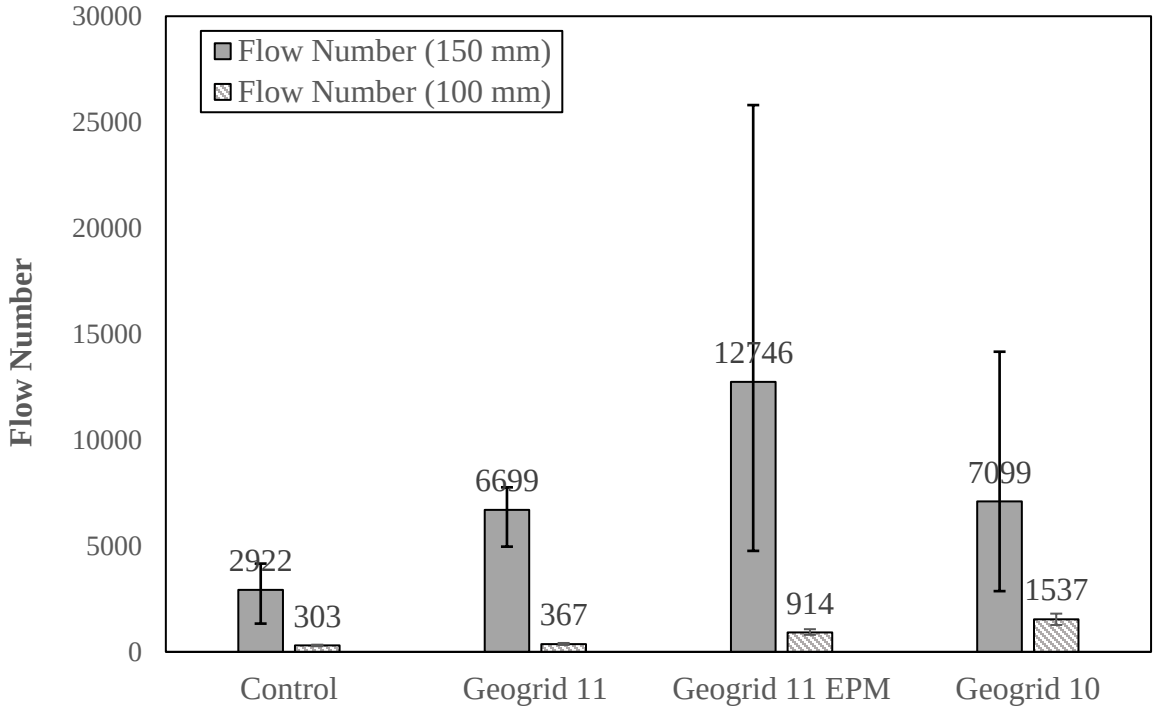

Figure 6-19 Flow Number Results for Samples in Diameter 100 mm and 150 mm

Furthermore, the mean creep rates and the ultimate creep moduli were also computed after failure in Figure 6-20 and Figure 6-21, respectively. The comprehensive evaluation of the mean creep rate results provides a representative reflection of the resultant curves. In the case of the 150 mm samples, the unreinforced specimens exhibited the fastest creep rate, followed sequentially by samples featuring Geogrid 11, Geogrid 10, and finally Geogrid 11 EPM. This clear progression in the creep rates highlights the significant influence of geogrid reinforcement on mitigating the rate of deformation in asphalt mixtures. A notable contrast emerges between the results of the mean creep rate and the flow number, with the Geogrid 10 samples exhibiting a higher creep rate than the Geogrid 11 samples, aligning closely with the slopes observed in the corresponding curves. Furthermore, in the context of the 100 mm samples, the unreinforced specimens consistently displayed the highest creep rate, while the Geogrid 11 EPM and Geogrid 10 samples exhibited the slowest rates of creep.

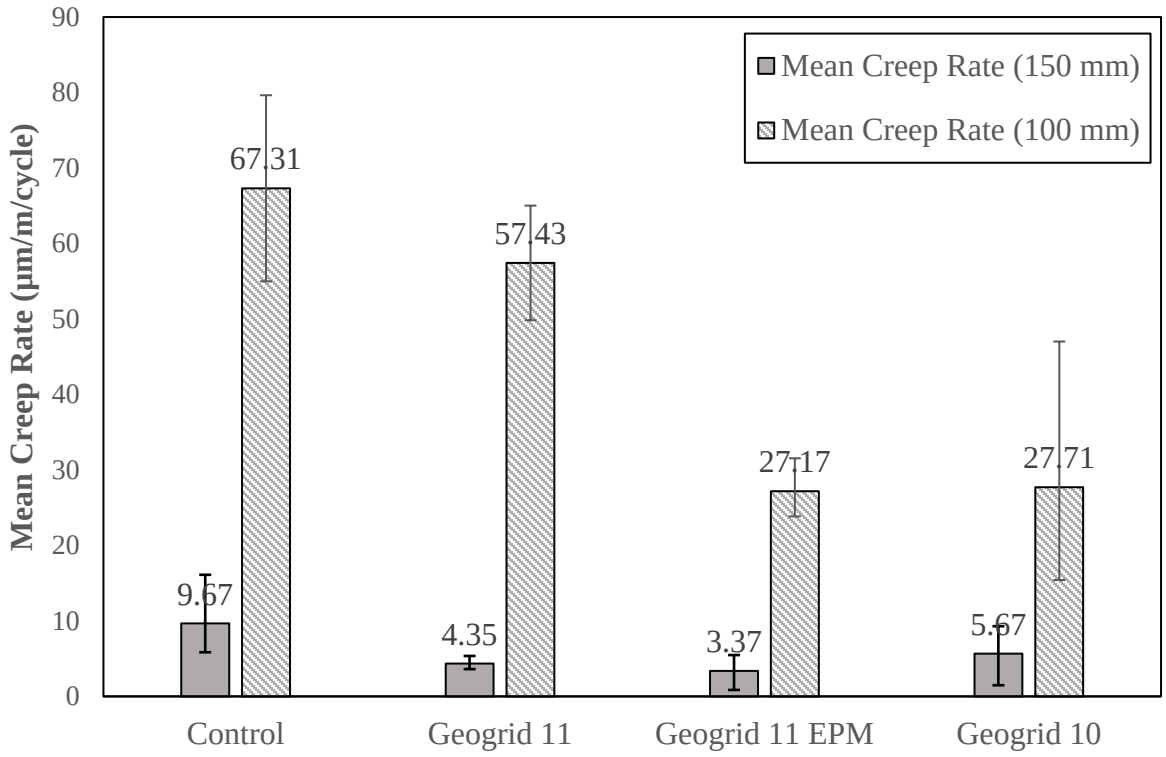

Figure 6-20 Mean Creep Rate in Diameter 100 mm and 150 mm Until Failure

However, the ultimate creep modulus results show similar results among different types of samples. The analysis of the ultimate creep modulus data reveals some inconsistencies among the different sample types, indicating a discrepancy between the results derived from this parameter and those obtained from other analyses. Notably, the 150 mm control samples demonstrate a higher creep modulus compared to the Geogrid 11 samples, contradicting the trends observed in the other analyses. Similarly, in the case of the 100 mm samples with Geogrid 10, the ultimate creep modulus suggests relatively poor performance, while the flow number and mean creep rate analyses suggest the opposite. These discrepancies serve to validate the aforementioned assertion that the mean creep rate serves as a more reliable indicator compared to the ultimate creep modulus, primarily due to its independence from the initial strain. The ultimate creep modulus, being derived from the ultimate strain, is inherently influenced by the initial strain, which can sometimes lead to inconsistencies in the interpretation of the material's deformation behaviour. On the other hand, the mean creep rate, being a more direct measure of the rate of deformation, offers a clearer and more representative understanding of the material's performance characteristics, particularly in response to applied loads and varying environmental conditions.

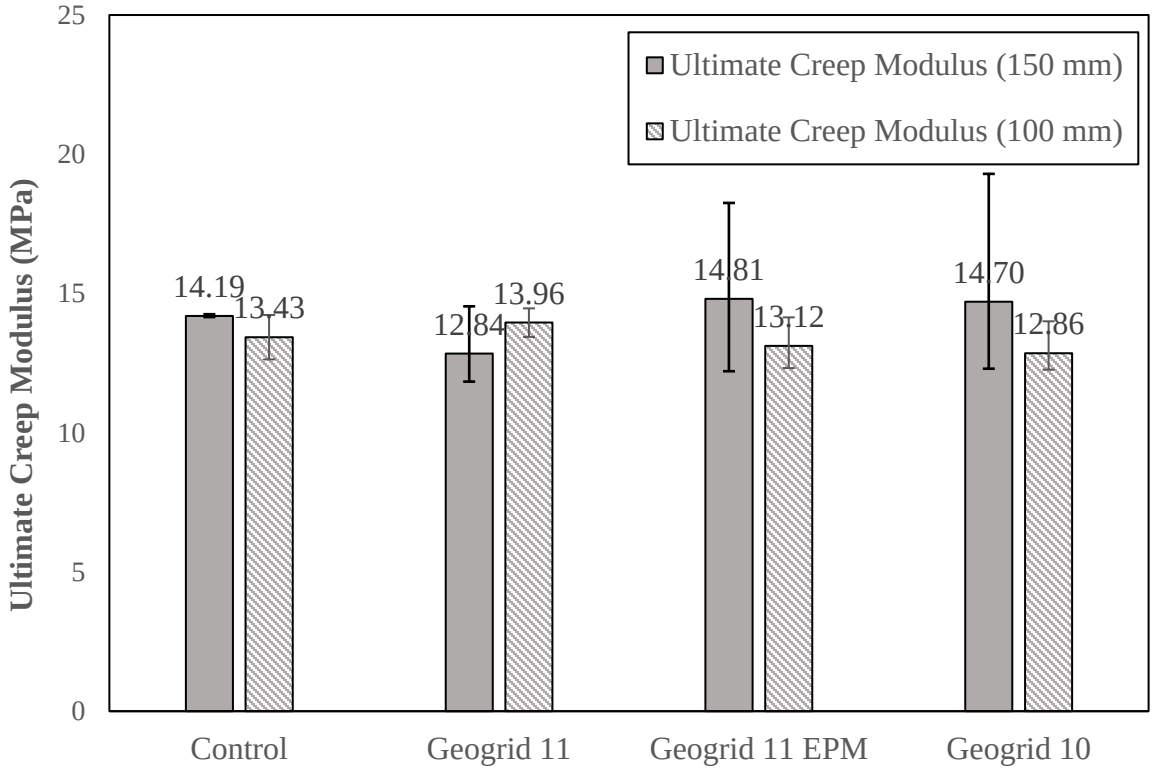

Figure 6-21 Ultimate Creep Modulus in Diameter 100 mm and 150 mm Until Failure

6.6 Evaluation of Moisture Susceptibility

A separate set of 150-diameter samples underwent preconditioning through a freeze-thaw (F-T) cycle before undergoing the actual dynamic creep test to evaluate the moisture susceptibility. The resultant curves were plotted in Figure 6-22. The uniformity of the initial stage across all four types of samples, as depicted in the figure, establishes a crucial foundation for the reliable comparison of the secondary stage and facilitates an accurate evaluation of the asphalt mixtures' potential to resist permanent deformation.

The comparative analysis of Figure 6-17 and Figure 6-22 provides valuable insights into the overall impact of the freeze-thaw process on the service life of the asphalt samples. The observed shortening of the general life for the freeze-thawed samples highlights the detrimental effects of moisture damage on the material's performance. This critical finding emphasizes the need for proactive measures and effective mitigation strategies to address the challenges posed by moisture-induced damage in asphalt pavements, particularly in regions characterized by fluctuating temperature conditions and exposure to varying environmental elements.

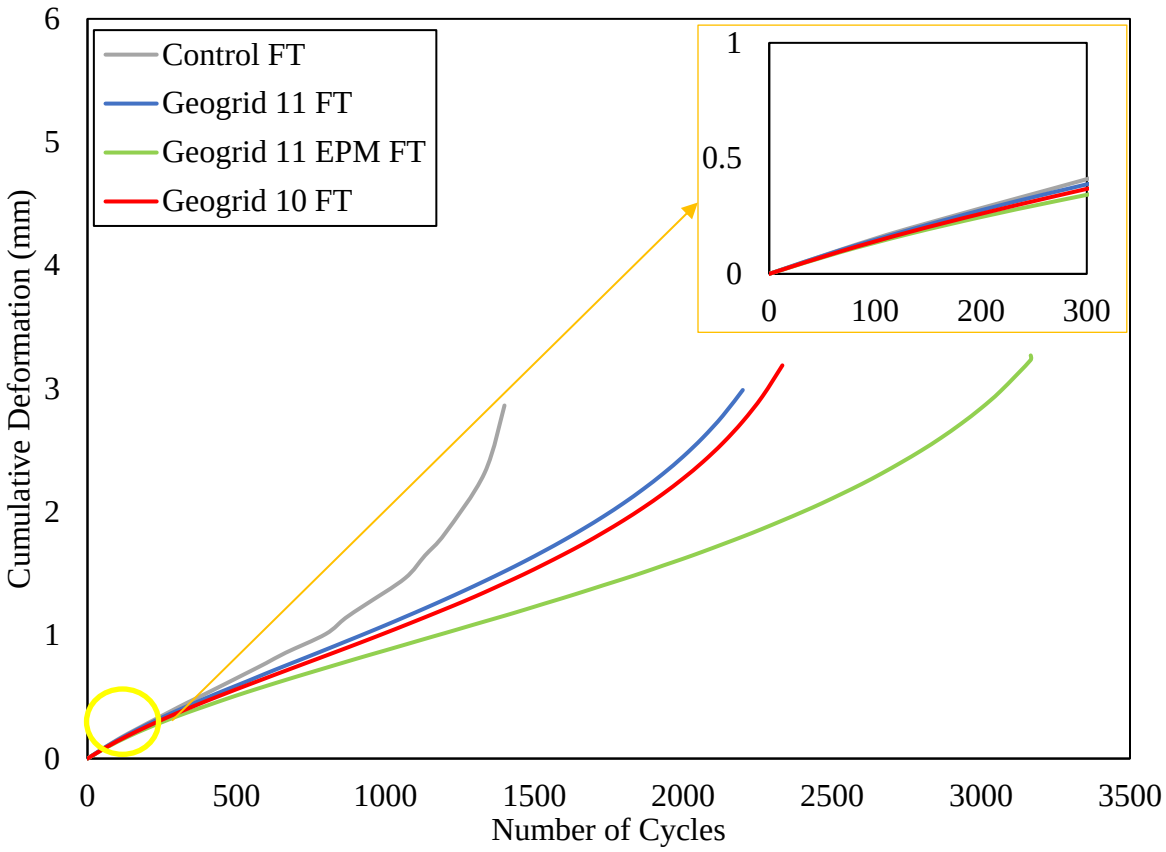

Figure 6-22 Permanent Deformation Curve for 150 mm Diameter Samples with Freeze-Thaw Conditioning

Moreover, the same analyses were conducted to compute flow numbers, with the results presented in Figure 6-23, alongside the results of the samples that did not undergo freeze-thaw conditioning for comparison. Again, it can be seen that the flow number significantly decreased after the samples were freeze-thawed. Meanwhile, the control samples still have the lowest flow number, while the samples with Geogrid 11 and Geogrid 11 EPM have the highest flow number. This signifies the crucial role of geogrid in reinforcing samples with moisture damage. Geogrid 11 EPM, with its superior performance compared to Geogrid 11, demonstrated a positive impact on reinforcing the asphalt samples, owing to the additional membrane. Also, in contrast to the samples without freeze-thaw conditioning, the Geogrid 11 samples showed a higher flow number than the Geogrid 10 samples, which indicates that fibreglass geogrid with larger apertures could provide better reinforcement to asphalt samples susceptible to moisture damage.

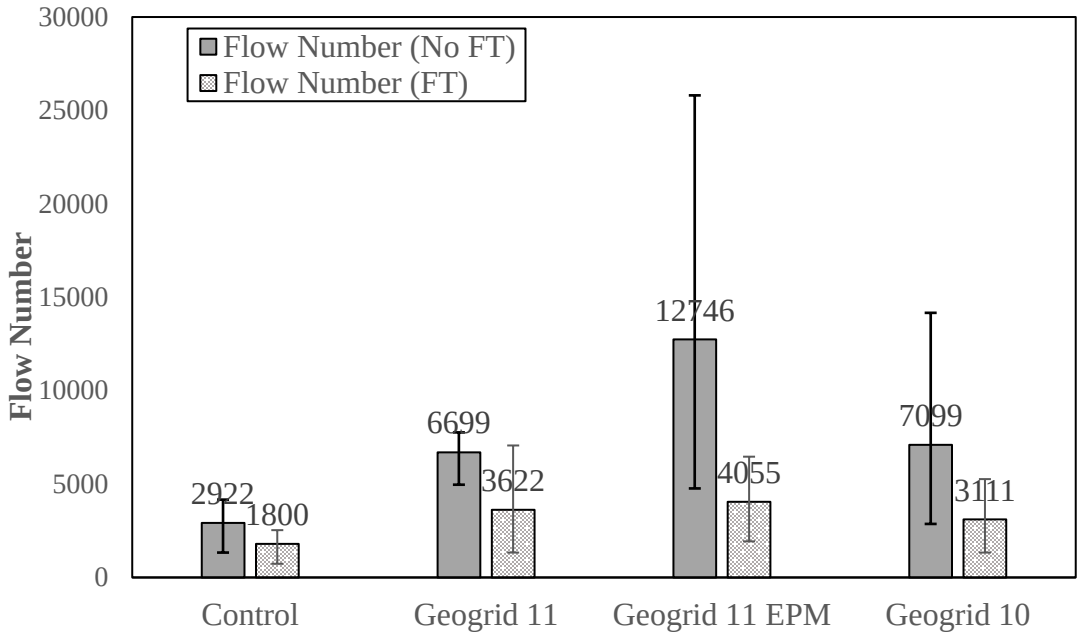

Figure 6-23 Flow Number Results of 150 mm Diameter Samples with and without Freeze-Thaw Conditioning

Another notable finding emerged from the comparison of the flow numbers between the FT samples and the 150 mm samples. Despite the absence of freeze-thaw cycles in the 100 mm samples, indicating the lack of exposure to moisture damage, the 150 mm samples still demonstrated higher flow numbers. This strengthens the conclusion that the current testing protocol, involving smaller samples without surrounding confinement, could potentially lead to underestimation.

Mean creep rate and ultimate creep modulus were computed and shown in Figure 6-24 and Figure 6-25, respectively, together with results of 150 mm samples without FT. The comparative analysis between the FT and non-FT samples highlights a clear pattern, with the FT samples exhibiting a higher creep rate and a lower ultimate creep modulus, indicative of the pronounced influence of moisture-induced damage resulting from the FT process. Samples without reinforcement have the highest creep rate and the lowest ultimate creep modulus, while the Geogrid 11 EPM samples have the best performances after FT, followed by the Geogrid 11 samples. Such findings indicate that the geogrid with larger apertures can provide significant reinforcement benefits to asphalt samples in enhancing the material's resistance to moisture-induced damages.

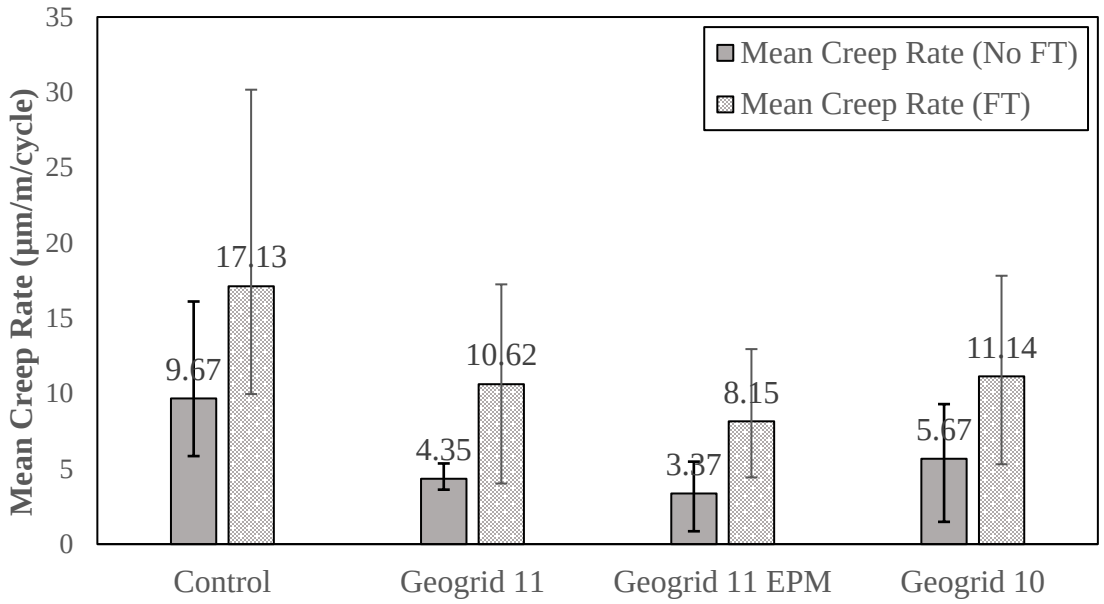

Figure 6-24 Mean Creep Rate Results Until Failure of 150 mm Diameter Samples with and without Freeze-Thaw Conditioning

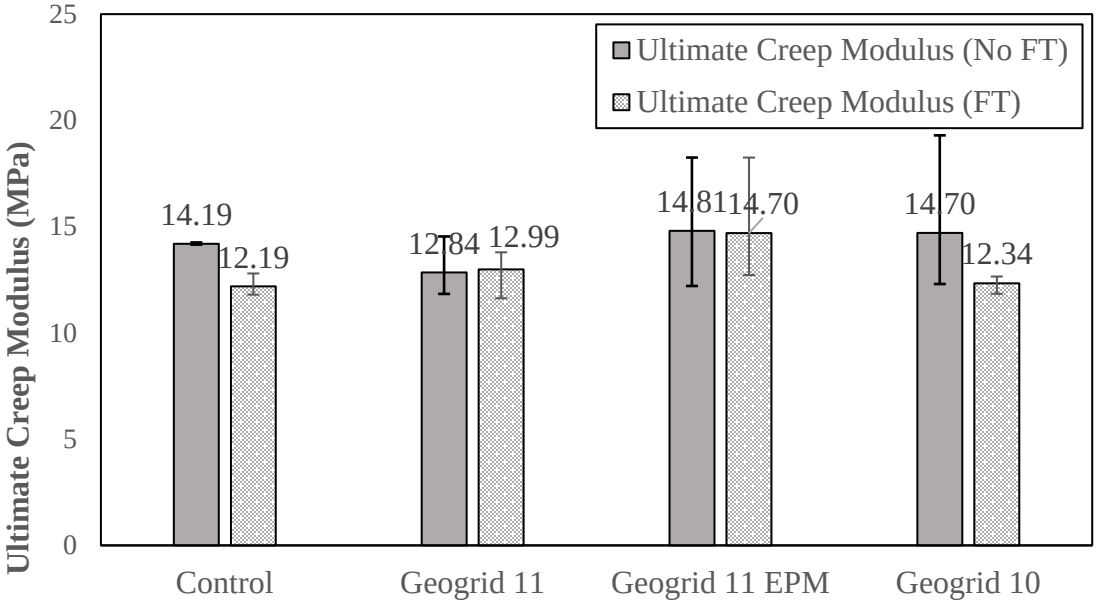

Figure 6-25 Ultimate Creep Modulus Results Until Failure of 150 mm Diameter Samples with and without Freeze-Thaw Conditioning

A student's t-test was also performed on the three indicators that represent the potential of resisting permanent deformation between the results of samples with and without FT, based on a null hypothesis

at a 95% significance level, whose results are listed in Table 6-7. The findings derived from the two-tailed p-values, with values of flow number and mean creep rate falling below the threshold of 0.05, provide compelling evidence of the significant differences between the freeze-thawed and non-freeze-thawed samples. This statistical validation indicates the effectiveness of the adopted freeze-thaw process in inducing moisture damage within the samples. The p-value of ultimate creep modulus showing no significant difference (> 0.05) further validates the lower level of reliability of such an indicator.

Table 6-7 Student's T-Test Analysis on Samples With/Without FT

Analyzed Indicator	P(T<=t)
Flow Number	0.034
Mean Creep Rate	0.027
Ultimate Creep Modulus	0.103

6.7 Chapter Summary

In summary, this study provides a comprehensive laboratory study on the resistance to permanent deformation and moisture damage of geogrid-embedded asphalt samples. A dynamic creep test was developed based on the current AASHTO T378 standard, in which the specimens are prepared with the same diameter as the loading plate. In this study, apart from the standardized testing, larger samples were prepared with the loading plate penetrating into the samples so that the surrounding asphalt could serve as confinement. The samples were first conditioned and tested under -10 °C, 25 °C, and 50 °C. The following conclusions can be made:

- The lower ultimate creep modulus and faster mean creep rate of 100 mm samples (compared with 150 mm samples) indicate the importance of re-evaluating the existing testing methodologies and standards to ensure that they accurately reflect the in-situ conditions and behaviour of asphalt pavements.
- A significant trend appears that the ultimate creep modulus decreases as the temperature increases. Subsequently, the asphalt samples creep faster as the temperature increases. The temperature-induced changes in the viscoelastic properties of asphalt have implications for the performance and durability of asphalt pavements, particularly in regions where temperature fluctuations are commonplace.

- Despite the lower ultimate creep modulus and the faster creep rate of reinforced samples under different temperatures, the statistical analysis showing no significant differences indicates the 50 cycles may not be sufficient to observe the creep behaviour. Meanwhile, the lower ultimate modulus was mainly caused by the fast mean creep rate under lower temperatures, while the creeping of asphalt mixtures is more substantial under higher temperatures.

Under 50 °C, the samples were loaded until failure, while the following conclusions can be made:

- The insights derived from the poorer performances of 100 mm samples emphasize the necessity of implementing extended testing protocols to better understand the deformation mechanisms and long-term performance characteristics of asphalt materials, especially under high-temperature conditions.
- The findings from samples of both sizes demonstrate that the fibreglass geogrid, utilized for reinforcement, aids in enhancing resistance to permanent deformation, thus extending the asphalt's resistance to rutting. Visual observation also reveals that the fibreglass geogrid can effectively resist the propagation of top-down cracking.
- Samples in 100 mm diameter with Geogrid 10 have the best potential to resist permanent deformation, while it has a lower potential in 150 mm diameter compared with Geogrid 11 EPM. These contrasting observations emphasize the critical influence of the geogrid's aperture size on its reinforcement efficacy and its ability to mitigate permanent deformation in asphalt pavements.
- It was proved that the ultimate creep modulus was not as reliable as the mean creep rate, with the contrasting observation against the resultant curves and flow number analysis. It is crucial to integrate multiple assessment criteria and consider the relative strengths and limitations of each parameter.

Finally, another set of 150 mm samples was conditioned with a proposed freeze-thaw process to induce moisture damage to the asphalt samples. The following conclusions can be made:

- The moisture susceptibility of asphalt mixtures is a critical parameter in evaluating the material's performance and durability, particularly in regions where temperature fluctuations and varying weather conditions are prevalent. By subjecting the samples to the freeze-thaw process, the study effectively simulates the negative effects of moisture and subsequent

freeze-thaw cycles, providing critical insights into the material's susceptibility to moisture-induced damage.

- The results demonstrate that the samples without any form of reinforcement consistently display the highest creep rate and the lowest ultimate creep modulus, underscoring the vulnerability of unreinforced asphalt samples to moisture-induced damage and deformation under environmental stresses.
- The observed better performance in the Geogrid 11 samples undergone FT compared to the Geogrid 10 samples provides compelling evidence to support the notion that fibreglass geogrids with larger apertures can indeed offer superior reinforcement to asphalt samples that are susceptible to moisture-induced damages. By demonstrating a higher flow number, a slower creep rate, and a higher creep modulus, the Geogrid 11 samples underscore their superior capacity to mitigate the detrimental impacts of moisture-induced damages and effectively resist the development of rutting and other forms of deformation.
- The Geogrid 11 EPM samples show the best performances. With the same fibreglass geogrid materials used in Geogrid 11, the additional bonding plays a critical role in reinforcing asphalt samples and mitigating the adverse effects of moisture-induced damage, ultimately contributing to the development of more resilient and durable asphalt pavements capable of withstanding the challenges posed by varying environmental conditions and traffic loads.

Chapter 7
Evaluation and Monitoring of Pavement Structural Capacity by Field Testing

7.1 Introduction

In this chapter, field testing was conducted to evaluate the pavement performance. Stiffness was measured in the field during construction on compacted subgrade, granular base, asphalt binder course, and asphalt surface course. The tested results were compared with laboratory testing in Section 4.3.

For in-service pavements, visual inspection was done monthly to inspect any distress. Stiffness was measured every season from the completion of construction (August 2022) to one year after (August 2023) to evaluate the structural capacity of the three trial sections. Roughness is one critical indicator of pavement conditions. A profiler was used to measure the roughness of the pavement in August 2022, November 2022, and April 2023. Statistical analyses were conducted on the measurements to evaluate the variances. In addition, utilizing the instrumentation, a driving test was also performed in August 2022 and August 2023. The driving test can aid in evaluating the mechanical responses of identical traffic loading on the trial sections.

Also, considering the impact of temperature on pavement stiffness, especially on asphalt concrete, the tested results were correlated with pavement temperatures measured by the temperature sensors.

7.2 Testing Equipment and Methodology

The equipment used for evaluating and monitoring the pavement performance by field testing was introduced in this section, including the visual condition inspections to detect the development of surface distresses on the pavement, Light Weight Deflectometer (LWD) used for stiffness evaluation and SurPro used for roughness measurement. A driving test was proposed to capture the mechanical response caused by heavy traffic using instrumentation.

7.2.1 Light Weight Deflectometer

Light Weight Deflectometer (LWD) is a portable device that conducts non-destructive testing on pavement and soils. It drops a lighter weight (15 kg) onto the tested surface. The “light” weight can be raised at the height of 1 m and secured by a lock attached to a rod. The weight can be then dropped by a release handle after the device is ensured to be levelled and properly seated. The falling weight can

produce dynamic stress through a circular plate at the bottom of the device, which is transmitted to the underlying structure. The response can be measured as the deflection by the equipped center geophone, by which the stiffness can be computed. Computation theory follows Boussinesq's Equation as shown in Equation 7-1.

Equation 7-1

$$E_0 = \frac{f \times (1 - v^2) \times \sigma_0 \times a}{d_0}$$

where:

E_0 = surface deflection modulus (MPa)

f = factor for stress distribution (= 2 for uniform distribution)

v = Poisson's ratio (= 0.35)

σ_0 = stress under the plate (kN)

a = radius of plate (mm) (150 mm for unbound material; 100 mm for asphalt concrete)

d_0 = center deflection (μm)

The outputs can be transferred to the equipped laptop immediately so that reliable results can be ensured with at least three consistent outputs at one testing spot. Two alternative circular bearing plates can be switched. A 300-mm diameter plate was used on unbound materials, and a 200-mm diameter plate was used on asphalt surfaces.

During construction, two evenly distributed spots were tested in each section on compacted subgrade and granular base. After the placement of the asphalt binder course and asphalt surface course, the tests were performed on both the left wheel path (LWP) and right wheel path (RWP) on the westbound lane. LWD test was performed every 5 m along the lane on both wheel paths on the binder course and surface course, as shown in Figure 7-1. After construction completion, LWD was performed seasonally (summer 2022 to summer 2023) on in-service pavement. Similar to the testing plan during construction, the test was performed on both wheel paths every 5 m. Additionally, the test was also performed on the eastbound lane, as shown in Figure 7-2.

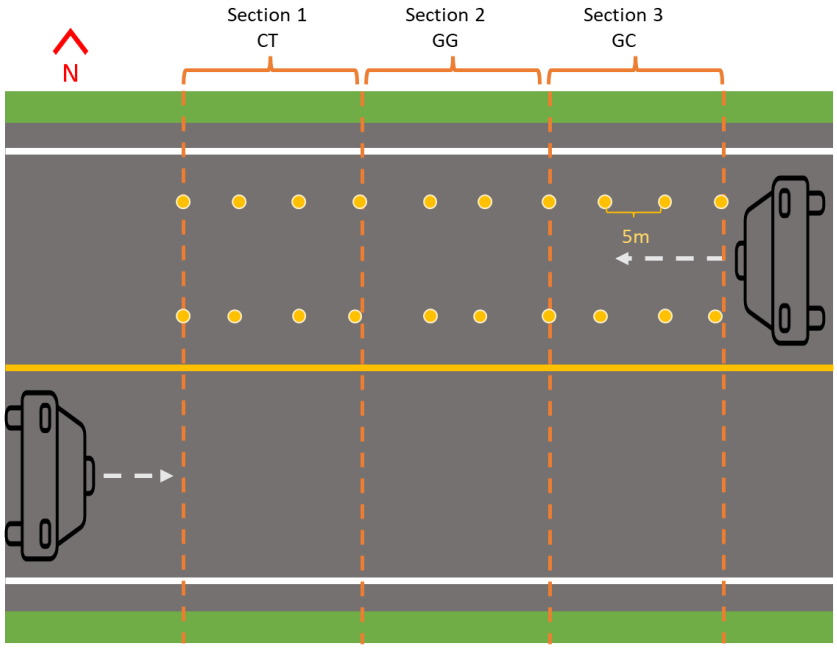

Figure 7-1 LWD Testing Points on Asphalt Surface During Construction

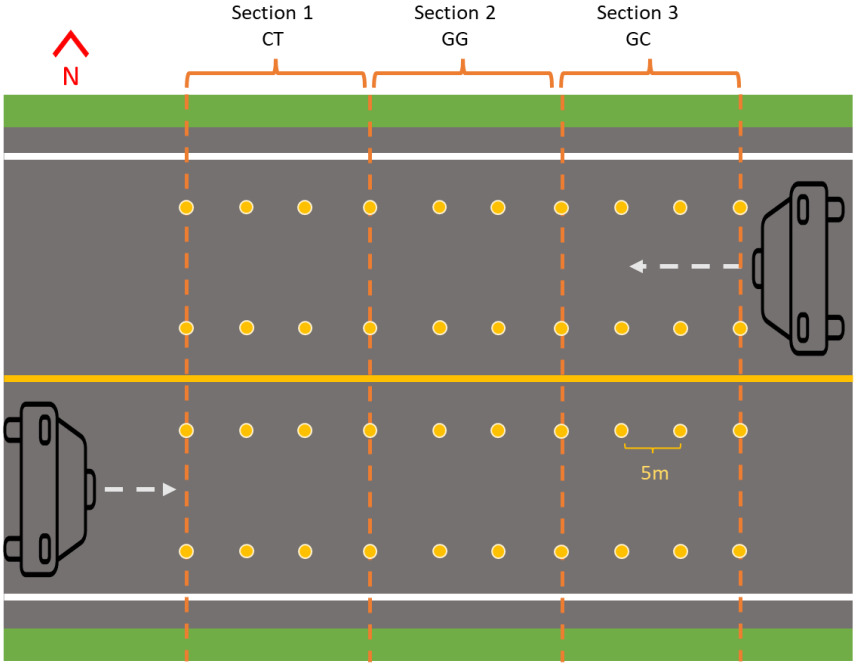

Figure 7-2 LWD Testing Points on In-Service Pavement

7.2.2 SurPro

Pavement roughness is one of the threshold performance criteria to assess pavement conditions in Ontario (MTO, 2019). Pavement roughness can reflect unevenness and irregularity of the pavement, which can be due to various distresses, wearing and tearing caused by traffic and environmental factors, as well as poor construction and material quality. The roughness of a road surface can affect fuel consumption, vehicle maintenance costs, as well as the comfort of drivers. Therefore, it is an important factor to be evaluated to better monitor the pavement performance.

The International Roughness Index (IRI) is a standardized indicator to quantify the roughness of pavements, which is commonly used in North America. It is typically measured using a profilometer, which obtains IRIs by analyzing the vertical movement of the equipment when it was travelling along the longitudinal road. An IRI of 0 m/km represents a completely smooth road surface, while the higher the IRI the rougher the surface is. Based on Sayers (1998), the following figure illustrates different IRI ranges corresponding to various types of pavements (Sayers & Karamihas, 1998).

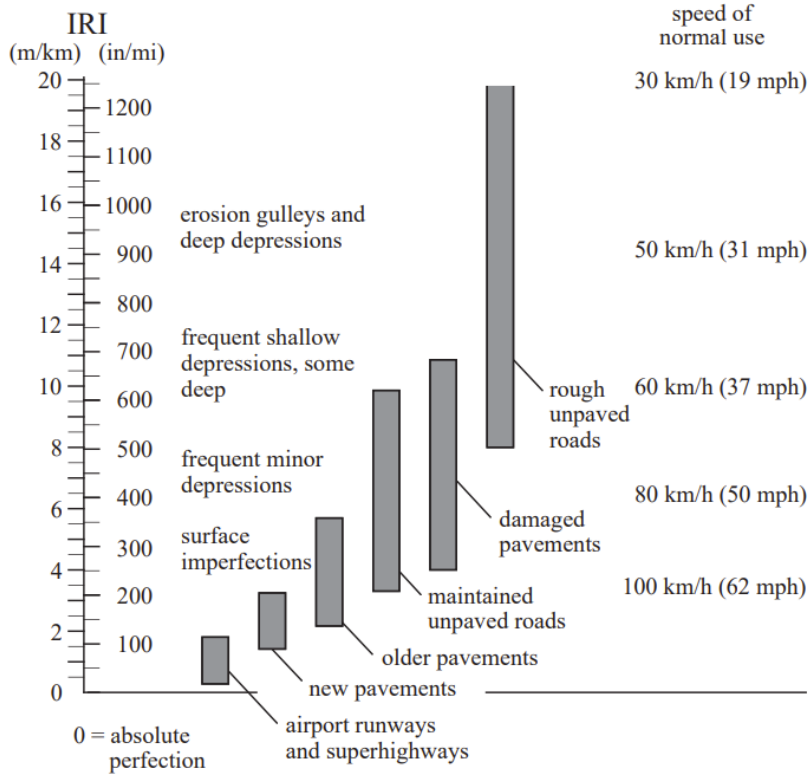

Figure 7-3 IRI Ranges for Different Classes of Road (Sayers & Karamihas, 1998)

In this study, SurPro 3500 was used as a walking profiler to measure the roughness by walking the equipment at walking speed (<2.5 m/s). The equipment is fully automated with spaced wheels. The data was sampled at an interval of 25 mm. The software, ProVAL, provided by the FHWA, was used to analyze the profile data.

The roughness of asphalt pavement (binder course and surface course) was measured during construction, as well as after construction in winter 2023 and spring 2023. Both LWP and RWP on both lanes were tested by walking the device two times on each wheel path. The testing plan is illustrated in Figure 7-4.

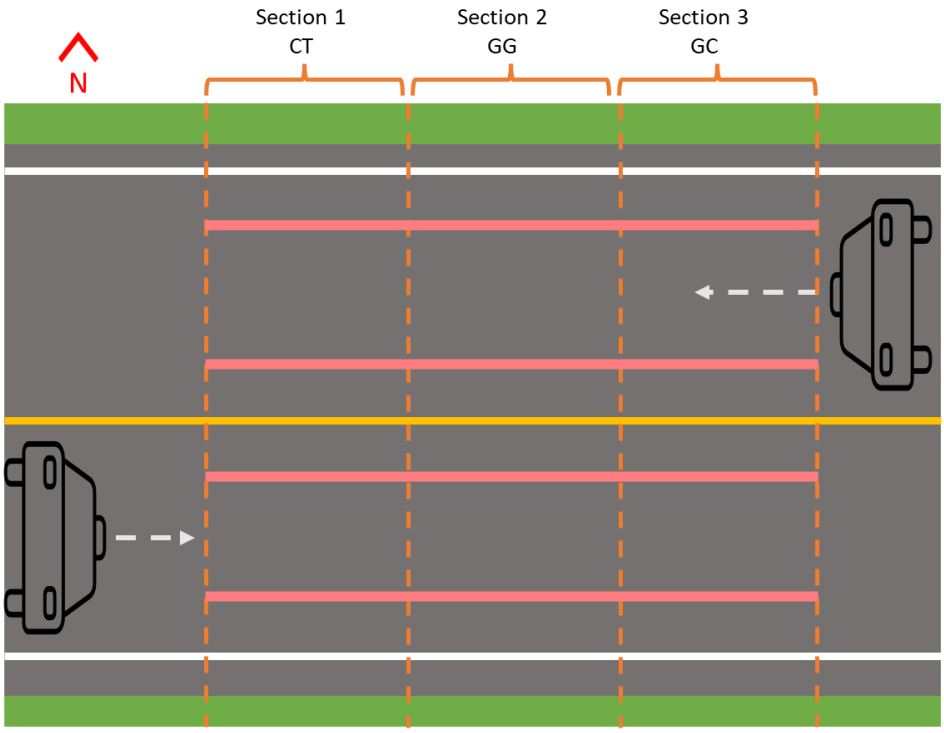

Figure 7-4 SurPro Testing Plan

7.2.3 Driving Test

A driving test was performed on the test sections in summer 2022 and summer 2023, by having a dump truck driving slowly on the instrumented lane so that the sensors could capture the mechanical responses of the pavement. The truck that was loaded and unloaded materials was driven considering two scenarios, as shown in Figure 7-5 and Table 7-1.

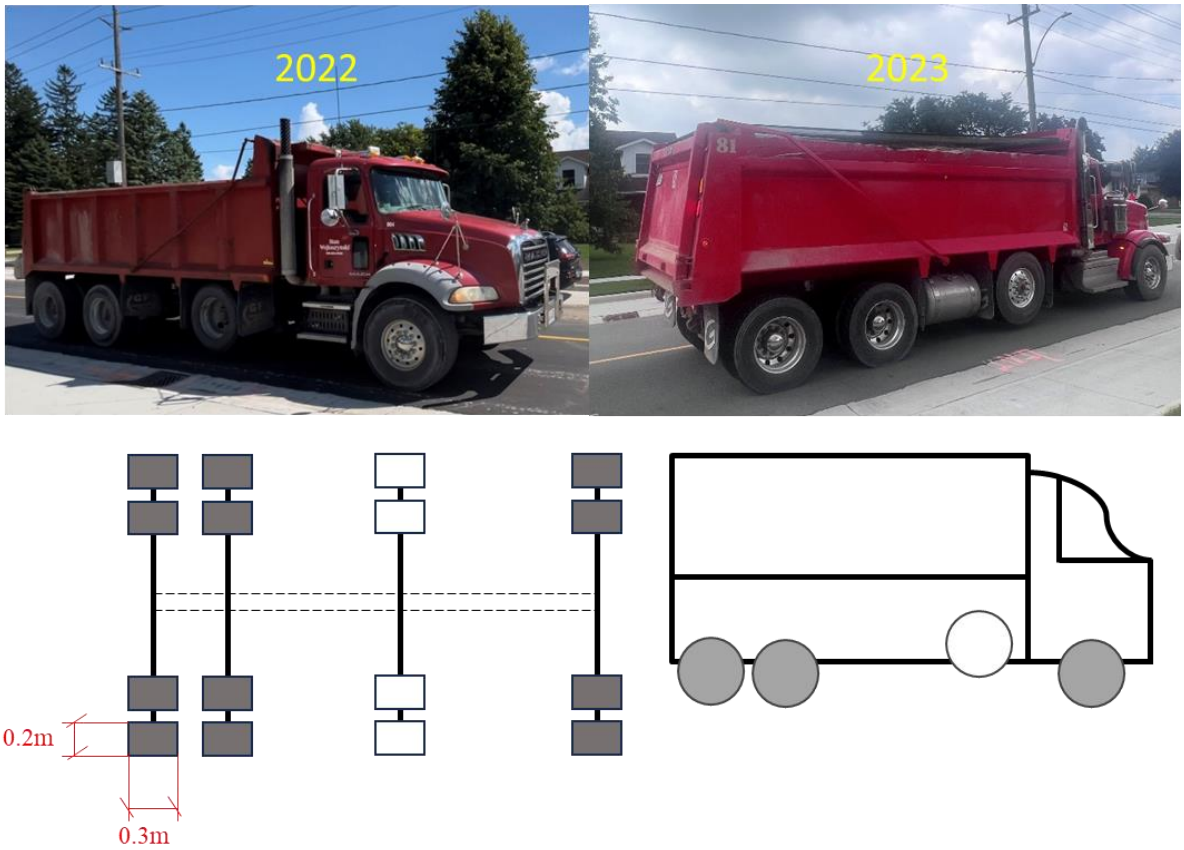

Figure 7-5 Truck Configuration

Table 7-1 Load Configuration

Test Scenario	Gross Weight (kg)	# of Tires	Contact Areas (m^2)	Load (kN)	Mean Tire Pressure (kPa)
Loaded Truck 2022	34380	10	0.06	336.92	562
Unloaded Truck 2022	13600	10	0.06	133.28	222
Loaded Truck 2023	35400	10	0.06	346.92	578
Unloaded Truck 2023	13600	10	0.06	133.28	222

The trucks used in both 2022 and 2023 have similar configurations, with one steering axle with single tires on both sides and three rear axles with dual tires on both sides including one lifting axle raised all the time. Therefore, a total of ten tires were loaded on the pavement. The truck configuration for both trucks used in 2022 and 2023 is shown in Figure 7-5. The contact patch area was assumed to be 0.06 m^2 for each tire (R. Liu, Ji, Wang, Chen, & Maeno, 2015; Oyeyi, 2022). The gross weight of loaded

and unloaded materials is listed in Table 7-1, provided by the contractor. The tare weight was used as the unloaded truck weight. The loading was assumed to be distributed evenly on each tire.

7.3 Testing Results During Construction

LWD was performed on the subgrade and base layer in the field during construction using a 300-mm diameter bearing plate. A 200-mm diameter bearing plate was used on the asphalt binder course and surface course. The former results were compared to the results from CBR performed in the laboratory after correlation.

7.3.1 Stiffness of Each Layer of Pavement Structure

7.3.1.1 Unbound Materials

During the construction, LWD was performed on the compacted subgrade, whose results are shown in Figure 7-6. An empirical model was developed by the Louisiana Transportation Research Center (LTRC) to correlate the resilient modulus of soils with the tested modulus by LWD, shown in Equation 7-2 (Mohammad et al., 2008).

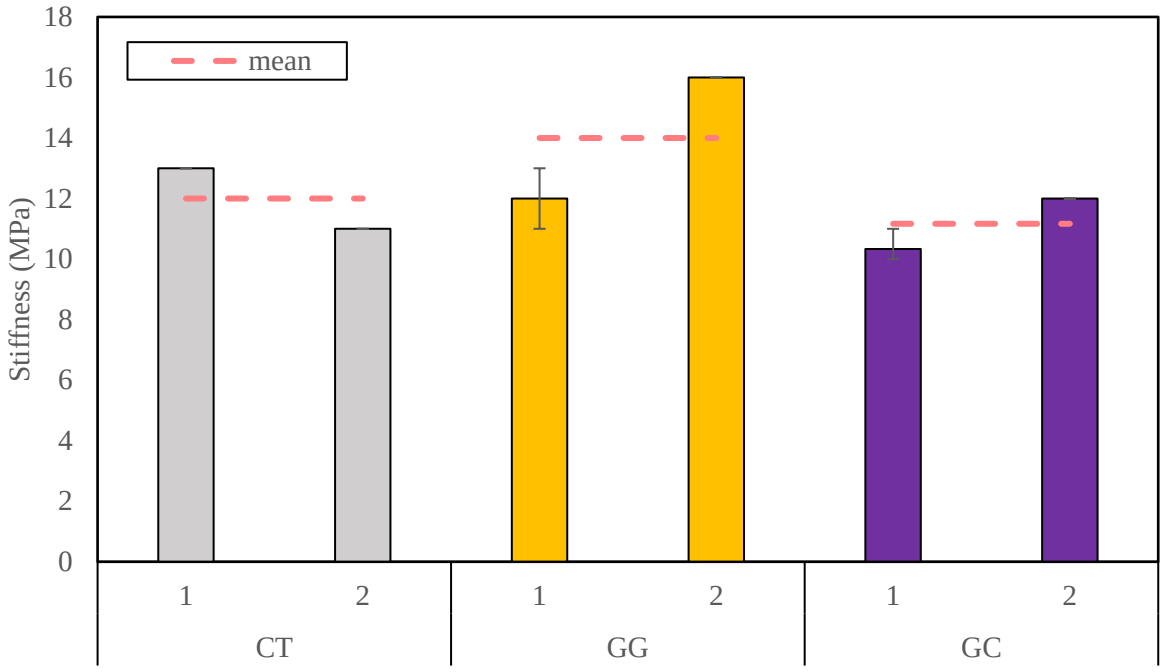

Figure 7-6 LWD Tested Stiffness on Subgrade

Equation 7-2

$$M_R = 27.76 \times (E_{LWD})^{0.18}$$

where:

E_{LWD} = modulus obtained from LWD test (MPa)

Resilient modulus correlated from CBR and LWD tests are shown in Figure 7-7. CBR correlated M_R by the two models are similar to each other. CT has the highest resilient modulus, while GG and GC show similar values. However, resilient moduli correlated from LWD show consistent results for all three sections, with GC having a slightly lower value. The correlated resilient modulus from both CBR models and LWD for CT is close, which may indicate the sampled subgrade soil from the CT section is more representative of the actual site conditions. As LWD was performed in the field showing the in-situ soil properties, while CBR was performed on the sampled soil in the laboratory, external factors could contribute to the differences, including a drier condition in the field, a soaked condition in the laboratory, destruction during sampling, consistent compaction effort in the field (Makwana & Kumar, 2019).

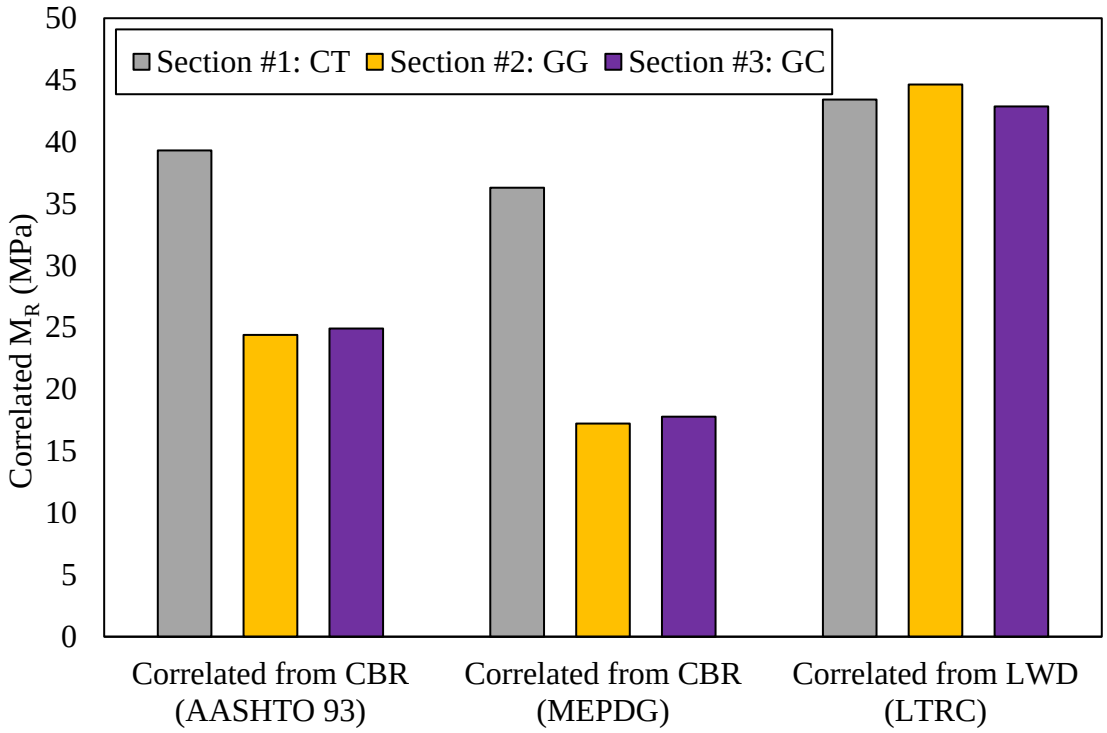

Figure 7-7 Correlated Resilient Modulus of Sample Soil from CBR and LWD

LWD was also performed on the compacted base layer, whose results of stiffness are shown in Figure 7-8. Equation 4-15 was used to calculate CBR results with resilient modulus, and Equation 7-2 was used to correlate LWD test results with resilient modulus. Correlation results are shown in Figure 7-9.

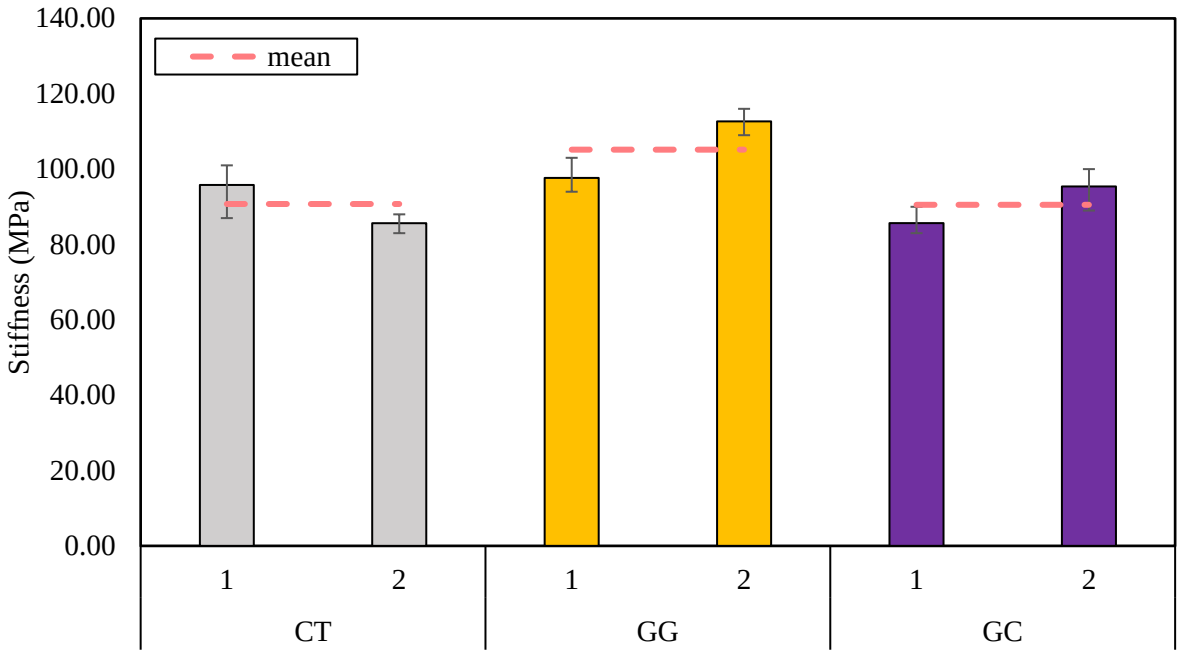

Figure 7-8 LWD Tested Stiffness on Granular Base Layer

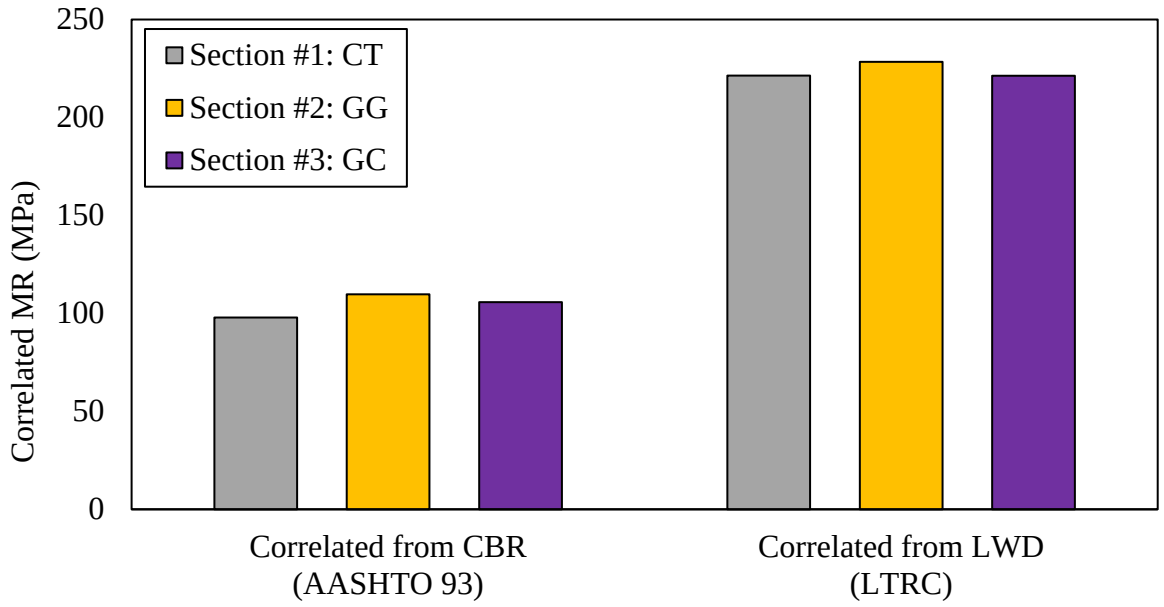

Figure 7-9 Correlated Resilient Modulus of Sample Base Aggregates from CBR and LWD

With consistent results of CBR and LWD test, the LWD-correlated resilient modulus was about two times of CBR-correlated ones, which may be attributed to similar reasons for higher in-situ results of subgrade soils, including a drier condition in the field, a soaked condition in the laboratory, destruction during sampling, consistent compaction effort in the field (Makwana & Kumar, 2019). The typical value of Granular A provided by the Ontario Ministry of Transportation (MTO) is 250 MPa, which is close to the in-situ resilient modulus (MTO, 2013).

7.3.1.2 Asphalt Layers

LWD test was performed on the asphalt binder course and asphalt surface course in the westbound lane, whose results are plotted in Figure 7-10 and Figure 7-11, respectively.

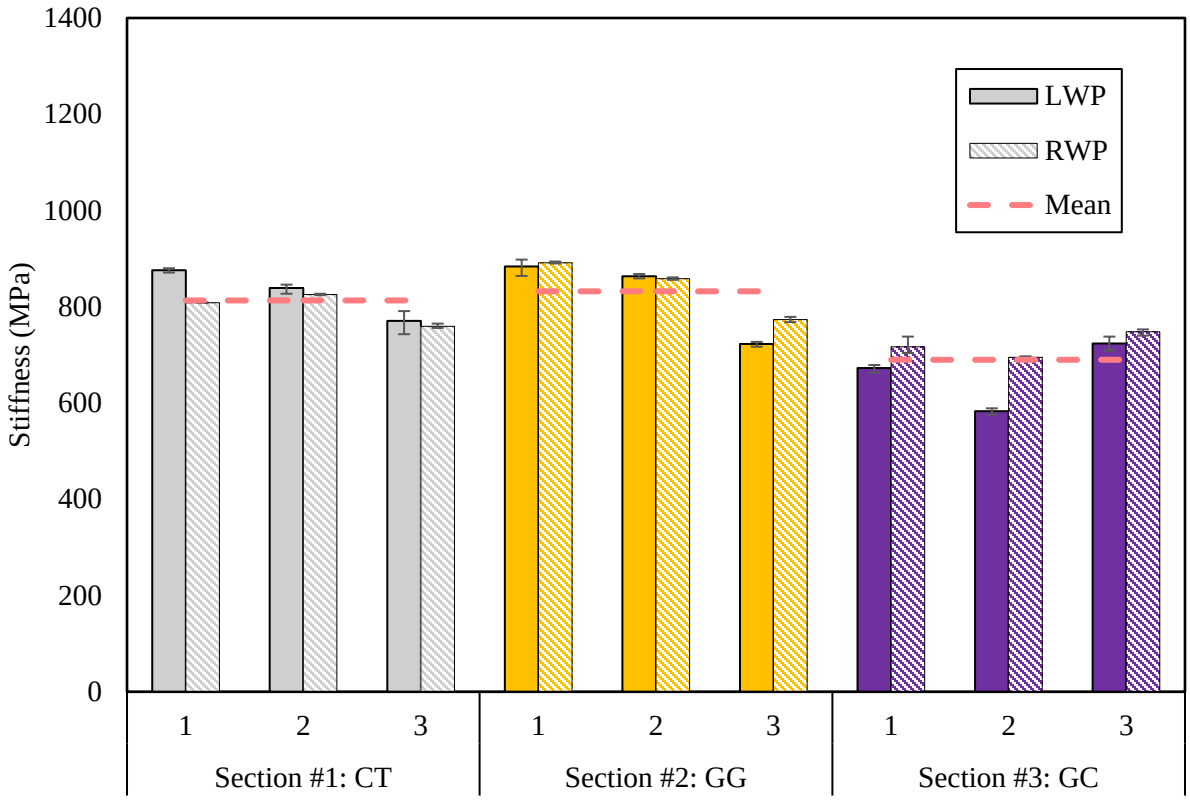

Figure 7-10 LWD Tested Stiffness on Asphalt Binder Course

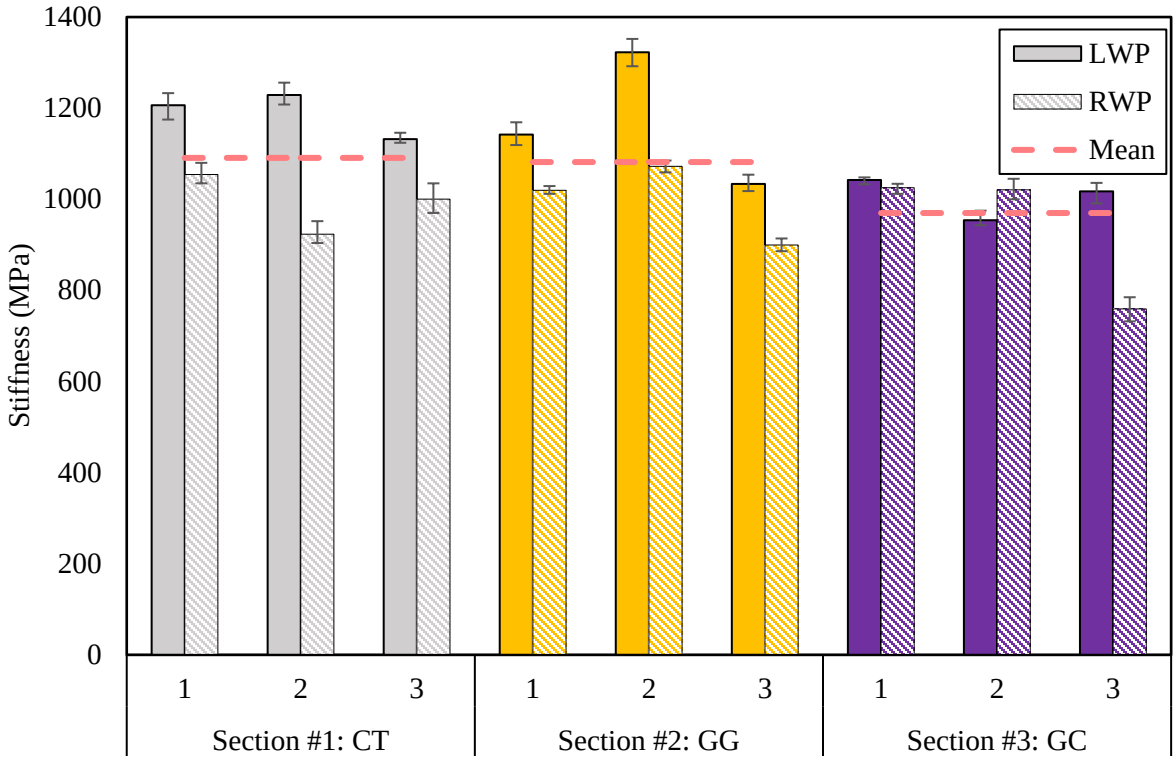

Figure 7-11 LWD Tested Stiffness on Asphalt Surface Course

The stiffness on the binder course is generally lower than that on the surface course, with the stiffness in the GC section showing a lower stiffness compared to the other two sections. Potential reasons could be the lower construction and material qualities in the GC section. Also, the differences between the wheel paths are not significant on the binder course. However, after the placement of the asphalt surface course, the impacts of traffic loading were more significant with more variances between wheel paths. This can be further verified with the analysis of CoVs listed in Table 7-2, with higher CoVs on surface course. This can be attributed to more traffic loading on the pavement due to the construction activities on the other side of the road.

Figure 7-12 compares the stiffness measurements on the binder and surface course. The stiffness was improved, and the level of improvement was consistent among the three sections.

Table 7-2 Variances Analysis of Stiffness Value During Construction

	Mean (MPa)	Std. dev. (MPa)	CoV
		Asphalt Binder Course	
Section #1: CT	813.11	42.02	5.17%
Section #2: GG	832.11	64.43	7.74%
Section #3: GC	689.85	54.32	7.87%
		Asphalt Surface Course	
Section #1: CT	1090.89	114.49	10.49%
Section #2: GG	1081.67	134.58	12.44%
Section #3: GC	969.83	102.28	10.55%

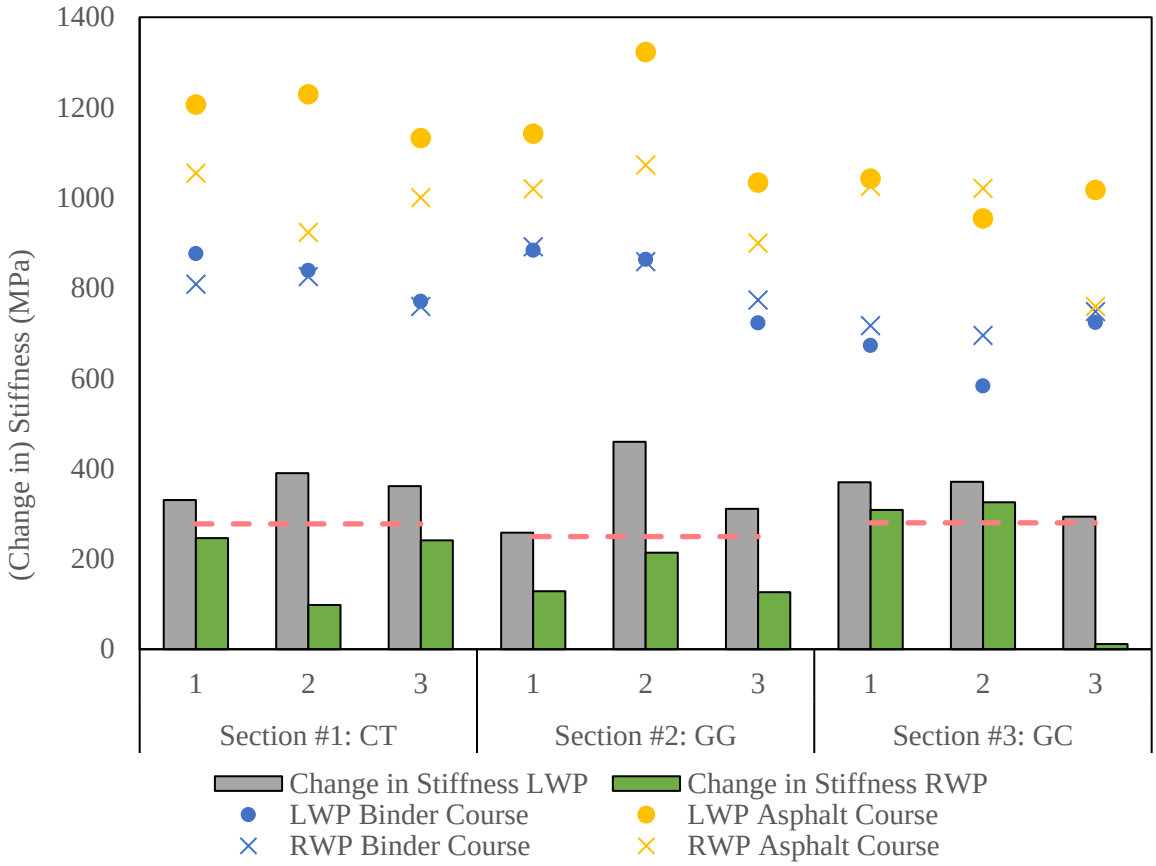

Figure 7-12 Comparison of Stiffness on Binder Course and Surface Course

7.3.2 Roughness of Asphalt Layers

The roughness was measured using Surpro after the construction of the binder course and surface course. The IRI was calculated and analyzed at every 1 m interval. The results tested after the binder course construction are shown in Figure 7-13. The highest IRI is shown in the geogrid section with an average of 3.96. The average IRI in the control section is 3.16, and the lowest IRI is in the geogrid composite section with an average of 2.34.

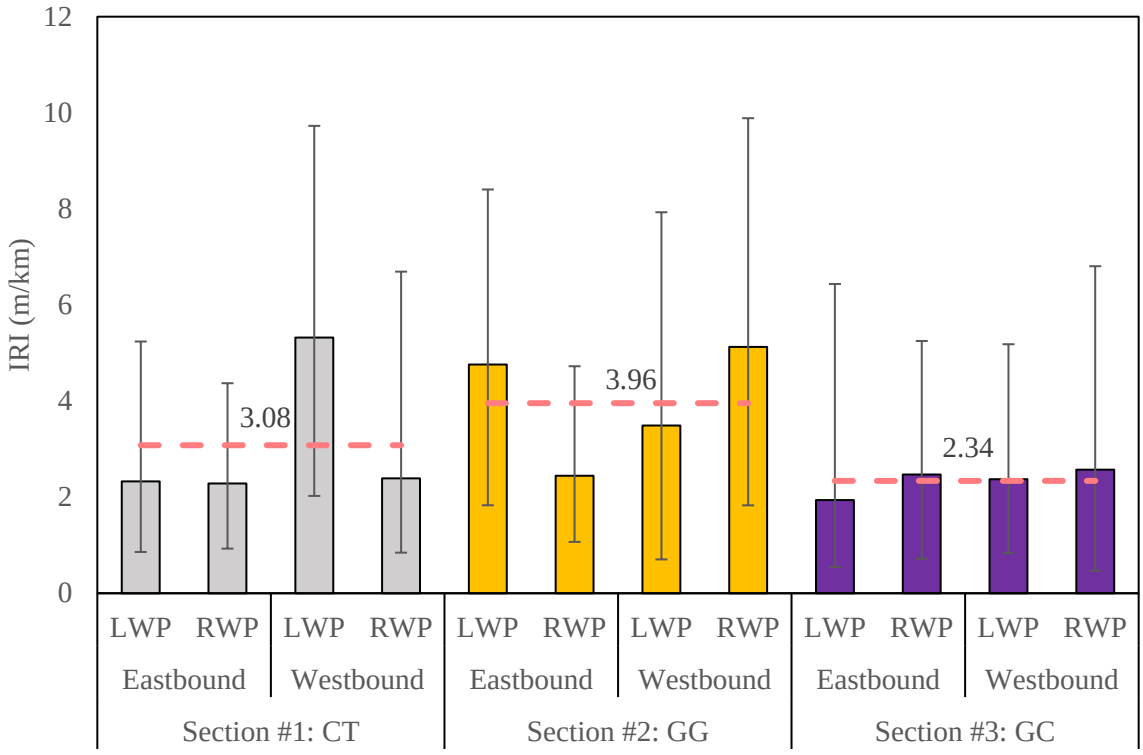

Figure 7-13 IRI Results Tested after Binder Course Placement

With the large error bar shown in Figure 7-13, statistical analysis was performed with the computation of standard deviation and coefficient of variance (CoV), which are listed in Table 7-3. It can be seen that the variances are high, with the CT section showing the highest CoV while the GG section showing the lowest, which indicates a more consistent roughness in the GG section. Generally, the reliability of the profilometry equipment in this study may be deemed to be relatively low. Large variabilities were also observed in other studies using the same equipment (Oyeyi, Ni, & Tighe, 2023).In this case, statistical analysis is needed to present more accurate observations.

Table 7-3 IRI on Binder Course Results Analysis for All Data

	Mean (m/km)	Std. dev. (m/km)	CoV
Section #1: CT	3.08	2.16	69.96%
Section #2: GG	3.96	2.16	54.71%
Section #3: GC	2.34	1.44	61.75%

Furthermore, analysis was performed on the variation between lanes and between wheel paths, as listed in Table 7-4. The CoV in different lanes indicates the deviation between different wheel paths with more loadings tending to be applied on RWP. The CoV in different wheel paths indicates the deviation between different lanes which may indicate the impact of instrumentation as the conduits and instrumentation are in the westbound lane. The variance between lanes and between wheel paths are similar, which implies the instrumentation in the westbound lane does not affect the surface smoothness.

Table 7-4 IRI on Binder Course Results Analysis for All Data

	Mean (m/km)	Std. dev. (m/km)	CoV	Mean (m/km)	Std. dev. (m/km)	CoV
	Eastbound			**Westbound**		
Section #1: CT	2.31	1.00	43.52%	3.86	2.69	69.64%
Section #2: GG	3.60	2.00	55.58%	4.31	2.33	54.04%
Section #3: GC	2.21	1.40	63.50%	2.47	1.52	61.46%
	LWP			**RWP**		
Section #1: CT	3.82	2.61	68.15%	2.34	1.24	52.85%
Section #2: GG	4.13	2.18	52.84%	3.79	2.21	58.34%
Section #3: GC	2.16	1.36	63.21%	2.52	1.54	61.19%

A student's t-test was performed on the measurements between the lanes to further evaluate the impact of instrumentation on roughness. The t-test was performed based on a null hypothesis at a 95% significance level. The t-test was performed on each wheel path and overall to evaluate the variances between lanes, whose results are listed in Table 7-5. The two-tailed p-values show that there are significant differences with a p-value less than 0.05 between lanes.

Table 7-5 T-test Analysis of IRI Value Between Lanes After Binder Course Placement

	LWP		RWP		Overall	
	Eastbound	Westbound	Eastbound	Westbound	Eastbound	Westbound
Mean (MPa)	3.034	3.841	2.421	3.377	2.727	3.609
Variance (MPa)	0.686	1.413	0.294	0.624	0.571	1.039
t Stat	2.793		3.970		4.757	
P(T<=t)	0.014		0.001		0.000	

The results tested after the surface course construction are shown in Figure 7-14, which shows a lower level of IRI compared to Figure 7-13. The IRI in the control section and geogrid section is close, with an average of 2.35 and 2.29, respectively. The lowest IRI is still in the geogrid composite section with an average of 1.53.

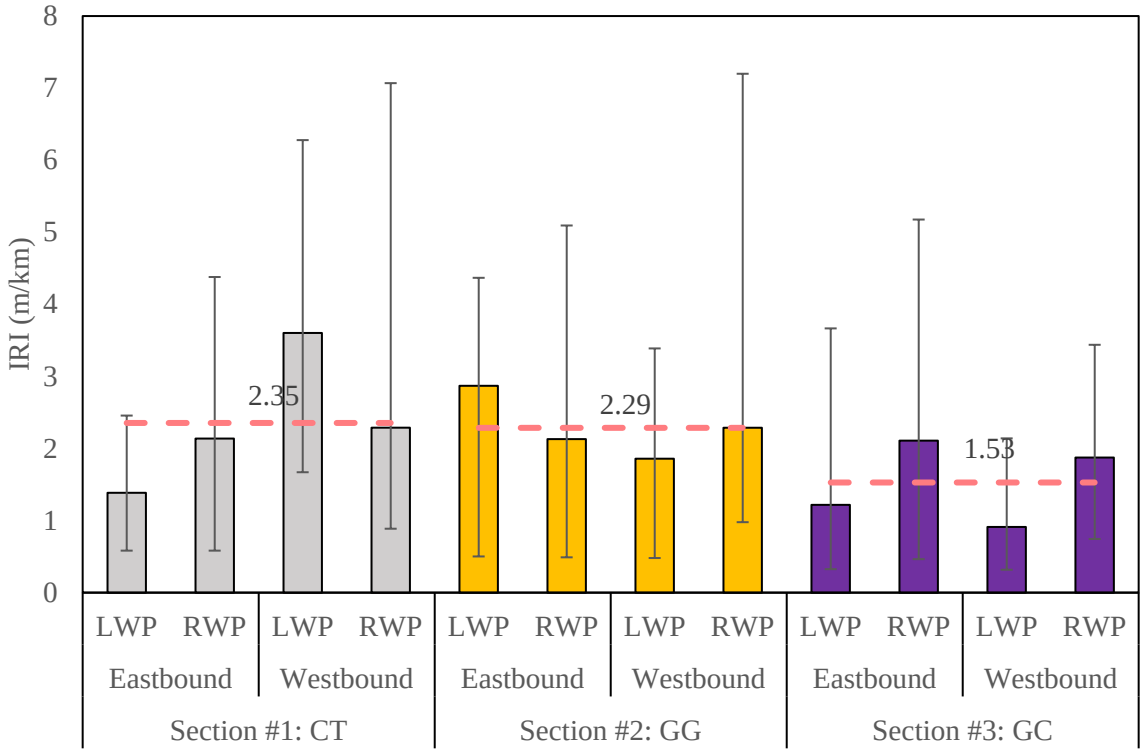

Figure 7-14 IRI Results Tested after Surface Course Placement

Despite the higher IRI on the binder course in the geogrid section, it appears that the roughness was reduced to the same level as that in the control section after the surface course was paved. Therefore,

an overlay of the surface course is necessary with the geogrid reinforcement in the asphalt concrete course. Additionally, the IRI measurements in the geogrid composite were shown to be the lowest on both the binder course and surface course, which implies a higher construction quality.

The variance was also analyzed on the IRI measurements after surface course placement, which are listed in Table 7-6. Significant variances were noticed with IRIs on GG still showing the least CoV, similar to the results for the binder course.

Table 7-6 IRI on Surface Course Results Analysis for All Data

	Mean (m/km)	Std. dev. (m/km)	CoV
Section #1: CT	2.35	1.42	60.13%
Section #2: GG	2.29	1.26	55.32%
Section #3: GC	1.53	1.05	68.88%

IRI measurements still show the least variances between LWP and RWP on eastbound lanes, which indicates the function of geogrid within the asphalt concrete by evenly distributing the loading exerted by construction trucks. The variances between instrumented and non-instrumented lanes are similar for all three sections on RWP, with less variance in the GG section on LWP.

Table 7-7 IRI on Surface Course Analysis for Data on Different Lanes and Wheel Paths

	Mean (m/km)	Std. dev. (m/km)	CoV	Mean (m/km)	Std. dev. (m/km)	CoV
	Eastbound			**Westbound**		
Section #1: CT	1.76	0.93	52.71%	2.95	1.58	53.60%
Section #2: GG	2.50	1.26	50.20%	2.07	1.28	61.80%
Section #3: GC	1.66	1.22	73.48%	1.39	0.87	62.40%
	LWP			**RWP**		
Section #1: CT	2.49	1.51	60.37%	2.21	1.33	60.15%
Section #2: GG	2.36	1.25	52.76%	2.21	1.32	59.76%
Section #3: GC	1.06	0.72	67.80%	1.99	1.15	57.74%

As per Ontario standard, a new / reconstruction of AC pavement should generate an initial IRI of 0.8 m/km, 1 m/km, and 1 m/km for freeway, arterial, and collector, respectively. No recommended initial IRI is provided for local roads. This may indicate an overestimation of the IRI generated by SurPro. The typical terminal IRI in Ontario for a local road is 3.3 m/km (MTO, 2019). However, based on

Figure 7-3, for new pavements, the IRI is typically from 1.5 – 3.5 m/km (Sayers & Karamihas, 1998). The IRI values of all three trial sections satisfy this range.

Compared with IRI measured after binder course placement, as plotted in Figure 7-15, IRI generally dropped after surface course placement, which means the riding quality was improved. Among the three sections, the riding quality in the GG section improved the most. This concludes that an overlay is required to ensure the riding quality for pavement with geogrid embedded in the asphalt.

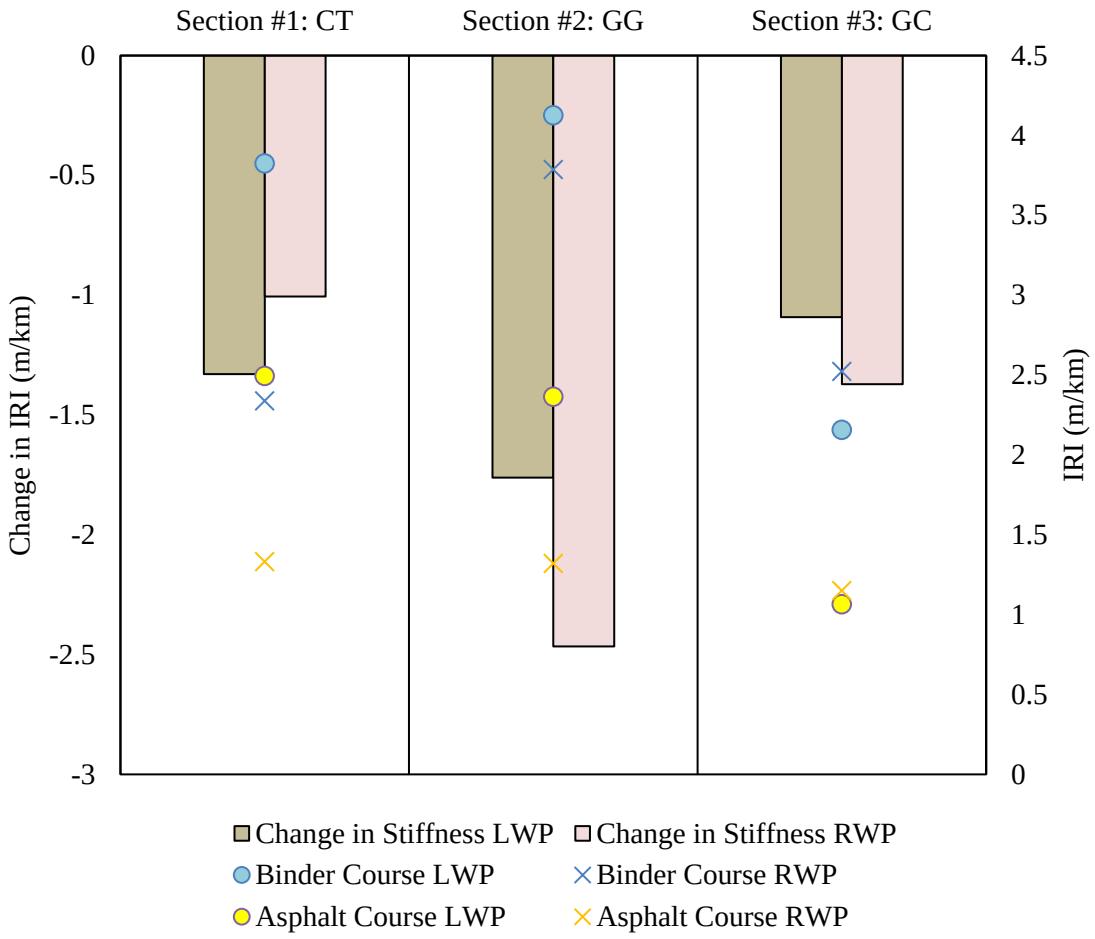

Figure 7-15 Comparison of IRI on Binder Course and Surface Course

Similar to what has been done after binder course placement, a t-test was performed on IRI measured after surface placement to evaluate the impact of instrumentation on roughness, as listed in Table 7-8. It can be seen that no significant difference between lanes occurred after surface course placement with a p-value greater than 0.05.

Table 7-8 T-test Analysis of IRI Value Between Lanes After Surface Course Placement

	LWP		RWP		Overall	
	Eastbound	Westbound	Eastbound	Westbound	Eastbound	Westbound
Mean (m/km)	1.824	2.146	2.146	2.156	1.985	2.127
Variance (m/km)	0.284	0.376	0.376	0.688	0.346	0.531
t Stat	1.527		0.035		0.822	
P(T<=t)	0.149		0.973		0.418	

7.4 Testing Results on In-Service Pavement

Field construction was also performed post-construction to monitor the performance of in-service pavements, including stiffness and roughness evaluation like what was done during construction, as well as a proposed driving test to capture the mechanical responses on the pavements by the instrumentation. The results were analyzed statistically against external factors such as environmental factors and different traffic loading.

7.4.1 Visual Condition Inspection

Visual condition inspection has been conducted monthly since the construction completion. No visible distress was observed until January 2024. Figure 7-16 presents the pavement surface condition in August 2022 and January 2024.

Figure 7-16 Pavement Surface Conditions

7.4.2 Stiffness Evaluation

LWD was used to monitor the stiffness of pavement seasonally after construction in summer 2022, fall 2022, winter 2023, spring 2023, and summer 2023. The test was performed on both wheel paths on both lanes.

7.4.2.1 Results

LWD measurements tested in summer 2022, fall 2022, winter 2023, spring 2023, and summer 2023 were illustrated in Figure 7-17.

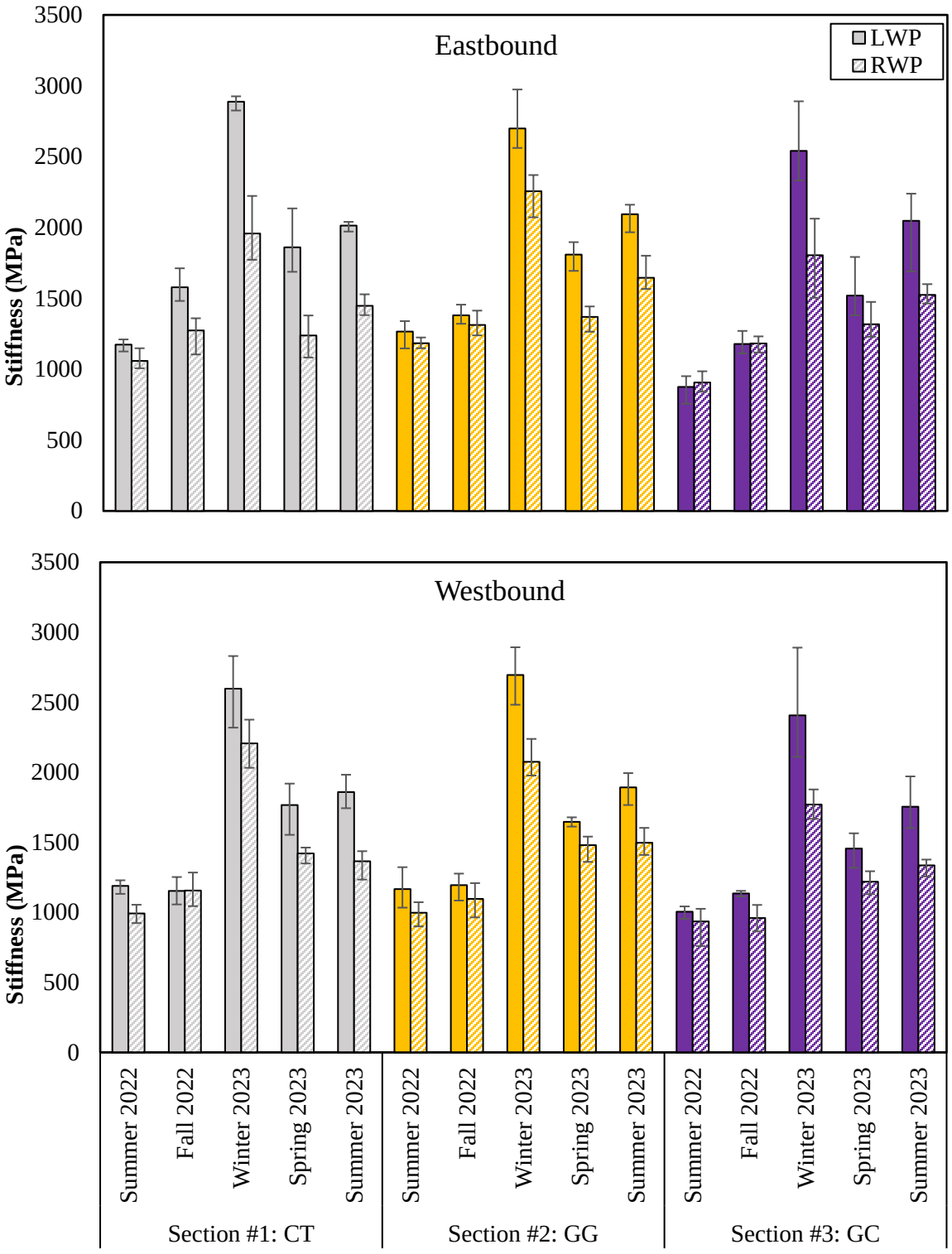

Figure 7-17 Stiffness Tested by LWD

Right after the construction completion, the testing results in the summer of 2022 showed that stiffness in the GC section was lower than that in the CT and GG sections, which matched the ranking from the testing results afterwards. Also, it can be seen that the stiffness in RWP is generally lower than that in LWP for all sections, especially starting from 2023, after the pavement was open to traffic for about 6 months. The difference is contributed by the heavier loading on the RWP by the driving behaviours and typical geometry of roads (van der Walt, Scheepbouwer, & Tighe, 2018). Thus, the impact of traffic should be analyzed. Also, the stiffness is the highest in winter when the temperatures are lower, and the lowest in fall and spring when precipitation is usually the most. Similar findings were reported in other studies with higher pavement stiffness in colder seasons (Oyeyi, Ni, et al., 2023). Impacts of moisture and temperature need to be analyzed as well.

Furthermore, due to the operating nature of this equipment, human errors are inevitable. To evaluate the variances, the CoVs were computed in Table 7-9, which indicates reliable measurements with most CoVs less than 20%. From the table, CT had the least variance right after construction completion in summer 2022, with the GG section showing a slightly higher variance. However, after the pavement opens to traffic, the GG section shows the lowest CoVs in every season.

In addition, a similar analysis was performed a level down on the variation between eastbound lane and westbound lane, whose results are listed in Table 7-10. The CoVs are mostly less than 15% except the one in LWP in the CT section in fall 2022 (16.36%). These results imply that the instrumentation in the westbound lane does not affect the stiffness of pavements from LWD measurements. Among the sections, the GG section still shows a better consistency between different lanes after the pavement was opened to traffic with lower CoVs.

A student's t-test was performed on the measurements between the lanes to further investigate the differences between instrumented and non-instrumented lanes. The t-test was performed based on a null hypothesis at a 95% significance level. The t-test was performed on each wheel path and overall to evaluate the variances between lanes, whose results are listed in Table 7-11. The two-tailed p-values show that there are significant differences with a p-value less than 0.05 between lanes on LWP, which may be attributed to the significant differences overall between lanes.

Table 7-9 Overall Variances Analysis of Stiffness Value

	Mean (MPa)	Std. dev. (MPa)	CoV
		Summer 2022	
Section #1: CT	1103.44	98.97	8.97%
Section #2: GG	1153.11	131.38	11.39%
Section #3: GC	930.31	99.48	10.69%
		Fall 2022	
Section #1: CT	1290.34	197.16	15.28%
Section #2: GG	1245.82	133.12	10.69%
Section #3: GC	1113.63	109.34	9.82%
		Winter 2023	
Section #1: CT	2412.19	399.21	16.55%
Section #2: GG	2431.24	321.65	13.23%
Section #3: GC	2130.52	426.81	20.03%
		Spring 2023	
Section #1: CT	1571.31	294.95	18.77%
Section #2: GG	1576.11	188.42	11.95%
Section #3: GC	1377.84	168.27	12.21%
		Summer 2023	
Section #1: CT	1671.14	288.68	17.27%
Section #2: GG	1782.10	252.24	14.15%
Section #3: GC	1665.47	300.67	18.05%

Table 7-10 Variances Analysis of Stiffness Value Between Lanes

	Mean (MPa)	LWP Std. dev. (MPa)	CoV	Mean (MPa)	RWP Std. dev. (MPa)	CoV
			Summer 2022			
Section #1: CT	1181.33	44.39	3.76%	1025.56	70.30	6.86%
Section #2: GG	1215.94	116.93	9.62%	1090.28	109.51	10.04%
Section #3: GC	939.89	93.95	10.00%	920.72	101.17	10.99%
			Fall 2022			
Section #1: CT	1365.91	223.48	16.36%	1214.77	124.26	10.23%
Section #2: GG	1287.43	113.33	8.80%	1204.21	137.20	11.39%
Section #3: GC	1156.58	54.89	4.75%	1070.68	131.92	12.32%
			Winter 2023			
Section #1: CT	2742.50	209.96	7.66%	2081.89	212.41	10.20%
Section #2: GG	2696.99	184.33	6.83%	2165.48	154.42	7.13%
Section #3: GC	2473.77	306.40	12.39%	1787.26	171.75	9.61%
			Spring 2023			
Section #1: CT	1813.33	185.65	10.24%	1329.28	132.43	9.96%
Section #2: GG	1727.67	106.21	6.15%	1424.56	106.49	7.48%
Section #3: GC	1487.63	151.67	10.20%	1268.06	113.76	8.97%
			Summer 2023			
Section #1: CT	1936.28	113.33	5.85%	1406.00	92.76	6.60%
Section #2: GG	1993.11	140.92	7.07%	1571.10	120.25	7.65%
Section #3: GC	1900.83	251.02	13.21%	1430.11	111.95	7.83%

Table 7-11 T-test Analysis of Stiffness Value Between Lanes

	LWP		RWP		Overall	
	Eastbound	Westbound	Eastbound	Westbound	Eastbound	Westbound
Mean (MPa)	1794.85	1661.04	1431.70	1366.96	1613.27	1514.00
Variance (MPa)	354283.0	307673.2	127311.4	155077.9	205391.5	207003.0
t Stat	3.75		1.71		4.12	
P(T<=t)	0.002		0.110		0.001	

7.4.2.2 Impact of Temperature and Moisture

The mean stiffness value for each section in every season is listed in Table 7-12. A one-way ANOVA analysis was performed to evaluate the variances between the measurements in each section from every season based on a null hypothesis at a 95% significance level, listed in Table 7-12. From the p-value obtained from ANOVA on the average stiffness of all three sections, the entire pavement stiffness is

significantly affected by environmental factors with seasonal change. By looking at the p-values for each section, though all three sections were analyzed to be affected by environment with p-values all less than 0.05, stiffness in the GC section is less affected by environment factors with a higher p-value (i.e., 0.038).

Table 7-12 ANOVA Analysis of Environmental Impacts on Stiffness

	Section #1: CT	Section #2: GG	Section #3: GC	Average
Summer 2022 (MPa)	1103.44	1153.11	930.31	1062.29
Fall 2022 (MPa)	1290.34	1245.82	1113.63	1216.60
Winter 2023 (MPa)	2412.19	2431.24	2130.52	2324.65
Spring 2023 (MPa)	1571.31	1576.11	1377.84	1508.42
Summer 2023 (MPa)	1671.14	1782.10	1665.47	1706.24
p-value	0.000	0.016	0.038	0.000

To evaluate how temperature and moisture would impact the pavement stiffness separately, regression analysis was performed. Table 7-13 lists the temperature data on the testing days measured by the temperature sensors instrumented in the pavement structure. Due to the significant differences in temperature between day and night and the delay of pavement temperature change affected by the ambient temperature, the average temperature from 8 a.m. to 5 p.m. was taken as the LWD tests were done during the daytime. The ambient temperature data was obtained from historical data in Kitchener–Waterloo from the Environment Canada website (Government of Canada, 2023). By looking at the ambient temperature, the stiffness of pavement generally decreases as the temperature increases. One exception is the one in summer 2023, which has higher stiffness compared to spring 2023 with higher temperatures. The one in fall 2022 also exhibits a similar trend, with lower temperature and lower stiffness compared with summer 2023. This can be attributed to the weaker structure with more moisture content from thawing soils.

Table 7-13 Temperature Data on LWD Testing Days

Date		2022-08-18	2022-12-02	2023-03-01	2023-04-14	2023-08-16
Season		Summer	Fall	Winter	Spring	Summer
Ambient (°C)		19.60	0.10	-1.90	17.00	19.90
Asphalt (°C)	CT	26.09	3.14	4.84	24.18	-
	GG	24.09	0.14	0.81	22.67	25.01
	GC	24.80	1.87	2.21	23.96	25.97
Base (°C)	CT	30.02	8.30	9.30	21.34	28.43
	GG	27.01	13.79	4.18	15.90	25.84
	GC	27.60	4.82	2.54	16.59	25.16
Subgrade (°C)	CT	28.21	8.09	6.17	16.79	27.29
	GG	27.80	6.49	3.85	13.04	26.74
	GC	26.25	7.50	2.54	16.59	25.16

A regression analysis was performed on data from all five tests first, a weak correlation between temperature and stiffness was obtained with R-square less than 0.3. To focus on the analysis of the impact of temperature on the pavement solely, regression analysis was performed on data without fall 2022, data without spring 2023, and data without both tests, to eliminate the bias effect that could be caused by moisture. The comparison of R-square for all regression analyses between temperature data and stiffness is illustrated in Figure 7-18. The strongest correlation was shown in the analysis on data without fall and spring, followed by the one on data without fall 2022. This also implies that moisture plays a critical role in the test in fall 2022.

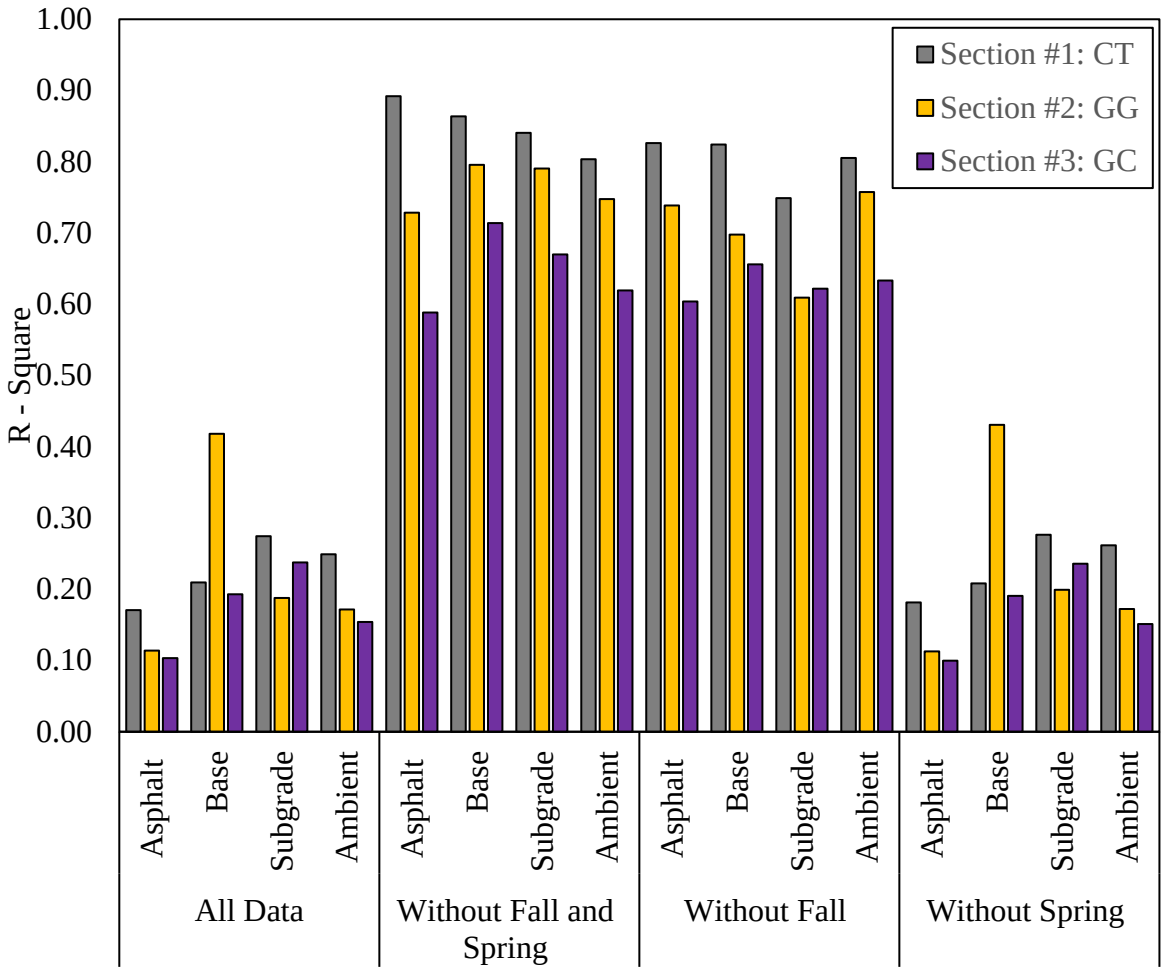

Figure 7-18 R-Square Values of Regression Analyses on Temperature and Stiffness

By eliminating the greatest bias effect by moisture content, the regression analyses show a strong correlation between temperature and stiffness, which is plotted in Figure 7-19. The correlation is the weakest between temperature in the subgrade and stiffness on the pavement surface, which indicates the stiffness tested on the pavement surface is the most impacted by asphalt and ambient temperature. Between the sections, the regression is always the strongest in the CT section with the highest R–square. With similar slopes shown in the figure, this indicates that the pavement stiffness in the CT section tends to be affected by ambient and pavement temperatures, which also implies the reinforcement provided by geosynthetic material.

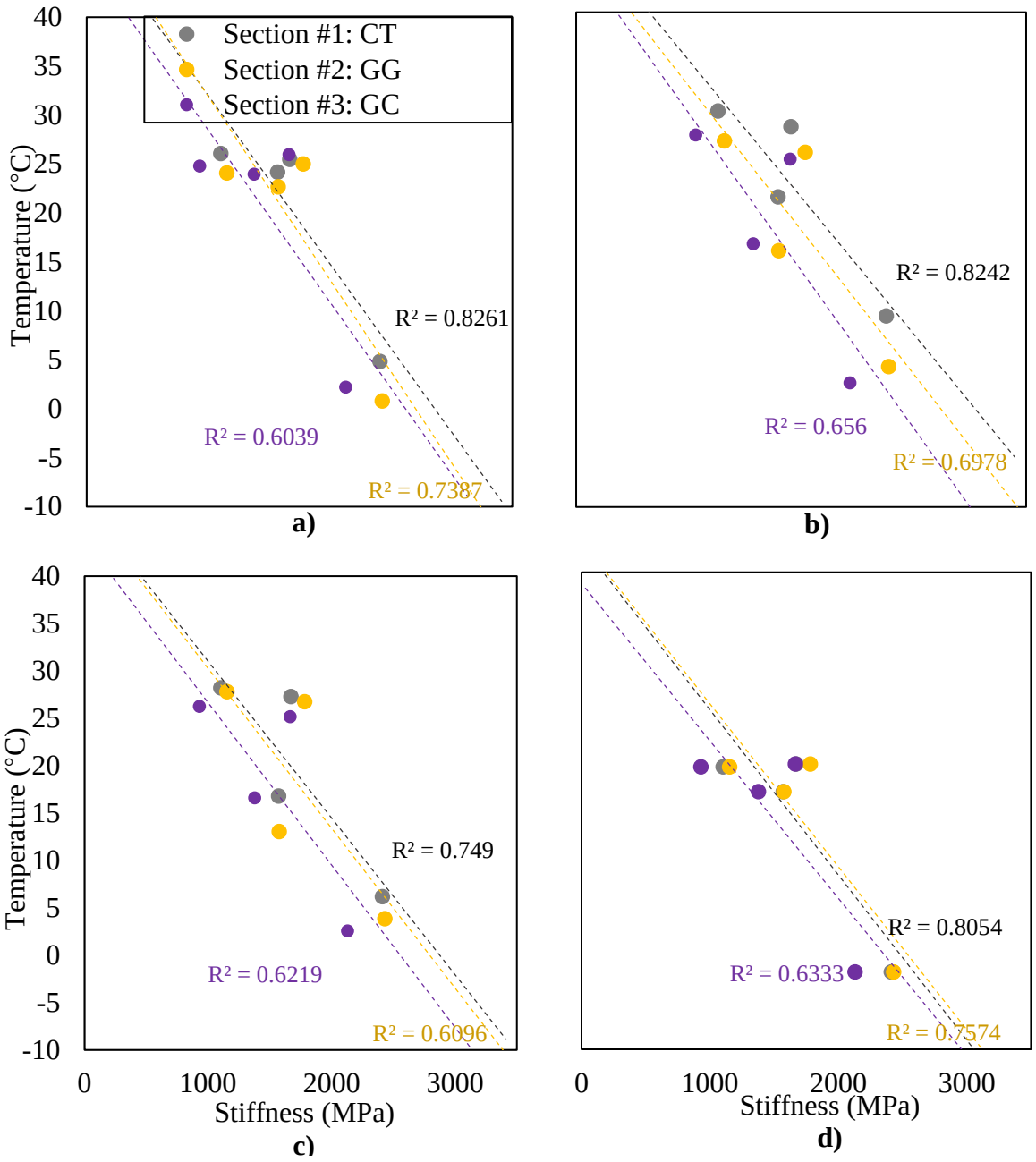

Figure 7-19 Regression Analyses on Stiffness and Temperature at a) lower asphalt binder lift; b) middle of base layer; c) 10 cm below subgrade; d) ambient

From Figure 7-18, it has been justified that moisture can also play a crucial role in affecting pavement stiffness. Table 7-14 lists the moisture data collected on testing days, including daily precipitation (Government of Canada, 2023), and daily average water potential obtained from moisture probes

installed in the pavement. The data verifies the implication in Figure 7-18 that the most impact on stiffness caused by moisture factor is the test in fall 2022 with the most precipitation.

Table 7-14 Moisture Data on LWD Testing Days

Date		2022-08-18	2022-12-02	2023-03-01	2023-04-14	2023-08-16
Season		Summer	Fall	Winter	Spring	Summer
Precipitation (mm)		0.20	1.70	0.00	0.00	0.00
Top of Base (kPa)	CT	-3.09	-9.03	-4.52	-0.23	-0.27
	GG	-12.64	-13.42	-8.65	-4.79	-5.77
	GC	-53.36	-17.72	-9.49	-2.13	-3.08
Middle of Base (kPa)	CT	0.00	-1.04	-0.66	0.00	-0.63
	GG	-11.75	-15.18	-155.44	-175.47	-200.00
	GC	-20.26	-11.29	-8.64	-4.86	-4.42
Subgrade (kPa)	CT	0.00	0.00	-0.08	0.00	0.00
	GG	0.00	-9.59	-3.72	-2.21	0.00
	GC	-49.94	-104.12	-167.95	-75.42	-125.86

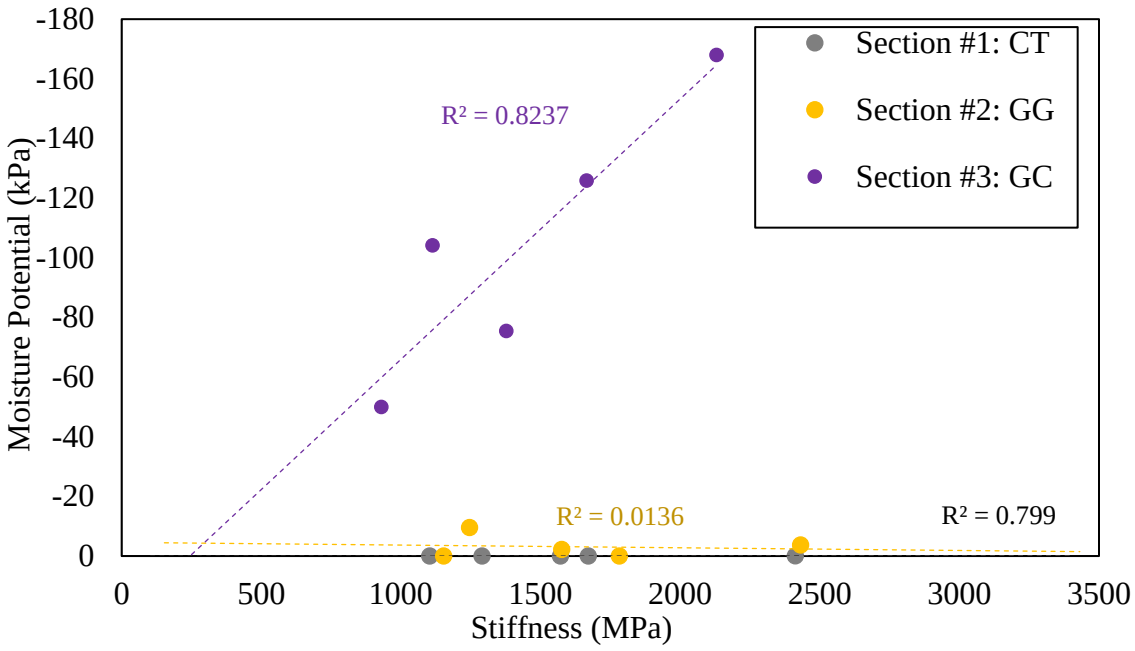

Figure 7-20 Regression Analyses on Stiffness and Water Potential at 10 cm below subgrade

Regression analyses were also performed between moisture data and stiffness. However, no strong correlation was observed with R-square values less than 0.5. The only exception is the one between water potential in the subgrade and stiffness, as plotted in Figure 7-20. With CT and GG sections

showing a wet to saturated subgrade (i.e., water potential from 0 to -20 kPa), the regression was not reliable for these two sections. However, water potential in the subgrade in the GC section shows an obvious regression with stiffness, while from dry to wet conditions, the stiffness drops. This behaviour shows the filtering and draining effect throughout the year with one annual freeze-thaw cycle provided by the geogrid composite on the subgrade.

7.4.2.3 Impact of Traffic

From Figure 7-17, stiffness measured after the road was opened to traffic was lower in RWP, which implies the impact of traffic loading on pavement stiffness, as the pavement is more deteriorated in the outside wheel path compared to the one closer to the middle of the lane (van der Walt et al., 2018). This is attributed to the larger force required to support the axle outside. Therefore, in Canada, more damage is expected in RWP. Table 7-15 lists the variances analysis of stiffness to evaluate the variation between two wheel paths. Compared with Table 7-10, higher CoVs were observed, which indicates that the impact of traffic loading is more critical than that of instrumentation.

Furthermore, a student's t-test was performed on the measurements between the wheel paths to further verify the impact of traffic loading. It was performed based on a null hypothesis at a 95% significance level. The t-test was performed on each lane and overall data, whose results are listed in Table 7-16. The two-tailed p-values show that there are significant differences with a p-value less than 0.05 between different wheel paths, which indicates the critical impact of traffic loading.

Table 7-15 Variances Analysis of Stiffness Value Between Wheel Paths

	Eastbound			Westbound		
	Mean (MPa)	Std. dev. (MPa)	CoV	Mean (MPa)	Std. dev. (MPa)	CoV
			Summer 2022			
Section #1: CT	1116.00	82.01	7.35%	1090.89	114.49	10.49%
Section #2: GG	1224.56	81.34	6.64%	1081.67	134.58	12.44%
Section #3: GC	890.78	85.50	9.60%	969.83	102.28	10.55%
			Fall 2022			
Section #1: CT	1426.06	185.54	13.01%	1154.61	98.85	8.56%
Section #2: GG	1346.42	85.06	6.32%	1145.22	107.39	9.38%
Section #3: GC	1180.05	60.95	5.16%	1047.20	112.16	10.71%
			Winter 2023			
Section #1: CT	2422.65	496.39	20.49%	2401.74	274.99	11.45%
Section #2: GG	2477.46	293.93	11.86%	2385.01	353.36	14.82%
Section #3: GC	2172.60	443.29	20.40%	2088.43	414.25	19.84%
			Spring 2023			
Section #1: CT	1549.17	362.55	23.40%	1593.44	215.93	13.55%
Section #2: GG	1589.07	247.72	15.59%	1563.15	107.50	6.88%
Section #3: GC	1418.52	188.07	13.26%	1337.17	152.44	11.40%
			Summer 2023			
Section #1: CT	1730.28	297.11	17.17%	1612.00	275.49	17.09%
Section #2: GG	1869.49	256.75	13.73%	1694.72	225.00	13.28%
Section #3: GC	1786.00	299.12	16.75%	1544.94	248.07	16.06%

Table 7-16 T-test Analysis of Stiffness Value Between Wheel Paths

	Eastbound		Westbound		Overall	
	LWP	RWP	LWP	RWP	LWP	RWP
Mean (MPa)	1794.85	1431.70	1661.04	1366.96	1727.95	1399.33
Variance (MPa)	354283	127311	307673	155078	326202	135791
t Stat	4.88		5.82		5.68	
P(T<=t)	0.000		0.000		0.000	

Then, the t-test was performed between two wheel paths for each section to evaluate the level of variation caused by traffic loading in each section. The analysis results are shown in Table 7-17. GC section has the highest p-value (i.e., 0.076), which indicates that no significant differences were noticed between LWP and RWP in the GC section. CT and GG sections are affected by traffic loading with a p-value less than 0.05, while the GG section has a higher p-value, which means the CT section is mostly affected by traffic loading. This concludes that pavement performance can be enhanced by geosynthetic

materials by distributing the traffic loading and providing less variation in stiffness throughout the pavement.

Table 7-17 T-test Analysis of Stiffness Value Between Wheel Paths in Each Section

	Section #1: CT		Section #2: GG		Section #3: GC	
	LWP	RWP	LWP	RWP	LWP	RWP
Mean (MPa)	1807.87	1411.50	1784.23	1491.12	1591.74	1295.37
Variance (MPa)	369484	160966	362428	177147	374659	112926
t Stat	3.84		3.43		2.38	
P(T<=t)	0.019		0.026		0.076	

Additionally, the stiffness measured in summer 2022 and summer 2023 was compared, as plotted in Figure 7-21.

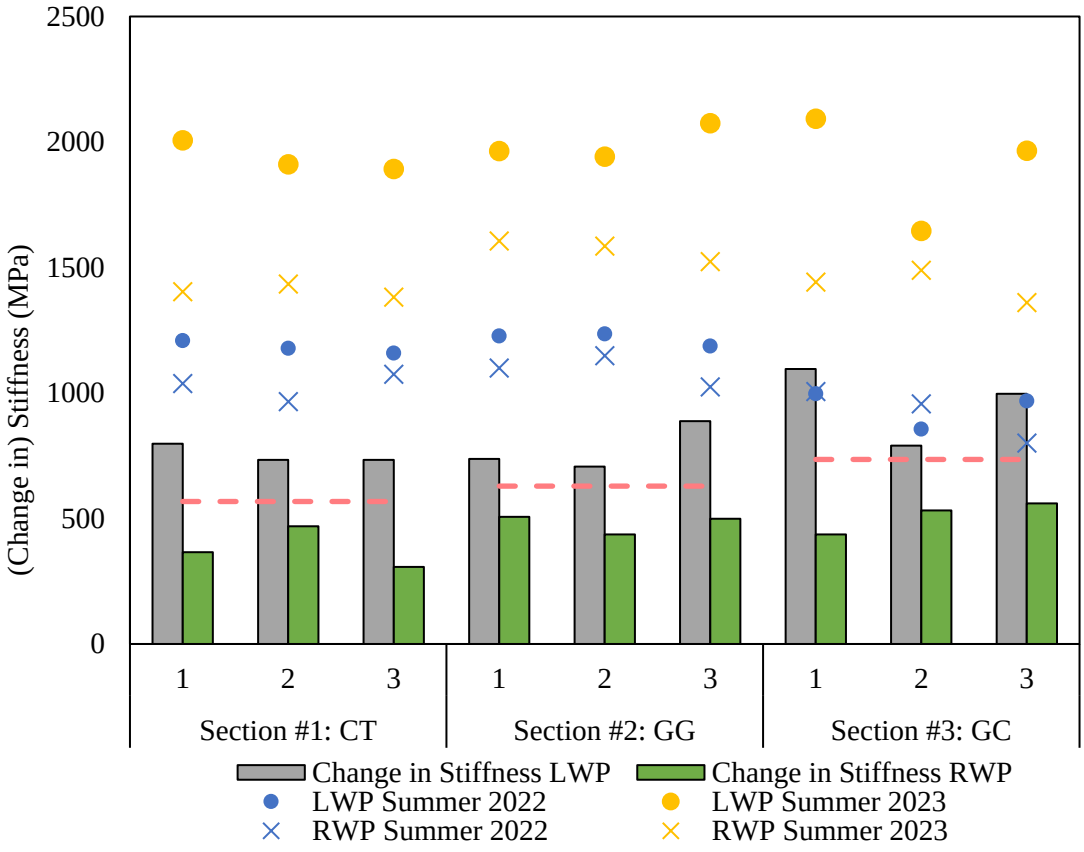

Figure 7-21 Comparison of Stiffness in Summer 2022 and Summer 2023

From the figure, the pavement stiffness in RWP increases more in GG and GC compared to the increase in CT, while the stiffness in LWP increases the most in the GC section. The comparison verifies the t-test results that the GC section is affected the least by traffic loading. The comparison of stiffness measured in summer 2022 and summer 2023 cannot only show the impact of traffic accumulated in one year but also the impact of the freeze-thaw action during the year.

7.4.3 Roughness

IRI was tested to monitor the roughness of pavement after construction in summer 2022, winter 2023, and spring 2023. The test was performed on both wheel paths on both lanes.

7.4.3.1 Results

IRI measurements tested in summer 2022, winter 2023, and spring 2023 were illustrated in Figure 7-22. From the figure, IRI is generally lower in the eastbound lane, which may be attributed to the instrumentation in the westbound lane. GC section has the lowest IRI throughout the year among the three sections, while it also shows the lowest variability between different seasons. Generally, IRI on RWP is higher than that on LWP in the GC section, which can be attributed to heavier loading applied on the outside wheel path. However, the IRIs in CT and GG sections on LWP are sometimes higher. Thus, a statistical analysis is required to justify the impact of traffic loading on riding quality.

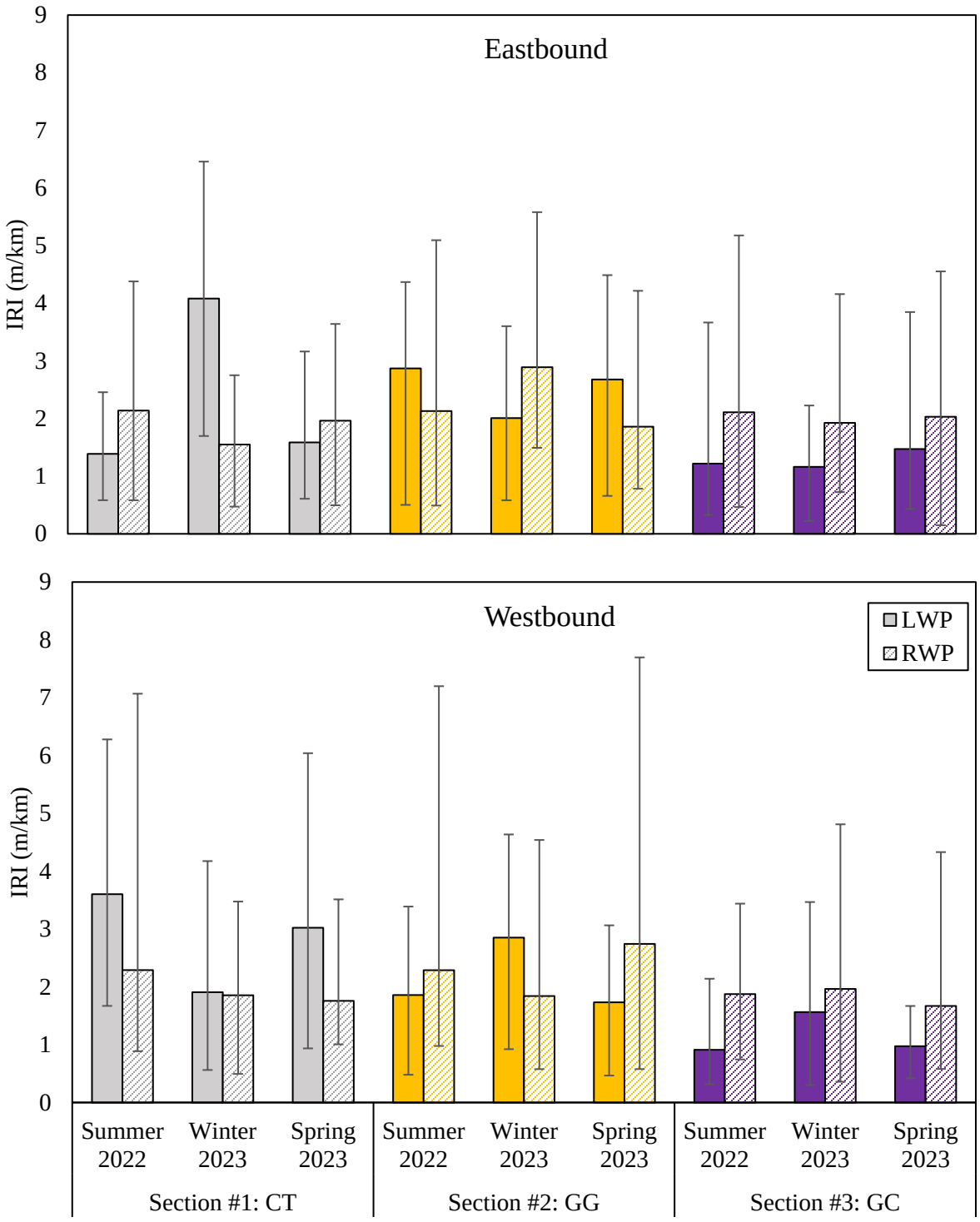

Figure 7-22 Roughness Tested by SurPro

To evaluate the variances, the CoVs were computed in Table 7-18. With high CoV values, it can be concluded that the roughness was not consistent even within the sections. In addition, a similar analysis was performed on the variation between the eastbound lane and the westbound lane, whose results are listed in Table 7-19. The CoVs are still high, which verifies the inconsistency of roughness within the section.

Table 7-18 Overall Variances Analysis of IRI Value

	Mean (m/km)	Std. dev. (m/km)	CoV
		Summer 2022	
Section #1: CT	2.35	1.42	60.13%
Section #2: GG	2.29	1.26	55.32%
Section #3: GC	1.53	1.05	68.88%
		Winter 2023	
Section #1: CT	2.35	1.44	61.52%
Section #2: GG	2.40	1.17	48.64%
Section #3: GC	1.65	0.98	59.00%
		Spring 2023	
Section #1: CT	2.08	1.13	54.38%
Section #2: GG	2.25	1.41	62.72%
Section #3: GC	1.54	1.01	65.46%

A student's t-test was also performed on the measurements between the lanes to investigate the variability between instrumented and non-instrumented lanes, based on a null hypothesis at a 95% significance level, whose results are listed in Table 7-20. The two-tailed p-values show that there are no significant differences with all p-values greater than 0.05 between lanes. This analysis can lead to the conclusion that the instrumentation does not affect the riding quality of the pavement.

Table 7-19 Variances Analysis of IRI Value Between Lanes

	LWP			RWP		
	Mean (m/km)	**Std. dev. (m/km)**	**CoV**	**Mean (m/km)**	**Std. dev. (m/km)**	**CoV**
			Summer 2022			
Section #1: CT	2.49	1.51	60.37%	2.21	1.33	60.15%
Section #2: GG	2.36	1.25	52.76%	2.21	1.32	59.76%
Section #3: GC	1.06	0.72	67.80%	1.99	1.15	57.74%
			Winter 2023			
Section #1: CT	2.99	1.66	55.34%	1.70	0.80	47.02%
Section #2: GG	2.43	1.20	49.30%	2.37	1.17	49.61%
Section #3: GC	1.36	0.81	59.43%	1.94	1.07	54.77%
			Spring 2023			
Section #1: CT	2.30	1.35	58.49%	1.86	0.83	44.72%
Section #2: GG	2.21	1.24	56.23%	2.30	1.61	69.93%
Section #3: GC	1.22	0.77	62.61%	1.85	1.14	61.60%

Table 7-20 T-test Analysis of IRI Value Between Lanes

	LWP		**RWP**		**Overall**	
	Eastbound	Westbound	Eastbound	Westbound	Eastbound	Westbound
Mean (m/km)	2.051	2.047	2.066	2.031	2.049	2.049
Variance (m/km)	0.958	0.856	0.129	0.118	0.444	0.053
t Stat	0.009		0.198		0.002	
P(T<=t)	0.993		0.848		0.998	

7.4.3.2 Impact of Temperature and Moisture

A one-way ANOVA analysis was performed to evaluate the variances between the IRIs in each section from every test based on a null hypothesis at a 95% significance level. The analysis and the mean IRIs are listed in Table 7-21. From the p-value obtained from ANOVA on the average IRI of all three sections, seasonal changes do not have a big impact on the entire pavement roughness with p-values greater than 0.05.

Table 7-21 ANOVA Analysis of Environmental Impacts on IRI

	Section #1: CT	Section #2: GG	Section #3: GC	Average
Summer 2022 (m/km)	2.35	2.29	1.53	2.06
Winter 2023 (m/km)	2.35	2.4	1.65	2.13
Spring 2023 (m/km)	2.08	2.25	1.54	1.96
p-value	0.897	0.915	0.913	0.337

A regression analysis was performed on IRI from all three tests against temperature data listed in Table 7-13 as the IRI tests were performed on the same day as when LWD tests were conducted. The comparison of R-square for the regression analysis between temperature data and IRI is illustrated in Figure 7-23. IRI in the GC section has the strongest correlation with temperature with R^2 greater than 0.8, followed by the GG section. IRI in the CT section was correlated with temperature.

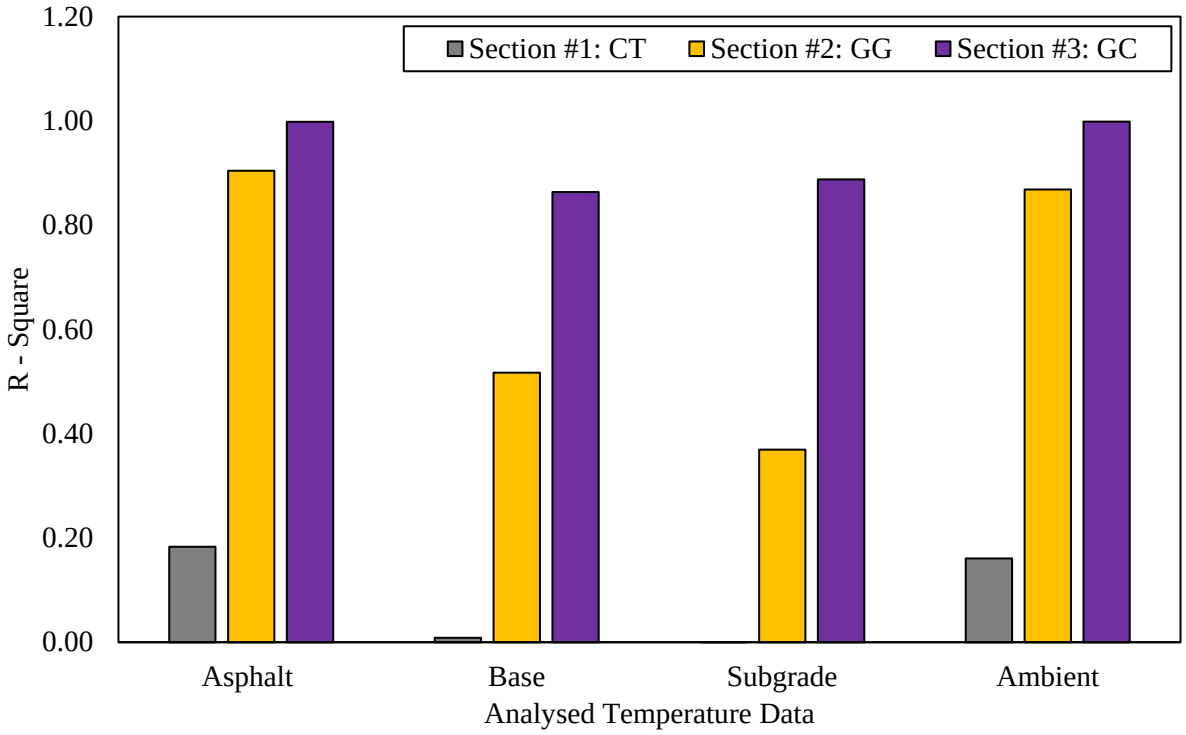

Figure 7-23 R – Square Values of Regression Analyses on Temperature and IRI

The regression analyses are plotted in Figure 7-19. Despite the good correlation in GG and GC sections, the high slopes indicate that the ambient temperature and pavement temperature barely affect the surface roughness.

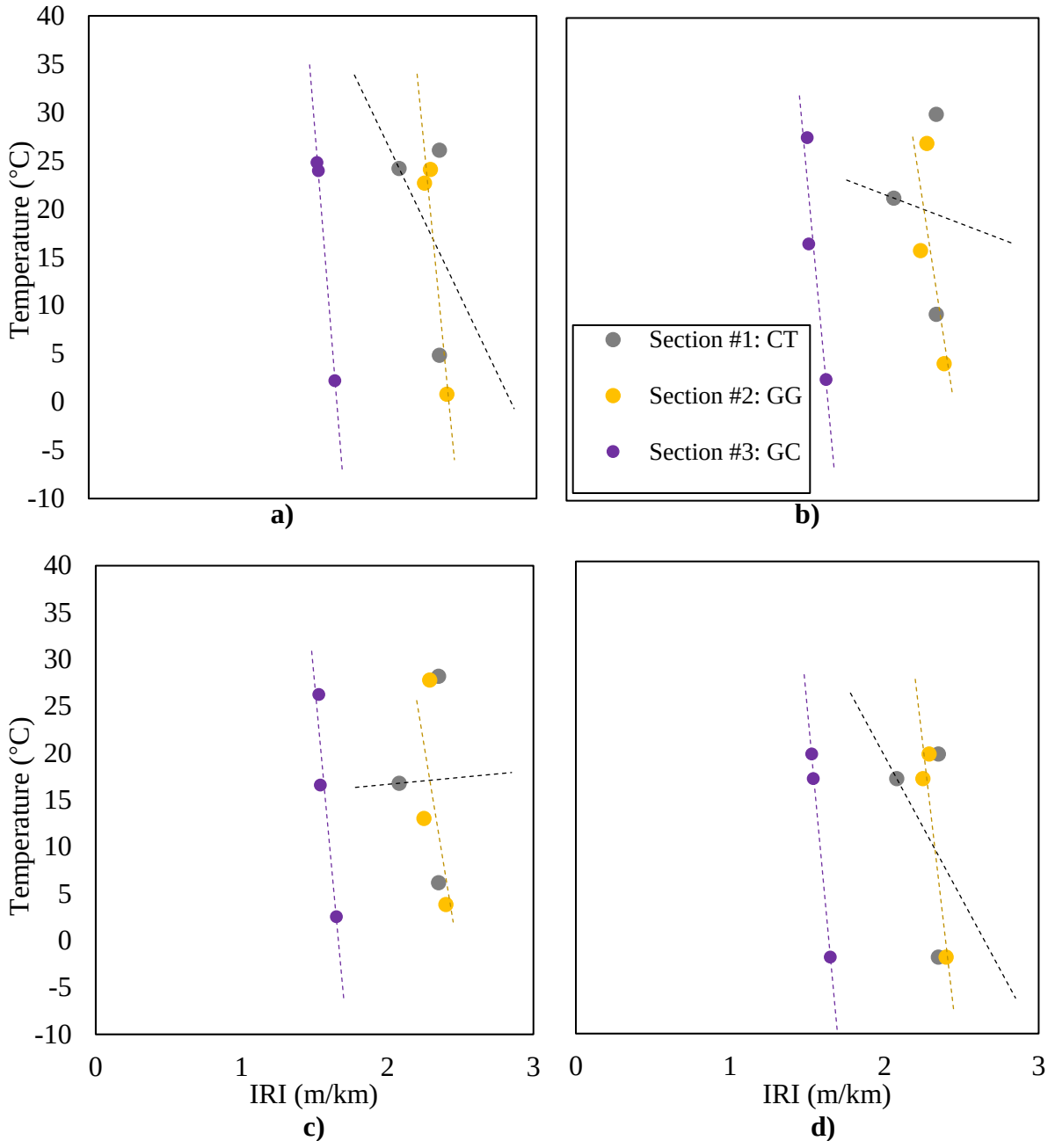

Figure 7-24 Regression Analyses on IRI and Temperature at a) lower asphalt binder lift; b) middle of the base layer; c) 10 cm below subgrade; d) ambient

Regression analyses were then performed between moisture data and IRI. All R-square values were less than 0.5, except for the one in the subgrade in the GC section due to the filtering and draining ability provided by the geogrid composite. With the high slope of linear regression, it means that the IRI of the pavement was not affected by water potential even if the regression is strong. Generally, the riding quality tested by SurPro was not affected by environmental factors.

7.4.3.3 Impact of Traffic

From Figure 7-22, roughness measured on different wheel paths needs to be evaluated to see the impact of traffic loading on it. Table 7-22 shows the variance analysis of IRI measurements between two wheel paths. Compared with Table 7-19, higher CoVs were observed, which indicates that the impact of traffic loading is more critical than that of instrumentation.

Table 7-22 Variances Analysis of IRI Value Between Wheel Paths

	Eastbound			Westbound		
	Mean (m/km)	**Std. dev. (m/km)**	**CoV**	**Mean (m/km)**	**Std. dev. (m/km)**	**CoV**
			Summer 2022			
Section #1: CT	1.76	1.11	62.87%	2.95	1.65	56.08%
Section #2: GG	2.50	1.37	54.94%	2.07	0.85	40.78%
Section #3: GC	1.66	1.21	72.47%	1.39	0.85	60.84%
			Winter 2023			
Section #1: CT	2.82	1.67	59.45%	1.88	1.00	53.07%
Section #2: GG	2.45	1.14	46.58%	2.35	1.23	52.33%
Section #3: GC	1.54	0.90	58.62%	1.76	1.06	60.04%
			Spring 2023			
Section #1: CT	1.77	0.94	52.91%	2.39	1.24	51.80%
Section #2: GG	2.27	1.21	53.47%	2.24	1.63	72.88%
Section #3: GC	1.75	1.12	63.91%	1.32	0.86	65.12%

Furthermore, a student's t-test was performed on the measurements between the wheel paths to further verify the impact of traffic loading on each lane and overall data, whose results are listed in Table 7-23. The two-tailed p-values prove that different loading does not impact the roughness of pavement with no significant differences between wheel paths with a p-value greater than 0.05.

Table 7-23 T-test Analysis of Stiffness Value Between Wheel Paths

	Eastbound		Westbound		Overall	
	LWP	RWP	LWP	RWP	LWP	RWP
Mean (m/km)	2.05	2.07	2.05	2.03	2.05	2.05
Variance (m/km)	0.96	0.13	0.86	0.12	0.44	0.05
t Stat	0.04		0.05		0.00	
P(T<=t)	0.970		0.961		0.998	

Additionally, the t-test was performed between two-wheel paths for each section. From the analysis results shown in Table 7-24, IRIs in CT and GG sections are affected by different traffic loading, in which roughness in the GG section is the most consistent between different wheel paths with the highest p-value (i.e., 0.630). This can lead to a conclusion that the pavement riding quality can be enhanced by embedding geogrid in the asphalt by distributing the traffic loading and providing less variation in the roughness throughout the pavement. Nevertheless, IRI in the GC section was analyzed to be impacted by traffic loading with a p-value less than 0.05.

Table 7-24 T-test Analysis of Stiffness Value Between Wheel Paths in Each Section

	Section #1: CT		Section #2: GG		Section #3: GC	
	LWP	RWP	LWP	RWP	LWP	RWP
Mean (m/km)	2.60	1.93	2.33	2.29	1.22	1.93
Variance (m/km)	0.13	0.07	0.01	0.01	0.02	0.01
t Stat	2.15		0.56		6.58	
P(T<=t)	0.165		0.630		0.022	

7.4.4 Driving Test

The driving test was performed in August 2022 and August 2023. The truck was driven on test sections in 2022 at approximately 1.5 km/hr, while it was driven in 2023 at approximately 4 km/hr. The truck was driven twice in both years and the average was taken. The ambient temperature during testing was 28.1 °C and 26.9 °C in 2022 and 2023, respectively, obtained from the weather station installed in the same township.

7.4.4.1 Pressure on the Subgrade

The changes in the readings obtained from pressure cells installed at the interface of the subgrade and base layer were analyzed and compared to evaluate the impact of traffic loading. The truck was driven directly on wheel paths so that the pressure cells installed on RWP could capture the responses. The pressure results of the truck driving test performed in 2022 are plotted in Figure 7-25.

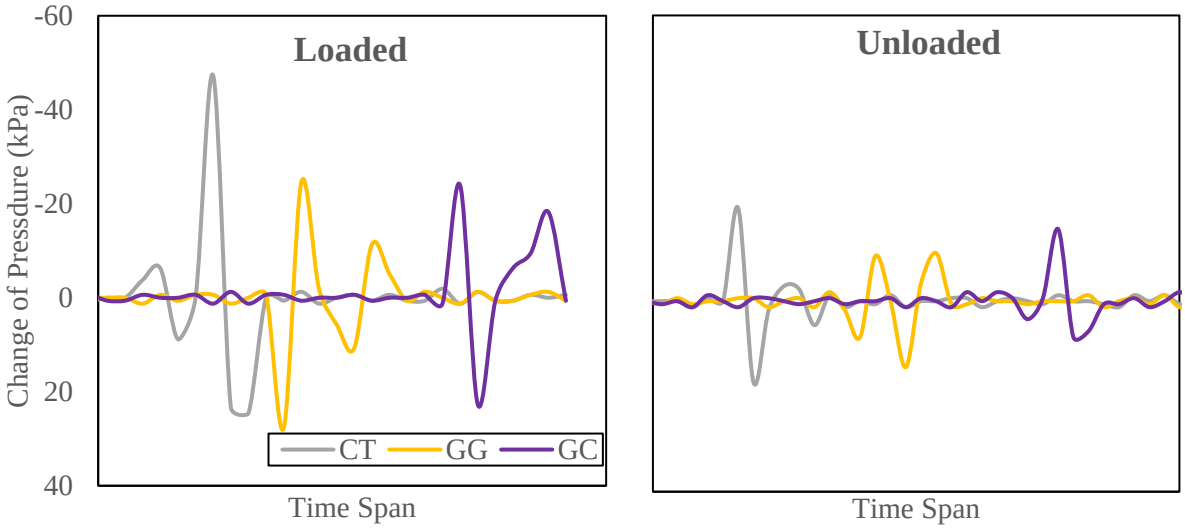

Figure 7-25 Pressure Response on Subgrade of Truck Driving Test in 2022

As the truck was driven from Section #1 (CT) to Section #2 (GG) to Section #3 (GC), the results were plotted against the time span. The negative value indicates compressive pressure, while the positive value is tension, which indicates the rebound when pressure leaves the position of the sensor in this context. The first pressure shown in each section was exerted from the steering axle, while the second one was from the rear ones. In the loaded scenario, more pressure was experienced from the rear axles in the CT section, while the peak pressure values were lower and closer between that from the steering and rear axles in the GG and GC sections. This explains the capability of geogrid and geogrid composite to distribute loading by acting as an interlayer system. In the unloaded scenario, the pressure was generally lower compared with the loaded one, while a higher pressure was experienced from the steering axle in the CT section. The GG section still exhibits similar pressure from the steering and rear axles. The pressure from rear axles was higher than that from steering axles in GC sections, while the maximum peak pressure (listed in Table 7-25) experienced in GG and GC sections was lower than that in CT section, establishing the reinforcement function provided by geogrid in the asphalt and

geogrid composite on the subgrade. Geogrid in asphalt concrete shows the best performances with the lowest peak pressure.

Table 7-25 Peak Pressure Experienced at Subgrade (kPa)

	Loaded		Unloaded	
	2022	**2023**	**2022**	**2023**
Section #1 CT	47.28	20.17	19.54	10.72
Section #2 GG	24.58	10.71	10.09	6.93
Section #3 GC	23.95	26.47	15.12	2.52

The pressure results of the truck driving test performed in 2023 are plotted in Figure 7-26. The truck was driven at a faster speed in 2023, thus only pressure from one axle was captured. The subgrade in the GG section still experienced a lower pressure compared with the CT section with the geogrid in the asphalt concrete distributing the load. GC section has the lowest pressure at the interface of subgrade and base with unloaded trucks, while it shows the highest pressure under the traffic of the loaded truck. A sudden stop at the GC section could also be the reason contributing to this.

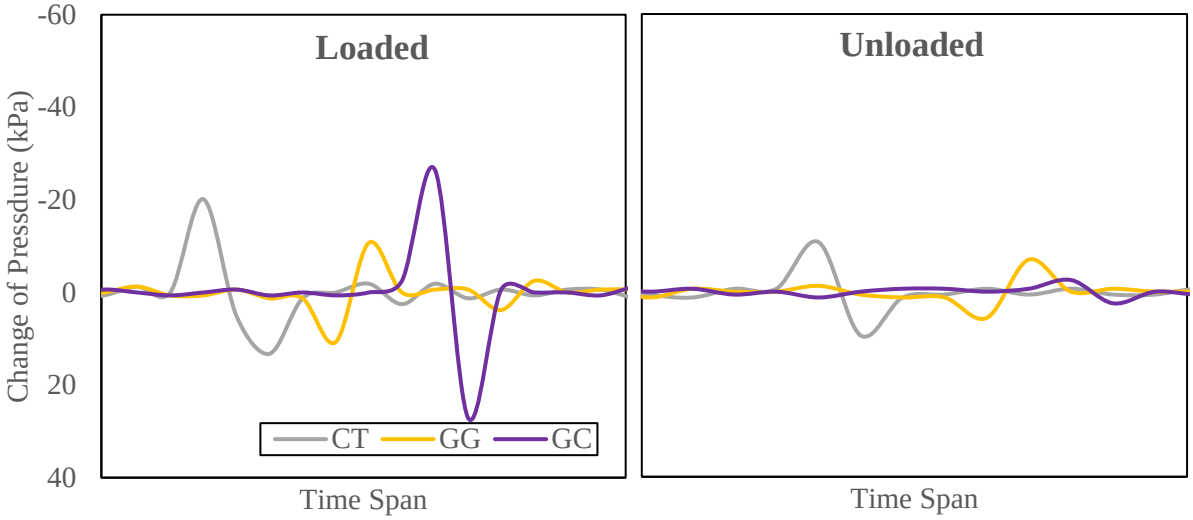

Figure 7-26 Pressure Response on Subgrade of Truck Driving Test in 2023

Referring to Table 7-25, the sections generally experienced lower pressure at the interface of the subgrade in 2023. Several reasons could be attributed to this pattern, the driving test was performed shortly after the placement of the asphalt surface course. The truck was driven at a faster speed (around 4 km/hr) in 2023, which disabled the pressure cells to capture loading from both the steering and rear

axles. The ambient temperature on the testing day in 2023 was lower than that in 2022, which led to a "cooler" pavement structure. Based on previous discussions, lower temperatures could result in higher stiffness of the pavement. Also, a sudden stop after the truck left the last section (GC section) may cause a higher pressure measured.

7.4.4.2 Strain on the Subgrade and in the Asphalt

Based on the instrumentation plan illustrated in Figure 4-1, a strain gauge was installed in the subgrade in the longitudinal direction along RWP in the CT section and GC section. The locations are close to where the pressure cells are located. The longitudinal strain on the subgrade of the truck driving test performed in 2022 is plotted in Figure 7-27. Negative value means compressive strain while positive value means tensile strain. The longitudinal strain experienced on the subgrade in GC sections is much lower than that in the CT section, which can be attributed to the geogrid composite installed above the sensor to serve as a lateral restraint.

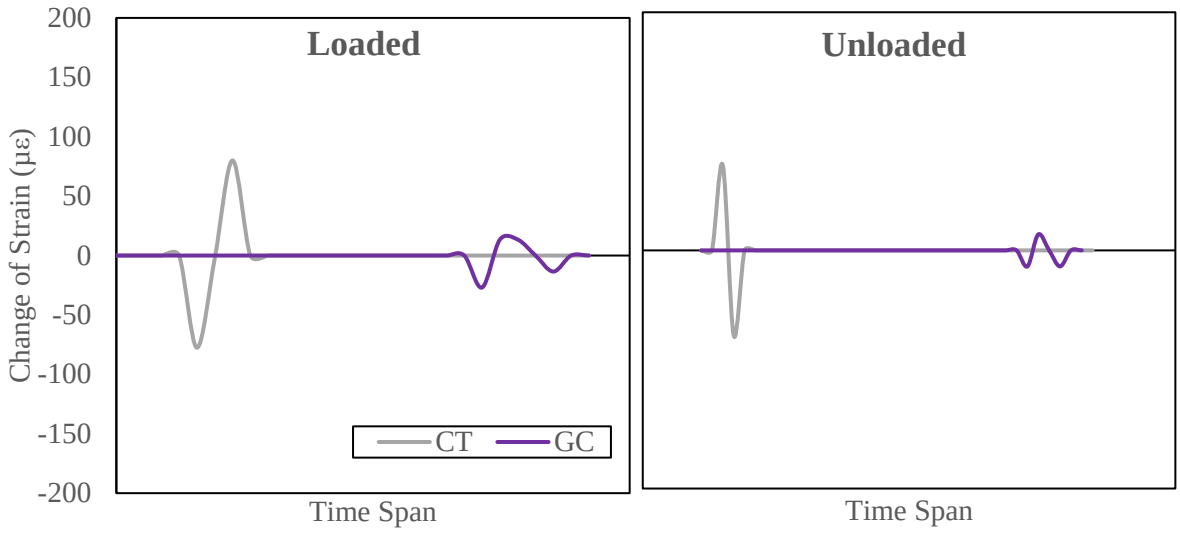

Figure 7-27 Longitudinal Strain Response on Subgrade of Truck Driving Test in 2022

The longitudinal strain on the subgrade of the truck driving test performed in 2023 is plotted in Figure 7-28. In 2023, the subgrade in the GC section experienced higher longitudinal strains. The weaker subgrade in GC can be one reason leading to these results.

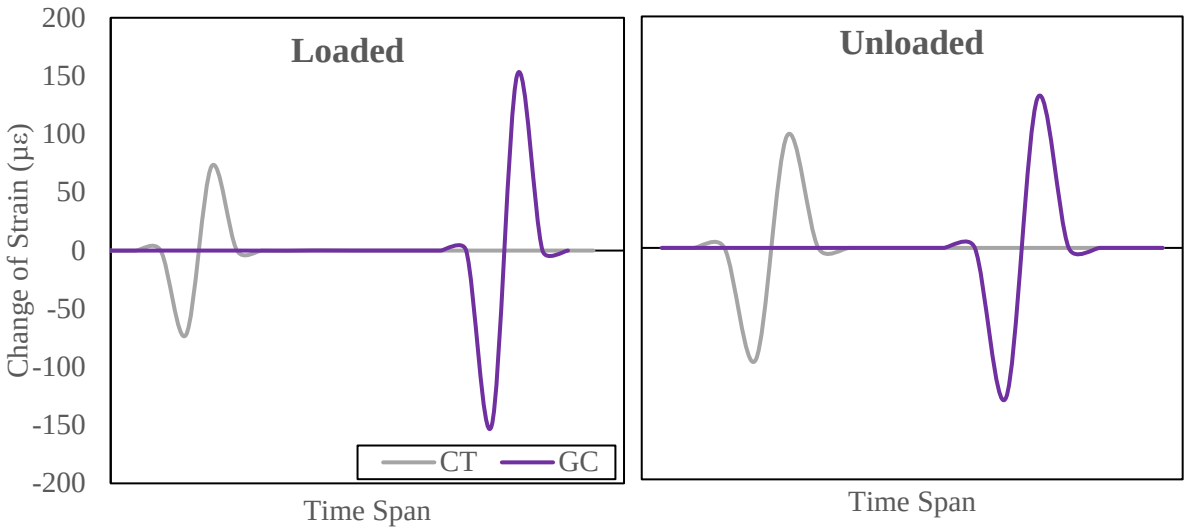

Figure 7-28 Longitudinal Strain Response on Subgrade of Truck Driving Test in 2023

The maximum longitudinal strain (compressive) experienced on the subgrade in CT and GC sections is listed in Table 7-26. It should be noted that the strain from the unloaded truck in 2022 was lower than that from the loaded truck, while the strain from the unloaded one was higher than that from the loaded one in the CT section in 2023. This may indicate a potential problem with the strain gauge in the CT section.

Table 7-26 Peak Longitudinal Strain Experienced at Subgrade (με)

	Loaded		Unloaded	
	2022	**2023**	**2022**	**2023**
Section #1 CT	-77.57	-72.32	-71.48	-96.80
Section #3 GC	-26.93	-150.57	-13.47	-129.28

Other than the strain gauges at the subgrade, the asphalt strain gauges in both longitudinal and transverse directions installed at the base lift of the asphalt binder course were analyzed. Table 7-27 and Table 7-28 present peak strain experienced at the bottom of the asphalt course in longitudinal and transverse directions, respectively. If no value was shown, it represents that the sensor was not able to capture the loading. The strain values were mostly higher under the traffic of the loaded truck, while the only exception was the transverse strain in 2022.

The longitudinal strain experienced in the asphalt binder course in 2023 was the lowest in the GG section, which examines the reinforcement of geogrid embedded in the asphalt above. It also has the

lowest transverse strain. By serving as a tensile element, the geogrid was proved to be able to distribute the load and restrain the lateral movement.

Table 7-27 Peak Longitudinal Strain Experienced at the Bottom of Asphalt Concrete (με)

	Loaded		Unloaded	
	2022	**2023**	**2022**	**2023**
Section #1 CT	-	-35.07	-	15.45
Section #2 GG	-	3.99	-	2.00
Section #3 GC	-	-90.44	-	-2.11

Table 7-28 Peak Transverse Strain Experienced at the Bottom of Asphalt Concrete (με)

	Loaded		Unloaded	
	2022	**2023**	**2022**	**2023**
Section #1 CT	-33.90	5.54	-68.45	-10.76
Section #2 GG	-0.35	-1.06	-	-
Section #3 GC	-11.68	-27.16	-59.84	-5.55

7.5 Chapter Summary

This chapter presents the field testing performed on the trial sections. Non-destructive testing such as LWD and SurPro was used to evaluate the pavement stiffness and roughness. A driving test was proposed to utilize the instrumented sensors to capture the mechanical responses exerted by a construction truck. Visual inspection performed monthly showed that no cracking or obvious distress occurred.

During construction, the stiffness of compacted subgrade, granular base, asphalt binder course, and asphalt surface course was tested separately. The results were compared with the laboratory testing (CBR) conducted on the unbound materials. The unbound materials have similar structural capacity tested by LWD for the three sections. More variability between two-wheel paths was shown on the asphalt surface course compared to that on the asphalt binder course. The stiffness was improved generally after the surface course was paved, and the level of improvement is consistent among the three sections. The significant reduction of IRI in the GG section after the surface course was paved indicates the necessity of an overlay of the surface course with the geogrid reinforcement in the asphalt concrete course. Additionally, the IRI measurements in the geogrid composite were the lowest on both the binder course and surface course, which implies a higher construction quality. No significant impact of instrumentation on roughness existed after surface course placement was analyzed by t-test.

LWD was used to test the stiffness on both wheel paths in both lanes seasonally. The GG section shows the lowest CoVs in every season, which indicates a better consistency in stiffness throughout the pavement reinforced by geogrid. Regression analysis was performed between temperature and stiffness, with the strongest regression in the CT section. With similar slopes, this indicates that the pavement stiffness in the CT section tends to be affected by ambient and pavement temperatures the most. This implies the reinforcement provided by geosynthetic material. No correlation was shown from the regression analysis between moisture and stiffness, except that with water potential in the subgrade in the GC section, which shows the filtering and draining effect throughout a year with one annual freeze-thaw cycle provided by the geogrid composite on the subgrade. The student's t-test done between wheel paths shows that the CT section is mostly affected by traffic loading with the lowest p-value, which demonstrates geosynthetic materials can better distribute the traffic loading.

IRI was tested on both wheel paths on both lanes in summer 2022, winter 2023, and spring 2023. Both ANOVA and regression analysis examine that environmental factors do not have a big impact on the entire pavement roughness. In terms of the impact of traffic loading, pavement riding quality can be enhanced by embedding geogrid in the asphalt by providing less variation in the roughness throughout the pavement. However, IRI in the GC section was analyzed to be significantly impacted by traffic loading. Generally, as one year after construction completion is still considered as the early life of the pavement, it would be difficult to find major differences due to environmental factors unless there was some major defect that occurred during construction.

A dump truck was driven on the test sections in 2022 and 2023 with instrumented mechanical sensors capturing the responses. GG section experienced the lowest peak pressure and more distributed loading from steering and rear axles on the subgrade, with less horizontal strain at the bottom of asphalt in both longitudinal and transverse directions. Compared with the CT section, the GC section had a lower pressure and horizontal strain at the interface of the subgrade in 2022, but a higher pressure and strain in 2023.

Chapter 8
In-Service Pavement Performance Monitoring by Instrumentation

8.1 Introduction

This chapter introduces a comprehensive analysis of the field trial sections and weather station data spanning the period from August 2022 to August 2023, focusing on an exploration of the relationship between environmental factors and the performance of geosynthetic-reinforced pavements. Emphasizing the significance of temperature and precipitation as key environmental influencers, the study investigates an in-depth examination of the layer temperature data, layer moisture levels, asphalt strain characteristics, and subgrade stresses and strains, establishing critical correlations between these parameters and the impacts of environmental variations. The investigation encompasses a meticulous evaluation of seasonal changes and daily temperature fluctuations, highlighting their substantial influence on the pavement's structural response and performance. Moreover, the chapter investigates a comprehensive assessment of the frost condition within the pavement and subgrade, offering crucial insights into the dynamics of freezing and thawing phenomena.

8.2 Environmental Factor Analysis

The environmental factors were analyzed through the ambient temperature and rainfall data obtained from a weather station installed on Notre Dame Drive (NDD), which is close to the site. The cartesian coordinates of the weather station location are 43°26'11.0"N and 80°37'49.9"W, which is about 3.9 km away from the trial sections. To ensure the consistency and accuracy of the environmental data, they were compared with the data from Environment Canada (EC), while the weather station owned by Environment Canada was located at the Region of Waterloo International Airport (Government of Canada, 2023), whose straight-line distance away from the trial sections is about 22.4 km. The location of both weather stations from the site is shown in Figure 8-1.

The NDD weather station collects hourly temperature and rainfall data and also outputs daily mean, minimum, and maximum temperatures plus daily cumulative rainfall. The daily data were compared with those obtained from the EC weather station. Environment data from August 16, 2022, to August 16, 2023, were analyzed.

Figure 8-1 Location of Weather Stations

8.2.1 Ambient Temperature

The daily temperature data obtained from the NDD weather station included mean, maximum and minimum temperatures. It was compared to those obtained from Environment Canada weather station, as plotted in Figure 8-2, highlighting a consistent and similar trend in the temperature patterns recorded by both stations. This alignment in the temperature data highlights the reliability and consistency of the measurements obtained from the respective weather stations.

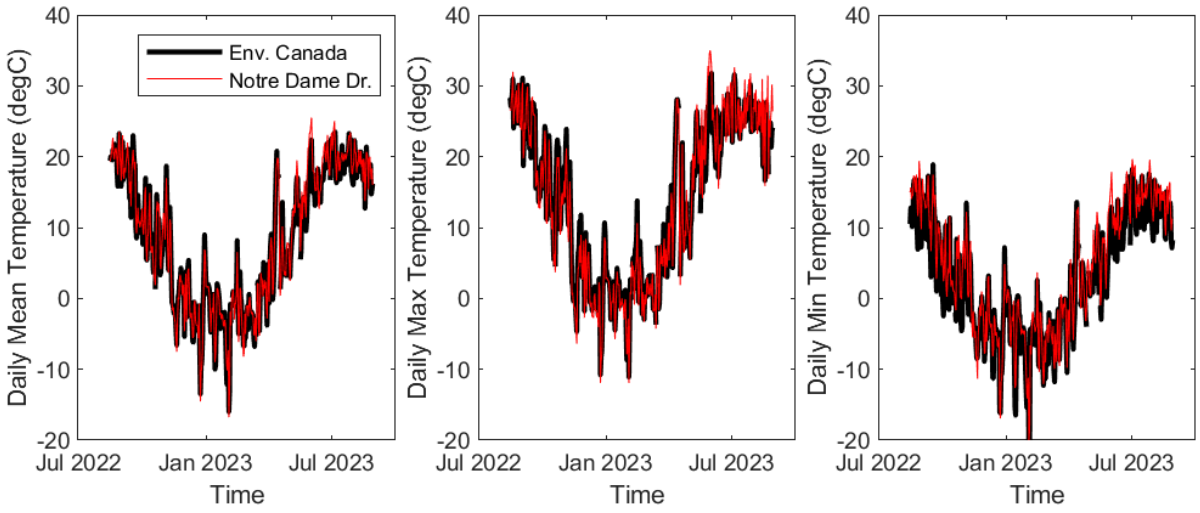

Figure 8-2 Comparison of Weather Station Temperature Data

To further validate the reliability of the temperature data, a student's t-test was conducted between the data obtained from both weather stations, using a null hypothesis at a 95% significance level. The results of the t-test revealed that the p-values for the mean and maximum temperatures were 0.574 and 0.881, respectively, indicating the absence of statistical differences between the temperature data

obtained from the two weather stations for both the mean and maximum temperatures. These results, with p-values exceeding 0.05, suggest a high degree of consistency and agreement between the temperature measurements recorded by the NDD weather station and the Environment Canada weather station, further corroborating the reliability and accuracy of the data obtained from both sources. However, the t-test results for the minimum temperature data yielded a p-value of 0.013, indicating the presence of statistical differences between the minimum temperature measurements obtained from the two weather stations.

8.2.2 Precipitation

The comparison of daily cumulative precipitation data between the two weather stations is plotted in Figure 8-3. reveals some variabilities compared to the consistency of the temperature data. This variation in the precipitation data suggests that the differences observed could be attributed to the varying levels of rainfall experienced at the respective locations of the weather stations. Considering the proximity of the site to the NDD weather station, the environmental data obtained from the NDD weather station were selected for further analysis.

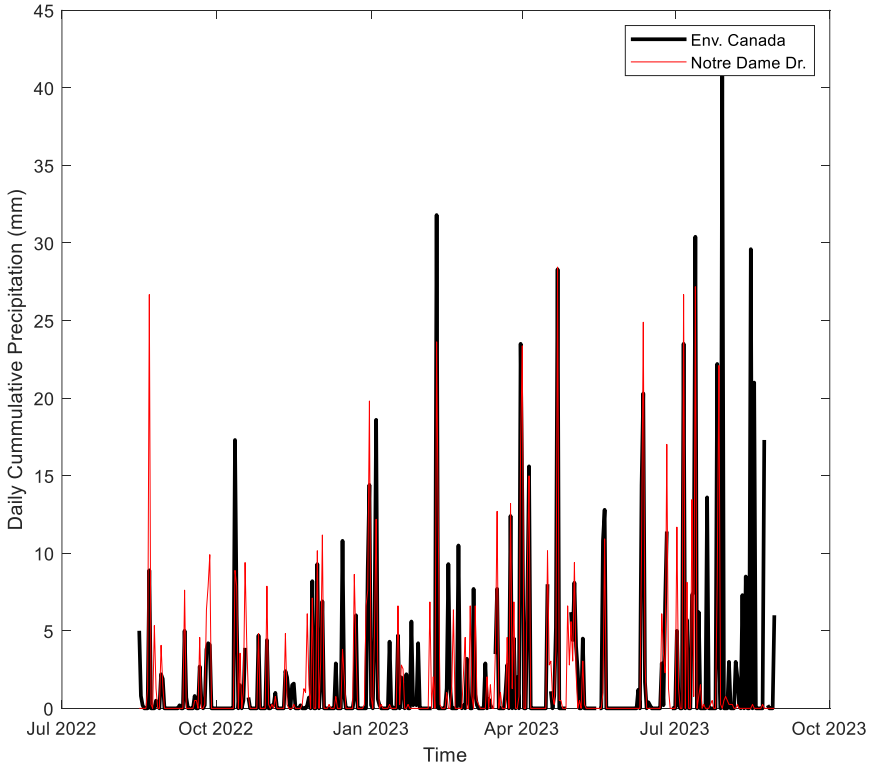

Figure 8-3 Validation of Weather Station Precipitation Data

A two-sample t-test was also performed on the daily cumulative precipitation data from both weather stations. The resulting p-value of 0.572 indicates the statistical equivalency between the cumulative precipitation data recorded by the two weather stations. This finding suggests a high degree of agreement and consistency in the cumulative precipitation measurements obtained from both the NDD weather station and the Environment Canada weather station, further confirming the reliability and accuracy of the data collected from these sources.

The identification of wet days, defined as those with daily precipitation exceeding 1 mm, serves as a crucial parameter for assessing the frequency and intensity of rainfall events within the study area (McErlich et al., 2023). A total of 96 wet days were counted out of 365 days. This implies that the study area experienced precipitation events meeting this defined threshold taking up approximately 26% of the year.

8.2.3 Freezing Index

There are three major factors that can be attributed to frost action, including the existence of frost susceptible soils, freezing conditions and moisture sources (Y. H. Huang, 2004). As classified in Section 4.3, the subgrade soil in the trial sections is mainly a clayey sand / sandy clay mixture, while the soil frost susceptibility is slight to severe. The freeze-thaw disturbance is necessary to be considered in this study.

In this case, analyzing the seasonal ground freezing characteristics is crucial for assessing the impact of freezing temperatures on various engineering and environmental processes. In this context, the air-freezing index (AFI) serves as a key parameter for evaluating the freezing information and estimating the depth of frost penetration, particularly in areas with shallow groundwater conditions. The AFI is a comprehensive measurement that accounts for both the magnitude and duration of freezing days when the daily mean temperature remains below 0°C. The calculation of the daily mean temperature incorporates the highest and lowest temperatures over the designated period of analysis, which can be computed by Equation 8-1. This process allows for a precise assessment of the temperature variations and enables the computation of the AFI using the cumulative degree-days. Subsequently, the cumulative freezing degree-days can be calculated using Equation 8-2 (Bilotta, Bell, Shepherd, & Arguez, 2015).

Equation 8-1

$$\bar{T} = 0.5(T_{min} + T_{max})$$

Equation 8-2

$$FDD = \sum_{i=1}^{N} \overline{T}_i$$

where:

$\bar{T}$ = daily mean temperature (°C)

T_{min} = daily minimum temperature (°C)

T_{max} = daily maximum temperature (°C)

FDD = freezing degree-days (°C)

N = number of days

The seasonal AFI value is determined by calculating the difference between the highest and lowest extrema points derived from the seasonal curve, which is plotted based on the cumulative freezing degree-days over the number of days. This approach allows for the observation of deviations in the daily mean temperature above or below 0°C during the colder seasons of the year (Steurer, Crandell,', & Member, 1995). The highest extrema point represents the beginning of frost action in the year, while the lowest represents the end of frost. With the accumulated freezing degree-days data over 365 days plotted in Figure 8-4, the highest extrema point is 1250 FDDs and the lowest is 955 FDD, which gives the seasonal AFI value as 295 FDDs.

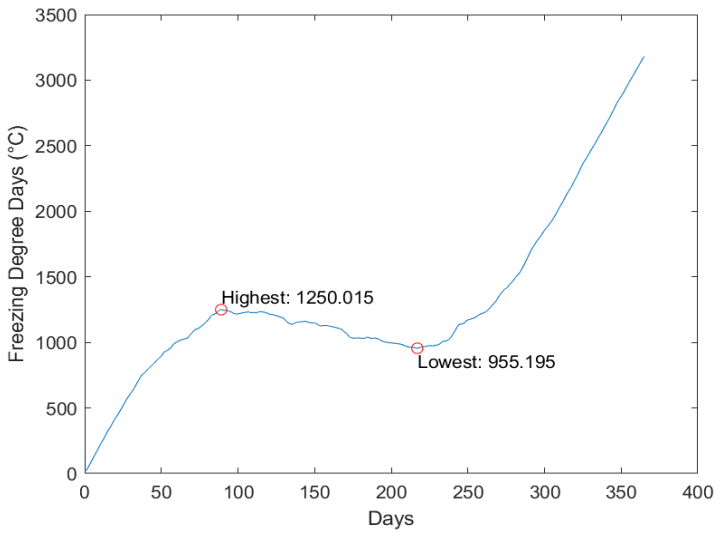

Figure 8-4 Freezing Degree-Days Curve

Ontario Ministry of Transportation (MTO) has developed an empirical model to estimate frost penetration depth with knowing the AFI, as presented in Equation 8-3 (MTO, 2013). Frost penetration refers to the depth beneath the paved surface. Therefore, the frost depth in the study area from 2022 to 2023 was estimated to be 61 cm.

Equation 8-3

$$P = -38.2 + 5.78\sqrt{AFI}$$

where:

P = frost penetration (cm)

8.3 Impact of Environment on Pavement Temperature

Pavement temperature plays a critical role in pavement design, as it significantly influences the distribution of temperature gradients and thermal variations within the pavement structure. This is particularly important for comprehending how temperature fluctuations impact the performance and durability of flexible pavement. Given the unique viscoelastic behaviour of asphalt materials, which are notably sensitive to changes in temperature, the effects of temperature differentials on pavement integrity and functionality can be significant. The cyclic thermal stresses induced by temperature changes can promote the development of fatigue damage within the asphalt concrete, ultimately forfeiting the structural integrity of the flexible pavement. The repeated thermal expansion and contraction of the asphalt layers contribute to the initiation and propagation of fatigue cracks, significantly impacting the overall service life and performance of the pavement structure (Khan, Islam, & Tarefder, 2019). Furthermore, the contraction of the asphalt layers under cold temperatures can lead to the development of transverse cracks (Faisal, Khan, & Tarefder, 2017). Moreover, pavement heaving may ensue due to the formation of ice lenses within the subgrade when temperatures drop below freezing. During the thawing, the pavement may experience differential settlement (Ud Din, Mir, & Farooq, 2020b). Therefore, achieving an accurate assessment of the in-situ performance of flexible pavements hinges on the precise prediction of temperature distribution within the various pavement layers.

The ambient temperature serves as a fundamental parameter that significantly influences the thermal dynamics within the pavement structure, contributing to the development of temperature gradients and thermal stresses. Solar radiation, with its direct impact on the heat absorption and dissipation characteristics of the pavement surface with the dark colour of asphalt materials, contributes

significantly to the temperature distribution within the pavement layers (Solaimanian & Kennedy, 1993). Additionally, the impact of freeze-thaw cycles on pavement temperature is a critical consideration, given its direct influence on pavement performance. These cycles can be broadly categorized into two distinct types: seasonal freeze-thaw cycles and daily freeze-thaw cycles. Seasonal freeze-thaw cycles encompass the variations in temperature patterns that occur over the course of a year, contributing to the repeated freezing and thawing of the pavement structure. Daily freeze-thaw cycles represent the temperature fluctuations experienced within a 24-hour period, with temperatures typically rising during the daytime and dropping at night.

As presented in Figure 4-1 Section Side View of Field Instrumentation and Construction, the temperature sensors were installed in three locations in each section: in the base lift of the asphalt binder course; in the middle of the granular base layer; and at 10 cm below the subgrade. The depths of the sensors from the pavement surface are 200 mm, 425 mm, and 750 mm, respectively. The study period in this chapter is from August 16, 2022, to August 16, 2023, unless specified. All the temperature sensors collected readings every five minutes and were aggregated into hourly and daily means for analysis. The collected temperature sensor collected data within the timeframe specified below:

- Sensor in the asphalt layer in the control section: August 16, 2022, to Jun 11, 2023.
- Sensor in the base layer in the control section: August 16, 2022, to May 5, 2023.
- Sensor in the subgrade in the geogrid section: August 16, 2022, to December 17, 2022 & March 1, 2023, to August 16, 2023.
- All other sensors: August 16, 2022, to August 16, 2023.

8.3.1 Seasonal Changes in Pavement Temperature

The daily mean temperature profiles from August 16, 2022, to August 16, 2023, are presented in Figure 8-5, alongside the ambient temperature profile from the NDD weather station. The profiles illustrate a complete freeze-thaw cycle over the course of a year, with temperatures declining during the winter months and gradually rising as spring unfolds. It is noteworthy that the temperature variations within the asphalt binder course predominantly align with the changes in ambient temperature, underscoring the significant influence of external environmental factors on the thermal behaviour of the upper pavement layers. In contrast, the temperature profiles observed in the base and subgrade layers demonstrate a relatively stable trend, suggesting a diminished influence of ambient temperature variations with increasing depth. This highlights the subsurface layers' improved thermal stability and

reduced susceptibility to the immediate impacts of seasonal temperature fluctuations. Moreover, the temperature differentials between the asphalt surface and the ambient environment reveal a consistent pattern of the asphalt temperature exceeding the ambient temperature, particularly during the summer months. This disparity can be primarily attributed to the asphalt surface's unique capacity to absorb and retain heat from solar radiation, facilitated by its dark colour and high thermal absorption properties (Meza & Varas, 2000).

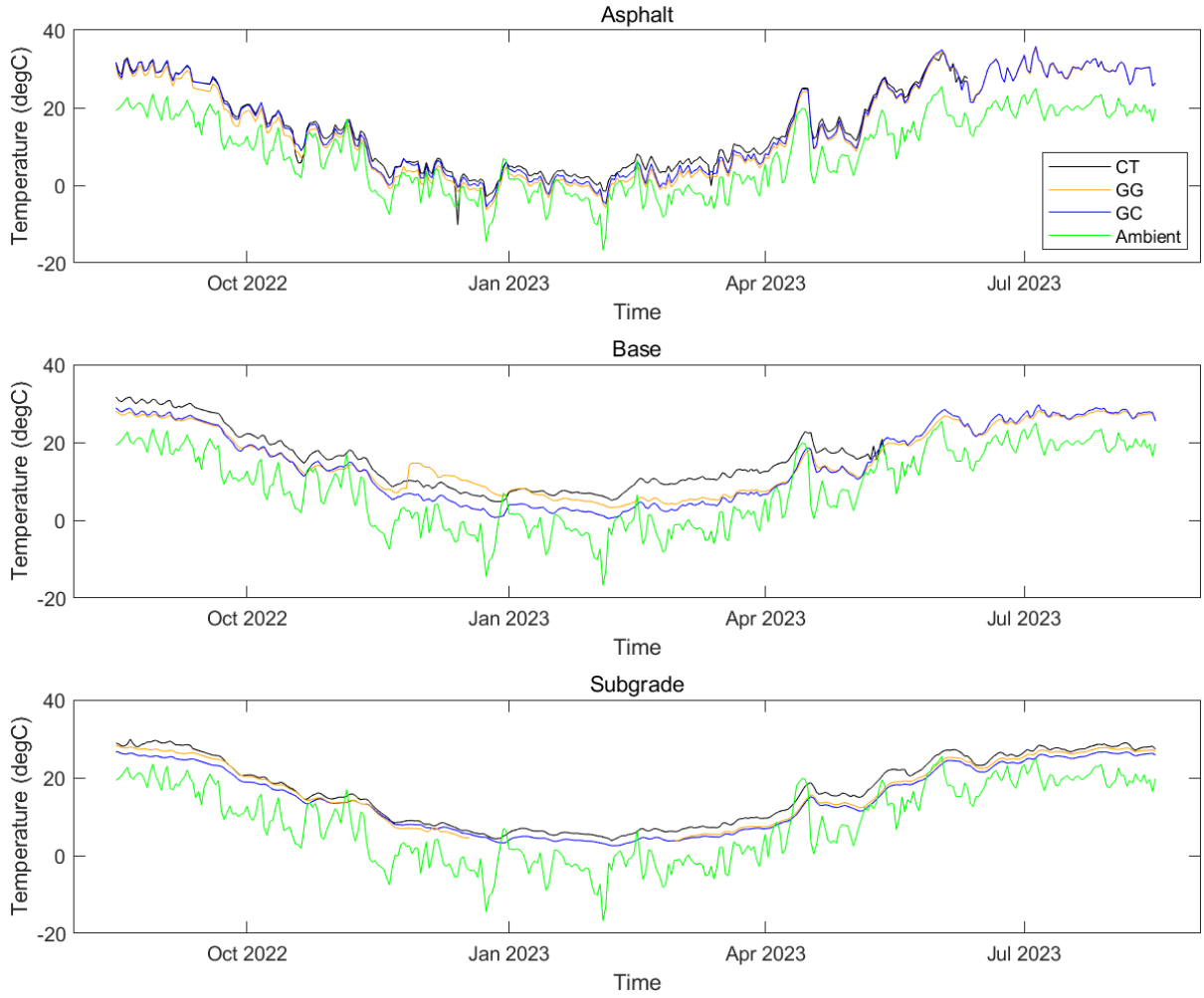

Figure 8-5 Daily Mean Layer Temperature Profiles

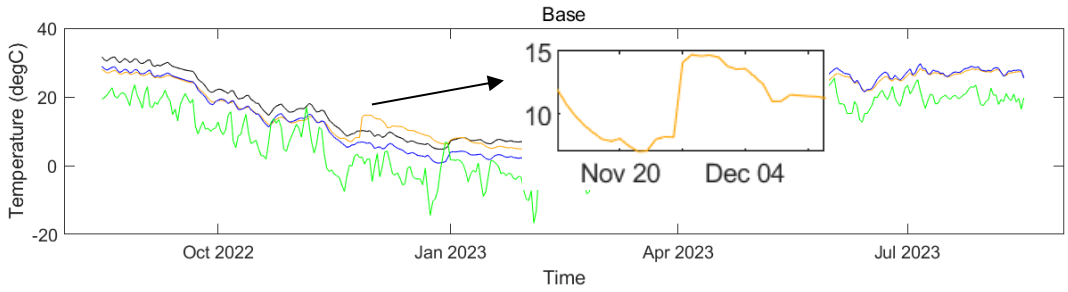

Figure 8-6 Temperature Fluctuation in Base Layer in the GG Section in November 2022

Additionally, the anomalous rise in temperature was observed in the base layer of the GG section around the end of November 2022, as highlighted in Figure 8-6. Upon further investigation, it was discovered that this unusual temperature spike coincided with a notable level of precipitation, as depicted in Figure 8-7.

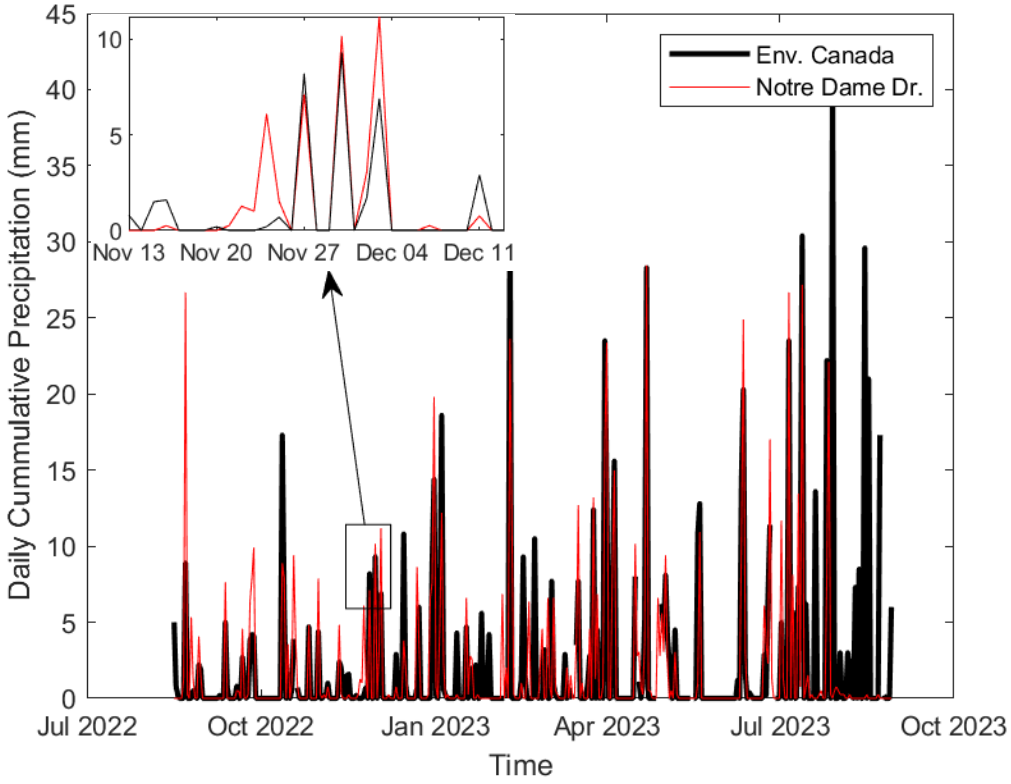

Figure 8-7 Precipitation November 2022

This correlation between the observed rise in temperature and the concurrent rainfall event strongly suggests the potential influence of moisture infiltration within the pavement structure, contributing to the atypical thermal response and temperature fluctuations within the base layer. The identification of

this relationship between the precipitation data and the irregular temperature variations emphasizes the importance of studying the moisture contents within the pavement structure. In the next section, the moisture data in the pavement structure will be studied regarding this observation as well.

Before comparing the temperature distribution in each section, ANOVA was conducted on the layer temperatures in three sections, using a null hypothesis at a 95% significance level. Significant differences were proved to exist between different sections with p-values all less than 0.05 (0.039 for asphalt temperatures, 0.000 for base layer, and 0.004 for subgrade temperatures). The distribution of data of all sections during the study period was illustrated in the box plot in Figure 8-8.

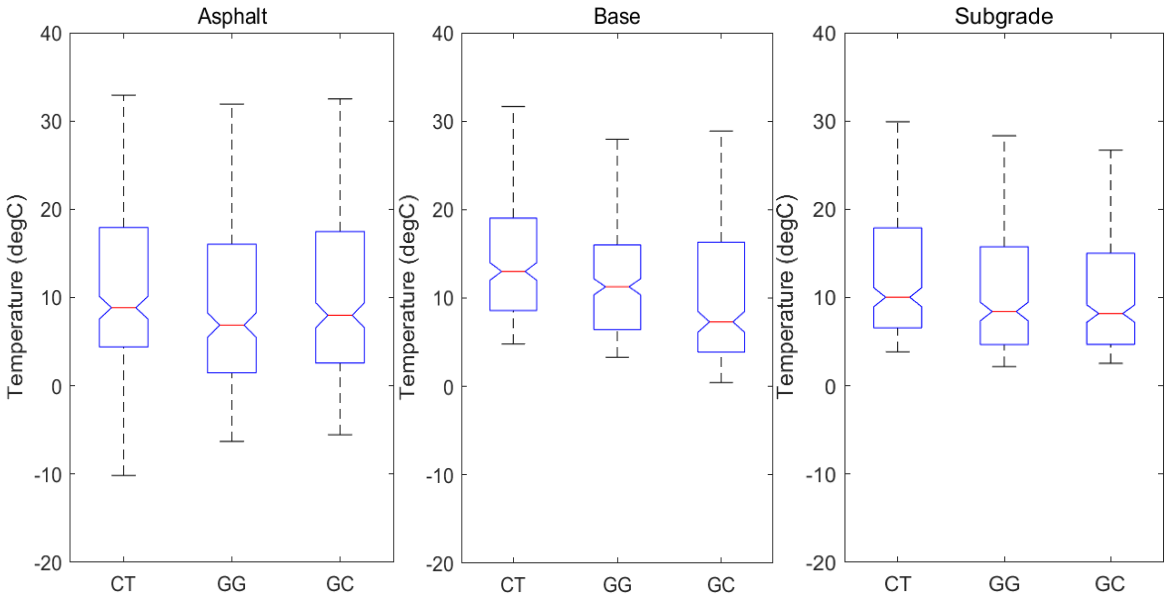

Figure 8-8 Box Plot of Layer Temperature Distribution in Three Sections

Following the observation of substantial temperature variations within the pavement structure across different sections, a study was conducted to assess the seasonal effects. Further statistical analyses were performed on layer temperatures, categorized into four distinct seasons. The results, as outlined in Table 8-1, indicate that the asphalt layer temperatures did not show statistical significance during the fall, spring, and summer seasons. However, the subgrade temperatures displayed significant differences among different sections across all seasons. Notably, the measurements of the CT sections in the asphalt and base layers were excluded from the ANOVA analysis during summer due to sensor damage.

Additionally, a two-sample t-test shown in Table 8-1 was conducted to compare the reinforced sections against the CT section. The analysis encompassed a comparison between the GG section and the CT section, as well as the GC section and the CT section. Apart from the already established

statistical equivalence in asphalt temperature as determined by ANOVA, the results highlighted that the subgrade temperature in the GG section during the fall season exhibited no statistically significant difference compared to that in the CT section. This implies a similar subgrade condition between the CT and GG sections. Conversely, the subgrade temperature in the GC section exhibited consistent significant differences across all four seasons when compared to the CT section. This observation suggests the role of the geogrid composite, installed on the subgrade with water drainage functionality, indirectly contributing to temperature insulation potential.

Table 8-1 P-values of Statistical Analysis of Pavement Temperatures in Different Seasons

		ANOVA (Three Sections)	T-test (CT/GG)	T-test (CT/GC)
Fall (2022-08-16 ~ 2022-11-16)	Asphalt	0.343	0.161	0.753
	Base	0.000	0.000	0.000
	Subgrade	0.037	0.255	0.010
Winter (2022-11-16 ~ 2023-03-16)	Asphalt	0.000	0.000	0.000
	Base	0.000	0.000	0.000
	Subgrade	0.000	-	0.000
Spring (2023-03-16 ~ 2023-06-16)	Asphalt	0.919	0.791	0.900
	Base	0.584	0.242	0.425
	Subgrade	0.001	0.007	0.000
Summer (2023-06-16 ~ 2023-08-16)	Asphalt	0.724	-	-
	Base	0.021	-	-
	Subgrade	0.000	0.000	0.000

To further investigate the insulation potential of geogrid composite on the subgrade in mitigating the impacts of temperature differentials on the underlying subgrade, the temperature difference between the middle of the base and subgrade was compared between CT and GG sections. The purpose is to see how temperatures transfer from the middle of the base layer to the subgrade in these two sections. Figure 8-9 provides a comprehensive visualization of the temperature variations, where the plotted values of the base temperature minus the subgrade temperature offer critical insights into the thermal dynamics and heat transfer mechanisms within the pavement structure. A value below zero implies that the subgrade temperature is greater than the base temperature, and vice versa. From the figure, the

fluctuations in the temperature differentials in the GG section, with values oscillating both above and below zero, were observed, while that in the CT section constantly remained above zero. Of particular significance is the observed negative temperature differentials in the GC section during the winter season, signifying that the subgrade temperature surpasses the base temperature. This critical finding emphasizes the insulation effectiveness of the geogrid composite in regulating and stabilizing the subgrade temperature, thereby mitigating the risk of frost heave and potential frost-related damages during the colder winter months. Conversely, the CT section demonstrates a consistent trend of the subgrade temperature being lower than the base temperature during the winter season, indicating a heightened susceptibility to frost actions and potential frost heave in the subgrade due to the lower temperatures. This concludes that the geogrid composite plays a critical role in insulating the subgrade and subsequently preventing the frost heave from the low temperature in winter.

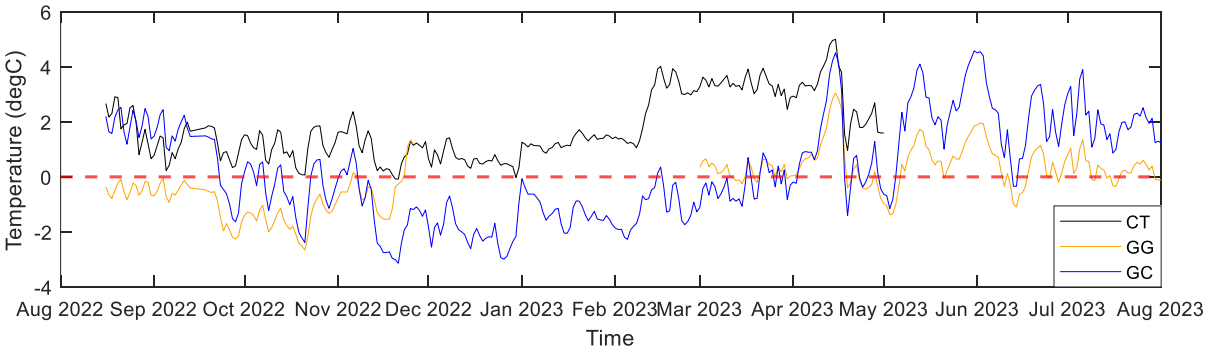

Figure 8-9 Temperature Differences Between Base Layer and Subgrade

8.3.2 Daily Temperature Changes on Pavement Temperature

The hourly mean temperature data was computed and presented in Figure 8-10, providing a detailed analysis of the temperature fluctuations throughout the day. Apart from the profile over one year, this figure offers a more granular view, enabling a comprehensive assessment of the impact of daily heating and cooling effects, characterized by higher temperatures during the daytime and lower temperatures at night.

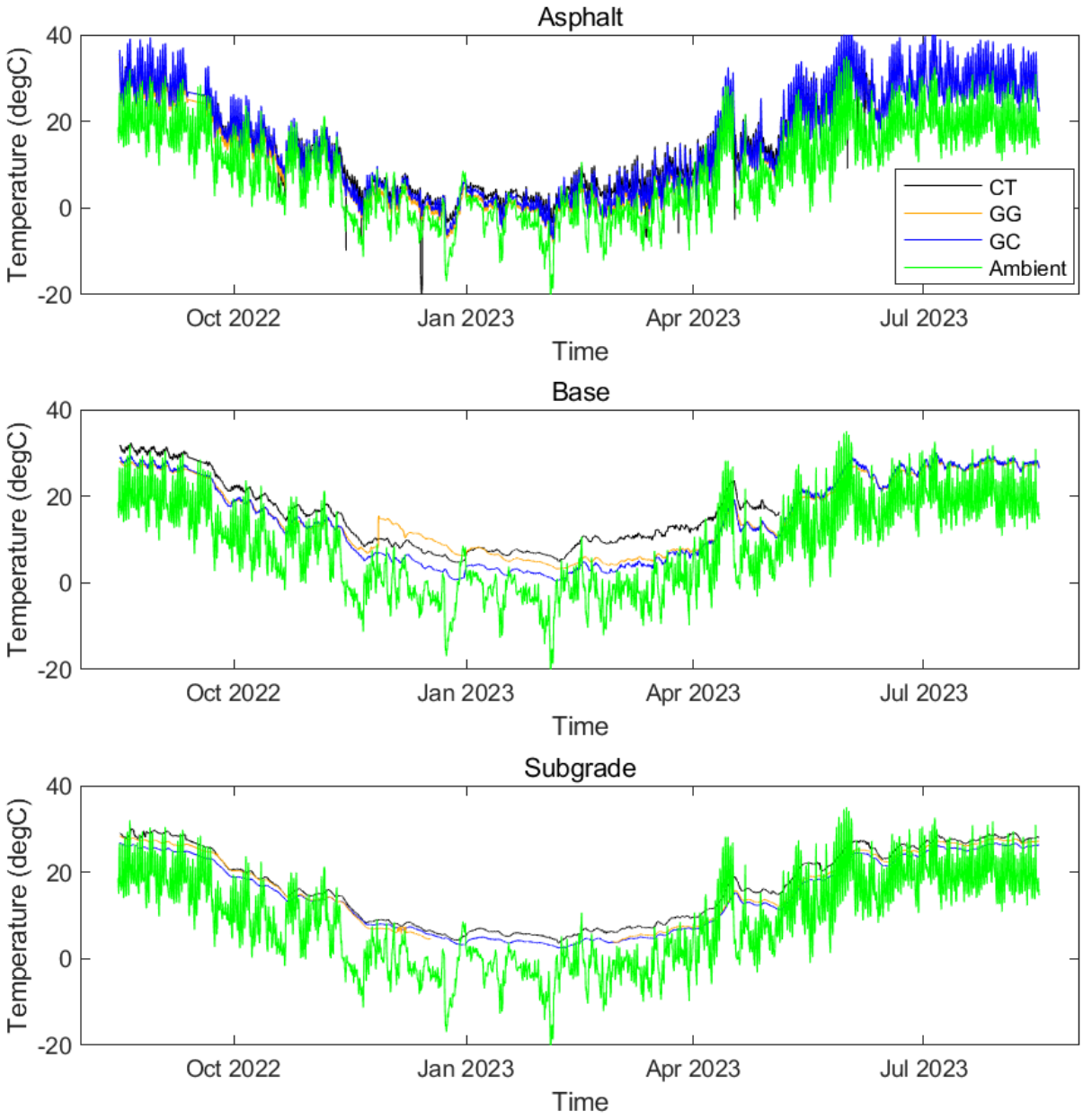

Figure 8-10 Hourly Mean Layer Temperature Profiles

Figure 8-11 specifically illustrates this dynamic in April 2023 as an example, demonstrating how daily temperature changes influence the temperatures of different pavement layers. The asphalt temperatures were clearly influenced by the ambient temperature, while the subgrade temperatures remained relatively stable, exhibiting a consistent trend. It is worth noting that the asphalt temperature exhibited a delayed response to changes in ambient temperature, indicative of the gradual process of heat transfer. Upon closer examination, it became apparent that the highest peak asphalt temperatures

in the GG section were slightly lower compared to those in the other two sections. Furthermore, both the base temperature and subgrade temperature in the CT section were higher than those observed in the GG and GC sections.

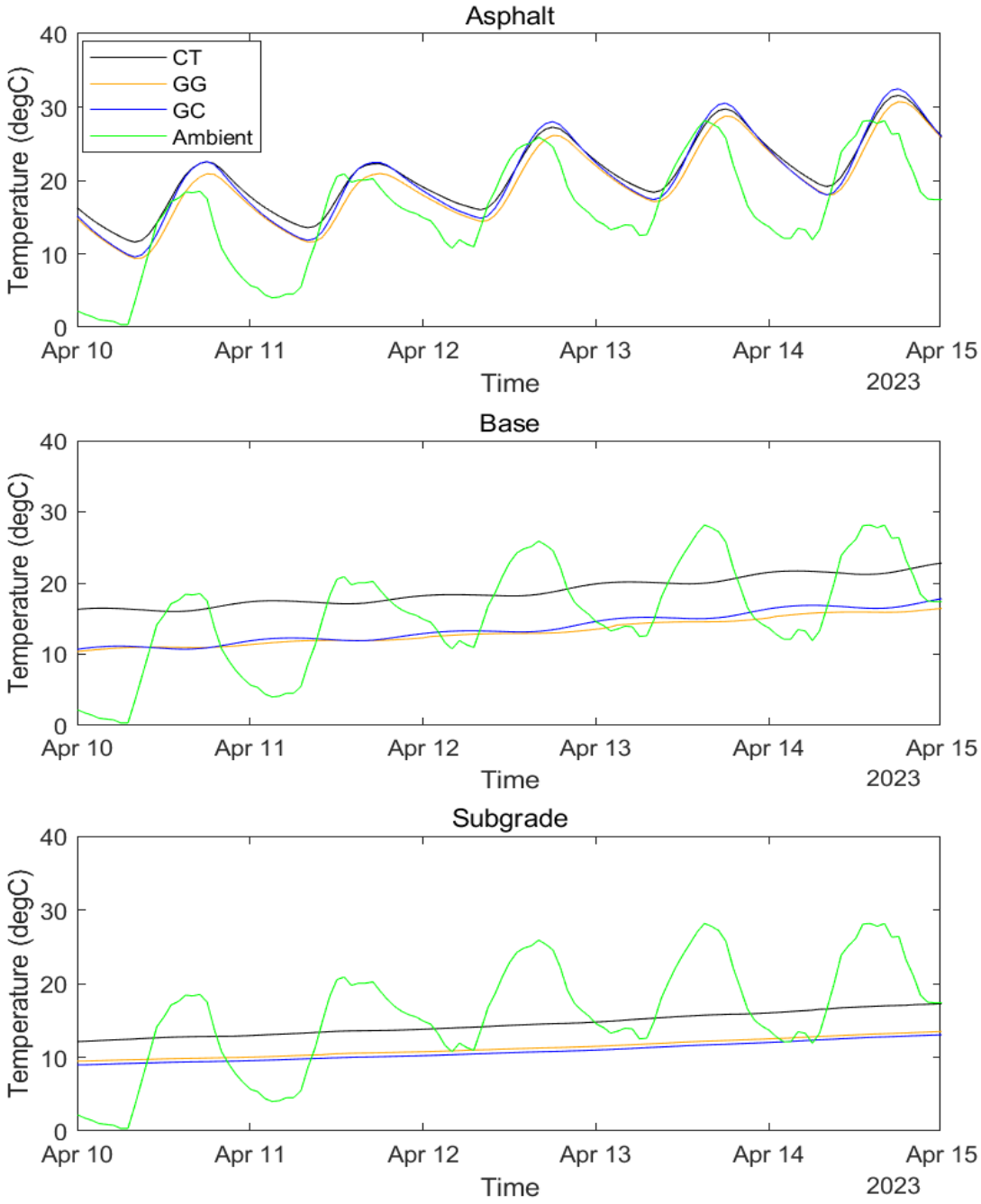

Figure 8-11 Pavement Temperature Profile with Daily Temperature Changes

The comparative assessment of the temperature differentials between noon and midnight, shown in Figure 8-12, provides valuable insights into the thermal response and dynamic temperature variations within the various layers of the pavement structure due to the daily heating and cooling effect. The detailed examination of the temperature differentials across the asphalt layer, base layer, and subgrade, specifically between the GG, GC, and CT sections, highlights the diverse thermal behaviour and distinct temperature fluctuations experienced within each section over the course of a day.

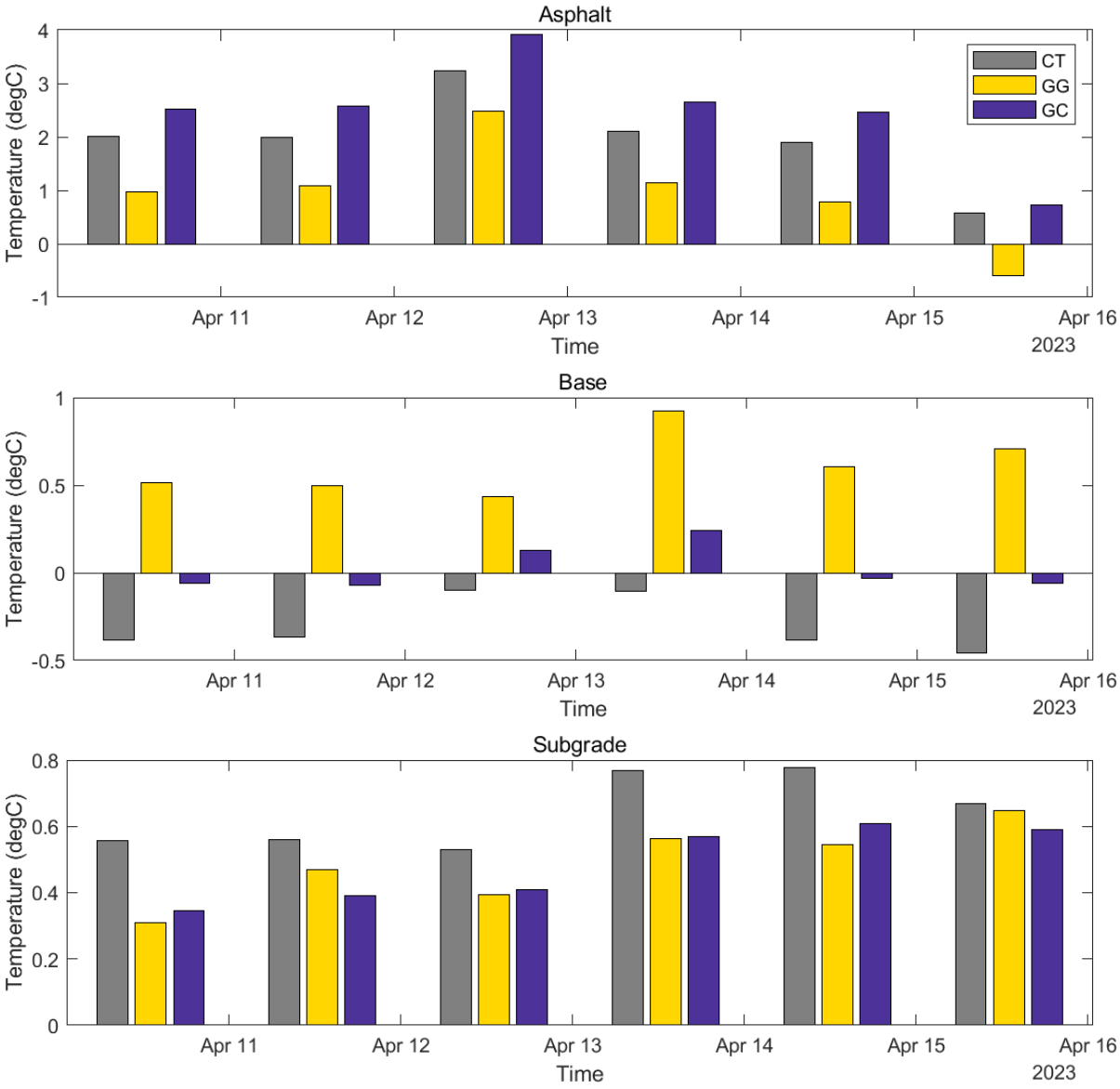

Figure 8-12 Differences of Pavement Temperature in the Noon and Midnight

Figure 8-12 illustrates the temperature differentials between noon and midnight, depicting the effect of heating and cooling effect during the day. The asphalt layer's temperature differentials reveal that the GG section consistently exhibits the lowest variation between noon and midnight temperatures, suggesting a relatively stable thermal response and enhanced temperature regulation within the asphalt layer, which may be attributed to the geogrid installed above. In contrast, the GC section displays the highest temperature variation, indicative of a more pronounced thermal response and increased susceptibility to temperature fluctuations within the asphalt layer. Within the base layer, the GG section demonstrates the highest variation between noon and midnight temperatures. Notably, in the subgrade, the CT section presents the highest temperature variation indicating a heightened susceptibility to temperature changes and thermal fluctuations within the subgrade layer.

8.4 Impact of Environment on Pavement Moisture

As mentioned, one of the dominant reasons contributing to frost actions in the pavement and soil is the moisture source, which facilitates the formation of ice lenses with high pore pressure that attracts the pore water. This phenomenon typically occurs during colder seasons, extending from late fall to winter. Conversely, in the warmer seasons, such as spring, the ice within the soil begins to thaw, leading to an accumulation of excess water, consequently elevating the overall moisture content (H. Miller, Cabral, Kestler, Berg, & Eaton, 2012). Other than the differential settlement of the pavement structure suffers from the change of the state of ice/water due to freezing and thawing in the soil, during the non-freezing wet period, the increase of moisture content leads to the loss of modulus of the unbound materials (Yunyan Huang, Nojumi, Hashemian, & Bayat, 2021). This can be attributed to two primary factors: changes in the state of stress resulting from suction actions caused by varying pore pressure, and the disruption of the interaction between soil particles due to high moisture content (Lekarp, Isacsson, & Dawson, 2000). Apart from the impact on the unbound materials, moisture can create significant damage to the asphalt layer by affecting the bonding between aggregates and asphalt binder and ultimately causing stripping, which could lead to various types of pavement distress (Bharath, Kakade, Reddy, Tandon, & Reddy, 2022).

Similarly, moisture probes were installed in three locations in each section: at the top of the base layer; in the middle of the granular base layer; and 10 cm below the subgrade. The depths of the sensors from the pavement surface are around 200 mm, 425 mm, and 750 mm, respectively. All the sensors collected readings every five minutes and were aggregated into daily means for analysis. Readings from August 16, 2022, to August 16, 2023, were analyzed. Figure 8-13 below illustrates the profile of water

potential at different depths in the pavement structure. As mentioned, water potential represents the amount of effort required for water to flow within the material. Therefore, the water potential of zero implies a saturated condition, while a water potential of 200 kPa measured by these probes indicates a dry condition. In the background of the figures, the daily total precipitation was plotted for comparison.

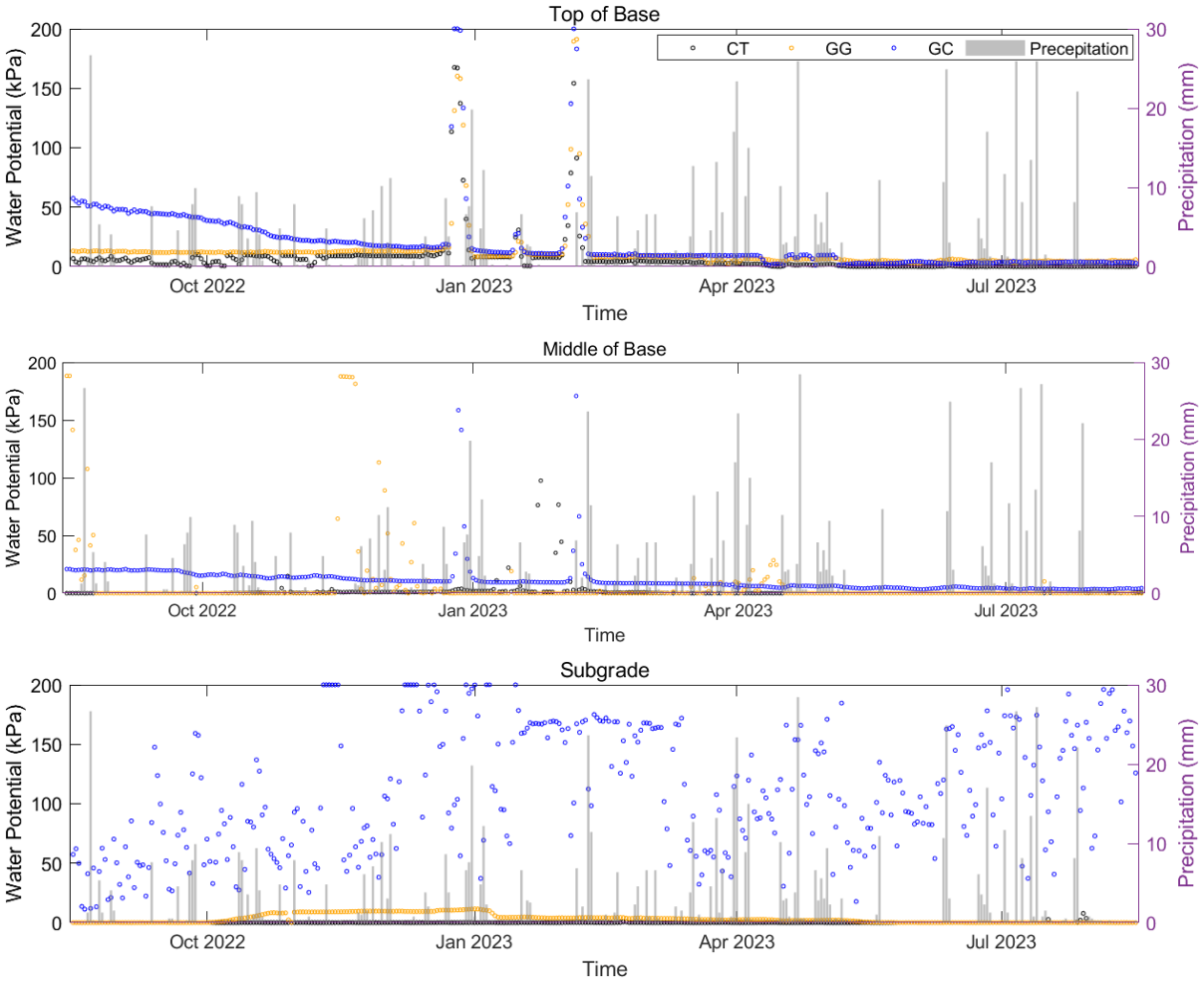

Figure 8-13 Daily Mean Layer Water Potential Profile Compared with Precipitation

It is crucial to recognize the influential role of temporary precipitation events in modulating the moisture content within the pavement layers. Various studies have highlighted the substantial influence of temporary precipitation, often resulting from rainfall or other forms of moisture intrusion, on the moisture dynamics and overall moisture content within the pavement structure. Temporary precipitation events can contribute to a considerable increase in pavement moisture content, with studies indicating potential moisture increments of up to 50%. (Hedayati, Hossain, Mehdibeigi, & Thian Student, 2014; Manosuthikij, 2008; Nguyen, Fredlund, Samarasekera, & Marjerison, 2010).

The observed trends, particularly the differences in precipitation levels between different seasons, highlight the significant influence of seasonal variations on moisture accumulation and saturation within the various pavement layers. From Figure 8-13, the precipitation was generally lower in fall and winter compared to that in spring and summer, which led to a more saturated condition at the top and middle of the base layer in spring and summer in all three sections. The comparative assessment of the moisture content profiles at the top of the base, particularly during specific time periods such as around January 2023, highlights the direct correlation between precipitation events and the subsequent fluctuations in moisture content within the pavement structure. The moisture content decreased when there was no precipitation and increased after the rainfall took place, with the noticeable increase in moisture content following rainfall events, which signifies the critical role of precipitation in augmenting the moisture levels within the pavement surface, potentially leading to heightened saturation and increased moisture-induced risks, particularly during the spring and summer seasons. A similar observation could be made around February 2023.

Subsequently, in the middle of the base, the moisture content showed less variation and a weaker correlation with precipitation, which indicates the impact of precipitation on pavement moisture content becomes less as the depth increases. Similar findings have been reported in other relevant studies, corroborating the effects of precipitations on pavement moisture content (Salour & Erlingsson, 2013).

Finally, the analysis of the moisture content in the subgrade layer, with distinct observations in the GG, GC, and CT sections, further emphasizes the critical role of the geogrid composite in facilitating effective water drainage and filtration mechanisms, particularly in the GC section. In the subgrade, the GG and CT sections are mostly saturated, while the water-draining effect can be obviously noted in the GC section. The presence of the geogrid composite in this specific section, strategically positioned at the interfaces of the base layer and the subgrade, facilitates efficient water drainage and filtration, thereby minimizing the potential risks of frost susceptibility and enhancing the overall integrity and stability of the subgrade and the pavement structure. These critical observations highlight the importance of implementing robust drainage and filtration systems, alongside the strategic integration of geogrid composites, in optimizing moisture management and subgrade stability within the pavement structure.

Apart from the impact of precipitation, in colder regions, the variation in pavement moisture content may be more affected by layer temperature compared to precipitation (Yunyan Huang et al., 2021). The comprehensive analysis of the layer water potential in relation to the corresponding layer temperatures,

as depicted in Figure 8-14, provides crucial insights into the relationship between temperature variations, frost actions, and moisture content within the pavement layers.

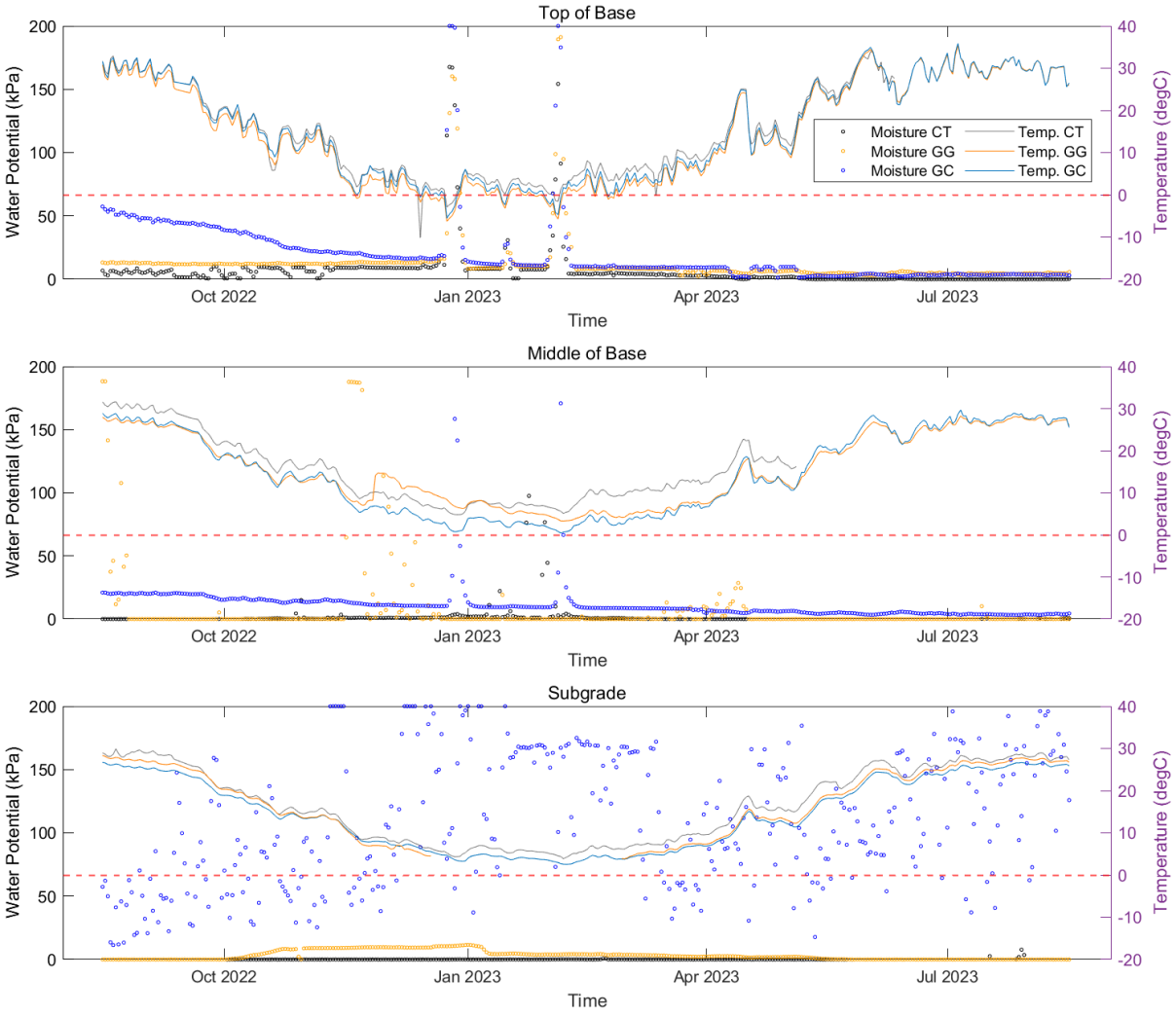

Figure 8-14 Daily Mean Layer Water Potential Profile Compared with Layer Temperatures

The observed correlations between the layer water potential, layer temperatures, and the occurrence of F-T events underscore the critical relationships between temperature fluctuations and moisture content variations, particularly in regions characterized by colder climates and frost-susceptible pavement structures. The notable observations at the top of the base layer, specifically during the identified time periods in January and February 2023, highlight the direct influence of sub-zero layer temperatures on the frost action and subsequent moisture content fluctuations within the pavement structure. The observed decrease in moisture content, coinciding with the occurrence of freezing events, indicates the critical role of temperature-dependent frost actions in modulating the moisture dynamics

and water potential within the pavement structure. This finding highlights the significant impact of frost-susceptible conditions on the moisture management and frost resistance of the pavement structure, emphasizing the need for effective frost protection measures and proactive design strategies aimed at mitigating the detrimental effects of F-T events on pavement performance.

Given that the base and subgrade temperatures consistently remained above 0°C throughout the year, the fluctuation of the water potential in these layers cannot be attributed to F-T actions. Notably, the subgrade in both the CT and GG sections remained consistently saturated, irrespective of the variations in subgrade temperature. In contrast, the subgrade in the GC section exhibited a relatively drier condition during winter in comparison to other seasons. This observation is in line with the documented low pavement moisture content during winter, followed by an increase during fall, spring, and summer, as indicated by previous studies (Oyeyi, 2022). Evidently, the subgrade in the GC section demonstrates effective drainage behaviour, particularly notable during spring and summer when precipitation levels are comparatively higher. This finding points out the significance of proper drainage measures.

Figure 8-15 provides a comprehensive comparison of the layer moisture content within each section on the 15th day of each month. The data indicates that the CT section predominantly exhibited the highest saturation levels at the top of the base, while the GC section experienced the driest conditions during the fall and winter months. Moreover, the moisture content at the top of the base in the GC section demonstrated higher saturation levels in spring and summer in contrast to the GG section. Furthermore, it was observed that the mid-base and subgrade moisture content in the GC section remained consistently drier compared to the other two sections. This observation serves as a noteworthy indicator of the effective draining capability facilitated by the geogrid composite at the interface of the base and subgrade layers. This finding accentuates the critical role played by the geogrid composite in managing moisture levels, ensuring proper drainage, and ultimately contributing to the stability and durability of the pavement structure.

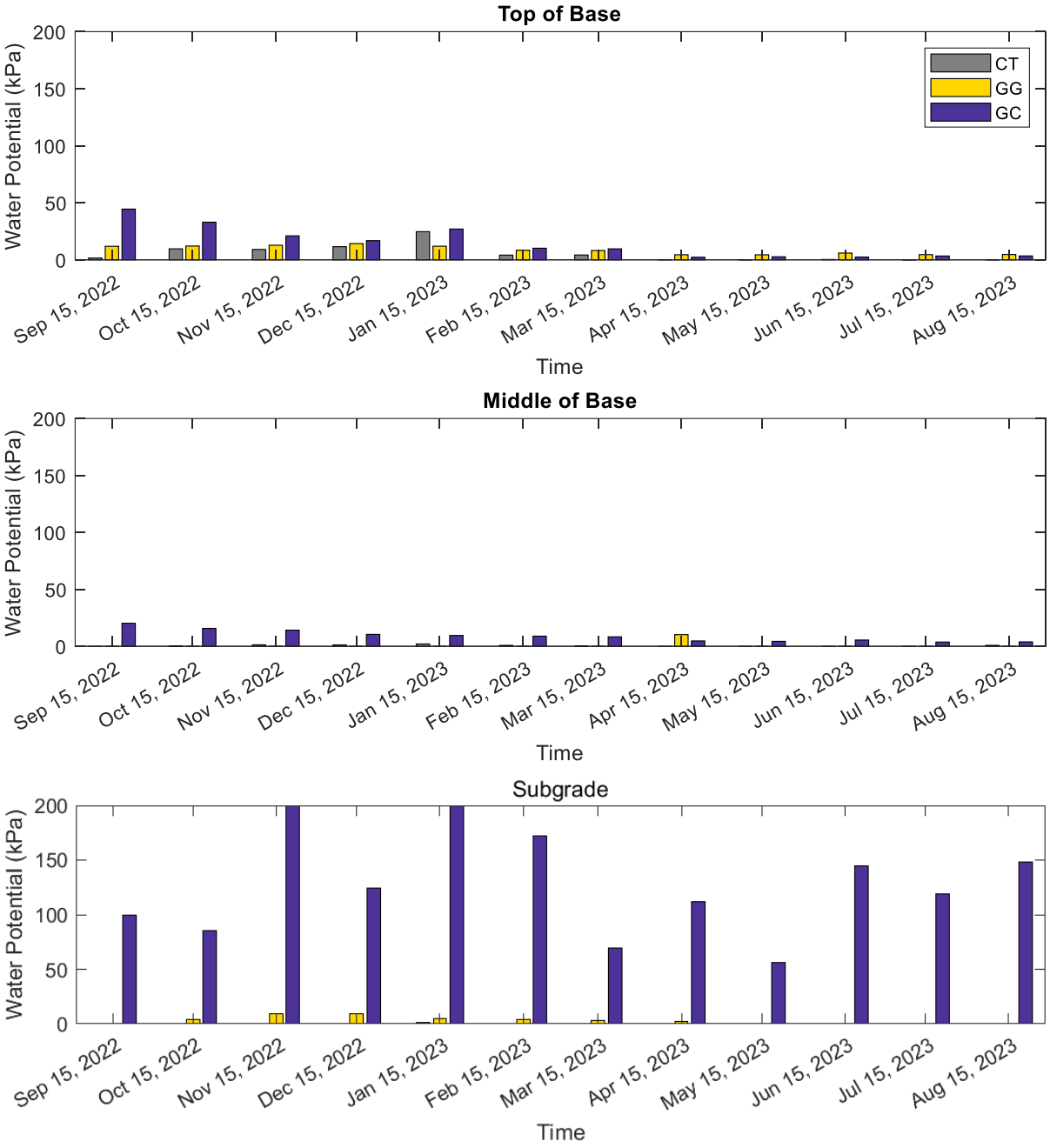

Figure 8-15 Layer Moisture on the 15th of Each Month from September 2022 to August 2023

To evaluate the geogrid composite as a draining and filtering material, the moisture gradient was computed for every 15th of each month as per Equation 8-4. The results are illustrated in Figure 8-16.

Equation 8-4

$$Moisture\ Gradient = \frac{\Delta\Psi}{\Delta d}$$

where:

$\Delta\Psi$ = difference in water potential from the shallower to the deeper sensor (kPa)

Δd = distance between moisture probes (cm)

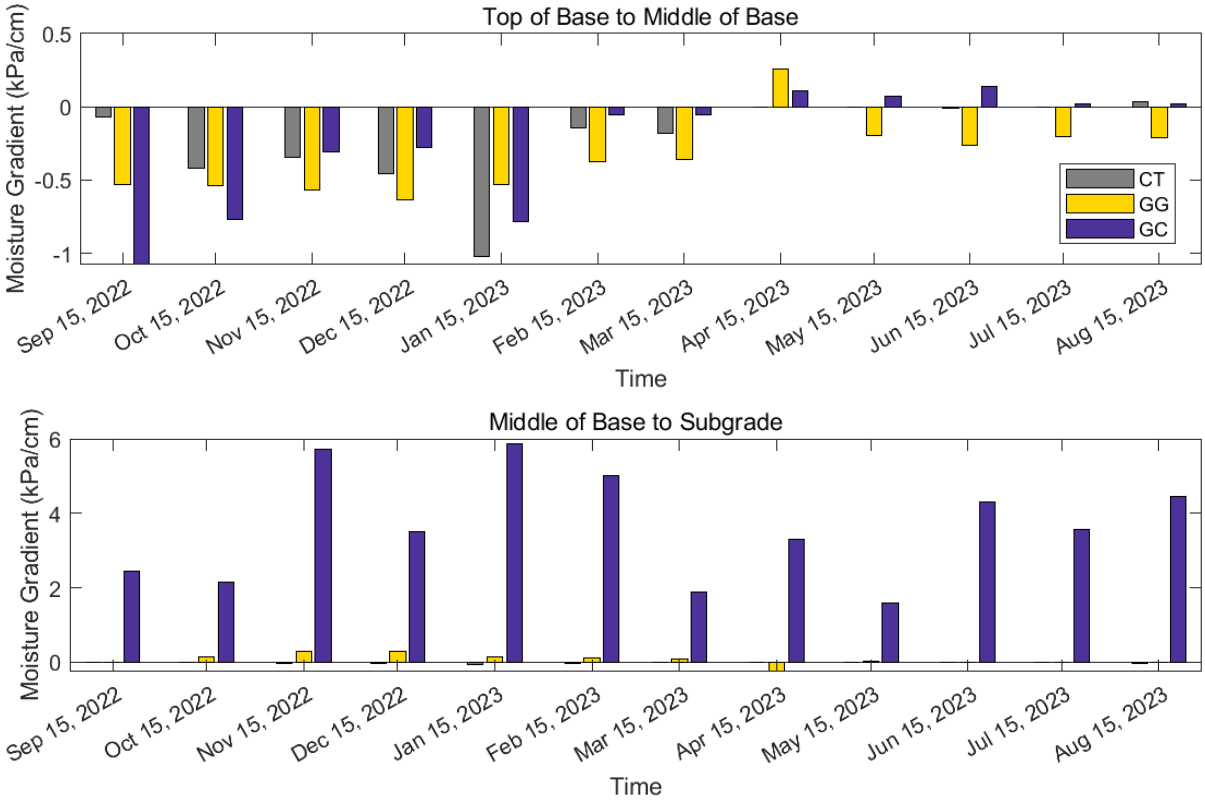

Figure 8-16 Moisture Gradient on the 15th of Each Month from September 2022 to August 2023

It was observed that the moisture movement from the top of the base to the middle of the base exhibited comparable patterns across all three sections, with the moisture gradient ranging from -1.08 kPa/cm to 0.25 kPa/cm. However, notable disparities were observed in the moisture gradients from the middle of the base to the subgrade, particularly in the GC section where the geogrid composite was strategically implemented between these two layers. In this case, the moisture gradient reached as high as 5.87 kPa/cm, signifying a significantly enhanced draining capacity. In contrast, the GG and CT sections exhibited lower moisture gradients, indicative of a comparatively limited capacity for moisture

drainage, thereby leading to minimal changes in moisture potential along the depth of the pavement. This emphasizes the critical role of the geogrid composite in effectively managing moisture movement within the pavement structure, highlighting its potential to mitigate moisture-related issues and enhance the overall performance and longevity of the pavement.

8.5 Impact of Environment on Pavement Horizontal Strain

Flexible pavement mainly suffers from fatigue cracking, rutting, low-temperature cracking, and various other forms of deterioration. The main factors contributing to such distress include traffic loading, weak subgrade, unregulated construction practices, poor material quality, and environmental impacts. (Y. H. Huang, 2004). The integration of stress and strain analysis as reliable indicators for evaluating the pavement's resistance to distress further emphasizes the critical role of comprehensive mechanical assessments and structural evaluations in predicting potential failure mechanisms and identifying vulnerable areas within the pavement structure (H. M. Park & Kim, 2003). Thus, in addition to the data obtained from environmental sensors, it is important to understand the pavement's mechanical responses with the reinforcement of geosynthetics.

Due to the viscoelastic nature of asphalt concrete, temperature is also a critical factor contributing to the deterioration of flexible pavement. Temperature is a function of the generation of stress and strain in asphalt materials, which is mainly dominated by the variation of temperature and relaxation modulus. (Aurilio, Aurilio, & Baaj, 2020). Thermal-induced stresses could build up in extremely hot and cold weather, developing in the asphalt layer, and subsequently creating thermal cracking. As mentioned, the effect of temperature changes on pavement is associated with two aspects, including seasonal changes causing the change of pavement's structural responses; and daily temperature changes causing asphalt thermal expansion and contraction (Bayat, Knight, & Soleymani, 2012; R. A. Tarefder, Asce, Islam, Asce, & Student, 2014). Therefore, it is important to strain developed in the asphalt layer during the day at maximum and minimum temperatures, as well as in different seasons.

Several studies have been done to study the asphalt strain by instrumented field studies. The instrumented strain gauges in Virginia Smart Road in Southwest Virginia revealed that the pavement response to thermal loading was characterized by a substantial strain range, up to 350 με (Bayat et al., 2012). Centre for Pavement and Transportation Technology (CPATT) at the University of Waterloo has conducted studies investigating pavement performances under similar climate conditions to this study. It was studied that the thermal-induced strain monitored over a year was higher than the load-induced strain developed from the heavy wheel load with up to 650 με (Bayat et al., 2012). Another

study done at CPATT also revealed that the asphalt concrete tensile strain increased with the increase in daily temperature (Oyeyi, Al-Bayati, Ni, & Tighe, 2023).

Other than the mechanical responses in the asphalt layer, the evaluation of the subgrade is also vital. Seasonal variation also significantly affects the structural capacity of the subgrade with the changes in temperature and moisture content. Integrated Road Research Facility in Alberta, Canada has an instrumented road with installed polystyrene boards to insulate the subgrade, while it signifies the improvement of the subgrade with insulation materials with an increasing minimum ratio of the back-calculated subgrade resilient modulus (Haghi, Hashemian, & Bayat, 2016). Therefore, with the drainage function and indirect insulation ability provided by geogrid composite as highlighted in the previous sections, the importance of stress and strain analysis is also emphasized.

By recognizing the interaction between pavement temperature and the associated thermal-induced critical responses of pavements, the detrimental effects of temperature fluctuations on flexible pavement systems can be subsequently considered and treated. Two asphalt strain gauges (ASG) were installed in the asphalt base lift in each section with one measuring longitudinal strain in the bottom of the asphalt layer and the other one measuring transverse strain. The depth of the ASG is 200 mm from the pavement surface. Additionally, one soil strain gauge (SSG) was installed at the interface of the base layer and subgrade with a depth of 650 mm in the CT section and the GC section to measure longitudinal strain on the subgrade. The readings were taken every five minutes and were aggregated into hourly and daily means. The results were the change in strains to show the critical responses of the pavements. The study period was from October 1, 2022, when the road opened to traffic, to August 16, 2023.

8.5.1 Seasonal Changes on Pavement Horizontal Strain

Figure 8-17 presents the longitudinal and transverse strain variations experienced at the bottom of the asphalt layer, and offers crucial insights into the critical mechanical behaviour and the strain response of the asphalt concrete under varying temperature conditions. The layer temperature was plotted as the background for comparison. The observed higher amplification of longitudinal strains compared to the transverse ones, coupled with the noticeable peak values, highlights the substantial strain variations experienced by the asphalt concrete, emphasizing the critical impact of temperature changes and the resulting thermal-induced strain on the longitudinal deformation patterns within the pavement structure. Such observations were also made in previous studies (Talebsafa et al., 2019). The asphalt concrete experienced a higher amplitude of strain variation in the longitudinal direction starting from February

2023 when the layer temperature started to increase. A similar trend was observed in the transverse direction the strain was significantly increased in spring and reduced afterward. These findings were in line with the strain experienced in another instrumented road close to the study area (Oyeyi, Al-Bayati, et al., 2023), which indicates the reliability of the data obtained from the pavement instrumentation, highlighting the critical role of comprehensive strain analysis in assessing the pavement's mechanical behaviour and structural performance under varying environmental conditions and temperature regimes.

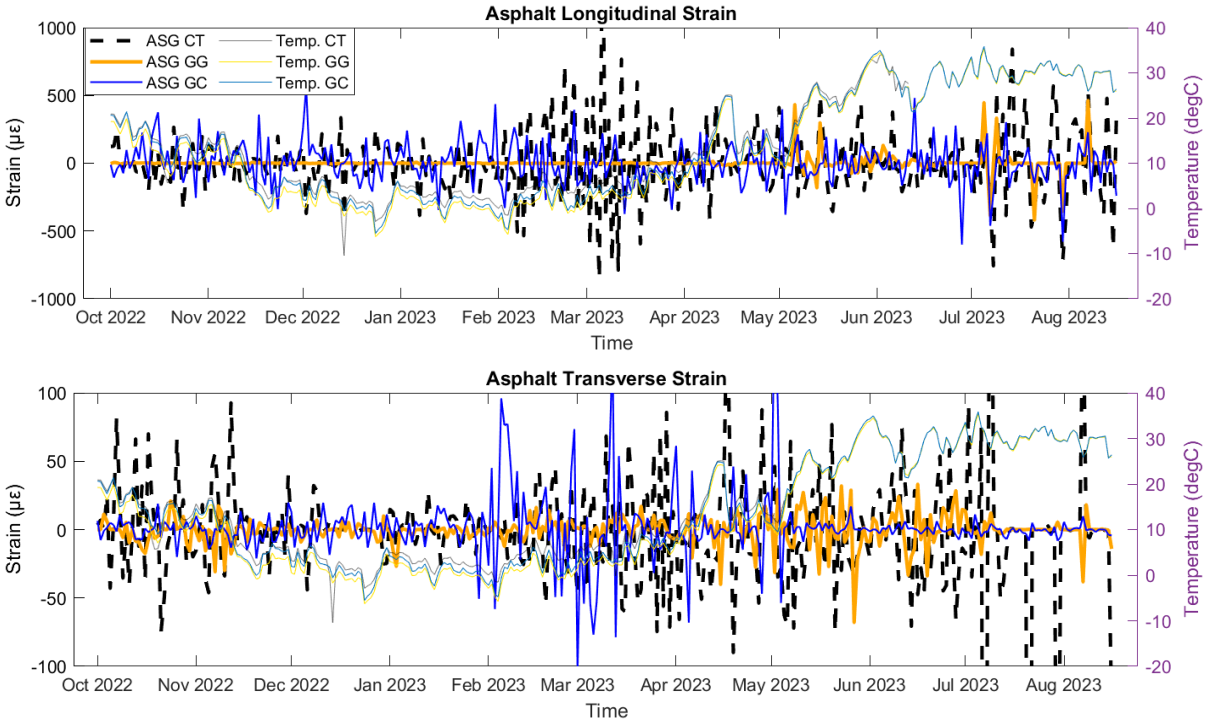

Figure 8-17 Asphalt Strain Profiles over the Study Period

The detailed analysis presented in the longitudinal and transverse strain comparisons between the GG, GC, and CT sections highlights the critical role of the embedded fibreglass geogrid in influencing and mitigating the strain characteristics and load distribution mechanisms within the asphalt concrete. The notable differences in longitudinal strain experienced by the GG section, particularly the observed lower strain levels, emphasize the resilient load-bearing capabilities and strain-absorption properties facilitated by the fibreglass geogrid, underscoring its critical role in reducing the strain magnitude and enhancing the structural integrity of the asphalt layer. The GC section experienced a similar level of longitudinal strain to the CT section. In the transverse direction, a similar level of strain in the GC and CT sections was again observed due to the nature that the asphalt layer was not reinforced in these two

sections. However, a significant reduction in transverse strain in the GG section was noted. The consistency of these findings with the previous observations made during the construction phase, as discussed in Chapter 4, further validates the significant contributions of the fibreglass geogrid in reinforcing the asphalt concrete and improving its load-bearing capacity and strain distribution characteristics, ensuring the long-term stability and functionality of the pavement structure under diverse loading and temperature regimes.

Figure 8-18 below illustrates the longitudinal strains experienced on the subgrade in the CT and GC sections. Similar to the strain experienced in the asphalt, the subgrade strain experienced a lower strain variation on colder days. Notably, the CT section experienced significantly higher strain compared to the GC section, which may be attributed to the geogrid composite installed at the interface of the base and subgrade, located above the strain gauge. This underlines the impact of geogrid composite on reinforcing the subgrade by providing interlocking effects.

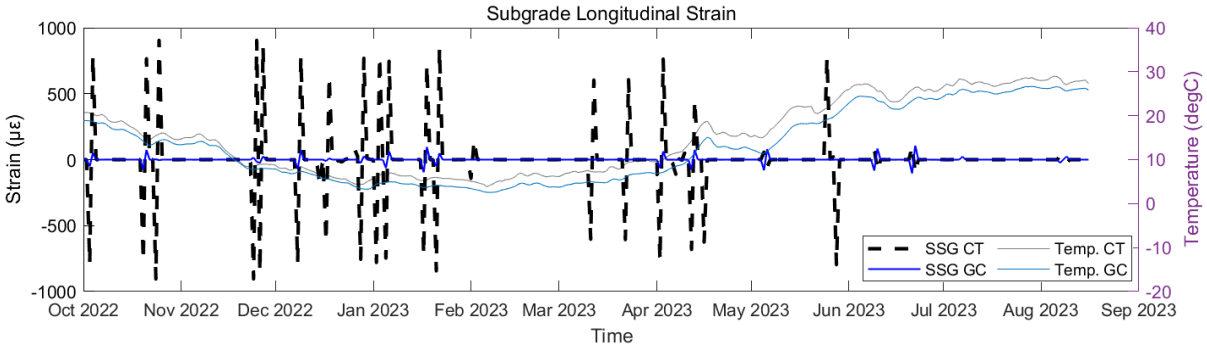

Figure 8-18 Subgrade Longitudinal Strain Profiles over the Study Period

8.5.2 Daily Temperature Changes on Pavement Horizontal Strain

The strain measurements were also aggregated into hourly averages to investigate the impact of daily temperature variations on strains, as plotted in Figure 8-19. The study period was chosen to be April 10, 2023, to April 15, 2023, with a precipitation of 0 mm during the study period. The figure clearly presents the daily cooling and heating effect due to temperature changes during the course of a day. A positive result of the strain indicates the tensile strain, while a negative value indicates the compressive strain.

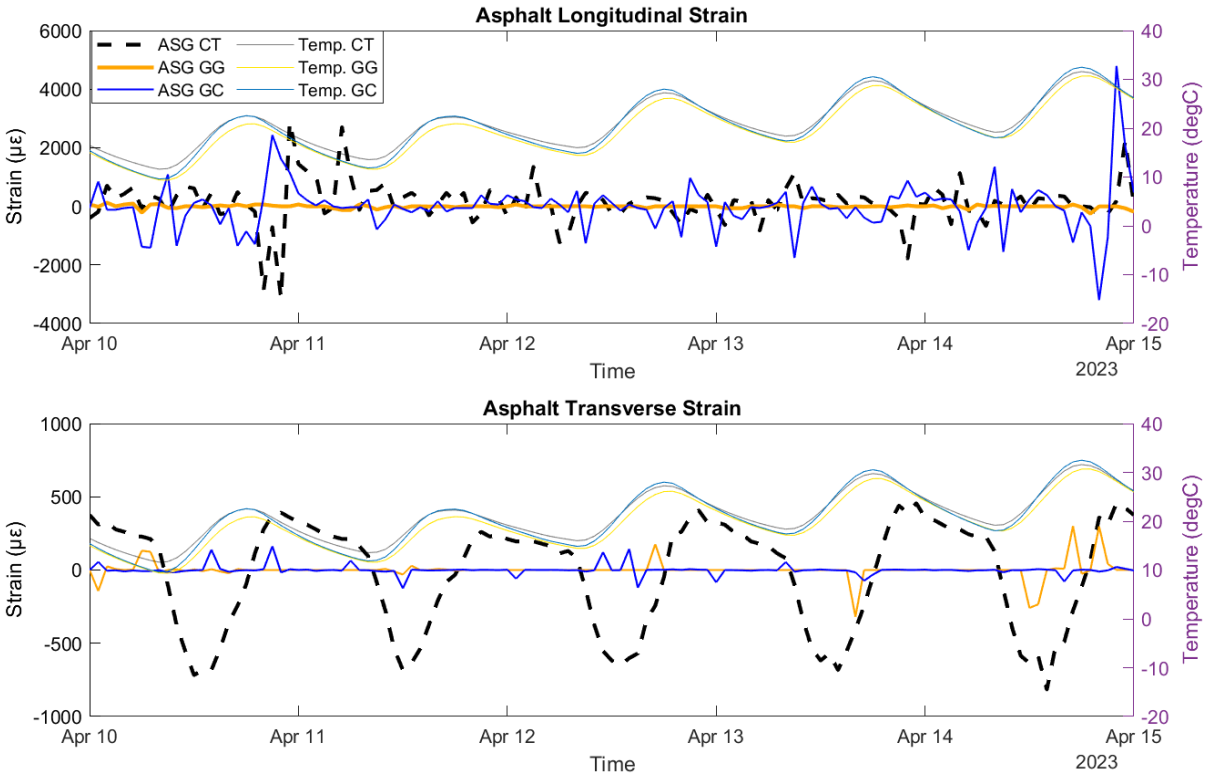

Figure 8-19 Asphalt Strain Profile with Daily Temperature Changes

It can be observed that the longitudinal strain experienced in the asphalt mainly tended to stay in a tension state during the nighttime with the peak tension state happening around 9 pm to 10 pm. Furthermore, the GG section experienced a significantly lower strain, which makes the effect of daily temperature variation on the longitudinal strain in the GG section not obvious. This may imply the effect of the fibreglass geogrid on reinforcing the asphalt layer by distributing the load. On April 10, the peak tensile strain experienced in the GG section was about 10 times lower than that in the other two sections.

On the other hand, the asphalt transverse strain was generally lower than the longitudinal strain. The heating and cooling effect illustrated a similar case in the transverse direction, where the transverse strain started to develop towards a compression state when the heating period started around 8 am, while it increased to the maximum compression around noon. Then, the transverse strain decreased and moved to a tension state around 6 pm while it reached the peak around 9 pm. Similarly, with a lower level of strain amplitude, such a phenomenon was not obvious in the GG and GC sections. On April 10, the peak compressive strain experienced in the GG section was about 2.2 times lower than that in the GC section and 10 times lower than that in the CT section.

Figure 8-20 presents the subgrade longitudinal strain from April 10, 2023, to April 15, 2023.

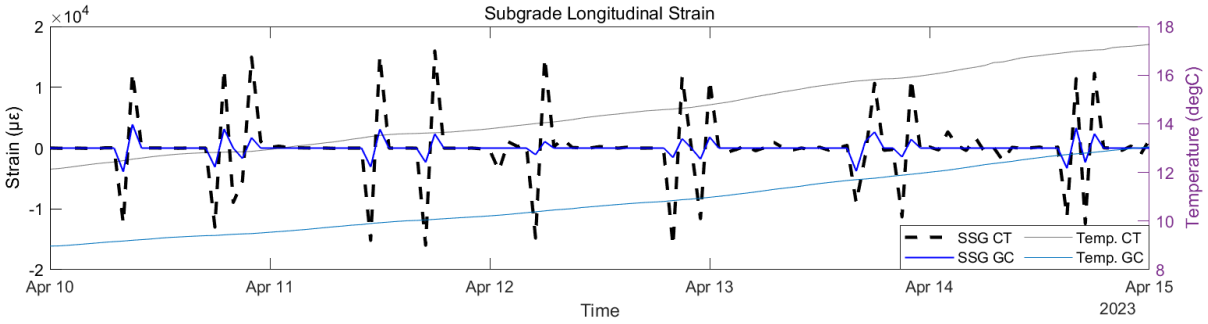

Figure 8-20 Subgrade Longitudinal Strain Profile with Daily Temperature Changes

With the approximately 4°C increase in subgrade temperatures, the strain amplitude was 8% lower on April 15 than that on April 10 in the CT section and was 15% lower in the GC section. However, the effect of the daily cooling and heating effect was not apparent on subgrade strain. This can be attributed to the deeper location of the pavement structure and the special viscoelastic nature of asphalt materials. Nevertheless, the CT section experienced about 5 times higher strain on the subgrade in the longitudinal direction compared to the GC section, which signifies the critical role of geogrid composite in mitigating the deformation of the pavement structure and the subgrade.

8.6 Impact of Environment on Subgrade Vertical Pressure

Aside from the strain, the pressure cells installed on the subgrade in each section were analyzed with the effect of seasonal changes and daily temperature variations. The depth of the pressure cells was 650 mm from the surface. The readings were taken every five minutes. The study period was from October 1, 2022, to August 16, 2023.

8.6.1 Seasonal Changes on Subgrade Vertical Pressure

Figure 8-21 presents the daily subgrade pressure profile with the subgrade temperatures plotted as background. A negative reading denotes the pressure in compression while a positive one denotes tension. To better visualize the pressure profile, the axis was reversed. From Figure 8-21, it was noted in all sections the subgrade pressure was affected by the temperature changes associated with seasonal changes from fall to winter. The pressure experienced on the subgrade decreased with the drop in temperature. The lowest pressure was noticed in winter. Then, the pressure increased since spring and a maximum pressure was noticed around July in summer. Similar findings were reported in other studies with lower subgrade pressure in the colder season (Oyeyi, Al-Bayati, et al., 2023; Rajbongshi

& Das, 2009). A clearer view was presented in Figure 8-22 with the pressure readings aggregated into monthly means. Among these three sections, the subgrade pressure in the GC section was less affected by temperature changes with a more stable trend shown over the study year.

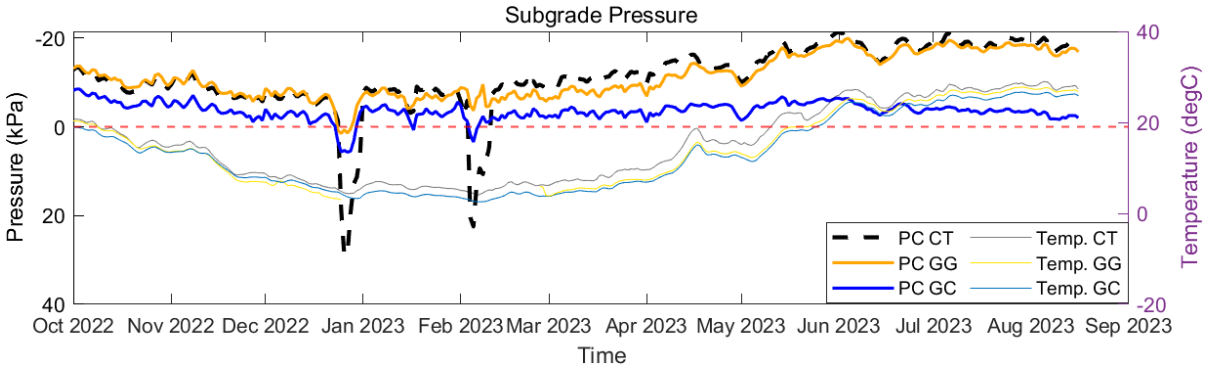

Figure 8-21 Daily Mean Subgrade Pressure Profile over the Study Period

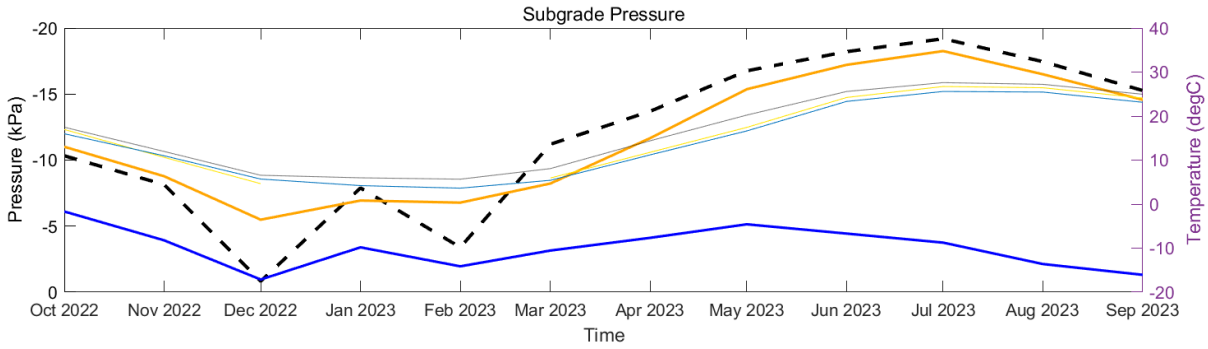

Figure 8-22 Monthly Mean Subgrade Pressure Profile over the Study Period

In winter 2023, two exceptional incidents were noticed with a sudden drop in pressure. These occurred around the same time when the notable fluctuation of moisture content presented in Figure 8-14 happened, with the influence of sub-zero layer temperatures on the frost action and subsequent moisture content fluctuations. Therefore, when the overlain pavement is frozen, the experienced pressure significantly drops. Such observation was documented in other similar studies with lower vertical strain measured by FWD in winter (Shafiee, Hashemian, & Bayat, 2015).

With that being said, the moisture content of the pavement structure has discernible effects on the pressure variation experienced at the subgrade. Figure 8-23 presents the pressure profile with the background plotting water potential at the top of the base, middle of the base, and subgrade, respectively. It was observed that the two events with substantial pressure drop coincided with the drop of saturation at the top of the base. As discussed, the drop in saturation was associated with the frost

action, particularly during instances when the temperature fell below 0°C. Therefore, the decreased pressure experienced at the subgrade can be attributed to the presence of a frozen pavement structure above the subgrade, leading to an increase in stiffness (Zapata, Witczak, Houston, & Andrei, 2007).

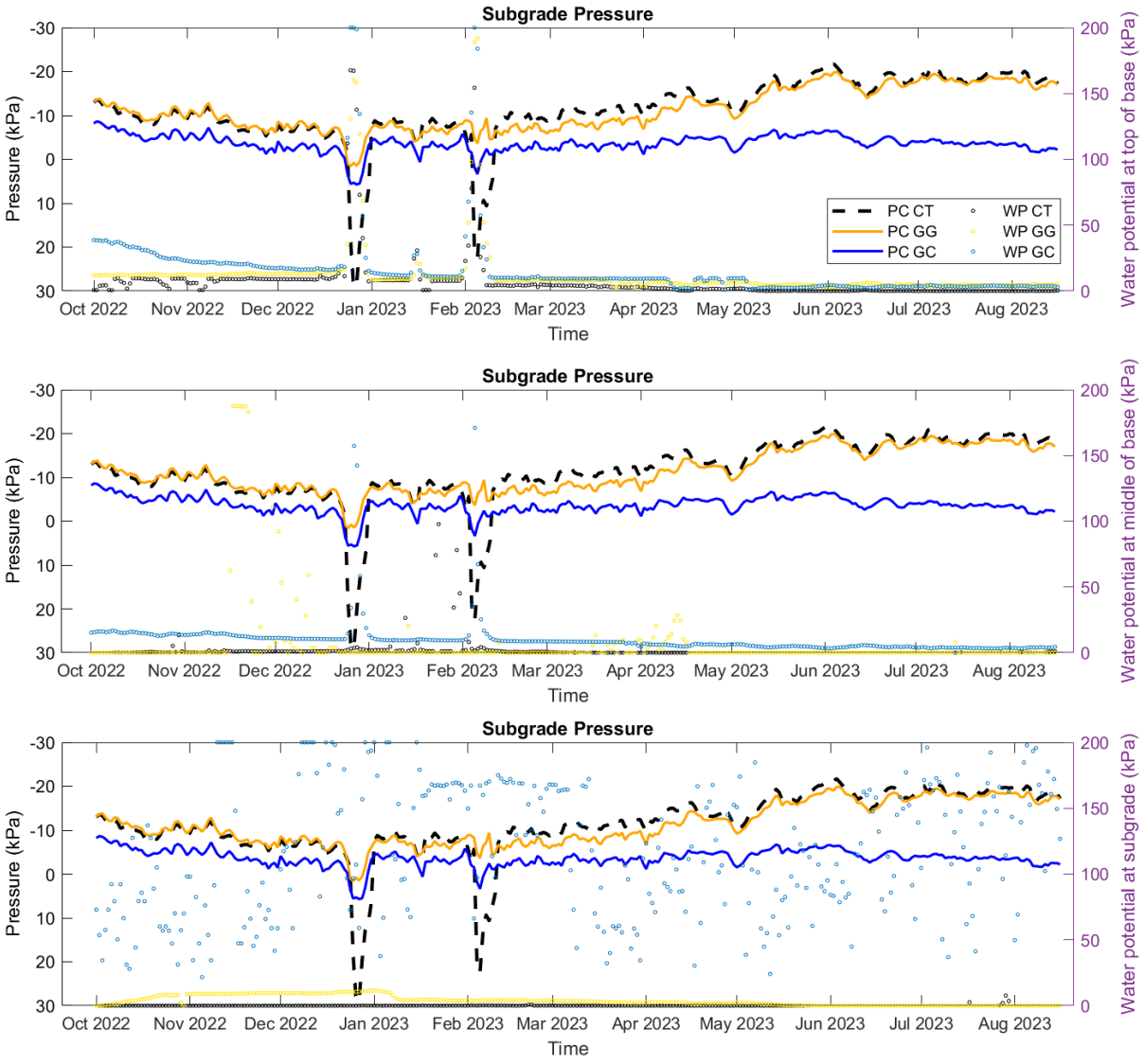

Figure 8-23 Subgrade Pressure Profile Compared with Layer Water Potential

Additionally, the relatively consistent moisture content levels observed in the three sections at the top and middle of the subgrade emphasized that the drier subgrade in the GC section could potentially account for the comparatively minimal variation in subgrade pressure when compared to the other two sections. This notable finding emphasizes the active role played by the geogrid composite in reinforcing a weak subgrade, effectively mitigating the pressure exerted at the subgrade level.

Similarly, the subgrade pressure measured on the 15th of each month from October 2022 to August 2023 was listed in Figure 8-24. With the ambient temperature illustrated in the figure, the lowest pressure was experienced when the weather was the coldest, and the pressure increased as the weather got warmer. Meanwhile, the CT section experienced the highest pressure on the subgrade starting from January 2023, followed by the GG section. The GG section experienced the highest pressure on October 15, November 15, and December 15, 2022. However, after the freezing period started followed by the thawing period, the fibreglass geogrid in the asphalt decreased the pressure on the subgrade significantly, up to 30% compared with the unreinforced pavement. On the other hand, the subgrade pressure in the GC section was the lowest, which signifies the critical role of geogrid composite in mitigating the exerted pressure. Also, the level of reduction of experienced subgrade pressure increased from about 40% in the fall before the F-T period, to approximately 80% in the summer after one F-T cycle. This underscores the critical role of geogrid composite on the subgrade in mitigating the F-T disturbances on the pavement, which further confirms the discussion of such potential offered by geogrid composite with its drainage capabilities with the findings during construction as mentioned in Chapter 4.

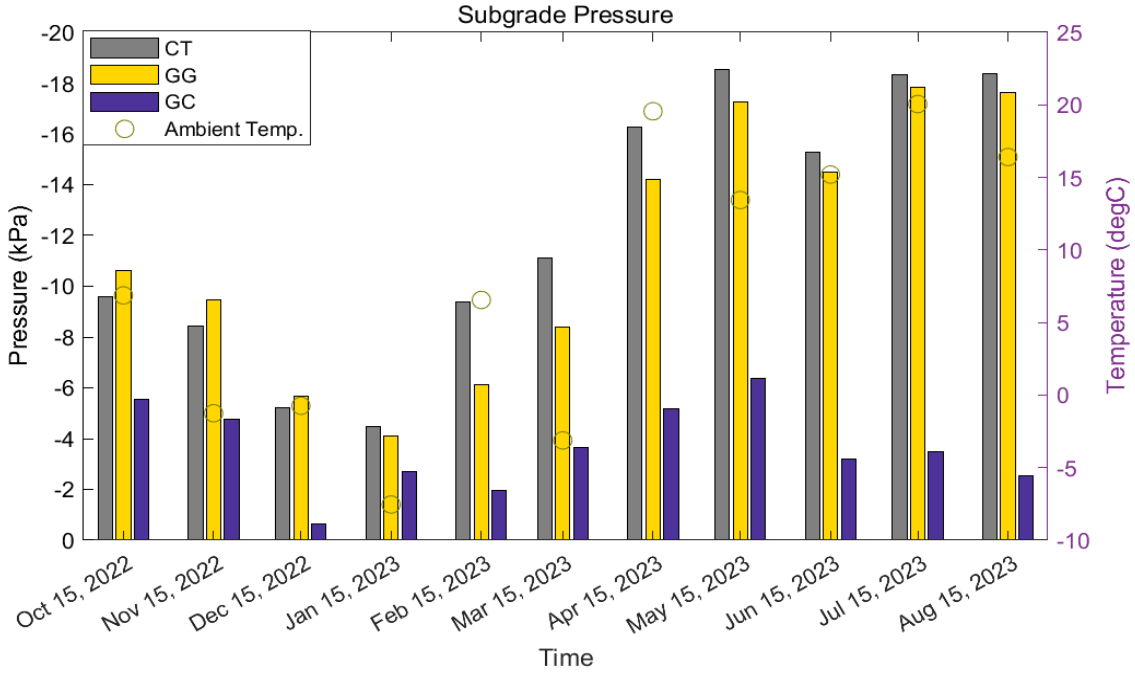

Figure 8-24 Subgrade Pressure on the 15th of Each Month from October 2022 to August 2023

8.6.2 Daily Temperature Changes on Subgrade Vertical Pressure

In examining the impact of daily temperature fluctuations on subgrade pressure, pressure measurements were aggregated and averaged on an hourly basis and plotted over the study period (April 10 - April 15, 2023) in Figure 8-25, with the precipitation of 0 mm during the study period. Given the limited influence of ambient temperature on the subgrade temperature, the asphalt layer temperatures were used for analysis in the figure alongside the ambient temperature. The delayed response of asphalt temperature to changes in ambient temperature, as discussed earlier, was found to correlate more closely with the variations in subgrade pressure. It was observed that the subgrade pressure in both the CT and GG sections was notably influenced by the daily temperature variations. Specifically, the lowest pressure readings were consistently recorded around 6 pm, coinciding with the period when the asphalt layer temperature reached its peak for the day. This observation features the significant influence of temperature dynamics, particularly the daily temperature fluctuations, on subgrade pressure levels within the pavement structure.

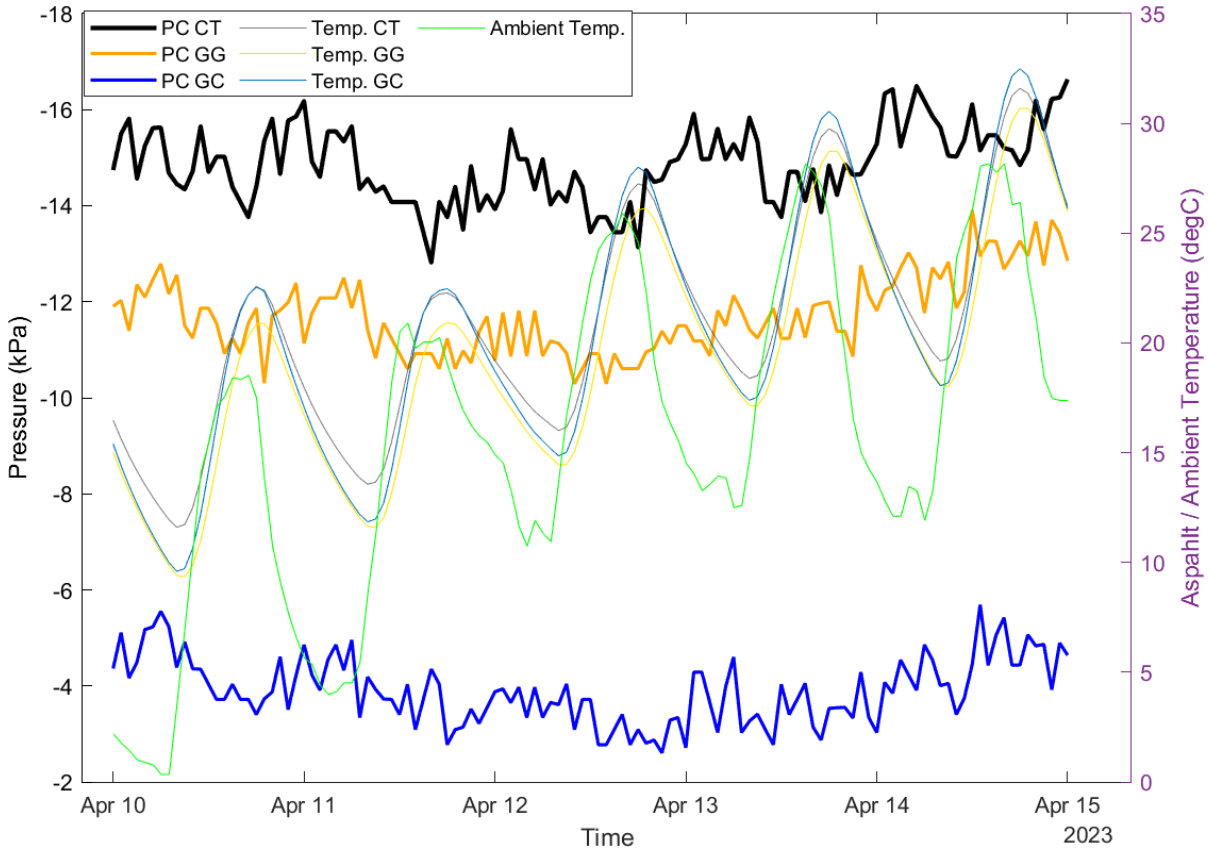

Figure 8-25 Subgrade Pressure Profile with Daily Temperature Changes

8.7 Frost Condition

The frost condition within the pavement and subgrade was monitored using the frost tubes installed in each section from the top of the base layer to 3 m below. The inner tubes filled with methylene solution were pulled about regularly from January to May 2023 to monitor the freezing and thawing actions within the pavement. Pictures were taken as provided in Figure 8-26 and Appendix A. These visual records serve as valuable documentation of the evolving frost conditions throughout the year, providing critical insights into the frost-related dynamics within the pavement structure.

Figure 8-26 Frost Tubes on February 13, 2023

Originally intended to monitor the frost depth in each specific location, the frost tubes were designed with a colour gradient, where a lighter shade indicated a more frozen state. However, regular inspections revealed that the variation in frost conditions was not readily apparent within a single location, with one notable exception observed on February 13 in the GG section. Notably, the segment approximately 350 mm from the top of the base layer exhibited a more pronounced frozen state compared to the portion below, as depicted in Figure 8-26. It is essential to highlight a critical factor influencing these observations, namely, the differential elevation of the three sections. The CT section, situated at the highest elevation, is followed by the GG section, while the GC section is positioned at the lowest elevation. This variation in elevation contributes to the presence of a more clayey subgrade in the GC section, where the accumulation of fine particles and water tends to flow towards the lower

elevation. Additionally, the absence of a geogrid composite in the GG section accentuated the prominence of the observed frozen state.

Upon thorough examination and comparison of the frost tubes across all three sections, it became evident that the GG section consistently displayed the most pronounced frozen state, characterized by the lightest coloration. On January 1, the GC section exhibited a more frozen state when compared to the CT section, although it demonstrated a comparable level of frozen state with the CT section on all other observed dates. These observations highlight the critical role played by the geogrid composite in mitigating the potential for freeze-thaw degradation, particularly evident in the context of lower elevations and the presence of a weaker subgrade within the GC section. The effectiveness of the geogrid composite in preventing adverse freeze-thaw-induced consequences is emphasized by the relatively consistent frost conditions observed across the CT and GC sections over the recorded dates.

8.8 Chapter Summary

This chapter presents the results of the instrumentation installed in the trial sections. It explores the effect of environmental factors such as temperature and precipitation on geosynthetic-reinforced pavement performance. The temperature and precipitation data were obtained from a weather station installed nearby, with confirmed reliability. The layer temperature data, layer moisture, asphalt strain, and subgrade stresses and strain were analyzed with the correlation with environmental impacts. The following points summarize the key findings:

- The observed negative temperature differentials in the GC section during winter emphasize the geogrid composite's effectiveness in regulating subgrade temperature and mitigating frost-related risks. Conversely, the consistently lower subgrade temperatures in the CT section highlight its heightened vulnerability to frost actions and potential frost heave, underscoring the importance of appropriate drainage and insulation measures in such contexts.
- The study demonstrates the influence of daily temperature fluctuations on various pavement layers, with the asphalt temperatures notably responsive to ambient temperature changes, and the subgrade temperatures displaying a stable, consistent trend. The asphalt temperature exhibited a delayed response to ambient temperature changes, indicating a gradual heat transfer process.

- The variation in pavement moisture content was more affected by layer temperature compared to precipitation. Despite variations in subgrade temperature, both the CT and GG sections remained mostly saturated, whereas the GC section displayed relatively drier conditions showing draining behaviour, particularly notable during thawing seasons.
- The asphalt concrete experienced a higher amplitude of strain variation in the longitudinal direction when the layer temperature increased. A lower level of strain variation experienced at the bottom of asphalt in the GG section emphasizes the resilient load-bearing capabilities and strain-absorption properties facilitated by the fibreglass geogrid. Moreover, the repeatability of strain measurements can be verified with multiple measurements obtained in the future as well as with different signal processing approaches.
- The CT section exhibited notably higher strain on the subgrade compared to the GC section, likely influenced by the presence of the geogrid composite at the base-subgrade interface, positioned above the strain gauge. This highlights the reinforcing impact of the geogrid composite through interlocking effects on the subgrade.
- The subgrade pressure in the GC section was less affected by temperature changes with a more stable trend shown over the study year, while the moisture content of the pavement structure also has impacts on the pressure experienced at the subgrade. This also signifies the critical role provided by the geogrid composite with its reinforcement on the subgrade.
- Following the freezing and thawing period, the fibreglass geogrid in the asphalt reduced subgrade pressure by up to 30% compared to unreinforced pavement. Meanwhile, the GC section exhibited the lowest subgrade pressure, with the level of subgrade pressure reduction increased from approximately 40% in the pre-freezing and thawing period to about 80% after one cycle, emphasizing the critical role of the geogrid composite in alleviating freeze-thaw disturbances on the pavement.
- From the inspection of frost tubes, the GC section demonstrated a frozen state comparable to the CT section, emphasizing the crucial role of the geogrid composite in minimizing freeze-thaw disturbances, especially in areas with weaker subgrade.

Chapter 9
Model Development for Pavement Reinforced by Geogrid Composite with the Impact of Freeze-Thaw Cycles

9.1 Introduction

Freezing and thawing actions have caused various problems to transportation infrastructures The problems brought by the freeze-thaw cycles of the soil to the infrastructures in the cold regions were studied starting from the last century (Ferrians et al., 1969). The major causes of the frost heave within the soil were demonstrated to be not only the freezing of the in-situ pore water but also the water migration (Taber, 1930). The capillary theory was raised to illustrate the thermodynamics of the soil and the formation of the ice lenses (Everett, 1961). The secondary heaving theory was suggested to address the underestimation of the heaving of the soils with the sole consideration of capillary theory (R. D. Miller, 1972). The secondary heaving theory generally proposed an idea of frozen fringe, referred to as the zone without frost heaves located between the freezing area and the base of warm ice lenses. The frozen fringe is greatly determined by the soil parameters and the overburden effect.

The interaction among heat, fluid, and stress within the soil is critical to the resultant displacements in thaw settlement and frost heave. When the temperature changes, the phase change of water/ice caused by freezing and thawing soil affects the hydraulic field, which then produces the volume expansion of the soil under mechanical loading. The stress change and fluid movement also affect the thermal condition leading to variations in void ratio and pore pressure (Nishimura, Gens, Olivella, & Jardine, 2009a). Coupled thermo-hydro-mechanical (THM) models have been extensively studied for the simulation of thaw settlement and frost heave in general (Nishimura, Gens, Olivella, & Jardine, 2009b; Y. Zhang & Michalowski, 2015; G. Zhou, Zhou, Hu, Wang, & Shang, 2018; J. Zhou & Li, 2012b).

This chapter provides the mathematical basis of the THM coupling processes involved in the determination of frost heave and thaw settlement in pavements. This includes the theory regarding the hydraulic and thermal fields, as well as the implementation of the phase change effect between freezing and thawing processes. The ice segregation was also introduced in the model to simulate frost heave in the mass balance equation to be coupled with the hydraulic field.

Based on the discussion and findings in the previous chapter, the mitigation of freeze-thaw disturbances provided by the geogrid composite was highlighted with its drainage and filtration capabilities. The model was established and solved using COMSOL Multiphysics by inputting material properties characterized by laboratory and field testing along with available literature. A layer

temperature predictive model was established, for both conventional pavement structure and geogrid composite-reinforced pavement, to correlate the ambient temperature and pavement temperature collected from the field instrumentation from the first year after construction completion (August 2022 to August 2023). The model was assigned with the developed layer temperature predictive model and calibrated by the data collected in the following three months (August 2023 to October 2023). While the temperature-dependent performances of asphalt materials are critical to flexible pavements, this study mainly focuses on the frost heave and thaw settlements due to freeze-thaw cycles.

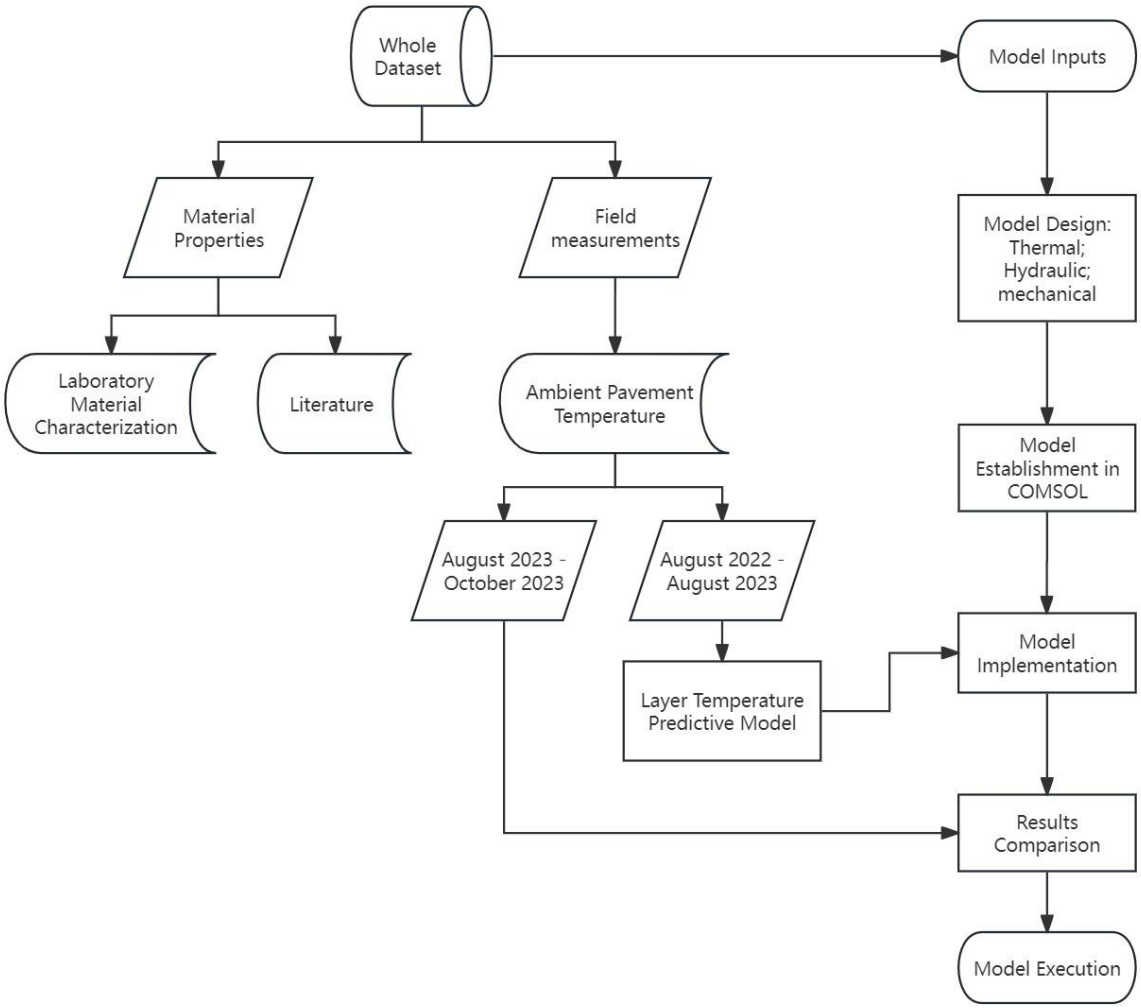

Figure 9-1 Chapter 9 Methodology

After calibrating the model with field measurements, the performance of the pavement structure can be used to simulate the effect of the geogrid composite in terms of minimizing the differential settlement of the pavement structure. The methodology of this chapter is illustrated in Figure 9-1.

9.2 Pavement Temperature Predictive Model

Temperature is one of the dominant factors affecting the performance of flexible pavements, which can influence the stresses and strain analysis under the asphalt layer with the impact of traffic loading due to the nature of asphalt as a viscoelastic material. On the other hand, the temperature in the unbound layers can be an important indicator of freezing and thawing actions in cold regions with the risks of water flow and the development of ice lenses in the pavement structure (J. Chen, Wang, & Xie, 2019). Various factors could be influencing the change in pavement temperature, including the ambient temperature, solar radiation, precipitations, wind speed, relative humidity, etc. (Wang, 2015). Among them, the latter ones are less significant while the ambient temperature is considered as a more effective contributor (Adwan et al., 2021). As observed in Chapter 8, the asphalt temperature showed a good response to the ambient temperature variability. The pavement temperature variation to the ambient temperature variation is less sensitive as the depth in the pavement structure increases, though the response to the seasonal temperature changes is still apparent.

To monitor the pavement layer temperature, like what has been done in this study, instrumentation such as thermistors and temperature sensors could be used. However, such a methodology is costly. Therefore, the development of pavement temperature prediction is deemed to be helpful in predicting pavement performance while saving costs. The pavement temperature models can be mainly categorized into three types: numerical models, empirical models, and analytical models. Numerical models mainly utilized the finite element, finite difference, and finite volume method to simulate the time-dependent temperatures. A numerical model predicting pavement surface temperature was developed using numerical methods based on the law of energy conservation and concludes the significance of albedo and emissivity on pavement temperatures (Gui, Phelan, Kaloush, & Golden, 2007). A sophisticated heat-transfer model was developed in a finite-difference pavement system which used climate data to forecast the first action in a multilayered pavement structure (Dempsey et al., 1971). The finite volume method can also be used to simulate the pavement temperature profile and a fully implicit time-integration method can significantly improve the computation efficiency (Alavi, Pouranian, & Hajj, 2014).

An analytical solution was proposed for pavement temperature prediction in winter and summer with the input of solar radiation, air temperature and wind velocity (Hermansson, 2004). The asphalt temperature was simulated with the concept of heat conduction by deriving an analytical solution based on Duhamel's principle, where the closed-form analytical solution was validated with field measurements (Wang, 2015).

However, due to the complexity of the utilization of the numerical and analytical models, engineers would prefer to use a more straightforward method practically with fewer inputs and less complication (Islam, Ahsan, & Tarefder, 2015). Statistical and empirical models could be a good choice with higher efficiency. The pavement temperature profile and frost penetration can be estimated using collected air and pavement temperature based on thermal equilibrium (J. J. Park, Shin, & Yoon, 2016). A regression model was proposed to predict the temperature in different layers of pavement structure to explore the effect of lightweight cellular concrete serving as pavement subbase (Oyeyi, Badewa, Ni, & Tighe, 2023). A statistical model was developed to predict the asphalt temperatures at any depths in cold and hot seasons, as well as the daily heating and cooling period (Asefzadeh, Hashemian, & Bayat, 2017).

Least Squares Regression fitting analysis was performed on the temperature measurements with 95% confidence bounds to develop a statistical model for pavement temperatures at the bottom of the asphalt layer, middle of the base, and 10 cm below the subgrade, with associated depths of 20 cm, 42.5 cm, and 75 cm, corresponding to the field trial sections instrumentation. Due to the damage of temperature sensors in the asphalt and base layer in the CT section in summer 2023, the data measured in the GG section replaced the missing data. The equation was used as shown in Equation 9-1.

Equation 9-1

$$y = p_1 x + p_2$$

where:

y = layer temperature (ºC)

x = ambient temperature (ºC)

p_1, p_2 = best-fit parameters

The fitting results are provided in Appendix B. The regression models and parameters for asphalt, base, and subgrade temperatures are listed in Table 9-1, with the correlation results including R-square, and RMSE (Root Mean Square Error). Generally, a good correlation was shown with all R-square

values greater than 0.8. From the regression results, the asphalt temperature is more affected by ambient temperatures compared to temperature in the unbound layers, with a higher slope as well as a higher R-square. Meanwhile, the subgrade temperature is more affected by ambient temperature compared to the base temperature in the CT section. On the contrary, the ambient temperature has a more significant impact on the base temperature than on the subgrade temperature in the GC section.

Table 9-1 Developed Regression Models for Pavement Layer Temperatures

Section	Equation	R^2	RMSE
	Asphalt Layer		
CT	$y = 1.1x + 7.01$	0.928	3.025
GC	$y = 1.172x + 5.607$	0.943	2.846
	Base Layer		
CT	$y = 0.753x + 11.174$	0.837	3.269
GC	$y = 0.939x + 6.786$	0.878	3.439
	Subgrade		
CT	$y = 0.825x + 9.61$	0.854	3.357
GC	$y = 0.786x + 7.77$	0.829	3.513

9.3 Mathematical Model

To simulate freeze-thaw cycles in the subgrade soil, underlying pavement structure, using numerical solutions. The finite element method was used to discretize the pavement and soils, with the time integration using the finite difference method. Heat transfer, fluid flow, and mechanical response were solved and coupled together. This section explains the theoretical foundation to establish and solve the finite element model.

9.3.1 Hydraulic Field

A regulating factor of freeze and thaw processes in the pavements is water migration. The fluid is considered to flow one-dimensional (i.e., vertically). Only the unfrozen zone is believed to experience fluid flow, whereas the frozen zone is impermeable. Additionally, it is believed that fluid mobility solely involves the migration of liquid water and that ice is immobile. Additionally ignored is the

movement of the vapour. Based on these presumptions, Darcy's Law, as illustrated in Equation 9-2 is used to explain the flow of fluid.

Equation 9-2

$$v = -K\frac{dh}{dz}$$

where:

v = fluid flux (m/s)

K = hydraulic conductivity (m/s)

h = hydraulic head

z = vertical spatial dimension (m)

The Richards equation (Richards, 1931), as shown in Equation 9-3, can be used to accomplish the law of mass conservation, which governs fluid movement in unsaturated soil.

Equation 9-3

$$\frac{\partial\theta_u}{\partial t} = \frac{\partial}{\partial z}\left[K(\theta_u)\left(\frac{\partial h}{\partial z} + 1\right)\right]$$

where:

θ_u = volumetric unfrozen water content

g = gravitational acceleration (= 9.8 m/s^2)

t = temporal dimension (s)

The standard Richard's equation has two unknowns with hydraulic head and volumetric content. By introducing the water retention capacity as shown in Equation 9-4 and unsaturated soil diffusivity in Equation 9-5 (Lu & Likos, 2004), the water content can be primarily solved in the saturation-based form of Richard's Equation in Equation 9-6 (Kuráž, Mayer, Lepš, & Trpkošová, 2010).

Equation 9-4

$$C(\theta_u) = \frac{d\theta_u}{dh}$$

Equation 9-5

$$D(\theta_u) = \frac{K(\theta_u)}{C(\theta_u)}$$

Equation 9-6

$$\frac{\partial \theta_u}{\partial t} = \frac{\partial}{\partial z}\left[D(\theta_u)\frac{\partial \theta_u}{\partial z} + K(\theta_u)\right]$$

where:

C = specific water retention capacity (1/m)

D = unsaturated soil diffusivity (m^2/s)

Based on the soil-water retention model proposed by Van Genuchten (1980) as shown in Equation 9-7, the constitutive relations can be established and Equation 9-6 can be written as Equation 9-8 (van Genuchten, 1980). The relationship between saturation and hydraulic conductivity was solved based on Equation 9-9 (Mualem, 1976). The relationship between saturation and soil water diffusivity was solved using Equation 9-10 (van Genuchten, 1980).

Equation 9-7

$$S = \frac{\theta_u - \theta_r}{\theta_s - \theta_r} = \left[\frac{1}{1 + (\alpha\psi)^{\frac{1}{1-m}}}\right]^m$$

Equation 9-8

$$\frac{\partial S}{\partial t} = \frac{\partial}{\partial z}\left[D(S)\frac{\partial S}{\partial z} + K(S)\right]$$

Equation 9-9

$$K(S) = K_s \cdot S^{\frac{1}{2}}\left(1 - \left(1 - S^{1/m}\right)^m\right)^2$$

Equation 9-10

$$C(S) = \alpha m/(1-m) \cdot (\theta_s - \theta_r) \cdot S^{1/m}\left(1 - S^{1/m}\right)^m$$

where:

S = actual degree of saturation

θ_s = saturated water content = porosity

θ_r = residual water content

ψ = soil water potential (m)

α = empirical soil parameter (1/m)

m = empirical soil parameter (0 < m < 1)

K_s = saturated hydraulic conductivity (m/s)

9.3.2 Thermal Field

Similar to the fluid flow, the heat conduction is considered to be one-dimensional by utilizing Fourier's law (Equation 9-11) and obtaining Equation 9-12,

Equation 9-11

$$q_T = -\lambda_T \frac{dT}{dz}$$

Equation 9-12

$$\lambda_T \frac{\partial^2 T}{\partial z^2} = C_T \frac{\partial T}{\partial t}$$

where:

q_T = heat flux (W/m^2)

λ_T = thermal conductivity (W/m·°C)

T = temperature (°C)

C_T = volumetric heat capacity (J/m^3·°C)

The temperature field follows the law of conservation of energy, while the heat convection can be taken into account with the movement of fluid flow, as shown in Equation 9-13 (Nassar & Horton, 1989, 1997).

Equation 9-13

$$\lambda_T \frac{\partial^2 T}{\partial z^2} = C_T \frac{\partial T}{\partial t} - C_w v \frac{\partial T}{\partial z}$$

where:

v = fluid flux (m/s)

C_w = volumetric heat capacity of water (J/m^3·°C)

The fluid velocity in the equation above can be then coupled with Darcy's Law（Equation 9-2), and substituted by Equation 9-4 and Equation 9-5, to obtain Equation 9-14

Equation 9-14

$$\lambda_T \frac{\partial^2 T}{\partial z^2} = C_T \frac{\partial T}{\partial t} - C_w D \frac{\partial S}{\partial z} \frac{\partial T}{\partial z}$$

Considering the freezing soils in winter, the thermal conductivity in the soil λ_T and volumetric heat capacity C_T in heat transfer equation (Equation 9-14) were considered to be composed of three main elements, solid, water, and ice, as shown in Equation 9-15 and Equation 9-16, respectively (DeVries, 1963). The porosity in the original expression was represented as saturated water content θ_S.

Equation 9-15

$$\lambda_T = \lambda_w \theta_u + \lambda_i \theta_i + \lambda_s (1 - \theta_s)$$

Equation 9-16

$$C_T = \rho_w c_w \theta_u + \rho_i c_i \theta_i + \rho_s c_s (1 - \theta_s)$$

where:

θ_i = volumetric ice content

λ_w = thermal conductivity of water (W/m·°C)

λ_i = thermal conductivity of ice (W/m·°C)

λ_s = thermal conductivity of solid (W/m·°C)

ρ_w = density of water (kg/m^3)

ρ_i = density of ice (kg/m^3)

ρ_s = density of solid (kg/m^3)

c_w = specific heat capacity of water (J/kg·°C)

c_i = specific heat capacity of ice (J/kg·°C)

c_s = specific heat capacity of solid (J/kg·°C)

9.3.3 Mechanical Field

A linear elastic relationship was assumed for the stress-strain performance of the unsaturated soil (Z. (Leo) Liu, 2018). Navier's equation was used to simulate the mechanical field, with the governing equation for the transient plane strain problem shown in Equation 9-17, while a strain is given in Equation 9-18. The constitutive equation is shown in Equation 9-19.

Equation 9-17

$$\rho_s \frac{\partial^2 u}{\partial t^2} = \frac{\partial}{\partial z}\left(D_E \frac{\partial u}{\partial z}\right) + \mathrm{F}$$

Equation 9-18

$$\varepsilon = \frac{1}{2}[(\nabla u)^T + \nabla u]$$

Equation 9-19

$$\sigma = D_E \varepsilon_{el} = D_E(\varepsilon - \varepsilon_{ext})$$

where:

u = displacement (m)

D_E = fourth order tensor of material stiffness (N/m)

F = body force (N)

ε = infinitesimal strain tensor

σ = Cauchy stress tensor (Pa) ($\sigma_{12} = \sigma_{21}$)

ε_{el} = elastic strain tensor

ε_{ext}= external strain

D_E is a matrix of material properties of the soil skeleton, which can be defined in Equation 9-20. Stress tensor σ can be defined in Equation 9-21, and strain tensor ε is in Equation 9-22.

Equation 9-20

$$D_E = \frac{E}{(1+v)(1-2v)}\begin{bmatrix} 1-v & v & 0 \\ v & 1-v & 0 \\ 0 & 0 & \frac{1-2v}{2} \end{bmatrix}$$

Equation 9-21

$$\{\sigma\} = \begin{Bmatrix} \sigma_{xx} \\ \sigma_{zz} \\ \tau_{xz} \end{Bmatrix}$$

Equation 9-22

$$\{\varepsilon\} = \begin{Bmatrix} \varepsilon_{xx} \\ \varepsilon_{zz} \\ \gamma_{xz} \end{Bmatrix}$$

where:

E = Young's modulus (Pa)

v = Poisson's ratio

τ = shear stress (Pa)

γ = shear strain

9.3.4 Phase Change Effect

As the relationship between soil water diffusivity and unfrozen water content is stated in Equation 9-5, it does not consider the change of diffusivity in the frozen zone. Therefore, to simulate the relationship in both frozen and unfrozen zones, an impedance factor in Equation 9-23 was introduced to simulate the reduction of soil water diffusivity in frozen soil (Taylor & Luthin, 1978a). Equation 9-5 can be rewritten as Equation 9-24.

Equation 9-23

$$I = 10^{10\theta_i}$$

Equation 9-24

$$D = \frac{K(\theta_u)}{C(\theta_u)} \times I^{-1}$$

where:

I = impedance factor

θ_i = volumetric ice content

D = modified soil diffusivity (m^2/s)

To integrate the relationship between ice and water, the governing equation of fluid flow (Equation 9-8) was modified by incorporating ice content as Equation 9-25 (Taylor & Luthin, 1978a); while that of heat transfer (Equation 9-14) can be re-written as Equation 9-26 by further introducing the concept of latent heat (De Vries, 1958).

Equation 9-25

$$\frac{\partial S}{\partial t}+\frac{\rho_i}{\rho_w}\frac{\partial \theta_i}{\partial t}=\frac{\partial}{\partial z}\left[D(S)\frac{\partial S}{\partial z}+K(S)\right]$$

Equation 9-26

$$\rho C_T\frac{\partial T}{\partial t}-L\cdot\rho_i\frac{\partial \theta_i}{\partial t}=\frac{\partial}{\partial z}\left(\lambda_T\frac{\partial T}{\partial z}\right)-\rho_w C_w D(s)\frac{\partial S}{\partial z}\frac{\partial T}{\partial z}$$

where:

L = latent heat coefficient

The latent heat, which is supposed to have a fixed value identical to that of the bulk water, is the "hidden" thermal energy change that occurs when the phase changes without a corresponding change in temperature (G L Guymon et al., 1993)

In the governing equations for moisture and temperature field, there are three unknowns, including ice content, saturation, and temperature. Therefore, another correlation is needed to solve the problem. The concept of solid-to-liquid ratio was proposed (Bai, 2015; Deng et al., 2021), which is used to describe the ratio of volumetric ice content and unfrozen water content, as shown in Equation 9-27.

Equation 9-27

$$B_i=\frac{\theta_i}{\theta_u}=\begin{cases}\dfrac{\rho_w}{\rho_i}\left(\dfrac{T}{T_f}\right)^B-\dfrac{\rho_w}{\rho_i} & T<T_f\\ 0 & T\geq T_f\end{cases}$$

where:

T_f = freezing-point depression (°C)

B = empirical fitting parameter

By incorporating Equation 9-27 and Equation 9-7 into Equation 9-25, the governing equation of fluid flow can be finalized as Equation 9-28. Similarly, the governing equation of heat transfer (Equation 9-26) can be finalized as Equation 9-29.

Equation 9-28

$$\frac{\partial S}{\partial t}+\frac{\rho_i}{\rho_w}\cdot\left[(\theta_s-\theta_r)\left(\frac{\partial B(T)}{\partial t}\cdot S+B(T)\cdot\frac{\partial S}{\partial t}\right)+\theta_r\cdot\frac{\partial B(T)}{\partial t}\right]=\frac{\partial}{\partial z}\left[D(S)\frac{\partial S}{\partial z}+K(S)\right]$$

Equation 9-29

$$\rho C_T\frac{\partial T}{\partial t}-L\cdot\rho_i\cdot(\theta_s-\theta_r)\cdot\left(\frac{\partial B(T)}{\partial T}\cdot S\cdot\frac{\partial T}{\partial t}+B(T)\cdot\frac{\partial S}{\partial t}\right)=\frac{\partial}{\partial z}\left(\lambda\frac{\partial T}{\partial z}\right)-\rho_w C_w D(S)\frac{\partial S}{\partial z}\frac{\partial T}{\partial z}$$

Other than the coupling between thermal and hydraulic fields, the strain caused by the phase change of water was also considered to simulate the heaves by the frost action. The strain of frozen pore water in a saturated system was defined to be the relative change in the volume of water when it becomes ice as shown in Equation 9-30 (Mellor, 1970).

Equation 9-30

$$\varepsilon_{ext,s}=\frac{V_i-V_w}{V_s}=\left(\frac{\rho_w}{\rho_i}-1\right)\phi=0.09\phi=\left(\frac{\rho_w}{\rho_i}-1\right)\theta_S$$

where:

V_i= volume of ice (m^3)

V_w= volume of water (m^3)

V_s= volume of soil (m^3)

ϕ= porosity (i.e., $=\theta_s$)

In other words, 9% of the volume increases when the pore water freezes. Then, the degree of water transition was incorporated to define the external strain ε_{ext} in Equation 9-19 caused by water phase change, as shown in Equation 9-31.

Equation 9-31

$$\varepsilon_{ext}=\left(\frac{\rho_w}{\rho_i}-1\right)\theta_s(S_0-S)$$

9.3.5 Thermal-Hydraulic-Mechanical Coupling

Based on the mathematical basis and phase change effect discussed in the previous sections, the thermal field and the hydraulic field were fully-coupled, which were then sequentially coupled with the mechanical field. The temperature change causes a change in unfrozen water content and a change in

the degree of saturation. This leads to a change in volumetric ice content, which also changes the total heat capacity and total thermal conductivity as the pavement structure is considered to be a porous media. Then, the change in ice content also affects the change in strain and stress in the mechanical field, which simulates the heaves by frost action. Figure 9-2 illustrates the coupling principle of the model.

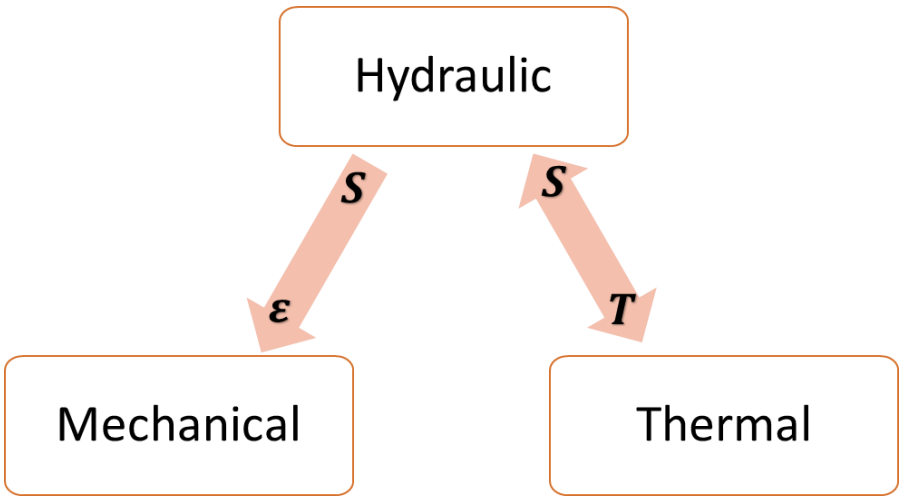

Figure 9-2 THM Coupling

9.4 Model Implementation in COMSOL

COMSOL Multiphysics is a numerical simulation software using finite element solutions. It is known for solving multiple physical processes and coupling the fields. With sufficient built-in equations for different physics, COMSOL also has a partial differential equation (PDE) that allows the users to customize the equations and redevelop them without being restrained by the built-in equations. The process of establishing and solving the model in COMSOL is discussed in this section.

9.4.1 Establishing the Model in COMSOL

To establish the model, first, geometry was created for the pavement structure. Different layers including asphalt surface course, asphalt binder course, granular base, and subgrade were drawn in width of 1 m and their corresponding depth consistent with field conditions from construction and borehole reports. The geometry was established from the surface at the coordinates (0, 0) downwards, as shown in Figure 9-3.

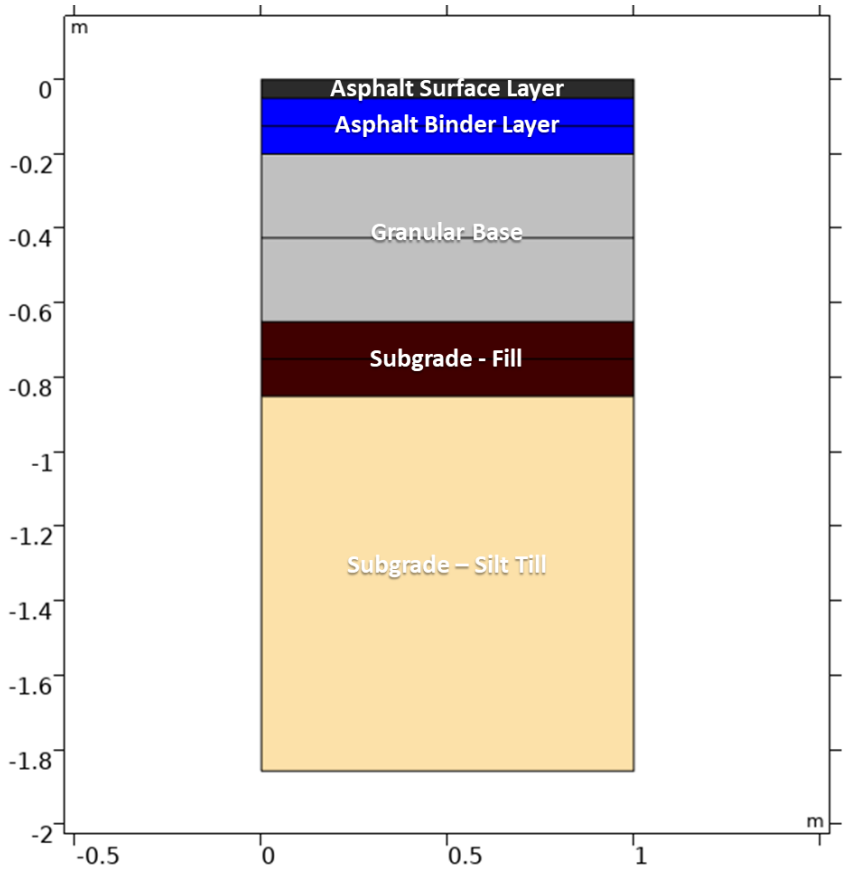

Figure 9-3 Model Geometry in COMSOL

Global definitions were predefined for global parameters with their values and units that were consistent for all types of materials. Material properties were defined in the "Materials" component by assigning local properties to corresponding domains/materials. Local variables were also defined and expressed as functions of parameters and materials properties for different materials.

The meshing was conducted in COMSOL by selecting suitable mesh sizes and meshing types. In this work, the mesh is refined in areas with larger thermal and hydraulic gradients.

9.4.2 Solving the Model in COMSOL

9.4.2.1 Interfaces of Physics

The coefficient form of PDE was used for both thermal and hydraulic fields, which allows users to define the coefficients of the PDEs to change them to the equations the users want to input as an interface to the model. The coefficient form of PDE is shown in Equation 9-32, while the boundary

conditions are expressed in Equation 9-33 as a Neumann boundary condition, and in Equation 9-34 as a Dirichlet boundary condition.

Equation 9-32

$$e_a \frac{\partial^2 u}{\partial t^2} + d_a \frac{\partial u}{\partial t} + \nabla \cdot (-c\nabla u - \alpha u + \gamma) + \beta \cdot \nabla u + au = f \qquad in\ \Omega$$

Equation 9-33

$$\mathbf{n} \cdot (c\nabla u + \alpha u - \gamma) = g - qu \qquad \text{on } \partial\Omega$$

Equation 9-34

$$u = r \qquad \text{on } \partial\Omega$$

where:

u = dependent variable

e_a = mass coefficient

d_a = damping or mass coefficient

c = diffusion coefficient

α = conservative flux convection coefficient

γ = conservative flux source term

β = convection coefficient.

a = source term

f = source term

Ω = computational domain

$\partial\Omega$ = boundary of the computational domain

$\mathbf{n}$ = outward unit normal vector on the boundary of the domain

g = boundary source term

q = boundary absorption coefficient

r = prescribed boundary condition

The dependent variable (u) is saturation (S) for the hydraulic field and temperature (T) for the temperature field. To establish the thermal field, as per its governing equation (Equation 9-29), the coefficients can be determined in Equation 9-35. Similarly, the coefficients of PDE in COMSOL for the hydraulic field can be determined in Equation 9-36 based on Equation 9-28. The coefficients that were not determined are 0 (zero).

Equation 9-35

$$\begin{cases} d_a = 1 + (\theta_s - \theta_r)\dfrac{\rho_i}{\rho_w}B(T) \\ c = D(S) \\ \gamma = -K(S) \\ a = \dfrac{\rho_i}{\rho_w} \cdot \dfrac{\partial B(T)}{\partial t}(\theta_s - \theta_r) \\ f = -\dfrac{\rho_i}{\rho_w} \cdot \theta_r \cdot \dfrac{\partial B(T)}{\partial t} \end{cases}$$

Equation 9-36

$$\begin{cases} d_a = \rho C(S) \\ c = \lambda(S) \\ \beta = \rho_w C_w D(S)\dfrac{\partial S}{\partial z} \\ f = L \cdot \rho_i \cdot \left[(\theta_s - \theta_r) \cdot \left(\dfrac{\partial B(T)}{\partial t} \cdot S + B(T) \cdot \dfrac{\partial S}{\partial t}\right) + \theta_r \cdot \dfrac{\partial B(T)}{\partial t}\right] \end{cases}$$

The mechanical field was established utilizing the built-in solid mechanics physics model in COMSOL by assuming the structure is linear elastic (Deng et al., 2021; Jasim, Fattah, Al-Saadi, & Abbas, 2021; Neaupane, Yamabe, & Yoshinaka, 1999). Yahaghi et al. (2021) also found that the experiment results agree well with stress-strain curves simulated by linear-elastic numerical models for sandstones under freeze-thaw cycles.

The built-in interface for solid mechanics in COMSOL has identical governing equations and boundary conditions equations as discussed in Section 9.3.3. Young's modulus, Poisson's ratio, and density were defined from material properties. From 2D approximation, the plane strain was selected. The external strain was defined by strain tensor as per Equation 9-31.

9.4.2.2 Solver and Studies

The hierarchy of solving the problem in COMSOL is shown in Figure 9-4. Under the top level, the study step is used to control the physics interfaces and equations. The next level contains the solver configuration that includes nodes to define dependent variables, configure the operation, and produce and store the solutions (COMSOL, 2022).

The problem to be solved in this study is a transient problem that uses time-dependent steps. The time integration method was set to be a Backward Differentiation Formula (BDF) solver, which is an implicit solver that indicates time integration method $\alpha = 1$. Implicit solver is the most used method with its stability. Direct solver was used to solve the problem in the form of $Ax = B$, which is commonly used for non-linear and multiphysics problems.

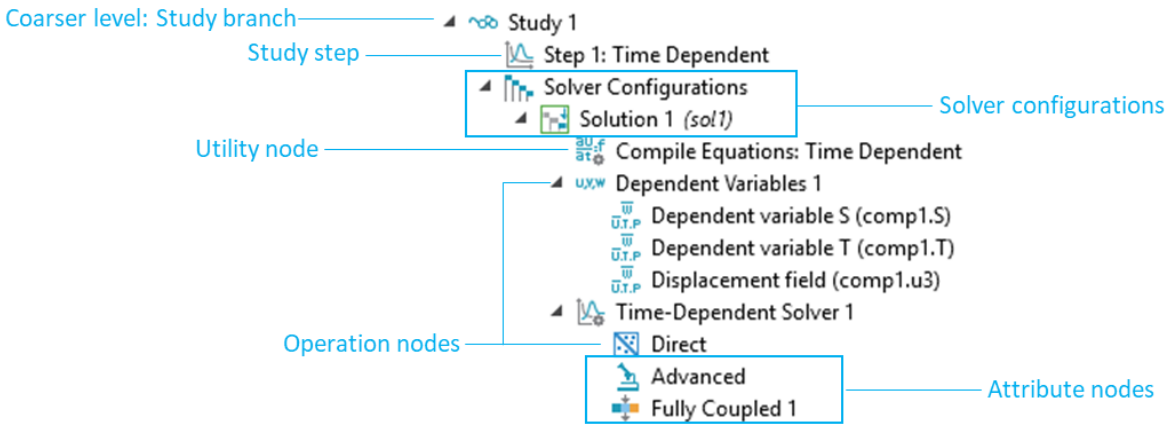

Figure 9-4 Hierarchy of the Study Node (COMSOL, 2022)

9.5 Pavement Structure Modelling

After implementing the mathematical model in COMSOL, the actual pavement structure that simulates the field trial sections was created based on site configurations and geotechnical conditions. The material properties were determined based on characterization. The field measurements were assigned to boundary conditions. Simulated results from one freeze-thaw cycle (i.e., 1 year) were discussed including temperature changes, saturation, and displacements.

9.5.1 Model Geometry and Discretization

To reflect the field conditions, the geometry of the pavement structure was built with one lift of 50 mm asphalt surface course (SP 12.5), two lifts of 75 mm asphalt binder course (SP 19), and a 450 mm

granular base. The subgrade was created with 200 mm fill and 1000 mm silt till. The subgrade was drawn with a limited depth to better visualize the changes from the simulation results.

Free triangular meshing was established with finer sizes, which completed mesh consists of 1132 domain elements and 201 boundary elements. The geometry and meshing are illustrated in Figure 9-5.

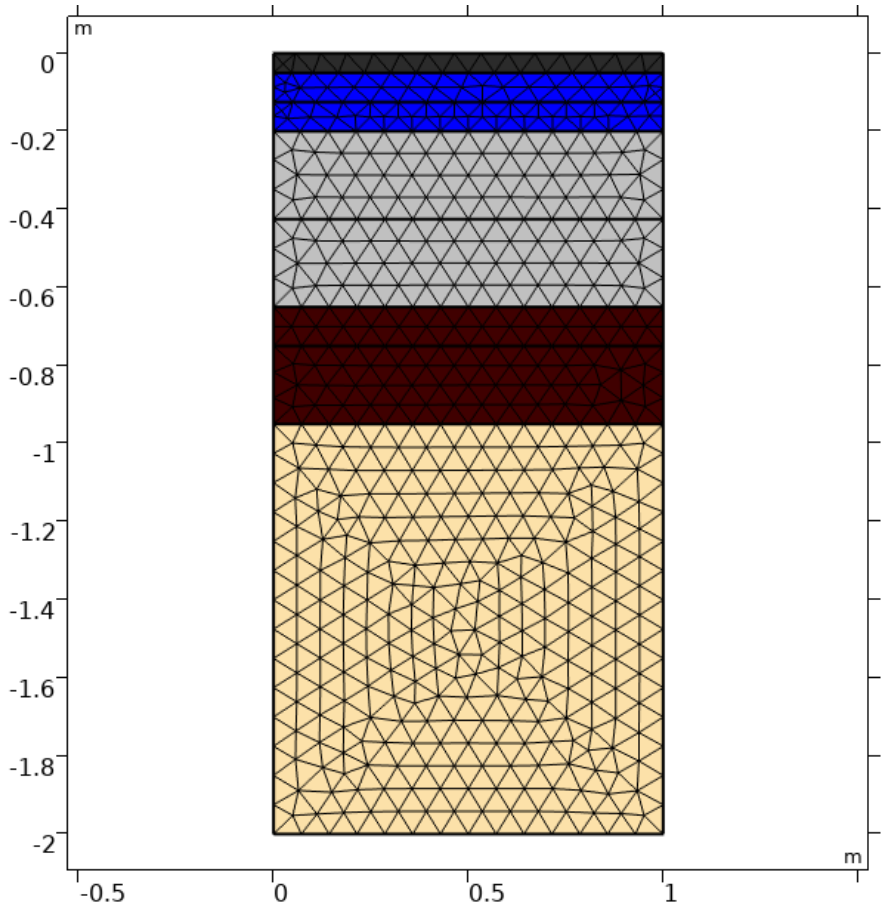

Figure 9-5 Model Geometry and Meshing

9.5.2 Parameter Inputs and Material Inputs

The global parameter inputs for physical constants are listed in Table 9-2, obtained from the literature (G L Guymon et al., 1993; Wu et al., 2022; Y. Zhang, Asce, Michalowski, & Asce, 2014b, 2014a). The material properties were determined from material characterization results in Section 4.3 and geotechnical reports provided by the Region. Other properties were obtained from the literature (Gardner, 1958; G L Guymon et al., 1993; Wu et al., 2022; Yasuoka et al., 2022). The material properties for mechanical, hydraulic, and thermal fields are listed in Table 9-3, Table 9-4, and Table 9-5, respectively.

Table 9-2 Global Parameter Inputs for Physical Constants

Notation	Parameter	Unit	Value
T_f	freezing point depression	°C	-0.540
c_w	heat capacity of water	J/kg·°C	4200.000
c_i	heat capacity of ice	J/kg·°C	2100.000
λ_w	thermal conductivity of water	W/m·°C	0.630
λ_i	thermal conductivity of ice	W/m·°C	2.310
ρ_w	density of water	kg/m^3	1000.000
ρ_i	density of ice	kg/m^3	918.000
L	specific latent heat	J/kg	3.3456E+05

Table 9-3 Material Mechanical Properties

Notation	Properties	Unit	Material	Value
ρ_s	density	kg/m^3	SP 12.5 asphalt mixes	2523
			SP 19 asphalt mixes	2468
			Granular A	2043
			Fill - sandy silt	2064
			Silt till - clay	1745
E	Young's modulus	Pa	SP 12.5 asphalt mixes	1.40E+09
			SP 19 asphalt mixes	1.10E+09
			Granular A	2.20E+08
			Fill - sandy silt	4.50E+07
			Silt till - clay	2.50E+07
v	Poisson's ratio	-	SP 12.5 asphalt mixes	0.35
			SP 19 asphalt mixes	0.35
			Granular A	0.35
			Fill - sandy silt	0.4
			Silt till - clay	0.4

Table 9-4 Material Hydraulic Properties

Notation	Properties	Unit	Material	Value
θ_r	residual water content	-	SP 12.5 asphalt mixes	0.001
			SP 19 asphalt mixes	0.001
			Granular A	0.001
			Fill - sandy silt	0.05
			Silt till - clay	0.1
θ_s	saturated water content	-	SP 12.5 asphalt mixes	0.1
			SP 19 asphalt mixes	0.1
			Granular A	0.1
			Fill - sandy silt	0.3
			Silt till - clay	0.5
S_0	initial saturation	-	SP 12.5 asphalt mixes	0.1
			SP 19 asphalt mixes	0.1
			Granular A	0.1
			Fill - sandy silt	0.3
			Silt till - clay	0.5
K_s	saturated hydraulic conductivity	m/s	SP 12.5 asphalt mixes	1.80E-02
			SP 19 asphalt mixes	1.60E-02
			Granular A	1.00E-03
			Fill - sandy silt	7.50E-05
			Silt till - clay	1.13E-06

Table 9-5 Material Thermal Properties

Notation	Properties	Unit	Material	Value
λ_s	thermal conductivity	W/m·°C	SP 12.5 asphalt mixes	2
			SP 19 asphalt mixes	1.5
			Granular A	2
			Fill - sandy silt	1.2
			Silt till - clay	1.2
c_s	heat capacity	J/kg·°C	SP 12.5 asphalt mixes	713
			SP 19 asphalt mixes	729
			Granular A	1370
			Fill - sandy silt	581
			Silt till - clay	561

9.5.3 Initial Condition and Boundary Conditions

As mentioned, for PDE interfaces, a Dirichlet boundary condition can be assigned with a specified value or function to the dependent variable. In addition, a Neumann boundary condition can be assigned to boundaries with a flux.

For the hydraulic field, zero flux was assigned to all vertical boundaries of all domains (Boundary 10 and 11 in Figure 9-6) so that the fluid flows in the structure vertically only, with the sides assumed to be impermeable. The initial conditions were set to be the initial saturation in Table 9-4.

The boundary conditions for the thermal field were calibrated with the field measurements. Boundaries 10 and 11 were assumed to be insulated with no external heat flux. Boundaries 1 and 9 were Dirichlet boundary conditions, where the prescribed temperature was parametric input based on ambient temperature data. The functions fitting the results were plotted in Figure 9-7. Measurements from temperature sensors in the asphalt, base layer, and at 100 mm below subgrade were assigned to Boundary 4, 5, and 7, respectively. The measurements were assigned with models developed in Section 9.2. The initial conditions were set to be the first value of the measurements.

As mentioned, the temperature boundary conditions in this model were calibrated from the field measurements. Least Squares Regression fitting analysis was performed on the temperature measurements with 95% confidence bounds to generalize the boundary conditions as functions. Fourier series was found to be representative of meteorological behaviour (Faye, Herrera, Bellomo, Silvain, & Dangles, 2014; Meza & Varas, 2000; Parton & Logan, 1981; Winter et al., 2021). A one-term Fourier series was used to fit the annual daily average air temperature measurements as shown in Equation 9-37.

The fitted results are shown in Figure 9-7. A strong correlation was shown with $R^2 = 0.838$. The daily average temperature measured from the weather station owned by Environment Canada is also plotted and validated in the figure, showing satisfactory alignment. The fitting results are summarized in Table 9-6, with the goodness of fit including R-square, and RMSE (Root Mean Square Error).

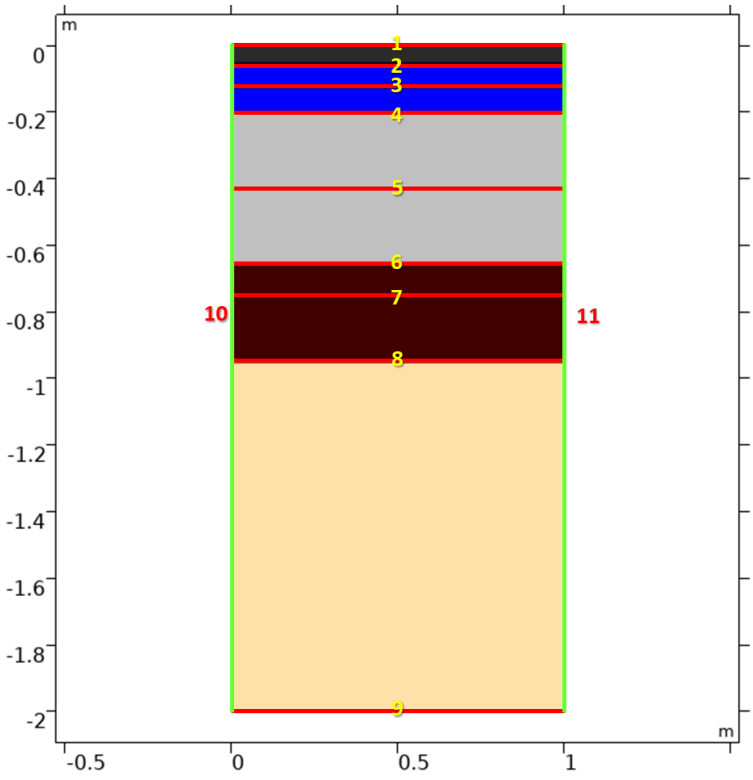

Figure 9-6 Boundaries of the Model

Equation 9-37

$$T(t) = a_0 + a_1 * cos(t * w) + b_1 * sin(t * w)$$

where:

T = temperature (ºC)

t = time (days)

a_0, a_1, b_1, m = best-fit parameters

Table 9-6 Fitting Results of Daily Average Ambient Temperature

Fitting Coefficients				Goodness of Fit		Goodness of Validation
a_0	**a_1**	**b_1**	**w**	**R^2**	**RMSE**	**RMSE**
8.229	11.872	-4.303	0.0175	0.838	3.968	4.024

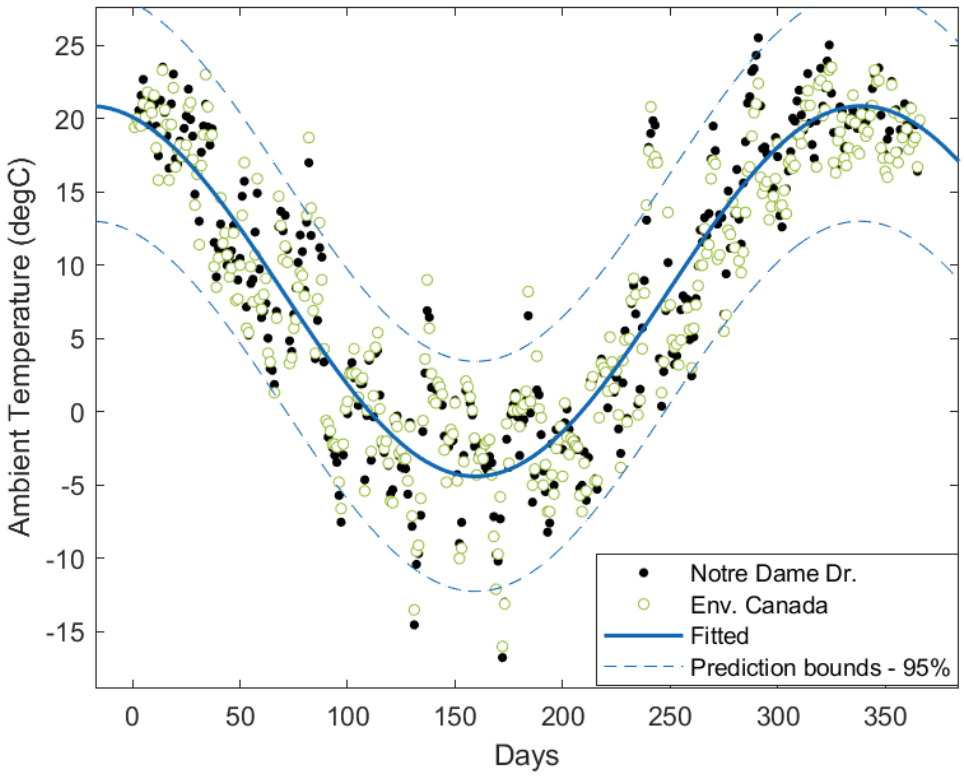

Figure 9-7 Best-fitted Function for Ambient Temperature Measurements

For the thermal boundary conditions in the pavement structures, the fitted model of ambient temperature was assigned to Boundary 1 and Boundary 9. Subsequently, the ambient temperature model was incorporated with the developed layer temperature predictive models with their slopes in Table 9-1 to assign to the pavement layers' boundary conditions. The asphalt temperature model was assigned to Boundary 4; the base temperature model was assigned to Boundary 5; the subgrade temperature model was assigned to Boundary 7. Notably, due to the warmer winter in 2023 with measured pavement temperature consistently remained above 0°C. The ambient temperature model was assigned to a lower level of subgrade at Boundary 9 model to maximize the impact of freeze-thaw actions.

In the mechanical field, the displacements in the horizontal direction (x-axis) were prescribed to be zero for Boundary 10 and 11. The displacement at Boundary 9 was also restrained to be zero. The initial condition for all domains was set to be no displacement.

9.5.4 Results

The model was run for 365 days with the developed temperature predictive model with a computational step of 1 day. The simulated results of temperature changes with time and depth, saturation, and displacements are discussed in the following.

9.5.4.1 Temperature

The simulated temperatures at depths of 0.05 m, 0.2 m, 0.45 m, 1 m, and 1.8m, were plotted in Figure 9-8, with the comparison of the CT section and GC section. The temperature variation over the year was similar for both sections. The major differences occurred in the base layer, where the temperature variation was higher in the GC section. However, in the subgrade layer, the GC section exhibited approximately the same level of temperature variation as that in the CT section. This can be attributed to the geogrid composite installed at the interface of the subgrade and base layer, which played an important role in maintaining stable temperature by draining and filtering.

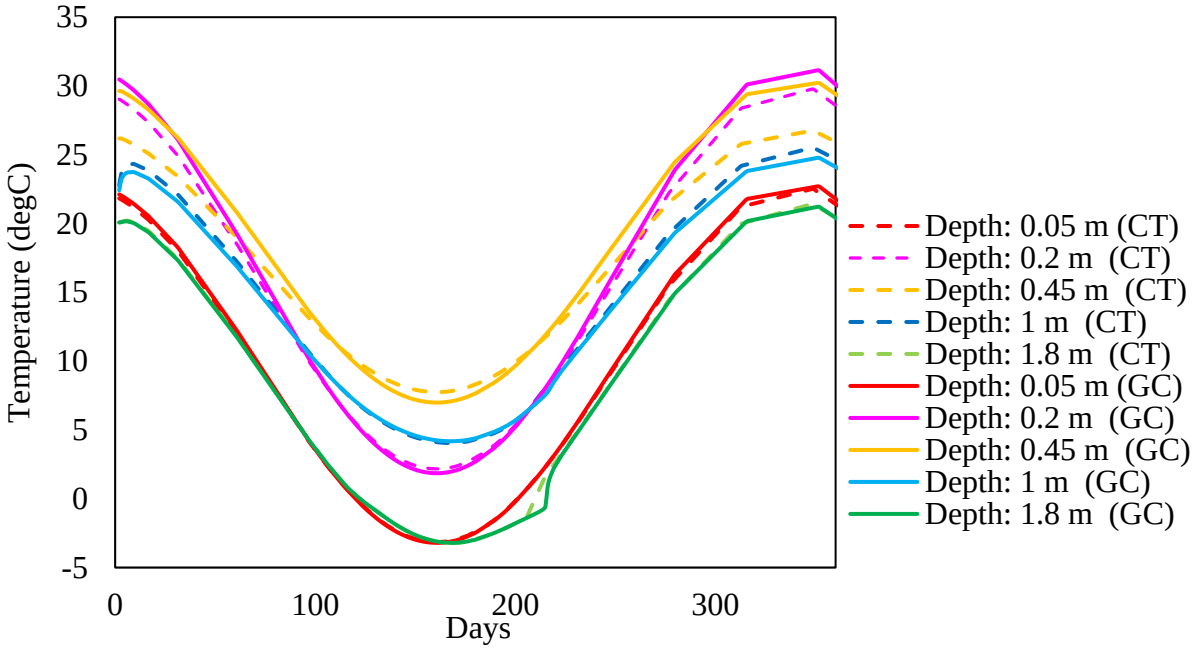

Figure 9-8 Simulated Pavement Temperatures from August 2022 to August 2023

To further look into the temperature fluctuation in a more detailed perspective, the maximum temperature variation was computed by subtracting the maximum temperature from the minimum one over the year. The results are plotted in Figure 9-9. It can be seen that the maximum temperature variation in the GC section was higher than that in the CT section above the subgrade, while it decreased

to be lower than that in the CT section below the subgrade. The critical role of the geogrid composite in minimizing temperature fluctuations in the subgrade was further highlighted.

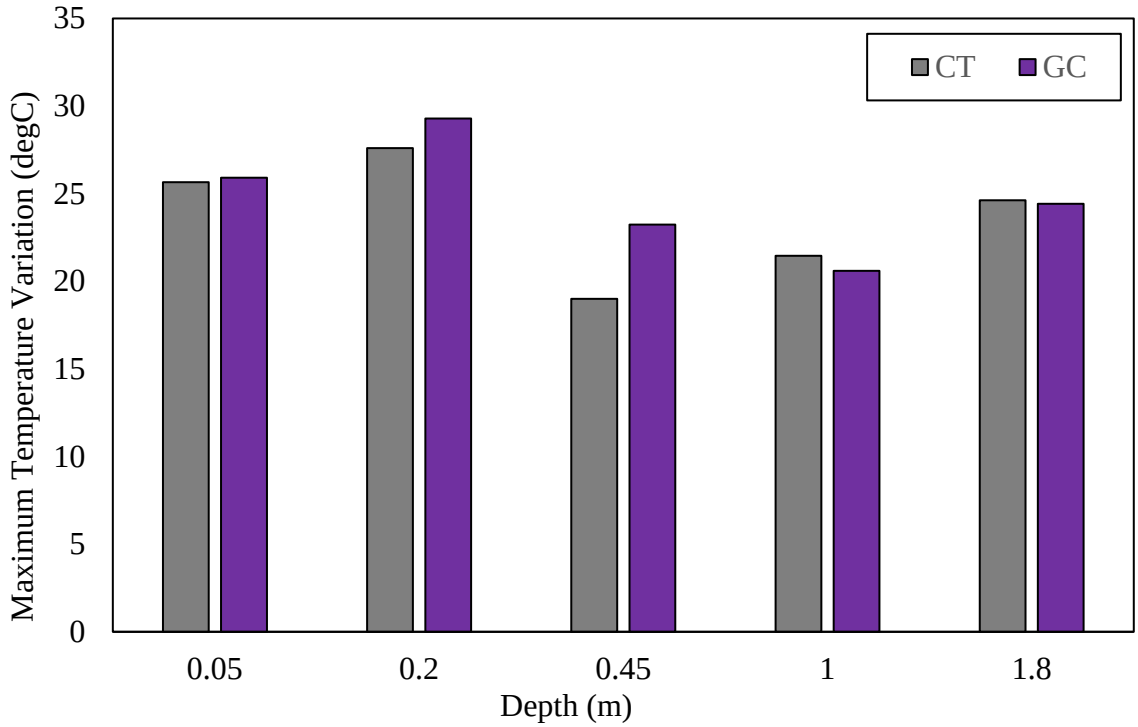

Figure 9-9 Simulated Maximum Pavement Temperatures Variation from 2022 to 2023

9.5.4.2 Moisture Content

With the coupling between moisture and temperature, the saturation degree within the pavement can also be evaluated, as plotted in Figure 9-10. The frost action can be clearly identified with the drop of saturation in the subgrade starting around Day 100, while from Day 170, the saturation degree increased, representing the thawing progress. The difference between the CT and the GC sections is not visible during the freezing period. However, after the thawing period, the saturation level in the pavement in the GC section was lower than that in the CT section, underscoring the draining and filtering capabilities provided by the geogrid composite.

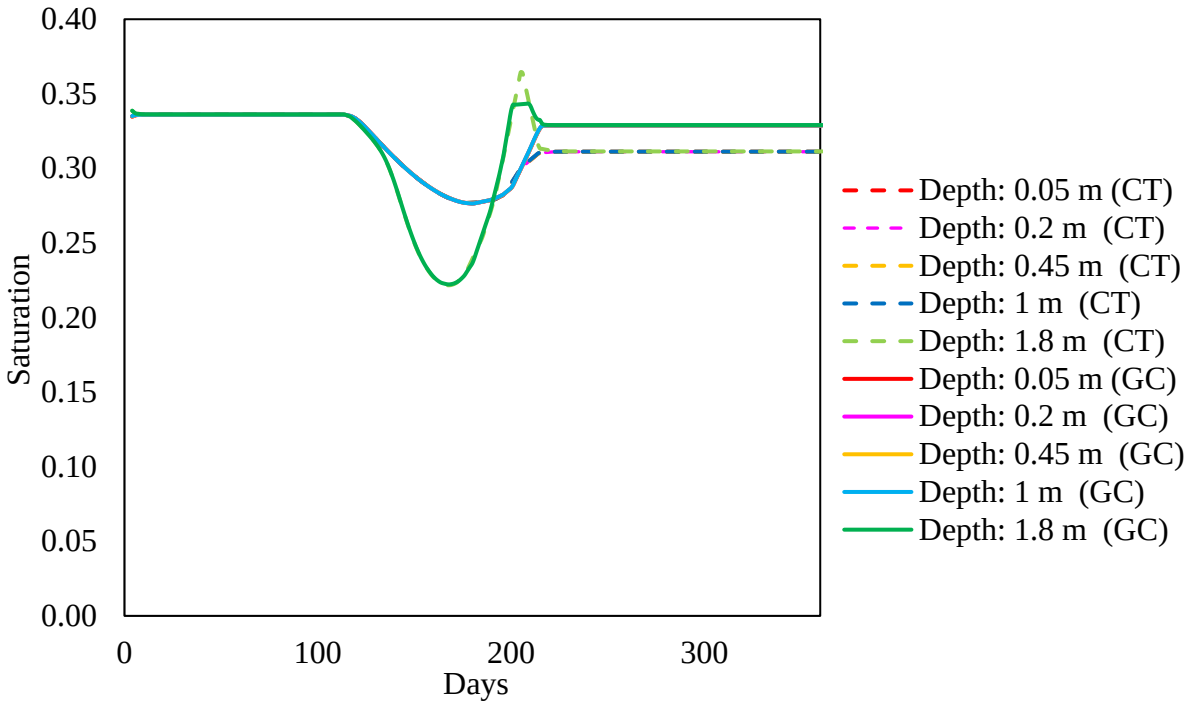

Figure 9-10 Simulated Pavement Saturation from August 2022 to August 2023

9.5.4.3 Pavement Deformation

Lastly, the deformation of the pavement structure was simulated with the change in saturation or ice content, as plotted in Figure 9-11. The level of deformation associated with the frost action, namely heaves, was similar in both sections, aligning with the corresponding observations related to changes in saturation. The simulation results highlighted that the development of frost heave predominantly originated within the subgrade, with the level of displacement maintaining a consistent pattern, gradually progressing upwards toward the pavement surface from the subgrade interface. However, following the thawing period, notable disparities in the level of deformation were observed between the two sections, with the GC section demonstrating a lower level of displacement. This finding highlights the significant impact of the geogrid composite in effectively mitigating the negative effects of frost-related deformations within the pavement structure.

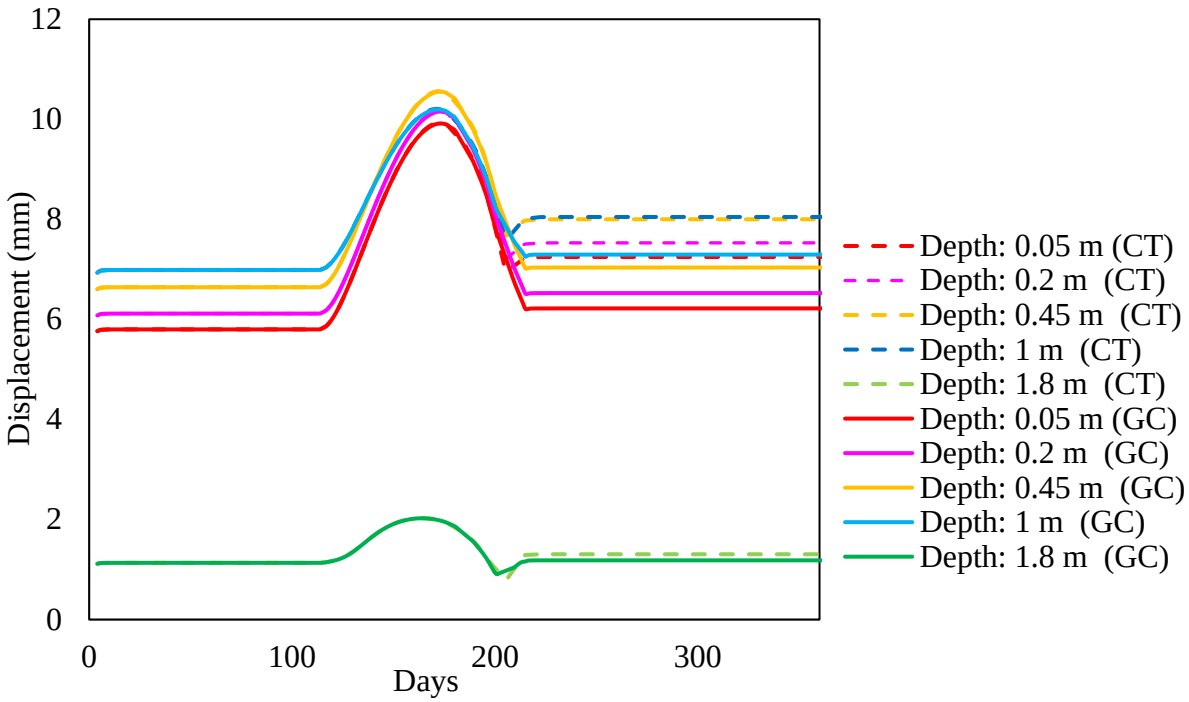

Figure 9-11 Simulated Pavement Deformation from August 2022 to August 2023

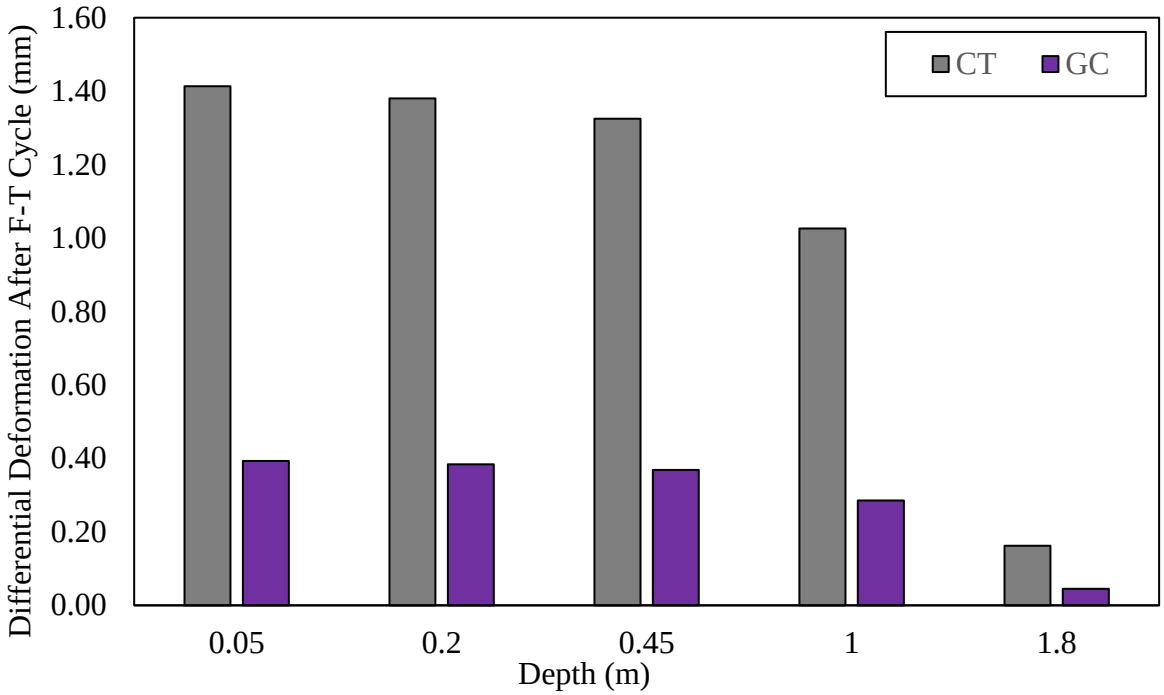

Figure 9-12 Simulated Pavement Differential Deformation After One F-T Cycle

In this case, the computation and comparison of the differential deformation before and after the F-T cycle were conducted and visually represented in Figure 9-12. The results notably indicated a significantly lower level of differential deformation attributed to the F-T actions in the GC section. This observation serves as a significant indicator of the critical role played by the geogrid composite in effectively mitigating the disruptive effects of the freeze-thaw cycle on the pavement structure. The pronounced reduction in differential deformation signifies the effectiveness of the geogrid composite in enhancing the structural resilience and durability of the pavement, thereby contributing to its overall longevity and performance under challenging environmental conditions.

9.6 Model Calibration

In order to validate the accuracy of the simulated pavement temperatures, comparisons were made with the field instrumentation data from August to October in 2023, considering measurements at the bottom of the asphalt layer, the middle of the base layer, and 10 cm below the subgrade interface. The comparison of the CT section and the GC section were plotted in Figure 9-13, and Figure 9-14, respectively. In the CT section, the simulated asphalt temperature demonstrated an agreement with the field measurements, whereas the simulated base and subgrade temperatures were slightly underestimated. Similarly, in the GC section, both the simulated asphalt and base temperature profiles exhibited an acceptable correlation with the corresponding field measurements, albeit with a slight underestimation observed for the subgrade temperature. Despite these minor deviations, the developed simulation model effectively captured the changing trends in temperature dynamics, showcasing a reliable and satisfactory performance in replicating the real-world temperature variations observed in the field measurements.

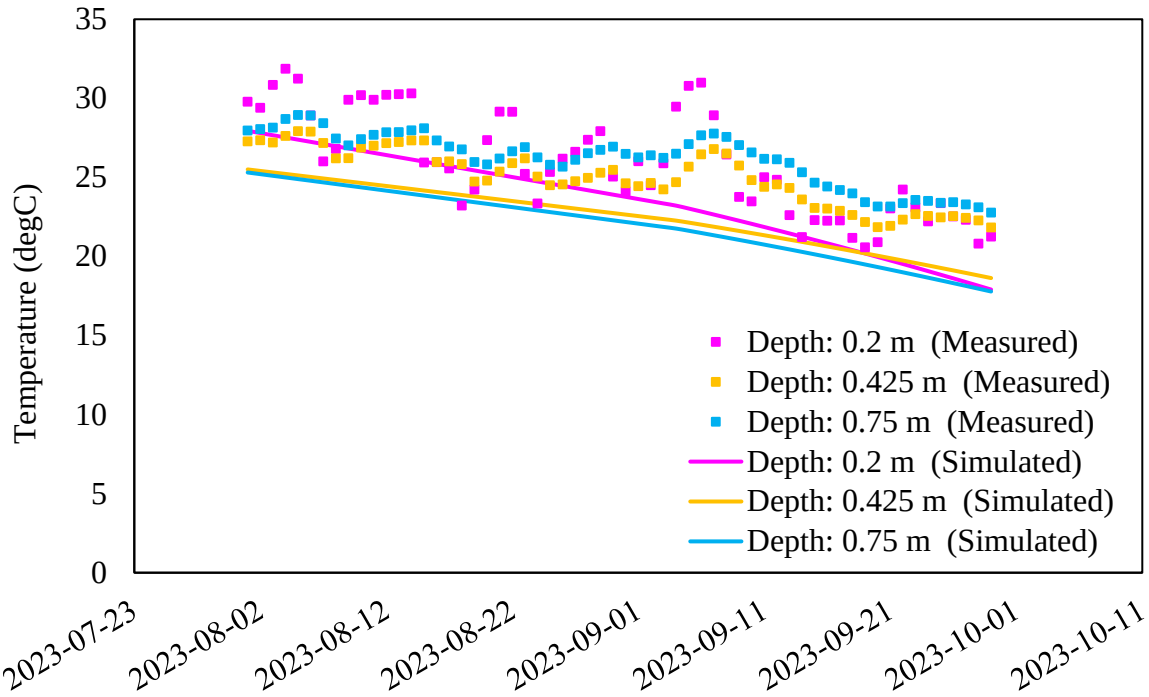

Figure 9-13 Validation of Simulated Pavement Temperature in the CT Section

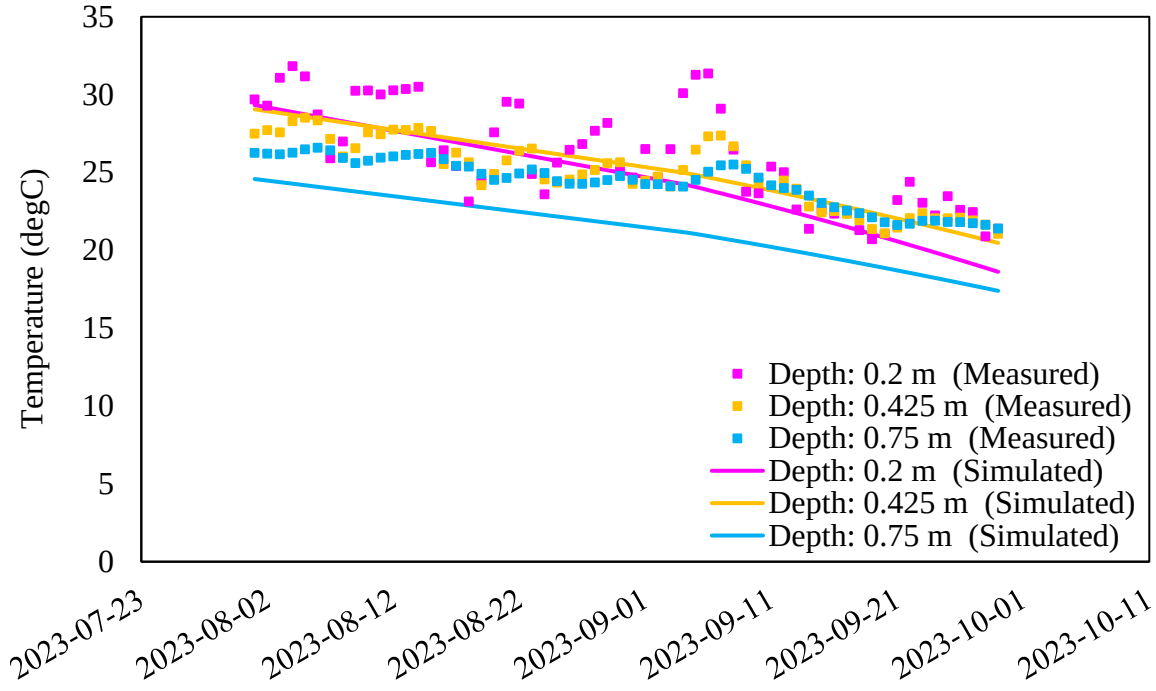

Figure 9-14 Validation of Simulated Pavement Temperature in the GC Section

9.7 Chapter Summary

In this chapter, a model that follows the laws of mass and energy conservation to simulate the fluid moisture transport and heat transfer in the pavement structure was presented. Approached through the isothermal process, the phase change was taken into account. These physical processes were solved using the finite element method and the finite difference method. This model was implemented in COMSOL. The inputs of the model include the material properties as well as the ambient and pavement temperatures. Pavement temperature predictive models were established for asphalt, base, and subgrade temperatures and assigned to the boundary conditions of the developed numerical model.

The results from the one-year simulation from 2022 to 2023 showed the change in pavement saturation and temperature due to F-T action, which consequently caused differential deformation of the pavement structure. The GC section exhibited less temperature variation over the year in the subgrade and a lower level of saturation after the thawing period, which highlighted the critical role of geogrid composite in draining the water and stabilizing the temperature in the subgrade. The frost heave was similar in both sections, which was mainly developed in the subgrade. The level of displacement maintained a similar level by moving upwards towards the pavement surface starting from the interface of the subgrade. However, after the thawing period, the GC section had a lower level of displacement. A significantly lower level of differential deformation caused by the F-T actions was observed in the GC section. This signifies the critical role of geogrid composite in mitigating the F-T disturbances to the pavement. The developed model was compared with the field measurements with field pavement temperature measured from the subsequent three months with the alignment of the changing trend.

Chapter 10
Conclusion

10.1 Overall Summary

This comprehensive study on geosynthetic-reinforced pavements was directed at the evaluation of two geosynthetic materials: fibreglass geogrid in the asphalt layer; and geogrid composite at the interface of base and subgrade. The constructability and impact of construction activities on the pavements reinforced by these two types of materials were evaluated during the construction of the field trial sections by comparing to the unreinforced control section with conventional flexible pavement design. The materials sampled from the field were tested in the laboratory to ensure the reliability of the information provided by the contractor and serve for further analyses. Geogrid-embedded asphalt samples were tested by small-scale laboratory testing to evaluate the rutting and moisture susceptibility with a conventional HWTT, as well as a proposed dynamic creep test plus an F-T conditioning procedure for such asphalt samples. The field instrumentation was monitored for one year after construction completion to evaluate the geosynthetic-reinforced pavements in real life with temperature, moisture, stress, and strain data under a complete F-T cycle. The use of geosynthetics in the in-service pavement performances by field testing to examine the roughness, stiffness, and critical mechanical response from heavy traffic loading was also investigated. Lastly, a numerical model was developed to simulate the pavement performance under freeze-thaw actions and examine the use of geogrid composite on the subgrade. The characterized material properties and field measurements were used to calibrate and validate the model.

10.2 Conclusions

The study examining the use of geosynthetics in pavements was conducted in three aspects: laboratory testing, field study, and numerical modelling. The findings were described in detail in the corresponding chapters, while the following presents the general conclusions:

- Installation of fibreglass geogrid within the asphalt requires more careful attention compared to the installation of geogrid composite on the subgrade. Special measures should also be taken on the application of tack coat, the wrinkle removal, the order of installing the geogrid materials in different widths, and the paving of the second lift overlying the geogrids.

- Critical responses measured within the pavement show that the geogrid in the binder course can diminish the mechanical disturbances vertically and horizontally exerted by construction activities. The geogrid composite can offer little reinforcement of the entire structure during the construction with a similar mechanical response to the control section.
- The HWTT results reveal that Geogrid 11, with larger openings, has a lower creep slope, which indicates a better rutting resistance. Geogrid 10 with smaller openings has a lower stripping slope and the highest SIP, representing less moisture susceptibility. Geogrid 11 EPM has the worst performance including rutting resistance and moisture susceptibility, which can be attributed to the extra membrane. The membrane likely did not melt during the compaction, which can be due to the small amount of material to compact the specimens, which brings little heat to melt the membrane.
- The proposed dynamic creep test demonstrates that the fibreglass geogrid, utilized for reinforcement, aids in enhancing resistance to permanent deformation, thus prolonging the asphalt's resistance to rutting. The test results show that geogrids with smaller apertures and extra bonding have better potential to resist permanent deformation. By understanding the specific contributions of geogrids with varying aperture sizes, engineers and researchers can make informed decisions when selecting and incorporating geogrid materials into pavement design and construction processes.
- A less aggressive F-T conditioning procedure was proposed on such geogrid-embedded asphalt samples to investigate the moisture susceptibility. The results demonstrate that the samples without any form of reinforcement consistently display the highest creep rate and the lowest ultimate creep modulus, while geogrids with larger openings and extra bonding could mitigate the detrimental impacts of moisture-induced damages.
- The field instrumentation results observed negative temperature differentials in the GC section during winter, which signifies the geogrid composite's effectiveness in regulating subgrade temperature and mitigating frost-related risks. Moisture data show the GC section displays relatively drier conditions showing the draining behavior, particularly notable during thawing seasons. A lower level of strain variation and pressure experienced at the bottom of asphalt in the GG section emphasizes the resilient load-bearing capabilities and strain-absorption properties facilitated by the fibreglass geogrid. The GC section also

exhibited a lower strain and pressure on the subgrade compared to the CT section, highlighting the reinforcing impact of the geogrid composite on the subgrade.

- The pavement stiffness in the CT section was affected by ambient and pavement temperatures the most. This implies the effect of geosynthetic materials in preventing pavement stiffness from varying from temperature changes. Roughness measurements signify the necessity of an overlay of the surface course with the geogrid reinforcement in the asphalt concrete course. Truck testing demonstrates the load-distribution capability offered by fibreglass geogrid embedded in the asphalt layer.
- In the one-year simulation from 2022 to 2023 performed by the developed model, the GC section demonstrated less temperature variation in the subgrade, lower saturation levels, and lower displacement levels after the thawing period compared to the CT section. This highlights the geogrid composite's vital role in drainage and subgrade temperature stabilization as well as in mitigating freeze-thaw disturbances to the pavement. Furthermore, the developed model was compared with field measurements, aligning well with observed trends in pavement temperature over the subsequent three months.

10.3 Contribution

This contribution provided by this thesis is listed as follows:

- A sophisticated plan was developed for full-scale studies with instrumentation calibration and installation to monitor the pavement performances. The installation guides and suggestions for geosynthetics on the pavements were provided. The evaluation of constructability and impacts of construction activities on geosynthetic-reinforced pavements during the construction were also demonstrated.
- A method of compaction and preparation of geogrid-embedded asphalt materials in the laboratory was developed, with the proposed measures to ensure the consistency of air void contents throughout the specimens.
- The rutting and moisture susceptibility of geogrid-embedded asphalt samples were tested by the conventional HWTT, which provides insight into little reliability with HWTT on geogrid-embedded asphalt samples.

- To replicate real-world traffic conditions that contribute significantly to permanent deformation in asphalt pavements, a fundamental test called the dynamic creep test was proposed on the basis of the current flow number test. The insights derived from the poorer performances of 100 mm samples emphasize the necessity of implementing extended testing protocols to better understand the deformation mechanisms and long-term performance characteristics of asphalt materials, especially under high-temperature conditions. This comprehensive approach will facilitate the development of more accurate testing standards. The function of fibreglass geogrid in enhancing rutting resistance was assessed with this test.
- A freeze-thaw conditioning procedure was proposed for this particular multilayered asphalt sample to assess moisture susceptibility. Their performance is subsequently compared with that of non-conditioned samples, which helps in understanding how moisture susceptibility impacts the asphalt's resistance to permanent deformation, providing insights into the function of the geogrid within the asphalt samples when they are subjected to moisture damage.
- The field performance monitored over one year by instrumentation and field testing examines the use of geosynthetic materials in the pavement in real life. The drainage and filtering capabilities provided by geogrid composite, and subsequently the effect of mitigating F-T disturbances was demonstrated. The load distribution and reinforcement provided by fibreglass geogrid were also demonstrated.
- A THM numerical model was developed in COMSOL to simulate the impact of F-T actions on pavement structures. Layer temperature predictive models were also proposed with the input of ambient temperature. The critical role of geogrid composite in mitigating freeze-thaw disturbances to the pavement was demonstrated with less temperature variation in the subgrade, lower saturation levels, and lower displacement levels after the thawing period.

10.4 Recommendation for Future Studies

The study successfully examines the use of geosynthetic materials in pavements. A framework with three aspects of study (i.e., laboratory testing, full-scale field study, and numerical modelling) was proposed and followed. The following summarizes the recommendation for future potential research:

- A field trial employing the geogrid composite at the interface of base and subgrade and the fibreglass geogrid in the asphalt layer in the same section can be evaluated to see if it yields the maximum benefits for the overall pavement design life.
- The reduction in thickness of the asphalt layer or base layer can be employed to quantify the amount of material the geosynthetics could save.
- The bonding between geogrid and asphalt can be studied to investigate the optimum type and usage of tack coat.
- More non-destructive testing can be performed with heavier loading to measure the mechanical behaviour of pavement structure.
- A life cycle cost analysis and life cycle assessment could be performed to analyze the sustainability, social and environmental impacts, to evaluate the life cycle performances of geosynthetic-reinforced pavement. The recyclability of fibreglass geogrid and geogrid composite can be studied such as the milling process.
- The repeatability of the compaction practice of geogrid-embedded asphalt specimens in the laboratory needs to be validated.
- The numerical model can be further elaborated by incorporating modelling of the viscoelasticity of the asphalt layer. Also, the modelling of geosynthetics can be enhanced by configuring the model.

References

AASHTO. (1993a). *AASHTO Guide for Design of Pavement Structure*. Washinton, D.C.

AASHTO. (1993b). *AASHTO guide for design of pavement structure, American Association of State and Highway Transportation Officials*. Washington, D.C.

AASHTO. (2014). *AASHTO T 283 Standard Method of Test for Resistance of Compacted Asphalt Mixtures to Moisture-Induced Damage*. Washington, D.C.

AASHTO. (2016a). *AASHOTO T 209 Standard Method of Test for Theoretical Maximum Specific Gravity (Gmm) and Density of Hot Mix Asphalt (HMA)*.

AASHTO. (2016b). *AASHTO T 166 Standard Method of Test for Bulk Specific Gravity (Gmb) of Compacted Asphalt Mixtures Using Saturated Surface-Dry Specimens*. Washington, D.C.

AASHTO. (2017). *AASHTO T 378-17 Standard Method of Test for Determining the Dynamic Modulus and Flow Number for Asphalt Mixtures Using the Asphalt Mixture Performance Tester (AMPT)*. Washington, D.C.

AASHTO. (2019a). *AASHTO T 324 Standard Method of Test for Hamburg Wheel-Track Testing of Compacted Asphalt Mixtures*. Washington, D.C.

AASHTO. (2019b). *AASHTO T 342 Standard Method of Test for Determining Dynamic Modulus of Hot Mix Asphalt (HMA)*. Washington, D.C.

AASHTO. (2021). *AASHTO M 145-91 Standard Specification for Classification of Soils and Soil–Aggregate Mixtures for Highway Construction Purposes*. Washington, D,C.

Abu-Farsakh, M. Y., & Chen, Q. (2011). Evaluation of geogrid base reinforcement in flexible pavement using cyclic plate load testing. *International Journal of Pavement Engineering*, *12*(3), 275–288. https://doi.org/10.1080/10298436.2010.549565

Abu-Farsakh, M. Y., Gu, J., Voyiadjis, G. Z., & Chen, Q. (2014). Mechanistic-empirical analysis of the results of finite element analysis on flexible pavement with geogrid base reinforcement. *International Journal of Pavement Engineering*, *15*(9), 786–798. https://doi.org/10.1080/10298436.2014.893315

Adwan, I., Milad, A., Memon, Z. A., Widyatmoko, I., Zanuri, N. A., Memon, N. A., & Yusoff, N. I. M. (2021). Asphalt Pavement Temperature Prediction Models: A Review. *Applied Sciences 2021, Vol. 11, Page 3794*, *11*(9), 3794. https://doi.org/10.3390/APP11093794

Ahirwar, S. K., & Mandal, J. N. (2017). Finite Element Analysis of Flexible Pavement with Geogrids. *Procedia Engineering*, *189*, 411–416. https://doi.org/10.1016/j.proeng.2017.05.065

Airey, G. D. (2004). Fundamental Binder and Practical Mixture Evaluation of Polymer Modified Bituminous Materials. *International Journal of Pavement Engineering*, *5*(3), 137–151. https://doi.org/10.1080/10298430412331314146

Alavi, M. Z., Pouranian, M. R., & Hajj, E. Y. (2014). Prediction of Asphalt Pavement Temperature Profile with Finite Control Volume Method. *Https://Doi.Org/10.3141/2456-10*, *2456*, 96–106. https://doi.org/10.3141/2456-10

Albayati, A. H. (2023). A review of rutting in asphalt concrete pavement. *Open Engineering*, *13*(1). https://doi.org/10.1515/ENG-2022-0463/MACHINEREADABLECITATION/RIS

Alimohammadi, H., Schaefer, V. R., Zheng, J., & Li, H. (2021). Performance evaluation of geosynthetic reinforced flexible pavement: a review of full-scale field studies. *International Journal of Pavement Research and Technology*, *14*(1), 30–42. https://doi.org/10.1007/s42947-020-0019-y

Al-Qadi, I. L., Dessouky, S. H., Kwon, J., & Tutumluer, E. (2008). Geogrid in flexible pavements validated mechanism. *Transportation Research Record*, (2045), 102–109. https://doi.org/10.3141/2045-12

Al-Qadi, I. L., Dessouky, S. H., Kwon, J., & Tutumluer, E. (2012). Geogrid-reinforced low-volume flexible pavements: Pavement response and geogrid optimal location. *Journal of Transportation Engineering*, *138*(9), 1083–1090. https://doi.org/10.1061/(ASCE)TE.1943-5436.0000409

Anderson, D. A., Petersen, J. C., & Christensen, D. W. (1986). *Variations in Asphalt Cements and Their Effects on Performance of Asphalt Concrete Mixtures*. *55*.

Anderson, D., Christensen, D. W., & Bahia, H. (1991). Physical Properties of Asphalt Cement and the Development of Performance Related Specifications. *Journal of the Association of Asphalt Paving Technologist*, *60*, 437–475.

Anisimov, O. A., Fitzharris, B., Hagan, J. O., Jeffries, R., Marchant, H., Nelson, F. E., … Vaughan, D. G. (2001). Polar regions (arctic and antarctic). In *Climate Change 2001: Impacts, Adaptation, and Vulnerability: Contribution of Working Group II of the Intergovernmental Panel on Climate Change* (pp. 801–841).

Aran, S. (2006). Geosynthetics : Soil and Aggregate Reinforcement Testing - Base Reinforcement with Biaxial Geogrid. *Transportation Research Record: Journal of the Transportation Research Board*, *1975*, 115–123.

Arsenie, I. M., Chazallon, C., Duchez, J. L., & Mouhoubi, S. (2016). Modelling of the fatigue damage of a geogrid-reinforced asphalt concrete. *Https://Doi.Org/10.1080/14680629.2016.1159973*, *18*(1), 250–262. https://doi.org/10.1080/14680629.2016.1159973

Asefzadeh, A., Hashemian, L., & Bayat, A. (2017). Development of statistical temperature prediction models for a test road in Edmonton, Alberta, Canada. *International Journal of Pavement Research and Technology*, *10*(5), 369–382. https://doi.org/10.1016/J.IJPRT.2017.05.004

ASTM. (2007). *ASTM D422-63 Standard Test Method for Particle-Size Analysis of Soils*. West Conshohocken, PA.

ASTM. (2016). *ASTM C666 Standard Test Method for Resistance of Concrete to Rapid Freezing and Thawing*. West Conshohocken, PA.

ASTM. (2017). *ASTM D6913/D6913M-17 Standard Test Methods for Particle-Size Distribution (Gradation) of Soils Using Sieve Analysis*. West Conshohocken, PA.

ASTM. (2018). *ASTM D4318-17e1 Standard Test Methods for Liquid Limit, Plastic Limit, and Plasticity Index of Soils*. West Conshohocken, PA.

ASTM. (2019). *ASTM D2216-19 Standard Test Methods for Laboratory Determination of Water (Moisture) Content of Soil and Rock by Mass*. West Conshohocken, PA.

ASTM. (2020). *ASTM D2487-17e1 Standard Practice for Classification of Soils for Engineering Purposes (Unified Soil Classification System)*. West Conshohocken, PA.

ASTM. (2021a). *ASTM D698-12 Standard Test Methods for Laboratory Compaction Characteristics of Soil Using Standard Effort*. West Conshohocken, PA.

ASTM. (2021b). *ASTM D1883-21 Standard Test Method for California Bearing Ratio (CBR) of Laboratory-Compacted Soils*. West Conshohocken, PA.

ASTM. (2022). *ASTM D4867 Standard Test Method for Effect of Moisture on Asphalt Mixtures*. West Conshohocken, PA.

Attia, M., Asce, S. M., Abdelrahman, M., & Asce, M. (2010). Sensitivity of Untreated Reclaimed Asphalt Pavement to Moisture, Density, and Freeze Thaw. *Journal of Materials in Civil Engineering*, *22*(12), 1260–1269. https://doi.org/10.1061/(ASCE)MT.1943-5533.0000135

Aurilio, R., Aurilio, M., & Baaj, H. (2020). *High-Performance Pavements: A Focus on Self-healing Asphalt Technologies*.

Austin, R. A., & Gilchrist, A. J. T. (1996). Enhanced Performance of Asphalt Pavements Using Geocomposites. *Geotextiles and Geomembranes*, *14*(3-4 SPEC. ISS.), 175–186. https://doi.org/10.1016/0266-1144(96)00007-6

Badeli, S., Carter, A., & Doré, G. (2018). Complex Modulus and Fatigue Analysis of Asphalt Mix after Daily Rapid Freeze-Thaw Cycles. *Journal of Materials in Civil Engineering*, *30*(4), 04018056. https://doi.org/10.1061/(ASCE)MT.1943-5533.0002236/ASSET/38DE6AA9-46BD-499F-B5F6-8908A966979B/ASSETS/IMAGES/LARGE/FIGURE18.JPG

Bai, Q. (2015). *Determination of Boundary Layer Parameters and a Preliminary Research on Hydrothermal Stability of Subgrade in Cold Region*. Beijing Jiaotong University (in Chinese).

Bayat, A., Knight, M. A., & Soleymani, H. R. (2012). Field monitoring and comparison of thermal- and load-induced strains in asphalt pavement. *International Journal of Pavement Engineering*, *13*(6), 508–514. https://doi.org/10.1080/10298436.2011.577776

Behera, B., & Nanda, R. P. (2022). Geogrid reinforced brick buildings for earthquake disaster mitigations. *Case Studies in Construction Materials*, *16*, e01113. https://doi.org/10.1016/J.CSCM.2022.E01113

Behiry, A. E. A. E. M. (2013). Laboratory evaluation of resistance to moisture damage in asphalt mixtures. *Ain Shams Engineering Journal*, *4*(3), 351–363. https://doi.org/10.1016/J.ASEJ.2012.10.009

Bharath, G., Kakade, V., Reddy, K. S., Tandon, V., & Reddy, M. A. (2022). Evaluation of effect of moisture on fatigue performance of pavement designed with recycled asphalt mixtures. *Canadian Journal of Civil Engineering*, *50*(1), 1–10. https://doi.org/10.1139/CJCE-2022-0086/ASSET/IMAGES/CJCE-2022-0086_TAB13.GIF

Bhat, S., & Thomas, J. (2015a). Design and construction of a geosynthetic reinforced pavement on weak subgrade. *Canadian Geotechnical Conference & Canadian Permafrost Conference*. Quebec， Canada.

Bhat, S., & Thomas, J. (2015b). Use of Polymer Geogrid Composite to support rail track over weak saturated clay subgrade – a case study. *Geo-Environmental Engineering 2015*. Montreal, Canada.

Bhowmik, R., Shahu, J. T., & Datta, M. (2023). Influence of Transverse and Longitudinal Members of Coated Polyester-Yarn Geogrid on Pullout Response Under Low Normal Stress. *International Journal of Civil Engineering*, *21*(1), 33–50. https://doi.org/10.1007/S40999-022-00741-0/FIGURES/21

Biligiri, K. P., Kaloush, K. E., Mamlouk, M. S., & Witczak, M. W. (2007). Rational modeling of tertiary flow for asphalt mixtures. *Transportation Research Record*, (2001), 63–72. https://doi.org/10.3141/2001-08

Bilotta, R., Bell, J. E., Shepherd, E., & Arguez, A. (2015). Calculation and Evaluation of an Air-Freezing Index for the 1981–2010 Climate Normals Period in the Coterminous United States. *Journal of Applied Meteorology and Climatology*, *54*(1), 69–76. https://doi.org/10.1175/JAMC-D-14-0119.1

Brown, S. F., Thom, N. H., & Sanders, P. J. (2001). A Study of Grid Reinforced Asphalt to Combat Reflection Cracking. *Journal of the Association of Asphalt Paving Technologists*, *70*.

BSI. (2018). *EN 12697-26: Bituminous mixtures - Test methods - Part 26: Stiffness*. London, UK.

Caltabiano, M. A., & Brunton, J. M. (1991). Reflection cracking in asphalt overlays. *Association of Asphalt Paving Technologists Technical Sessions*, *60*. Seattle, Washington.

Canestrari, F., Attia, T., Di Benedetto, H., Graziani, A., Jaskula, P., Kim, Y. R., … Zofka, A. (2022). Interlaboratory Test to Characterize the Cyclic Behavior of Bituminous Interlayers: An Overview of Testing Equipment and Protocols. *RILEM Bookseries*, *27*, 29–36. https://doi.org/10.1007/978-3-030-46455-4_4/FIGURES/2

Canestrari, F., D'Andrea, A., Ferrotti, G., Graziani, A., Partl, M. N., Petit, C., … Sangiorgi, C. (2018). Advanced interface testing of grids in asphalt pavements. *RILEM State-of-the-Art Reports*, *24*, 127–202. https://doi.org/10.1007/978-3-319-71023-5_4/FIGURES/62

Chen, J., Wang, H., & Xie, P. (2019). Pavement temperature prediction: Theoretical models and critical affecting factors. *Applied Thermal Engineering*, *158*, 113755. https://doi.org/10.1016/J.APPLTHERMALENG.2019.113755

Chen, X. Q., Li, C. H., Wang, W., & Zhang, X. (2012). Active geotechnical treatment technology for permafrost embankment of qinghai-tibet railway. *Electronic Journal of Geotechnical Engineering*, *17 Y*, 3635–3644.

Cheng, G., Wu, Q., & Ma, W. (2009). Innovative designs of permafrost roadbed for the Qinghai-Tibet Railway. *Science in China, Series E: Technological Sciences*, *52*(2), 530–538. https://doi.org/10.1007/s11431-008-0291-6

Cheng, G., & Wu, T. (2007). Responses of permafrost to climate change and their environmental significance, Qinghai-Tibet Plateau. *Journal of Geophysical Research: Earth Surface*, *112*(2). https://doi.org/10.1029/2006JF000631

Cheng, G., Zhang, J., Sheng, Y., & Chen, J. (2004). Principle of thermal insulation for permafrost protection. *Cold Regions Science and Technology*, *40*(1–2), 71–79. https://doi.org/10.1016/j.coldregions.2004.06.001

Collop, A. C., Cebon, D., & Hardy, M. S. A. (1995). Viscoelastic Approach to Rutting in Flexible Pavements. *Journal of Transportation Engineering*, *121*(1), 82–93. https://doi.org/10.1061/(ASCE)0733-947X(1995)121:1(82)

COMSOL. (2022). *COMSOL Documentation*. Retrieved from https://doc.comsol.com/6.1/docserver/#!/com.comsol.help.comsol/helpdesk/helpdesk.html

Correia, N. S., Esquivel, E. R., & Zornberg, J. G. (2018). Finite-Element Evaluations of Geogrid-Reinforced Asphalt Overlays over Flexible Pavements. *Journal of Transportation Engineering, Part B: Pavements*, *144*(2), 04018020. https://doi.org/10.1061/jpeodx.0000043

Correia, N. S., & Zornberg, J. G. (2016). Mechanical response of flexible pavements enhanced with geogrid-reinforced asphalt overlays. *Https://Doi.Org/10.1680/Jgein.15.00041*, *23*(3), 183–193. https://doi.org/10.1680/JGEIN.15.00041

Cuelho, E. V., & Perkins, S. W. (2017). Geosynthetic subgrade stabilization – Field testing and design method calibration. *Transportation Geotechnics*, *10*, 22–34. https://doi.org/10.1016/J.TRGEO.2016.10.002

Darzins, T., Qiu, H., & Xue, J. (2021). A preliminary laboratory study of fatigue performance of geogrid-reinforced asphalt beam. *Sustainable Civil Infrastructures*, 67–77. https://doi.org/10.1007/978-3-030-79857-4_4

Das, B. M. (2016). Use of geogrid in the construction of railroads. *Innovative Infrastructure Solutions*, *1*(1), 1–12. https://doi.org/10.1007/s41062-016-0017-8

Das, S. C., Paul, D., Fahad, M. M., & Islam, T. (2017). Geotextiles-A Potential Technical Textile Product Available online www.jsaer.com Journal of Scientific and Engineering Research , 2017 , 4 (10): 337-350. *Journal of Scientific and Engineering Research, 2017, 4(10):337-350*, (November), 1–15.

De Vries, D. A. (1958). Simultaneous transfer of heat and moisture in porous media. *Eos, Transactions American Geophysical Union*, *39*(5), 909–916. https://doi.org/10.1029/TR039I005P00909

Dempsey, B. J., Thompson, M. R., Program, I. C. H. R., of Illinois (Urbana-Champaign campus). Engineering Experiment Station. Highway Research Laboratory, U., of Highways, Illinois. D., & Administration, U. States. F. H. (1971). *A Heat-transfer Model for Evaluating Frost Action and Temperature Related Effects in Multilayered Pavement Systems*. University of Illinois. Retrieved from https://books.google.ca/books?id=SMafnQEACAAJ

Deng, Q., Liu, X., Zeng, C., He, X., Chen, F., & Zhang, S. (2021). A Freezing-Thawing Damage Characterization Method for Highway Subgrade in Seasonally Frozen Regions Based on Thermal-Hydraulic-Mechanical Coupling Model. *Sensors 2021, Vol. 21, Page 6251*, *21*(18), 6251. https://doi.org/10.3390/S21186251

DeVries, D. A. (1963). *Thermal Properties of Soils* (W.R. van W). Amsterdam: North-Holland Publishing Company.

Domingos, M. D. I., & Faxina, A. L. (2015). Susceptibility of Asphalt Binders to Rutting: Literature Review. *Journal of Materials in Civil Engineering*, *28*(2), 04015134. https://doi.org/10.1061/(ASCE)MT.1943-5533.0001364

Doré, G., & Zubeck, H. (2009). *Cold regions pavement engineering*. American Society of Civil Engineers.

Duojie, C., Si, W., Ma, B., Hu, Y., Liu, X., & Wang, X. (2021). Assessment of Freeze-Thaw Cycles Impact on Flexural Tensile Characteristics of Asphalt Mixture in Cold Regions. *Mathematical Problems in Engineering*, *2021*. https://doi.org/10.1155/2021/6697693

Englobe. (2022). *Grain Size Analysis Report*. Waterloo, Ontario.

Everett, D. H. (1961). The thermodynamics of frost damage to porous solids. *Transactions of the Faraday Society*, *57*(0), 1541–1551. https://doi.org/10.1039/TF9615701541

Faisal, H. M., Khan, Z. H., & Tarefder, R. (2017). *Modeling Nanoscale Rheological and Mechanical Properties of Thin Film Asphalt Binder*. https://doi.org/10.1115/IMECE2016-65531

Fang, H., Liu, Q., Mo, L., Javilla, B., Shu, B., & Wu, S. (2017). Characterization of three-stage rutting development of asphalt mixtures. *Construction and Building Materials*, *154*, 340–348. https://doi.org/10.1016/J.CONBUILDMAT.2017.07.222

Farashah, M. K., Salehiashani, S., Varamini, S., & Tighe, S. (2021). *Best Practices in Measuring Rutting and Shoving on Asphalt Pavements*. Transportation Association of Canada.

Fares, Abd E, Hassan, H., & Arab, M. (2020). Flexural Behavior of High Strength Self-Compacted Concrete Slabs Containing Treated and Untreated Geogrid Reinforcement. *Fibers*, Vol. 8. https://doi.org/10.3390/fib8040023

Fares, Abd El-rahman, Hassan, H., & Arab, M. (2020). Flexural Behavior of High Strength Self-Compacted Concrete Slabs Containing Treated and Untreated Geogrid Reinforcement. *Fibers*, *8*(4), 23. https://doi.org/https://doi.org/10.3390/fib8040023

Faruk, A. N. M., Lee, S. I., Zhang, J., Naik, B., & Walubita, L. F. (2015). Measurement of HMA shear resistance potential in the lab: The Simple Punching Shear Test. *Construction and Building Materials*, *99*, 62–72. https://doi.org/10.1016/J.CONBUILDMAT.2015.09.006

Faye, E., Herrera, M., Bellomo, L., Silvain, J. F., & Dangles, O. (2014). Strong discrepancies between local temperature mapping and interpolated climatic grids in tropical mountainous agricultural landscapes. *PLoS ONE*, *9*(8). https://doi.org/10.1371/JOURNAL.PONE.0105541

Ferrians, O. J., Kachadoorian, R., & Greene, G. W. (1969). Permafrost and Related Engineering Problems in Alaska. *U.S. Geological Survey Professional Paper*, *678*, 1–37. Retrieved from https://books.google.ca/books?hl=en&lr=&id=pbLf7M71qsgC&oi=fnd&pg=PA21&dq=Ferrians,+O.+J.,+Jr.,+Kachadoorian,+R.,+and+Green,+G.+W.,+1969.+Permafrost+and+Related+Engin

eering+Problems+in+Alaska,+U.S.+Geol.+Survey+Prof.+Paper+678,+37p.&ots=ADCnGN-2YB&sig=pui

FHWA. (2014). *Traffic Monitoring Guide*. Retrieved from https://www.fhwa.dot.gov/policyinformation/tmguide/tmg_2013/vehicle-types.cfm

Flerchinger, G. (2000). *The Simultaneous Heat and Water (SHAW) Model: Technical Documentation*. Boise, Idaho.

Fontes, L. P. T. L., Trichês, G., Pais, J. C., & Pereira, P. A. A. (2010). Evaluating permanent deformation in asphalt rubber mixtures. *Construction and Building Materials*, *24*(7), 1193–1200. https://doi.org/10.1016/J.CONBUILDMAT.2009.12.021

Fowler, A. C., & Krantz, W. B. (1994). Generalized secondary frost heave model. *SIAM Journal on Applied Mathematics*, *54*(6), 1650–1675. https://doi.org/10.1137/S0036139993252554

Freire, R. A., Di Benedetto, H., Sauzéat, C., Pouget, S., & Lesueur, D. (2021). Crack propagation analysis in bituminous mixtures reinforced by different types of geogrids using digital image correlation. *Construction and Building Materials*, *303*, 124522. https://doi.org/10.1016/J.CONBUILDMAT.2021.124522

Freire, R. A., Di Benedetto, H., Sauzéat, C., Pouget, S., & Lesueur, D. (2022). Linear viscoelastic behaviours of bituminous mixtures and fiberglass geogrids interfaces. *Geotextiles and Geomembranes*, *50*(5), 961–969. https://doi.org/10.1016/J.GEOTEXMEM.2022.06.003

Freire, R., Di Benedetto, H., Sauzéat, C., Pouget, S., & Lesueur, D. (2022a). Effect of Fiberglass Geogrid Reinforcement to Fatigue Resistance of Bituminous Mixtures. *RILEM Bookseries*, *27*, 585–590. https://doi.org/10.1007/978-3-030-46455-4_74/FIGURES/4

Freire, R., Di Benedetto, H., Sauzéat, C., Pouget, S., & Lesueur, D. (2022b). Tension Behavior of Bituminous Mixture Samples Reinforced by Fiberglass Geogrids in Different Directions. *Lecture Notes in Civil Engineering*, *165*, 521–531. https://doi.org/10.1007/978-3-030-77234-5_43/FIGURES/7

G. Rowe, G. Baumgardner, & M. Sharrock. (2009). Functional forms for master curve analysis of bituminous materials. *Advanced Testing and Characterization of Bituminous Materials*, 97–108. https://doi.org/10.1201/9780203092989-13

Gardner, W. (1958). Some Steady-State Solutions of the Unsaturated Moisture Flow Equation with Application to Evaporation from a Water Table. *Soil Science*, *85*(4), 228–232. Retrieved from 10.1097/00010694-195804000-00006

Ge, J. J., Wei, J., Bao, L. M., Shi, X. M., Xuan, L. H., & Li, X. L. (2008). Introduction and Application of Geosynthetic in Qinghai-Tibet Railway Construction. *The 4th Asian Regional Conference on Geosynthetics*, 817–822. Shanghai ,China. https://doi.org/10.4324/9780080940380

Ghazavi, M., & Roustaei, M. (2013). Freeze–thaw performance of clayey soil reinforced with geotextile layer. *Cold Regions Science and Technology*, *89*, 22–29. https://doi.org/10.1016/J.COLDREGIONS.2013.01.002

Gilpin, R. R. (1980). A model for the prediction of ice lensing and frost heave in soils. *Water Resources Research*, *16*(5), 918–930. https://doi.org/10.1029/WR016i005p00918

Giroud, J. P. (1984). Geotextiles and geomembranes. *Geotextiles and Geomembranes*, *1*(1), 5–40. https://doi.org/10.1016/0266-1144(84)90003-7

Giroud, J. P., Han, J., Tutumluer, E., & Dobie, M. J. D. (2022). The use of geosynthetics in roads. *Geosynthetics International*, *30*(1), 47–80. https://doi.org/10.1680/JGEIN.21.00046

Golalipour, A. (2020). Asphalt Material Creep Behavior. *Creep Characteristics of Engineering Materials*. https://doi.org/10.5772/INTECHOPEN.85783

Government of Canada. (2018). *Canada's Core Public Infrastructure Survey 2018*. Retrieved from https://www150.statcan.gc.ca/n1/daily-quotidien/230320/dq230320a-eng.htm

Government of Canada. (2023). Daily Data. Retrieved from https://climate.weather.gc.ca/climate_data/daily_data_e.html?StationID=51058

Grellet, D., Doré, G., & Bilodeau, J. P. (2012). Comparative study on the impact of wide base tires and dual tires on the strains occurring within flexible pavements asphalt concrete surface course. *Canadian Journal of Civil Engineering*, *39*(5), 526–535. https://doi.org/10.1139/L2012-031/ASSET/IMAGES/LARGE/L2012-031F10.JPEG

Gu, F., Luo, X., Luo, R., Hajj, E. Y., & Lytton, R. L. (2017). A mechanistic-empirical approach to quantify the influence of geogrid on the performance of flexible pavement structures. *Transportation Geotechnics*, *13*, 69–80. https://doi.org/10.1016/j.trgeo.2017.08.005

Gu, F., Luo, X., Luo, R., Lytton, R. L., Hajj, E. Y., & Siddharthan, R. V. (2016). Numerical modeling of geogrid-reinforced flexible pavement and corresponding validation using large-scale tank test. *Construction and Building Materials*, *122*, 214–230. https://doi.org/10.1016/J.CONBUILDMAT.2016.06.081

Gui, J. (Gavin), Phelan, P. E., Kaloush, K. E., & Golden, J. S. (2007). Impact of Pavement Thermophysical Properties on Surface Temperatures. *Journal of Materials in Civil Engineering*, *19*(8), 683–690. https://doi.org/10.1061/(ASCE)0899-1561(2007)19:8(683)/ASSET/C6A84F39-18FA-4FBD-8EBE-CEFED0A6B1CF/ASSETS/IMAGES/LARGE/8.JPG

Guo, D., & Sun, J. (2015). Permafrost thaw and associated settlement hazard onset timing over the Qinghai-Tibet engineering corridor. *International Journal of Disaster Risk Science*, *6*(4), 347–358. https://doi.org/10.1007/s13753-015-0072-3

Guo, D., & Wang, H. (2013). Simulation of permafrost and seasonally frozen ground conditions on the Tibetan Plateau, 1981-2010. *Journal of Geophysical Research Atmospheres*, *118*(11), 5216–5230. https://doi.org/10.1002/jgrd.50457

Gupta, R., & Mishra, D. (2016). Analysis of geogrid-reinforced flexible pavement systems using confined stiffness approach. *3rd Pan - American Conference on Geosynthetics*.

Guymon, G L, Berg, R. L., & Hromadka, T. V. (1993). *Mathematical Model of Frost Heave and Thaw Settlement in Pavements*. Hanover, NH.

Guymon, Gary L., & Luthin, J. N. (1974). A coupled heat and moisture transport model for Arctic soils. *Water Resources Research*, *10*(5), 995–1001. https://doi.org/10.1029/WR010i005p00995

Haghi, N. T., Hashemian, L., & Bayat, A. (2016). Effects of Seasonal Variation on the Load-Bearing Capacity of Pavements Composed of Insulation Layers. *Https://Doi.Org/10.3141/2579-10*, *2579*, 87–95. https://doi.org/10.3141/2579-10

Han, J., & Akins, K. (2002). *Use of Geogrid-Reinforced and Pile-Supported Earth Structures*. 668–679. https://doi.org/10.1061/40601(256)48

Hansson, K., Šimůnek, J., Mizoguchi, M., Lundin, L., & Genuchten, M. Th. (2004). Water Flow and Heat Transport in Frozen Soil: Numerical Solution and Freeze–Thaw Applications. *Vadose Zone Journal*, *3*(2), 693–704. https://doi.org/10.2136/vzj2004.0693

Harlan, R. L. (1973). Analysis of coupled heat-fluid transport in partially frozen soil. *Water Resources Research*, *9*(5), 1314–1323. https://doi.org/10.1029/WR009i005p01314

Hass, R., Walls, J., & Carroll, R. G. (1988a). Geogrid reinforcement of granular bases in flexible pavements. *Transportation Research Record*, (1188), 19–27.

Hass, R., Walls, J., & Carroll, R. G. (1988b). Geogrid reinforcement of granular bases in flexible pavements. *Transportation Research Record*, (1188), 19–27.

Hedayati, M., Hossain, S., Mehdibeigi, A., & Thian Student, B. (2014). Real-Time Modeling of Moisture Distribution in Subgrade Soils. *GSP*, *3015*, 3015–3024. https://doi.org/10.1061/9780784413272.293

Helstrom, C. L., Humphrey, D. N., & Hayden, S. A. (2007). Geogrid reinforced pavement structure in a cold region. *Proceedings of the International Conference on Cold Regions Engineering*, 57. American Society of Civil Engineers. https://doi.org/10.1061/40836(210)57

Henry, K. S. (1995). The Use of Geosynthetic Capillary Barriers to Reduce Moisture Migration in Soils. *Geosynthetics International*, *2*(5), 883–888. https://doi.org/10.1680/gein.2.0040

Henry, K. S., & Holtz, R. D. (2001). Geocomposite capillary barriers to reduce frost heave in soils. *Canadian Geotechnical Journal*, *38*(4), 678–694. https://doi.org/10.1139/t01-010

Hensley, M. J. (1980). *Open-graded asphalt concrete base for the control of reflectivity*. *49*.

Hermansson, Å. (2004). Mathematical model for paved surface summer and winter temperature: comparison of calculated and measured temperatures. *Cold Regions Science and Technology*, *40*(1–2), 1–17. https://doi.org/10.1016/J.COLDREGIONS.2004.03.001

Hildebrand, E. E. (1985). *Prediction of Thaw Settlement and Surface Roughness for Highways in Permafrost Areas*. University of Waterloo.

Hossain, M. Shabbir, Hoppe, E. J., & Weaver, C. B. (2019, March 21). *Long-Term Field Performance of Geosynthetics in Pavement Subgrades in Virginia*. 245–258. American Society of Civil Engineers (ASCE). https://doi.org/10.1061/9780784482124.026

Hossain, M. Shabbir, Schmidt, B. N., Council, V. T. R., & Transportation, Virginia. Dept. of. (2009). *Benefits of Using Geotextile Between Subgrade Soil and Base Course Aggregate in Low-Volume Roads in Virginia*. (434), 293–1900. https://doi.org/10.21949/1503647

Huang, Y. H. (2004). *Pavement Analysis and Design*. Prentice Hall, Kentucky: PEARSON.

Huang, Yue, Bird, R. N., & Heidrich, O. (2007). A review of the use of recycled solid waste materials in asphalt pavements. *Resources, Conservation and Recycling*, *52*(1), 58–73. https://doi.org/10.1016/J.RESCONREC.2007.02.002

Huang, Yunyan, Nojumi, M. M., Hashemian, L., & Bayat, A. (2021). Performance evaluation of different insulating materials using field temperature and moisture data. *Transportation Research Record*, *2675*(9), 595–607. https://doi.org/10.1177/03611981211003572/ASSET/IMAGES/LARGE/10.1177_03611981211003572-FIG13.JPEG

Iowa DOT. (2013). *IM 319 Moisture Sensitivity Testing of Asphalt Mixtures*. Retrieved from https://iowadot.gov/erl/current/im/content/319.htm.

Irrometer. (2022). Irrometer. Retrieved from https://www.irrometer.com

Islam, M. R., Ahsan, S., & Tarefder, R. A. (2015). Modeling temperature profile of hot-mix asphalt in flexible pavement. *International Journal of Pavement Research and Technology*, *8*(1), 47–52. https://doi.org/10.6135/IJPRT.ORG.TW/2015.8(1).47

Jain, S. K., Nusari, M. S., Shrestha, R., & Mandal, A. K. (2023). Use of RCC pile, anchor bolt and geogrid for building construction on the unstable slope. *Geoenvironmental Disasters*, *10*(1), 1–19. https://doi.org/doi.org/10.1186/s40677-023-00243-8

Jasim, A. F., Fattah, M. Y., Al-Saadi, I. F., & Abbas, A. S. (2021). Geogrid reinforcement optimal location under different tire contact stress assumptions. *International Journal of Pavement Research and Technology*, *14*(3), 357–365. https://doi.org/10.1007/S42947-020-0145-6/METRICS

Jayalath, C., Gallage, C., Wimalasena, K., Lee, J., & Ramanujam, J. (2021). Performance of composite geogrid reinforced unpaved pavements under cyclic loading. *Construction and Building Materials*, *304*, 124570. https://doi.org/10.1016/J.CONBUILDMAT.2021.124570

Jayalath, C. P. G., Gallage, C., & Wimalasena, K. (2022). Development of Design Guidelines for Composite-Geogrid Reinforced Unpaved Pavements. *Lecture Notes in Civil Engineering*, *193*, 375–387. https://doi.org/10.1007/978-3-030-87379-0_28

Jie, H., & Yan, J. (2013). Use of geosynthetics for performance enhancement of earth structures in cold regions. *Sciences in Cold and Arid Regions*, *5*(5), 517–529. https://doi.org/10.3724/sp.j.1226.2013.00517

Kaloush, K. E., Witczak, M. W., Roque, R., Brown, S., D'Angelo, J., Marasteanu, M., & Masad, E. (2002). Tertiary flow characteristics of asphalt mixtures. *Asphalt Paving Technology: Association of Asphalt Paving Technologists-Proceedings of the Technical Sessions*, *71*, 248–280.

Kavussi, A., & Hashemian, L. (2012). Laboratory evaluation of moisture damage and rutting potential of WMA foam mixes. *International Journal of Pavement Engineering*, *13*(5), 415–423. https://doi.org/10.1080/10298436.2011.597859

Khan, Z. H., Islam, M. R., & Tarefder, R. A. (2019). Determining asphalt surface temperature using weather parameters. *Journal of Traffic and Transportation Engineering (English Edition)*, *6*(6), 577–588. https://doi.org/10.1016/J.JTTE.2018.04.005

Khodaii, A., & Mehrara, A. (2009). Evaluation of permanent deformation of unmodified and SBS modified asphalt mixtures using dynamic creep test. *Construction and Building Materials*, *23*(7), 2586–2592. https://doi.org/10.1016/J.CONBUILDMAT.2009.02.015

Kim, Y. R., Zhang, J., & Ban, H. (2012). Moisture damage characterization of warm-mix asphalt mixtures based on laboratory-field evaluation. *Construction and Building Materials*, *31*, 204–211. https://doi.org/10.1016/J.CONBUILDMAT.2011.12.085

Koerner, R. M. (1998). *Designing with geosynthetics*. Prentice Hall.

Kongkitkul, W., Hirakawa, D., & Tatsuoka, F. (2007). Viscous Behaviour of Geogrids; Experiment and Simulation. *Soils and Foundations*, *47*(2), 265–283. https://doi.org/10.3208/SANDF.47.265

Kringos, N., Azari, H., & Scarpas, A. (2009). Identification of Parameters Related to Moisture Conditioning that Cause Variability in Modified Lottman Test. *Https://Doi.Org/10.3141/2127-01*, (2127), 1–11. https://doi.org/10.3141/2127-01

Kumar, V. V., Saride, S., & Zornberg, J. G. (2021). Fatigue performance of geosynthetic-reinforced asphalt layers. *Https://Doi.Org/10.1680/Jgein.21.00013*, *28*(6), 584–597. https://doi.org/10.1680/JGEIN.21.00013

Kuráž, M., Mayer, P., Lepš, M., & Trpkošová, D. (2010). An adaptive time discretization of the classical and the dual porosity model of Richards' equation. *Journal of Computational and Applied Mathematics*, *233*(12), 3167–3177. https://doi.org/10.1016/J.CAM.2009.11.056

Kwon, J., Kim, M., & Tutumluer, E. (2005). *Interface Modeling for Mechanistic Analysis of Geogrid Reinforced Flexible Pavements*. 1–15. https://doi.org/10.1061/40776(155)21

Lachance-Tremblay, É., Perraton, D., Vaillancourt, M., & Di Benedetto, H. (2017). Degradation of asphalt mixtures with glass aggregates subjected to freeze-thaw cycles. *Cold Regions Science and Technology*, *141*, 8–15. https://doi.org/10.1016/J.COLDREGIONS.2017.05.003

Lai, Y., Zhang, S., & Yu, W. (2012). A new structure to control frost boiling and frost heave of embankments in cold regions. *Cold Regions Science and Technology*, *79–80*, 53–66. https://doi.org/10.1016/j.coldregions.2012.04.002

Lee, S. J. (2008). Mechanical performance and crack retardation study of a fiberglass-grid-reinforced asphalt concrete system. *Canadian Journal of Civil Engineering*, *35*(10), 1042–1049. https://doi.org/10.1139/L08-049

Lekarp, F., Isacsson, U., & Dawson, A. (2000). State of the Art.II: Permanent Strain Response of Unbound Aggregates. *Journal of Transportation Engineering*, *126*(1), 76–83. https://doi.org/10.1061/(ASCE)0733-947X(2000)126:1(76)

Li, P., Jiang, X., Guo, K., Xue, Y., & Dong, H. (2018). Analysis of viscoelastic response and creep deformation mechanism of asphalt mixture. *Construction and Building Materials*, *171*, 22–32. https://doi.org/10.1016/J.CONBUILDMAT.2018.03.104

Li, Q., He, Y., Yang, G., Su, P., & Li, B. (2022). The Cracking Resistance Behavior of Geosynthetics-Reinforced Asphalt Concrete under Lower Temperatures Using Bending Test. *Coatings 2022, Vol. 12, Page 812*, *12*(6), 812. https://doi.org/10.3390/COATINGS12060812

Li, X., Jin, R., Pan, X., Zhang, T., & Guo, J. (2012). Changes in the near-surface soil freeze-thaw cycle on the Qinghai-Tibetan Plateau. *International Journal of Applied Earth Observation and Geoinformation*, *17*(1), 33–42. https://doi.org/10.1016/j.jag.2011.12.002

Liao, H., Tavassoti, P., Sharma, A., & Baaj, H. (2023). Evaluation of rutting resistance and moisture susceptibility of high RAP content asphalt mixtures containing bio-based rejuvenators.

Construction and Building Materials, *401*, 132859. https://doi.org/10.1016/J.CONBUILDMAT.2023.132859

Liu, R., Ji, B., Wang, M., Chen, C., & Maeno, H. (2015). Numerical Evaluation of Toe-Deck Fatigue in Orthotropic Steel Bridge Deck. *Journal of Performance of Constructed Facilities*, *29*(6), 04014180. https://doi.org/10.1061/(ASCE)CF.1943-5509.0000677/ASSET/1268ED5C-4973-4D54-BCF9-7FDB0C2691C8/ASSETS/IMAGES/LARGE/FIGURE24.JPG

Liu, Y., Ni, X., Pickel, D., Tighe, S., & Kou, C. (2022). Impact of Airport De-Icing Chemicals and Freeze-Thaw on Rutting Resistance of Asphalt Mixture in Canada. *SSRN Electronic Journal*. https://doi.org/10.2139/SSRN.4067100

Liu, Z. (Leo). (2018). Finite Element Method. *Multiphysics in Porous Materials*, 397–417. https://doi.org/10.1007/978-3-319-93028-2_30

Liu, Z., & Yu, X. (2011a). Coupled thermo-hydro-mechanical model for porous materials under frost action: Theory and implementation. *Acta Geotechnica*, *6*(2), 51–65. https://doi.org/10.1007/s11440-011-0135-6

Liu, Z., & Yu, X. (2011b). Coupled thermo-hydro-mechanical model for porous materials under frost action: Theory and implementation. *Acta Geotechnica*, *6*(2), 51–65. https://doi.org/10.1007/s11440-011-0135-6

Lu, N., & Likos, W. J. (2004). *Unsaturated soil mechanics* . Hoboken, N.J: J. Wiley.

Lv, Q., Huang, W., Sadek, H., Xiao, F., & Yan, C. (2019). Investigation of the rutting performance of various modified asphalt mixtures using the Hamburg Wheel-Tracking Device test and Multiple Stress Creep Recovery test. *Construction and Building Materials*, *206*, 62–70. https://doi.org/10.1016/J.CONBUILDMAT.2019.02.015

Lytton, R. L. (1989a). Use of geotextiles for reinforcement and strain relief in asphalt concrete. *Geotextiles and Geomembranes*, *8*(3), 217–237. https://doi.org/10.1016/0266-1144(89)90004-6

Lytton, R. L. (1989b). Use of geotextiles for reinforcement and strain relief in asphalt concrete. *Geotextiles and Geomembranes*, *8*(3), 217–237. https://doi.org/10.1016/0266-1144(89)90004-6

Maadani, O., Shafiee, M., & Egorov, I. (2021). Climate Change Challenges for Flexible Pavement in Canada: An Overview. *Journal of Cold Regions Engineering*, *35*(4), 03121002. https://doi.org/10.1061/(ASCE)CR.1943-5495.0000262

Makwana, AE. P., & kumar, Dr. R. (2019). Correlative Study of LWD, DCP and CBR for sub-grade. *International Journal of Engineering Trends and Technology*, *67*(9), 89–98. https://doi.org/10.14445/22315381/IJETT-V67I9P215

Manosuthikij, T. (2008). *STUDIES ON VOLUME CHANGE MOVEMENTS IN HIGH PI CLAYS FOR BETTER DESIGN OF LOW VOLUME PAVEMENTS*.

McErlich, C., McDonald, A., Schuddeboom, A., Vishwanathan, G., Renwick, J., & Rana, S. (2023). Positive correlation between wet-day frequency and intensity linked to universal precipitation drivers. *Nature Geoscience 2023 16:5*, *16*(5), 410–415. https://doi.org/10.1038/s41561-023-01177-4

Mellor, M. (1970). *Phase Composition of Pore Water in Cold Rocks*. https://doi.org/10.21236/AD0719236

Meza, F., & Varas, E. (2000). Estimation of mean monthly solar global radiation as a function of temperature. *Agricultural and Forest Meteorology*, *100*(2–3), 231–241. https://doi.org/10.1016/S0168-1923(99)00090-8

Michalowski, R. L., & Zhu, M. (2006). Frost heave modelling using porosity rate function. *International Journal for Numerical and Analytical Methods in Geomechanics*, *30*(8), 703–722. https://doi.org/10.1002/nag.497

Miller, H., Cabral, C., Kestler, M., Berg, R., & Eaton, R. (2012). Calibration of a Freeze-Thaw Prediction Model for Spring Load Restriction Timing in Northern New England. *Proceedings of the International Conference on Cold Regions Engineering*, 369–379. https://doi.org/10.1061/9780784412473.037

Miller, R. D. (1972). FREEZING AND HEAVING OF SATURATED AND UNSATURATED SOILS. *Highway Research Record*, (393).

Mohammad, L. N., Herath, A., Gudishala, R., Nazzal, M. D., Abu-Farsakh, M. Y., & Alshibli, K. (2008). *Development of models to estimate the subgrade and subbase layers' resilient modulus from in situ devices test results for construction control.* (L. T. R. Center, Ed.). Louisiana Transportation Research Center. Retrieved from https://rosap.ntl.bts.gov/view/dot/22137

MTO. (2013). *Pavement Design and Rehabilitation Manual* (Second Edi). Downsview, Ontario: Ministry of Transport Ontario (MTO).

MTO. (2019). *Ministry of Transportation Ontario's Default Parameters for AASHTOWare Pavement ME Design. Interim Report - 2019*. Retrieved from https://www.raqsb.mto.gov.on.ca

Mualem, Y. (1976). A new model for predicting the hydraulic conductivity of unsaturated porous media. *Water Resources Research*, *12*(3), 513–522. https://doi.org/10.1029/WR012I003P00513

Nader Ghafoori, & Sharbaf, M. (2016a). *Use of Geogrid for Strengthening and Reducing the Roadway Structural Sections*. Carson City, NV 89712.

Nader Ghafoori, & Sharbaf, M. (2016b). *Use of Geogrid for Strengthening and Reducing the Roadway Structural Sections*. Carson City, NV 89712.

Nassar, I. N., & Horton, R. (1989). Water Transport in Unsaturated Nonisothermal Salty Soil: II. Theoretical Development. *Soil Science Society of America Journal*, *53*(5), 1330–1337. https://doi.org/10.2136/SSSAJ1989.03615995005300050005X

Nassar, I. N., & Horton, R. (1997). Heat, Water, and Solute Transfer in Unsaturated Porous Media: I - Theory Development and Transport Coefficient Evaluation. *Transport in Porous Media*, *27*(1), 17–38. https://doi.org/10.1023/A:1006583918576/METRICS

Neaupane, K. M., & Yamabe, T. (2001). A fully coupled thermo-hydro-mechanical nonlinear model for a frozen medium. *Computers and Geotechnics*, *28*(8), 613–637. https://doi.org/10.1016/S0266-352X(01)00015-5

Neaupane, K. M., Yamabe, T., & Yoshinaka, R. (1999). Simulation of a fully coupled thermo–hydro–mechanical system in freezing and thawing rock. *International Journal of Rock Mechanics and Mining Sciences*, *36*(5), 563–580. https://doi.org/10.1016/S0148-9062(99)00026-1

Nelson, F. E., Anisimov, O. A., & Shiklomanov, N. I. (2002). Climate change and hazard zonation in the circum-arctic permafrost regions. *Natural Hazards*, *26*(3), 203–225. https://doi.org/10.1023/A:1015612918401

Nelson, Frederick E., Anisimov, O. A., & Shiklomanov, N. I. (2001). Subsidence risk from thawing permafrost. *Nature*, *410*(6831), 889–890. https://doi.org/10.1038/35073746

Nguyen, Q., Fredlund, D. G., Samarasekera, L., & Marjerison, B. L. (2010). Seasonal pattern of matric suctions in highway subgrades. *Canadian Geotechnical Journal*, *47*(3), 267–280. https://doi.org/10.1139/T09-099/ASSET/IMAGES/LARGE/T09-099F25.JPEG

Nishimura, S., Gens, A., Olivella, S., & Jardine, R. J. (2009a). THM-coupled finite element analysis of frozen soil: Formulation and application. *Geotechnique*, *59*(3), 159–171. https://doi.org/10.1680/geot.2009.59.3.159

Nishimura, S., Gens, A., Olivella, S., & Jardine, R. J. (2009b). THM-coupled finite element analysis of frozen soil: Formulation and application. *Geotechnique*, *59*(3), 159–171. https://doi.org/10.1680/geot.2009.59.3.159

Omar, H. A., Yusoff, N. I. M., Mubaraki, M., & Ceylan, H. (2020). Effects of moisture damage on asphalt mixtures. *Journal of Traffic and Transportation Engineering (English Edition)*, *7*(5), 600–628. https://doi.org/10.1016/J.JTTE.2020.07.001

O'Neill, K., & Miller, R. D. (1985). Exploration of a Rigid Ice Model of Frost Heave. *Water Resources Research*, *21*(3), 281–296. https://doi.org/10.1029/WR021i003p00281

OPSS. (2006). *OPSS 1151 Material Specification for Superpave and Stone Mastic Asphalt Mixtures*. Retrieved from https://www.roadauthority.com/Standards/

OPSS. (2013). *OPSS 1010 Material Specification for Aggregates - Base, Subbase, Select Subgrade, and Backfill Material*. Retrieved from https://www.roadauthority.com/Standards/

Oyeyi, A. G. (2022). *Lightweight Cellular Concrete as Flexible Pavement Subbase Material: Field Performance and Sustainability Study* (UWSpace). UWSpace. Retrieved from http://hdl.handle.net/10012/18938

Oyeyi, A. G., Al-Bayati, H. K. A., Ni, F. M.-W., & Tighe, S. (2023). Environmental impact on critical responses of lightweight cellular concrete subbase flexible pavements. *Https://Doi.Org/10.1139/Cjce-2023-0027*. https://doi.org/10.1139/CJCE-2023-0027

Oyeyi, A. G., Badewa, E. A., Ni, F. M. W., & Tighe, S. (2023). Field study on thermal behavior of lightweight cellular concrete as pavement subgrade protection in cold regions. *Cold Regions Science and Technology*, *214*, 103966. https://doi.org/10.1016/J.COLDREGIONS.2023.103966

Oyeyi, A. G., Ni, F. M. W., & Tighe, S. (2023). In-Service Performance Evaluation of Flexible Pavement with Lightweight Cellular Concrete Subbase. *Applied Sciences 2023, Vol. 13, Page 4757*, *13*(8), 4757. https://doi.org/10.3390/APP13084757

Painter, P. C., & Coleman, M. M. (1997). *Fundamentals of Polymer Science - An Introductory Text*. Lancaster, PA: Technomic Publishing Co. Inc.

Pant, A., Datta, M., Ramana, G. V., & Bansal, D. (2019). Measurement of role of transverse and longitudinal members on pullout resistance of PET geogrid. *Measurement*, *148*, 106944. https://doi.org/10.1016/J.MEASUREMENT.2019.106944

Park, H. M., & Kim, Y. R. (2003). Prediction of Remaining Life of Asphalt Pavement with Falling-Weight Deflectometer Multiload-Level Deflections. *Https://Doi.Org/10.3141/1860-06*, (1860), 48–56. https://doi.org/10.3141/1860-06

Park, J. J., Shin, E. C., & Yoon, B. J. (2016). Development of Frost Penetration Depth Prediction Model Using Field Temperature Data of Asphalt Pavement. *International Journal of Offshore and Polar Engineering*, *26*(04), 341–347. https://doi.org/10.17736/IJOPE.2016.TM79

Parton, W. J., & Logan, J. A. (1981). A model for diurnal variation in soil and air temperature. *Agricultural Meteorology*, *23*(C), 205–216. https://doi.org/10.1016/0002-1571(81)90105-9

Pasquini, E., Pasetto, M., & Canestrari, F. (2015). Geocomposites against reflective cracking in asphalt pavements: laboratory simulation of a field application. *Http://Dx.Doi.Org/10.1080/14680629.2015.1044558*, *16*(4), 815–835. https://doi.org/10.1080/14680629.2015.1044558

Pellinen, T. K., Witczak, M. W., & Bonaquist, R. F. (2003). Asphalt Mix Master Curve Construction Using Sigmoidal Fitting Function with Non-Linear Least Squares Optimization. *Recent Advances in Materials Characterization and Modeling of Pavement Systems*, 83–101. American Society of Civil Engineers. https://doi.org/10.1061/40709(257)6

Perkins, S. W. (2002). *Geosynthetic Reinforced Flexible Pavement Systems Using Two Pavement Test Facilities*. Bozeman, Montana.

Perkins, S. W., Christopher, B. R., Lacina, B. A., & Klompmaker, J. (2012). Mechanistic-Empirical Modeling of Geosynthetic-Reinforced Unpaved Roads. *International Journal of Geomechanics*, *12*(4), 370–380. https://doi.org/10.1061/(ASCE)GM.1943-5622.0000184

Philip, J. R., & De Vries, D. A. (1957). Moisture movement in porous materials under temperature gradients. *Eos, Transactions American Geophysical Union*, *38*(2), 222–232. https://doi.org/10.1029/TR038i002p00222

Pinchin Ltd. (2020). *Geotechnical Investigation - Proposed Snyder's Road Reconstruction*. Waterloo, Ontario.

PNJ Engineering Inc. (2022). *Superpave Mix Design Report*.

Powell, W. D., POTTER, J. F., Mayhew, H. C., & NUNN, M. E. (1984). THE STRUCTURAL DESIGN OF BITUMINOUS ROADS. *TRRL LABORATORY REPORT*, (1115).

Qamhia, I. I. A., & Tutumluer, E. (2021). *Evaluation of Geosynthetics Use in Pavement Foundation Layers and Their Effects on Design Methods*. https://doi.org/10.36501/0197-9191/21-025

Ragni, D., Canestrari, F., Allou, F., Petit, C., & Millien, A. (2020). Shear-Torque Fatigue Performance of Geogrid-Reinforced Asphalt Interlayers. *Sustainability 2020, Vol. 12, Page 4381*, *12*(11), 4381. https://doi.org/10.3390/SU12114381

Rajbongshi, P., & Das, A. (2009). Estimation of temperature stress and low-temperature crack spacing in asphalt pavements. *Journal of Transportation Engineering*, *135*(10), 745–752. https://doi.org/10.1061/(ASCE)TE.1943-5436.0000050/ASSET/9891509B-E967-4FE9-A721-6183C81CF6F7/ASSETS/IMAGES/LARGE/8.JPG

Randall MFG. (2023). Geotextile - Randall MFG. Retrieved November 13, 2023, from https://www.randallmfg.ca/geotextile.php#wovengeotextile

Raymond, G. P. (1999). Railway rehabilitation geotextiles. *Geotextiles and Geomembranes*, *17*(4), 213–230. https://doi.org/10.1016/S0266-1144(99)00002-3

Regehr, J. D., Milligan, C. A., Montufar, J., & Alfaro, M. (2013). Review of Effectiveness and Costs of Strategies to Improve Roadbed Stability in Permafrost Regions. *Journal of Cold Regions Engineering*, *27*(3), 109–131. https://doi.org/10.1061/(asce)cr.1943-5495.0000054

Region of Waterloo. (2021). *Regional Road No. 1 (Snyder's Road) Reconstruction Foundry Street to Gingerich Road (Regional Road No. 6), Village of Baden, Township of Wilmot*.

Richards, L. A. (1931). Capillary conduction of liquids through porous mediums. *Journal of Applied Physics*, *1*(5), 318–333. https://doi.org/10.1063/1.1745010

Roctest. (2018). *Frost Probe Instruction Manual*.

Saad, B., Mitri, H., & Poorooshasb, H. (2006). 3D FE analysis of flexible pavement with geosynthetic reinforcement. *Journal of Transportation Engineering*, *132*(5), 402–415. https://doi.org/10.1061/(ASCE)0733-947X(2006)132:5(402)

Saghebfar, M., Hossain, M., & Lacina, B. A. (2016). Performance of geotextile-reinforced bases for paved roads. *Transportation Research Record*, *2580*(2580), 27–33. https://doi.org/10.3141/2580-04

Salour, F., & Erlingsson, S. (2013). Investigation of a pavement structural behaviour during spring thaw using falling weight deflectometer. *Road Materials and Pavement Design*, *14*(1), 141–158. https://doi.org/10.1080/14680629.2012.754600

Sayers, M. W., & Karamihas, S. M. (1998). *The Little Book of Profiling Basic Information about Measuring and Interpreting Road Profiles*.

Shafiee, M. H., Hashemian, L., & Bayat, A. (2015). Seasonal Analysis of Flexible Pavement Response to Falling Weight Deflectometer. *International Journal of Pavement Research and Technology*, *8*(5), 346–352. https://doi.org/10.6135/ijprt.org.tw/2015.8(5).346

Sheng, D., Axelsson, K., & Knutsson, S. (1995a). Frost heave due to ice lens formation in freezing soils 1. Theory and verification. *Nordic Hydrology*, *26*(2), 125–146. https://doi.org/10.2166/nh.1995.0008

Sheng, D., Axelsson, K., & Knutsson, S. (1995b). Frost heave due to ice lens formation in freezing soils 1. Theory and verification. *Nordic Hydrology*, *26*(2), 125–146. https://doi.org/10.2166/nh.1995.0008

Sherman, G. (1982). Minimizing reflection cracking of pavement overlays. *NCHRP Synthesis of Highway Practice*, (92).

Shoop, S. A., & Bigl, S. R. (1997). Moisture migration during freeze and thaw of unsaturated soils: Modeling and large scale experiments. *Cold Regions Science and Technology*, *25*(1), 33–45. https://doi.org/10.1016/S0165-232X(96)00015-8

Simpson, A. L. (1999). Characterization of Transverse Profile. *Https://Doi-Org.Proxy.Lib.Uwaterloo.ca/10.3141/1655-24*, (1655), 185–191. https://doi.org/10.3141/1655-24

Sobhan, K., & Tandon, V. (2008). Mitigating reflection cracking in asphalt overlays using geosynthetic reinforcements. *Road Materials and Pavement Design*, *9*(3), 367–387. https://doi.org/10.1080/14680629.2008.9690124

Soenen, H., Vansteenkiste, S., & Kara De Maeijer, P. (2020). Fundamental Approaches to Predict Moisture Damage in Asphalt Mixtures: State-of-the-Art Review. *Infrastructures 2020, Vol. 5, Page 20*, *5*(2), 20. https://doi.org/10.3390/INFRASTRUCTURES5020020

Solaimanian, M., & Kennedy, T. W. (1993). *Predicting Maximum Pavement Surface Temperature Using Maximum Air Temperature and Hourly Solar Radiation*. 186.

Solatiyan, E., Bueche, N., & Carter, A. (2020). A review on mechanical behavior and design considerations for reinforced-rehabilitated bituminous pavements. *Construction and Building Materials*, *257*, 119483. https://doi.org/10.1016/J.CONBUILDMAT.2020.119483

Solatiyan, E., Bueche, N., & Carter, A. (2021). Laboratory evaluation of interfacial mechanical properties in geogrid-reinforced bituminous layers. *Geotextiles and Geomembranes*, *49*(4), 895–909. https://doi.org/10.1016/J.GEOTEXMEM.2020.12.014

Solatiyan, E., Ho, V. T., Bueche, N., Vaillancourt, M., & Carter, A. (2023). Evaluation of Crack Development Through a Bituminous Interface Reinforced With Geosynthetic Materials by Using a Novel Approach. *Transportation Research Record: Journal of the Transportation Research Board*, 036119812311660. https://doi.org/10.1177/03611981231166002/ASSET/IMAGES/LARGE/10.1177_03611981231166002-FIG9.JPEG

Stadler, A. T., & Carolina, N. (2001). *Geogrid Reinforcement of Piedmont Residual Soil*. Charlotte, North Carolina.

Steurer, P. M., Crandell,', J. H., & Member, A. (1995). Comparison of Methods Used to Create Estimate of Air-Freezing Index. *Journal of Cold Regions Engineering*, *9*(2), 64–74. https://doi.org/10.1061/(ASCE)0887-381X(1995)9:2(64)

Sudarsanan, N., Mohapatra, S. R., Karpurapu, R., & Amirthalingam, V. (2018). Use of Natural Geotextiles to Retard Reflection Cracking in Highway Pavements. *Journal of Materials in Civil Engineering*, *30*(4), 04018036. https://doi.org/10.1061/(asce)mt.1943-5533.0002195

Sun, B., Yang, L., Liu, Q., Wang, W., & Xu, X. (2011). Experimental study on cooling enhancement of crushed rock layer with perforated ventilation pipe under air-tight top surface. *Cold Regions Science and Technology*, *68*(3), 150–161. https://doi.org/10.1016/j.coldregions.2011.06.009

Sun, B.-X., Yang, L.-J., Wang, W., Zhang, J.-Z., & Wang, S.-J. (2012). Convective heat transfer and evaporative heat removal in embankment with perforated ventilation pipe. *Yantu Lixue/Rock and Soil Mechanics*, *33*, 674–680.

Sweidan, A. H., Heider, Y., & Markert, B. (2020). A unified water/ice kinematics approach for phase-field thermo-hydro-mechanical modeling of frost action in porous media. *Computer Methods in Applied Mechanics and Engineering*, *372*, 113358. https://doi.org/10.1016/j.cma.2020.113358

Taber, S. (1930). The Mechanics of Frost Heaving. *The Journal of Geology*, *38*(4), 303–317. Retrieved from http://www.jstor.org/stable/30058950

Talebsafa, M., Romanoschi, S. A., Papagiannakis, A. T., & Popescu, C. (2019). *Evaluation of Strains at the Bottom of the Asphalt Base Layer of a Semi-Rigid Pavement Under a Class 6 Vehicle; Evaluation of Strains at the Bottom of the Asphalt Base Layer of a Semi-Rigid Pavement Under a Class 6 Vehicle*. https://doi.org/10.1051/matecconf/201927108008

Tarefder, R. A., Asce, M., Islam, M. R., Asce, S. M., & Student, P. D. (2014). Measuring Fatigue Damages from an Instrumented Pavement Section due to Day-Night and Yearly Temperature Rise and Fall in Desert Land of the West. *Climatic Effects on Pavement and Geotechnical Infrastructure - Proceedings of the International Symposium of Climatic Effects on Pavement and Geotechnical Infrastructure 2013*, 78–88. https://doi.org/10.1061/9780784413326.008

Tarefder, R., Faisal, H., & Barlas, G. (2018). Freeze-thaw effects on fatigue LIFE of hot mix asphalt and creep stiffness of asphalt binder. *Cold Regions Science and Technology*, *153*, 197–204. https://doi.org/10.1016/J.COLDREGIONS.2018.02.011

Taylor, G. S., & Luthin, J. N. (1978a). A model for coupled heat and moisture transfer during soil freezing. *Canadian Geotechnical Journal*, *15*(4).

Taylor, G. S., & Luthin, J. N. (1978b). MODEL FOR COUPLED HEAT AND MOISTURE TRANSFER DURING SOIL FREEZING. *Canadian Geotechnical Journal*, *15*(4), 548–555. https://doi.org/10.1139/t78-058

Tighe, S. (2013). *Pavement Asset Design and Management Guide*. Ottawa, Ontario: Transportation Association of Canada (TAC).

Tingle, J. S., & Webster, S. L. (2003). Corps of Engineers Design of Geosynthetic-Reinforced Unpaved Roads. *Transportation Research Record*, (1849), 193–201. https://doi.org/10.3141/1849-21

Titan Environmental Containment. (n.d.). Products. Retrieved from https://www.titanenviro.com/products/soil-separation-and-filtration/

Titan Environmental Containment. (2017). *Spartan Road Grid TM 11EPM*.

Titan Environmental Containment. (2021a). *Product*.

Titan Environmental Containment. (2021b). *Swamp Grid 30*.

Titan Environmental Containment. (2022). *Installation Guide for Base Reinforcement*.

Tong, C., & Wu, Q. (1996). The effect of climate warming on the Qinghai-Tibet Highway, China. *Cold Regions Science and Technology*, *24*(1), 101–106. https://doi.org/10.1016/0165-232X(95)00012-Z

Tounsi, H., Rouabhi, A., & Jahangir, E. (2020). Thermo-hydro-mechanical modeling of artificial ground freezing taking into account the salinity of the saturating fluid. *Computers and Geotechnics*, *119*, 103382. https://doi.org/10.1016/j.compgeo.2019.103382

Tran, D. T., Sauzéat, C., Di Benedetto, H., & Pouteau, B. (2022). Effects of Water Saturation and Freeze-Thaw Cycles on Fatigue Behavior of Bituminous Mixtures. *RILEM Bookseries*, *27*, 671–677. https://doi.org/10.1007/978-3-030-46455-4_85/FIGURES/4

Ud Din, I. M., Mir, M. S., & Farooq, M. A. (2020a). Effect of Freeze-Thaw Cycles on the Properties of Asphalt Pavements in Cold Regions: A Review. *Transportation Research Procedia*, *48*, 3634–3641. https://doi.org/10.1016/J.TRPRO.2020.08.087

Ud Din, I. M., Mir, M. S., & Farooq, M. A. (2020b). Effect of Freeze-Thaw Cycles on the Properties of Asphalt Pavements in Cold Regions: A Review. *Transportation Research Procedia*, *48*, 3634–3641. https://doi.org/10.1016/J.TRPRO.2020.08.087

van der Walt, J. D., Scheepbouwer, E., & Tighe, S. L. (2018). Differential rutting in Canterbury New Zealand, and its relation to road camber. *International Journal of Pavement Engineering*, *19*(9), 798–804. https://doi.org/10.1080/10298436.2016.1208198

van Genuchten, M. T. (1980). A Closed-form Equation for Predicting the Hydraulic Conductivity of Unsaturated Soils. *Soil Science Society of America Journal*.

Wang, D. (2015). Simplified Analytical Approach to Predicting Asphalt Pavement Temperature. *Journal of Materials in Civil Engineering*, *27*(12), 04015043. https://doi.org/10.1061/(ASCE)MT.1943-5533.0000826/ASSET/82F5AAA1-BC39-4A38-BEDC-BE5EE60343C1/ASSETS/IMAGES/LARGE/FIGURE7.JPG

Wen, H., Wu, S., Mohammad, L. N., Zhang, W., Shen, S., & Faheem, A. (2016). Long-Term Field Rutting and Moisture Susceptibility Performance of Warm-Mix Asphalt Pavement. *Https://Doi.Org/10.3141/2575-11*, *2575*, 103–112. https://doi.org/10.3141/2575-11

West, R., Rodezno, C., Leiva, F., & Yin, F. (2018). *Development of a Framework for Balanced Mix Design, Project NCHRP, 20-07*.

Winter, J. M., Partridge, T. F., Wallace, D., Chipman, J. W., Ayres, M. P., Osterberg, E. C., & Dekker, E. R. (2021). Modeling the Sensitivity of Blacklegged Ticks (Ixodes scapularis) to Temperature and Land Cover in the Northeastern United States. *Journal of Medical Entomology*, *58*(1), 416–427. https://doi.org/10.1093/JME/TJAA179

Witczak, M. W., Kaloush, K., Pellinen, T., El-Basyouny, M., & Quintus, H. Von. (2002). Simple Performance Test for Superpave Mix Design. *Design*, 114. Retrieved from http://onlinepubs.trb.org/onlinepubs/nchrp/nchrp_rpt_465.pdf

Wong, W. G., Han, H. F., He, G. P., Qiu, X., Wang, K. C. P., & Lu, W. (2004). Effects of water on permanent deformation potential of asphalt concrete mixtures. *Materials and Structures 2004 37:8*, *37*(8), 532–538. https://doi.org/10.1007/BF02481577

Wu, Y., Ishikawa, T., Maruyama, K., Ueno, C., Yasuoka, T., & Okuda, S. (2022). Modeling Wicking Fabric Inhibition Effect on Frost Heave. *Applied Sciences 2022, Vol. 12, Page 4357*, *12*(9), 4357. https://doi.org/10.3390/APP12094357

Xu, T., & Huang, X. (2012). Investigation into causes of in-place rutting in asphalt pavement. *Construction and Building Materials*, *28*(1), 525–530. https://doi.org/10.1016/J.CONBUILDMAT.2011.09.007

Yaling, C., Gongqi, Y., Baoan, L., & Yu, S. (2014). Experimental study on application effects of thermal pipes along Chai-Mu Railway. *Electronic Journal of Geotechnical Engineering*, *19*(Z), 9623–9635.

Yasuoka, T., Ishikawa, T., Luo, B., Wu, Y., Maruyama, K., & Ueno, C. (2022). Coupled Analysis on Frost-Heaving Depression Effect of Geosynthetics Drainage Material for Road Pavement. *Lecture Notes in Civil Engineering*, *165*, 509–520. https://doi.org/10.1007/978-3-030-77234-5_42/FIGURES/9

Yin, F., Chen, C., West, R., Martin, A. E., & Arambula-Mercado, E. (2020). Determining the Relationship Among Hamburg Wheel-Tracking Test Parameters and Correlation to Field Performance of Asphalt Pavements. *Transportation Research Record*, *2674*(4), 281–291. https://doi.org/10.1177/0361198120912430

Yu, D., Jing, H., & Liu, J. (2022). Effects of Freeze–Thaw Cycles on the Internal Voids Structure of Asphalt Mixtures. *Materials*, *15*(10). https://doi.org/10.3390/MA15103560

Zakaria, M., & Lees, G. (1996). Rutting characteristics of unbound aggregate layers. *Construction and Building Materials*, *10*(3), 185–189. https://doi.org/10.1016/0950-0618(95)00084-4

Zapata, C. E., Witczak, M. W., Houston, W. N., & Andrei, D. (2007). Incorporation of Environmental Effects in Pavement Design. *Road Materials and Pavement Design*, *8*(4), 667–693. https://doi.org/10.1080/14680629.2007.9690094

Zhang, Jiupeng, Fan, Z., Fang, K., Pei, J., & Xu, L. (2016). Development and validation of nonlinear viscoelastic damage (NLVED) model for three-stage permanent deformation of asphalt concrete. *Construction and Building Materials*, *102*, 384–392. https://doi.org/10.1016/J.CONBUILDMAT.2015.10.201

Zhang, J.-Shan. (2010). *High temperature deformation and fracture of materials.* Cambridge, UK ; Woodhead Publishing.

Zhang, Jun, Alvarez, A. E., Lee, S. I., Torres, A., & Walubita, L. F. (2013). Comparison of flow number, dynamic modulus, and repeated load tests for evaluation of HMA permanent deformation. *Construction and Building Materials*, *44*, 391–398. https://doi.org/10.1016/J.CONBUILDMAT.2013.03.013

Zhang, M., Lai, Y., Li, S., & Zhang, S. (2006). Laboratory investigation on cooling effect of sloped crushed-rock revetment in permafrost regions. *Cold Regions Science and Technology*, *46*(1), 27–35. https://doi.org/10.1016/j.coldregions.2006.06.003

Zhang, T., Barry, R. G., Knowles, K., Heginbottom, J. A., & Brown, J. (1999). Statistics and characteristics of permafrost and ground-ice distribution in the Northern Hemisphere. *Polar Geography*, *23*(2), 132–154. https://doi.org/10.1080/10889379909377670

Zhang, Y., Asce, S. M., Michalowski, R. L., & Asce, F. (2014a). *Multiphysical Modeling and Numerical Simulation of Frost Heave and Thaw Settlement*. 2735–2744. https://doi.org/10.1061/9780784413272.264

Zhang, Y., Asce, S. M., Michalowski, R. L., & Asce, F. (2014b). *Thermal-Hydro-Mechanical Modeling of Frost Action in Frost-Susceptible Soils*. 735–744. https://doi.org/10.1061/9780784413388.077

Zhang, Y., & Michalowski, R. L. (2015). Thermal-Hydro-Mechanical Analysis of Frost Heave and Thaw Settlement. *Journal of Geotechnical and Geoenvironmental Engineering*, *141*(7), 04015027. https://doi.org/10.1061/(asce)gt.1943-5606.0001305

Zhao, Z., Jiang, J., Ni, F., Dong, Q., Ding, J., & Ma, X. (2020). Factors affecting the rutting resistance of asphalt pavement based on the field cores using multi-sequenced repeated loading test. *Construction and Building Materials*, *253*, 118902. https://doi.org/10.1016/J.CONBUILDMAT.2020.118902

Zheng, G., Alimohammadi, H., Zheng, J., Asce, M., Schaefer, V. R., Student, M. S., & Student, P. D. (2021). *Effectiveness of Geosynthetics in the Construction of Roadways: A Full-Scale Field Studies Review*. 223–232. https://doi.org/10.1061/9780784483411.022

Zhi, W., Yu, S., Wei, M., Jilin, Q., & Wu, J. (2005). Analysis on effect of permafrost protection by two-phase closed thermosyphon and insulation jointly in permafrost regions. *Cold Regions Science and Technology*, *43*(3), 150–163. https://doi.org/10.1016/j.coldregions.2005.04.001

Zhou, F., Fernando, E., Scullion, T., & Institute, T. T. (2008). *A review of performance models and test procedures with recommendations for use in the Texas m-e design program.* https://doi.org/10.21949/1503647

Zhou, G., Zhou, Y., Hu, K., Wang, Y., & Shang, X. (2018). Separate-ice frost heave model for one-dimensional soil freezing process. *Acta Geotechnica*, *13*(1), 207–217. https://doi.org/10.1007/s11440-017-0579-4

Zhou, J., & Li, D. (2012a). Numerical analysis of coupled water, heat and stress in saturated freezing soil. *Cold Regions Science and Technology*, *72*, 43–49. https://doi.org/10.1016/j.coldregions.2011.11.006

Zhou, J., & Li, D. (2012b). Numerical analysis of coupled water, heat and stress in saturated freezing soil. *Cold Regions Science and Technology*, *72*, 43–49. https://doi.org/10.1016/j.coldregions.2011.11.006

Zornberg, J. G. (2017). Functions and Applications of Geosynthetics In Roadways. *Procedia Engineering*, *189*, 298–306. https://doi.org/https://doi.org/10.1016/j.proeng.2017.05.048

Zornberg, J. G., Azevedo, M., Sikkema, M., & Odgers, B. (2017). Geosynthetics with enhanced lateral drainage capabilities in roadway systems. *Transportation Geotechnics*, *12*, 85–100. https://doi.org/10.1016/j.trgeo.2017.08.008

Appendices

Appendix A

Frost Tube Pictures

This appendix includes a series of photographs capturing the frost tubes on a monthly basis during the freezing and thawing period in 2023. The specific dates for these images are as follows: January 19, February 13, March 1, March 14, March 27, April 14, and May 10. Notably, the frost tubes were consistently positioned in a uniform order in all the pictures, with those in the CT section, GG section, and GC section arranged from left to right.


February 13, 2023


March 1, 2023


March 14, 2023


March 27, 2023


April 14, 2023
SLOW


May 10, 2023

Appendix B

Pavement Temperature Predictive Model Fitting Results

This appendix provides the fitting results of the regression models to predict the pavement temperatures discussed in Chapter 9. The scatter plots are the measured data, while the solid line represents the fitted model, with 95% prediction bounds shown as dashed lines.

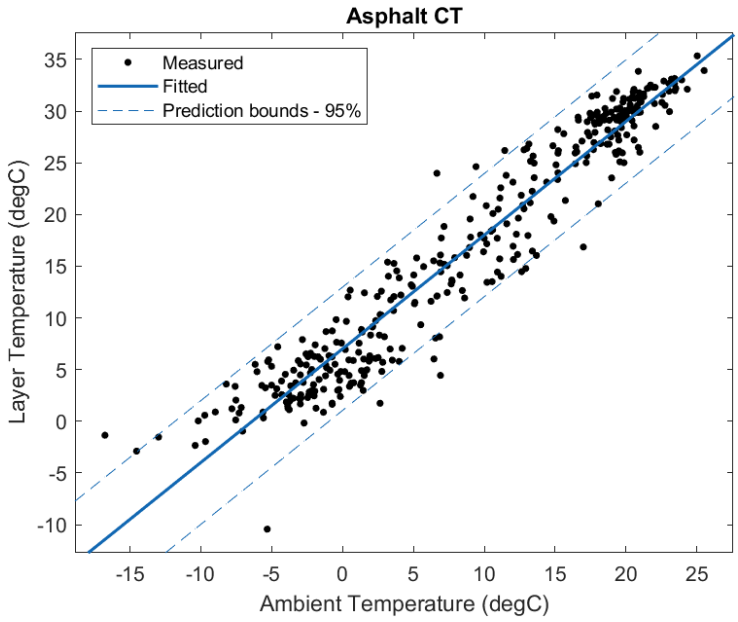

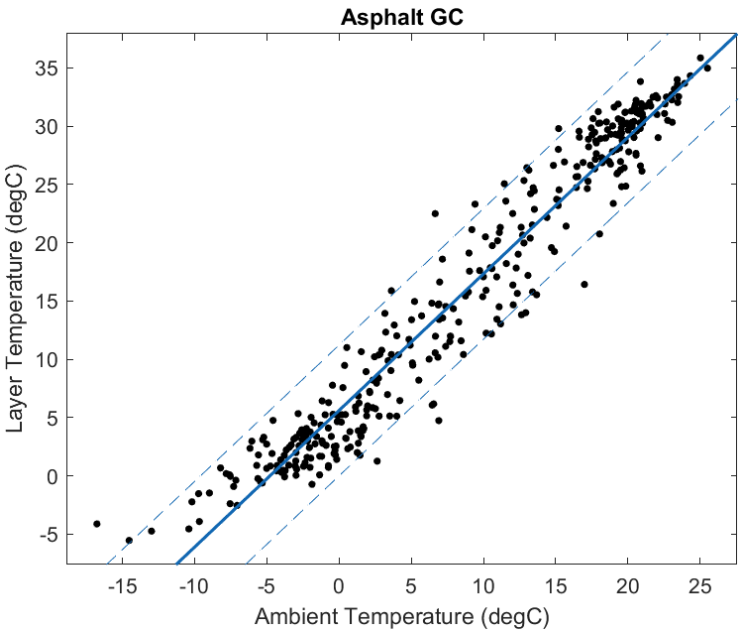

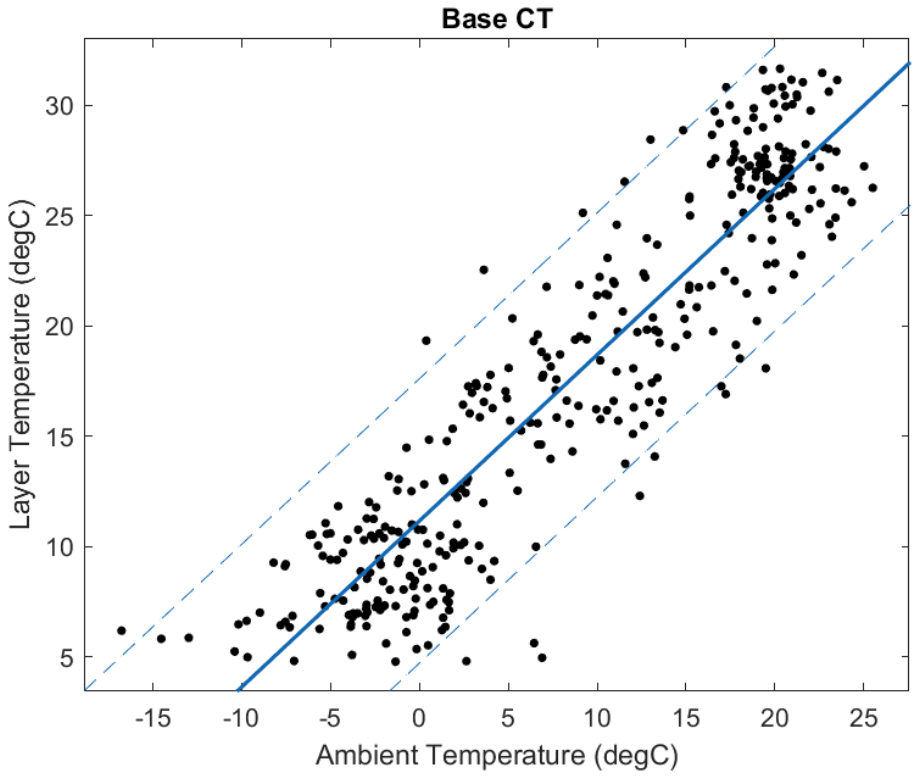
Base CT
Layer Temperature (degC)
Ambient Temperature (degC)
30
25
20
15
10
5
-15
-10
-5
0
5
10
15
20
25

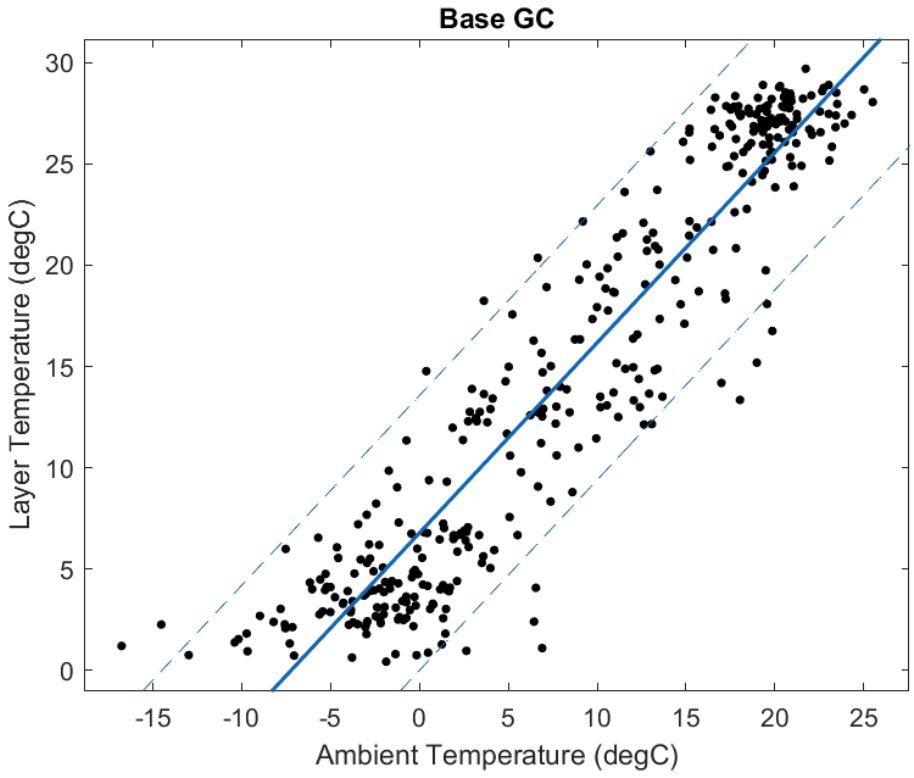
Base GC
Layer Temperature (degC)
Ambient Temperature (degC)
30
25
20
15
10
5
0
-15
-10
-5
0
5
10
15
20
25

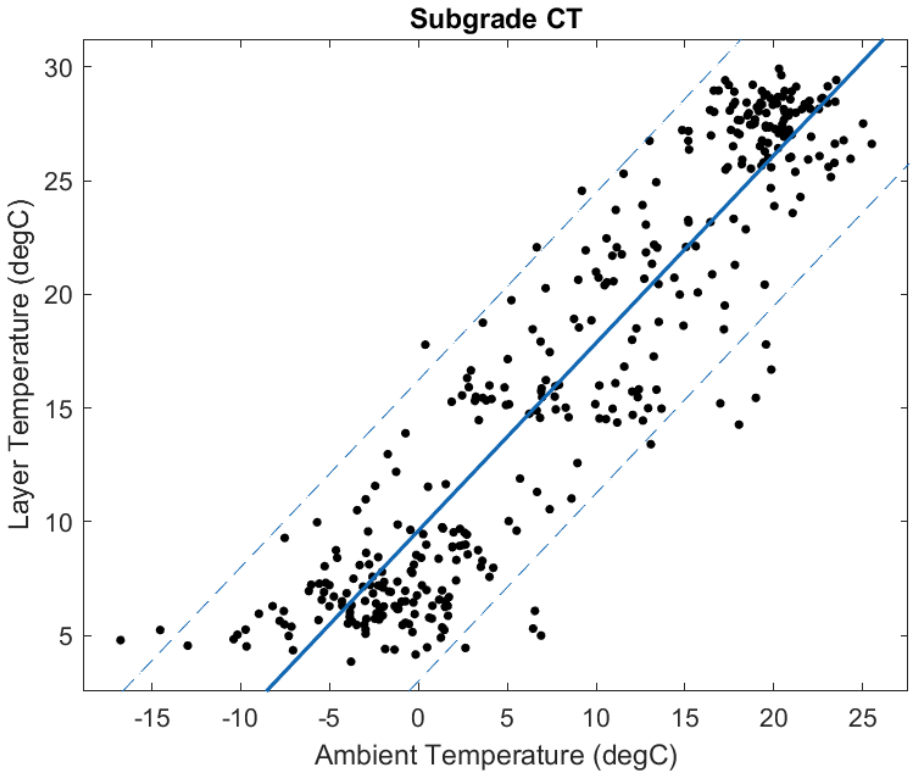
Subgrade CT
Layer Temperature (degC)
Ambient Temperature (degC)
30
25
20
15
10
5
-15
-10
-5
0
5
10
15
20
25

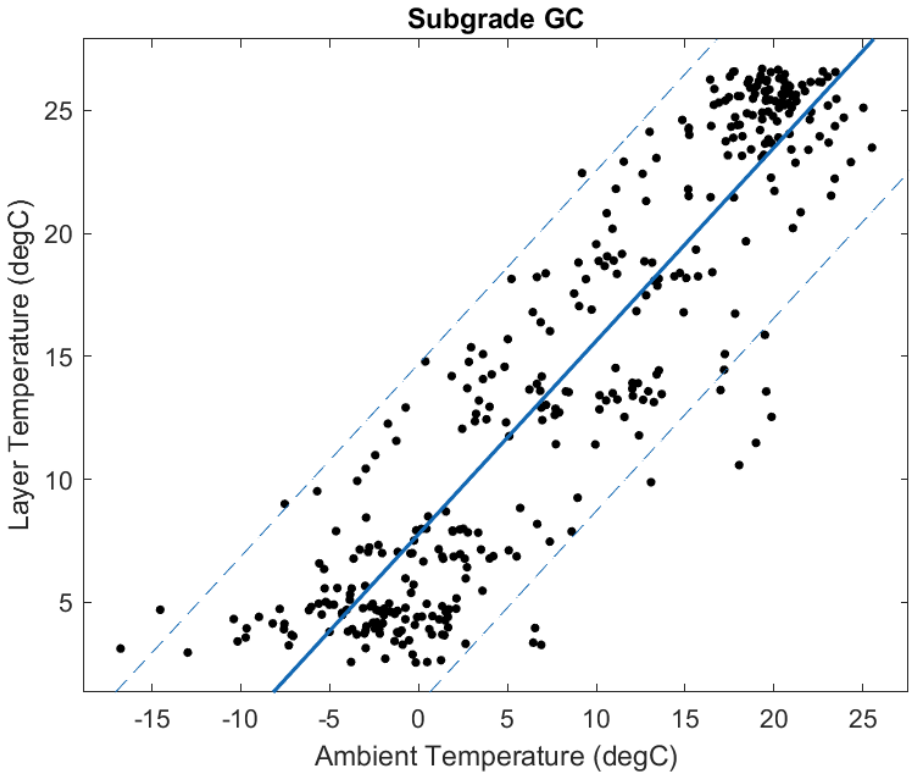
Subgrade GC
Layer Temperature (degC)
Ambient Temperature (degC)
25
20
15
10
5
-15
-10
-5
0
5
10
15
20
25